M&MS

INDEX 330930 ISSN 0860-8229

2017 3

METROLOGY
AND MEASUREMENT SYSTEMS

QUARTERLY, VOLUME 24

WARSAW 2017

PAN
POLSKA AKADEMIA NAUK

POLISH ACADEMY OF SCIENCES
COMMITTEE ON METROLOGY AND SCIENTIFIC INSTRUMENTATION

METROLOGY AND MEASUREMENT SYSTEMS
Quarterly of Polish Academy of Sciences

INTERNATIONAL PROGRAMME COMMITTEE

Andrzej ZAJĄC, Chairman
Military University of Technology, Poland

Bruno ANDO
University of Catania, Italy

Martin BURGHOFF
Physikalisch-Technische Bundesanstalt, Germany

Marcantonio CATELANI
University of Florence, Italy

Numan DURAKBASA
Vienna University of Technology, Austria

Domenico GRIMALDI
University of Calabria, Italy

Laszlo KISH
Texas A&M University, USA

Eduard LLOBET
Universitat Rovira i Virgili, Tarragona, Spain

Alex MASON
Liverpool John Moores University, The United Kingdom

Subhas MUKHOPADHYAY
Massey University, Palmerston North, New Zealand

Janusz MROCZKA
Wrocław University of Technology, Poland

Antoni ROGALSKI
Military University of Technology, Poland

Wiesław WOLIŃSKI
Warsaw University of Technology, Poland

Language Editor
Andrzej STANKIEWICZ
astankiewicz6@o2.pl

Technical Editor and Secretary
Agnieszka KONDRATOWICZ
Gdańsk University of Technology
metrology@pg.gda.pl

Webmaster
Michał KOWALEWSKI
Gdańsk University of Technology
Michal.Kowalewski@eti.pg.gda.pl

EDITORIAL BOARD

Editor-in-Chief

Janusz SMULKO
Gdańsk University of Technology, Poland
jsmulko@eti.pg.gda.pl

Associate Editors

Zbigniew BIELECKI
Military University of Technology, Poland
zbielecki@wat.edu.pl

Vladimir DIMCHEV
Ss. Cyril and Methodius University, Macedonia
vladim@feit.ukim.edu.mk

Krzysztof DUDA
AGH University of Science and Technology, Poland
kduda@agh.edu.pl

Janusz GAJDA
AGH University of Science and Technology, Poland
jgajda@agh.edu.pl

Teodor GOTSZALK
Wrocław University of Technology, Poland
teodor.gotszalk@pwr.wroc.pl

Ireneusz JABŁOŃSKI
Wrocław University of Technology, Poland
ireneusz.jablonski@pwr.wroc.pl

Piotr JASIŃSKI
Gdańsk University of Technology, Poland
pijas@eti.pg.gda.pl

Piotr KISAŁA
Lublin University of Technology, Poland
p.kisala@pollub.pl

Manoj KUMAR
University of Hyderabad, Telangana, India
manoj@uohyd.ac.in

Grzegorz LENTKA
Gdańsk University of Technology, Poland
lentka@eti.pg.gda.pl

Czesław ŁUKIANOWICZ
Koszalin University of Technology, Poland
czeslaw.lukianowicz@tu.koszalin.pl

Rosario MORELLO
University Mediterranean of Reggio Calabria, Italy
rosario.morello@unirc.it

Fernando PUENTE LEÓN
University Karlsruhe, Germany
f.puente@me.com

Petr SEDLAK
Brno University of Technology, Czech Republic
sedlakp@feec.vutbr.cz

Hamid M. SEDIGHI
Shahid Chamran University of Ahvaz, Ahvaz, Iran
hmsedighi@gmail.com

Roman SZEWCZYK
Warsaw University of Technology, Poland
szewczyk@mchtr.pw.edu.pl

Journal is indexed by Journal Citation Reports/Science. Impact Factor: 1.140 (5-Year Impact Factor 1.092).
More information about aims and scope of the journal – inner side of the back cover.
Instructions for Authors – last pages of the issue.

Edition was financially supported by the Polish Academy of Science and Gdańsk University of Technology,
Faculty of Electronics, Telecommunications and Informatics.

Ark. wyd. 11,48 Ark. druk. 9,18
Papier offsetowy kl. III 80g 70 x 100 cm
Print run 120 copies

Druk: Centrum Poligrafii Sp. z o.o.
ul. Łopuszańska 53
02-232 Warszawa

www.czasopisma.pan.pl PAN www.journals.pan.pl
POLSKA AKADEMIA NAUK

Metrol. Meas. Syst., Vol. 24 (2017), No. 3, pp. 441–461.

METROLOGY AND MEASUREMENT SYSTEMS
Index 330930, ISSN 0860-8229
www.metrology.pg.gda.pl

DEVELOPMENT AND EXPERIMENTAL VALIDATION OF A CORRELATION MONITOR TOOL BASED ON THE ENDOGENOUS PULSED NEUTRON SOURCE TECHNIQUE

Mohammad Arkani 1), **Hossein Khalafi** 1), **Naser Vosoughi** 2), **Samad Khakshournia** 1)

1) Reactor and Nuclear Safety Research School, Nuclear Science & Technology Research Institute (NSTRI), 143995-1113, Tehran, Iran
(✉ markani@aeoi.org.ir, +98 21 88 221 103, *hkhalafi@aeoi.org.ir, skhakshournia@aeoi.org.ir)*
2) Sharif University of Technology, Azadi Avenue, 11365-11155, Tehran, Iran (nvosoughi@sharif.ir)

Abstract

A correlation measuring tool for an endogenous pulsed neutron source experiment is developed in this work. Paroxysmal pulses generated by a bursts of neutron chains are detected by a 10-kbit embedded shift register with a time resolution of 100 ns. The system is implemented on a single reprogrammable device making it a compact, cost-effective instrument, easily adaptable for any case study. The system was verified experimentally in the *Esfahan heavy-water zero power reactor* (EHWZPR). The results obtained by the measuring tool are validated by the Feynman-α experiment, and a good agreement is seen within the boundaries of statistical uncertainties. The theory of the methods is briefly initiated in the text. Also, the system structure is described, the experimental results and their uncertainties are discussed, and neutron statistics in EHWZPR is examined experimentally.

Keywords: endogenous pulsed neutron source experiment, neutron noise fluctuation, zero power reactor noise, Esfahan heavy-water zero power reactor, neutron correlation.

1. Introduction

Neutron noise fluctuations observed in a form of correlated random pulses or signals from neutron detectors inside or nearby a nuclear reactor core are an object of a well-established and standard branch of studies, applications, and diagnosis in the field of stochastic experimental nuclear reactor physics. The knowledge of data treatment of neutron noise fluctuations originated by microscopic characteristics of the core is called *zero power reactor noise* (ZPRN) theory. The ultimate aim of ZPRN analysis is to measure and diagnose the kinetic parameters of the reactor core which are determined by the geometry and material composition of the system [1]. The main advantageous feature of the method is its complete independence from external excitation or perturbation of the system itself which makes it a valuable technique. The experimental methods of ZPRN analysis are categorized by several different techniques that might be classified in five major categories: analysis of probability profiles of neutron counts, analysis of moments of neutron count distributions, analysis of correlation among neutron counts in the time domain, correlation polarities in the time domain, and analysis of reactor power level in the frequency domain [2–6]. Each technique has its own data analysis and experimental data collection method [7–18]. The endogenous (inherent) pulsed neutron source technique is a branch of correlation analysis of neutron counts in the time domain [3] (the third item in the above categories of ZPRN analysis). The basic principle of the technique is the conditional start of a multichannel scaler. Bursts of neutron chains are detected by a conditional pulse counter and the delay time-dependent correlation function of the correlative chain neutrons is registered by the multichannel scaler. The time at which a burst of neutron chains

---

Article history: received on Feb. 13, 2017; accepted on Mar. 31, 2017; available online on Sep. 01, 2017; DOI: 10.1515/mms-2017-0043.

is detected is the time origin for all recorded data. A prompt neutron decay constant of the core is determined by analysing the acquired data.

Neutrons released by fission chains are correlated in time. Two types of correlations are possible. A positive correlation – the existence of a pulse or event at a certain time makes the probability of another pulse or event increased immediately afterwards; this kind of correlation is seen in nuclear reactor systems where neutrons are linked in time by fission chains. A negative correlation – the existence of a pulse or an event at a certain time makes the probability of another pulse or event decreased immediately afterwards; this type of correlation is usually generated by the dead time behaviour of particle detection systems. Radioactive particles emitted by decaying type radiation sources are random sequences obeying the Poisson distribution law. The time interval between consecutive pulses is not invariant but follows a purely exponential probability. This kind of random sequences is usually generated by constant sources of decaying types, whose half-lives are practically infinite in comparison with the observation time. A random sequence is not a correlated one; every decaying process is an independent nuclear process [19, 20].

Considering the statistics of the above mentioned random processes, three different values of *variance to mean* (VTM) ratio of the counts are possible: $VTM > 1$ for a positive correlation (in a multiplying medium), $VTM = 1$ for a pure Poisson process, and $VTM < 1$ for a process of negative correlation. Note that $VTM > 1$ means that the neutron fluctuations inside the medium are larger than those in the corresponding pure Poisson process (a Poisson process with the same mean value of neutron counts). It is noticeable that a cluster of condensed pulses appearing in time due to a burst of neutron chains means a long time separation of the bursts by the background or random statistics of the system.

In a multiplying medium, such as a subcritical system, random processes are not purely correlated in time. The whole process is the superimposition of an uncorrelated random process and the correlated process of neutrons originated from common ancestors of fission chains. The ratio of the correlated and uncorrelated portions of the process is usually called a *signal to background ratio* (SBR) which is a measure of correlation in the system. In fact, the uncorrelated portion is much larger than the correlated one, and the extraction of data needs a wisely adjusted experimental set-up based on physical knowledge about system statistics and its properties. Since the *Esfahan heavy-water zero power reactor* (EHWZPR), the case study of the problem in the present work, is a heavy-water reactor, producing photoneutrons is probable. Therefore, the background portion of the neutron statistics is physically strong in comparison with the correlated sequences in the system.

Some physical simplifications assumed in this work are summarized as follows:

- The first fundamental assumption for ZPRN analysis techniques is an ergodic hypothesis; the reactor is in steady-state operating conditions, and the evolution of neutron population is expected to be stationary. The reactor to be studied is stable, and its stochastic features do not vary with time. If different measurements are repeated in different periods, the same results within the statistical uncertainties are seen.
- The basic assumption of the background theory of the experiments is the point reactor supposition. Therefore, the point reactor assumption should be satisfied by the conditions of the problem. The results obtained by a detector positioned in the core should represent the features of the whole system.
- The delayed neutrons and photoneutrons are considered as the background radiation in EHWZPR. Only prompt neutron fluctuations are analysed.

Correlation monitors have been used in different applications for measurement of physical parameters [21, 22]. In reactor noise studies, the theory has been studied lately, and different apparatuses have been developed for ZPRN experiments [3–4, 9]. Analogue monitors based on a single rate meter or two inter-compensated rate meters and digital monitors are also applied [16−17, 23].

The main idea of the endogenous pulsed neutron source method is to compare the neutron counts with the average or a threshold level. Bursts of neutron chains are detected and selected by a comparator, then, a recording apparatus is triggered to collect the correlation data. This process is repeated for many times until acceptable statistical accuracy is met. In the present work, a correlation monitor is developed based on *field programmable gate arrays* (FPGAs). A shift register as a proven technique of neutron correlation measurement [25−25] is employed. A 10-kbit serial-in-serial-out shift register is implemented in the design to record enough history of the random input process with a fine discretization of time. Parameters of the design are possible to be adjusted by the experimenter according to the case study of the problem. Considering the physical properties of EHWZPR ($\alpha_c \approx 6.84 \pm 0.088$ s^{-1}, the prompt neutron decay constant at critical state of the core) [13], one millisecond of the input sequence is stored in the shift register at 100 ns of time resolution. Also, an embedded zero advanced time multichannel scaler is designed and built into the device. The neutron counts are registered by the device every millisecond after triggering by a digital burst detection circuit. The proposed equipment can save the accumulated data at a different number of scans performed on the burst of neutron chains. The system is tested and validated in EHWZPR by experiment, and the results are compared with the information obtained by the Feynman-α experiment. A good agreement between the results is seen. The proposed system is a cost-effective and compact instrument based on the state-of-the-art digital electronic technology. The data on neutron noise fluctuations in heavy-water moderated critical assemblies is published elsewhere [26] but − regarding the characteristic neutron noise in heavy-water and graphite-reflected reactors − few papers have been published in the literature on the subject. Thus, the ZPRN analysis is mainly applied to the fast and light-water moderated systems [27−30]. Using the proposed measuring tool, an experimental study on neutron noise fluctuations in EHWZPR is performed. Also, the uncertainty of the results is analysed. The results obtained by the endogenous pulsed neutron source method are validated by the Feynman-α experiment.

2. Background theory

2.1. Endogenous pulsed neutron source method

The natural fluctuations of neutron density in a multiplying medium produce prompt paroxysmal pulses (due to bursts of neutron chains) which are higher than the average level, and they decay to lower levels according to the exponential law. The slope of the exponent is the prompt neutron decay constant of the core. The paroxysmal pulses are detected to generate the triggering signal. This detection leads to selecting the most important portion of the random sequence which contains information about correlated neutrons. As pulses are produced by the natural fluctuations, the method is named as endogenous or inherent pulsed neutron source experiment. Note that, in the pulsed neutron source experiment [31], bursts of neutron chains are induced by an external pulse mode neutron source. The equation describing the experimental results of the two methods are the same as:

$$n(t)=C_C\,exp(-\alpha t)+U_C. \tag{1}$$

where: U_C is the mean neutron count (the background or uncorrelated count); C_C is the neutron count of the starting channel (the correlated count); α is the prompt neutron decay constant, and t is a time after detection of paroxysmal pulses (or after pulse injection in the pulsed neutron source method). Parameters of this equation are estimated by curve fitting to the experimental data. The mean neutron count in a time interval T is defined as [3]:

$$U_C = \begin{cases} <F> \varepsilon T, & \text{in critical reactor} \\ \\ \dfrac{S_o \varepsilon T}{\bar{\upsilon}\left(1-k_{eff}\right)}, & \text{in subcritical reactor drived by an external neutron source} \end{cases} \tag{2}$$

where: $<F> = \frac{1}{T}\int_0^T F(t)dt$. Mean fission rate: ε – neutron detection efficiency (number of neutrons detected per fission); S_o – external neutron source power; $\bar{\upsilon}$ – Mean number of neutrons released per fission; k_{eff} – effective multiplication factor.

Usually, the measuring time of the endogenous pulsed neutron source method is relatively long. The relation between the data collection time, $T_{Collection}$, correlated counts, C_C, and other physical parameters of the system is introduced as (3) [7]. Note that $T_{Collection}$ is the amount of time which is taken by the experiment for data collection to meet an acceptable experimental uncertainty. It is clear that the data acquisition system starts by paroxysmal pulses and then stops when the scan is finished:

$$T_{Collection} = \frac{C_C}{<F> \times \varepsilon \times T \times \theta}, \tag{3}$$

where θ is the product of a repetition rate and a signal to background ratio, which is defined by (4):

$$\theta = R \times SBR, \tag{4}$$

where: SBR is a signal to background ratio; and R is a repetition rate of paroxysmal neutron pulses. As the repetition rate increases, the number of scans per unit time is also increased. Therefore, the data collection time is decreased. A larger SBR means a lower background in comparison with the signal. A better signal to background ratio leads to a shorter time for data collection. As a result, there is an inverse relationship between $T_{Collection}$ and θ. The R and SBR parameters are defined by (5) and (6), respectively:

$$SBR = \frac{C_C}{U_C}, \tag{5}$$

$$R = \frac{1}{T} \times \sum_{i=\gamma}^{\infty} P_i, \tag{6}$$

where: P_i is the probability of counting i pulses within the time interval T; and γ is a threshold condition for detection of the bursts of neutron chains. Other parameters have the same definitions as given in the previous equations.

This type of technique can be considered as an intermediate method between the Rossi-α experiment [2] and the classic pulsed neutron source technique, showing similarities to both of them in the expression describing the experimental results (refer to (1)). Therefore, the endogenous pulsed neutron source technique enables to analyse neutron noise in thermal reactors for a reasonably acceptable measurement time, while the Rossi-α method is widely known as a time-consuming method in such systems. The endogenous pulsed neutron source experiment also features practical advantages when compared with pulsed neutron source measurements since the expensive apparatus of the pulsed neutron source is no longer necessary. Furthermore, the setting up of the experiment and the reactor operation procedure are considerably simplified.

2.2. Feynman-α method

Neutrons in a non-multiplying medium generated by a Poisson neutron source have zero correlation with each other. Therefore, the random process observed at the output of the neutron detector is mostly similar to a Poisson distribution, the only distortion on the process is the dead time effect of the detection system [32]. Conversely, in a multiplying medium, neutrons are chain-correlated. Therefore, the process is different from a Poisson distribution and a larger standard deviation in comparison with a non-multiplying medium is seen. A larger value of standard deviation means larger fluctuations of neutron density in the core. A ratio of variance and mean of neutron counts in a specific time window (τ) is a measure of statistical fluctuations. It is defined as:

$$VTM = \frac{\overline{C^2} - \overline{C}^2}{\overline{C}}. \tag{7}$$

where: C is the number of neutrons counted in a time window. As neutron chains in a nuclear reactor core are correlated in time, the distribution differs from the Poisson process. Therefore, besides uncorrelated neutron counts with a Poisson distribution (the background term or uncorrelated neutrons from other sources or other uncorrelated neutron chains), there also exist correlated neutrons. That is why the statistics deviate from the Poisson distribution. The degree of deviation is expressed by Y parameter in the Feynman-α formula as [2]:

$$\frac{\overline{C^2} - \overline{C}^2}{\overline{C}} = 1 + Y, \tag{8}$$

the Y parameter is expressed by (9):

$$Y = \frac{\overline{\nu_p(\nu_p - 1)}}{\tau_f^2}\frac{\varepsilon}{\alpha^2}\left(1 - \frac{1-\exp(-\alpha\tau)}{\alpha\tau}\right), \tag{9}$$

where: ε is a neutron detection efficiency (the number of neutrons detected per fission); τ_f is the inverse of $\upsilon\Sigma_f$ (the product of neutron velocity and microscopic fission cross-section), and ν_p is the average number of prompt neutrons released per fission. Y is a measure of deviation from the Poisson distribution. Y is determined at different values of time windows. The curve-fitting method is used to fit (9) to the experimental data to obtain an estimation of α parameter. A novel method of data analysis is proposed by [33] which reduces the machine time required for the experiment and increases the statistical accuracy. This technique is called bunching method. More details on the Feynman-α experiment are available elsewhere [3–4, 5–6, 34].

3. System design and its architecture

Neutron fluctuations in a multiplying medium are superimposition of correlated and uncorrelated random processes. Therefore, selected portions of the pulse sequences have to be recorded. As correlated pulse sequences are the desired data to be recorded, the trigger signal is asserted by positive fluctuations (burstsof neutron chains) to enable the data storage by the *multichannel scaler* (MCS). The heart of correlation monitor developed in the present work is a circuit for detecting bursts of neutron chains. Fig. 1 shows the method employed in this work for trigger generation. The first stage is a synchronizing block, for synchronization of random input pulses with a 10 MHz system clock. A 10-kbit serial-in serial-out shift register provides a moving storage for the previous pulses during the last millisecond with a 100 ns time resolution. Regarding the dead time of the neutron detectors (a few microseconds) and the counting rate of the detector during the experiment (~30000 cps), the time resolution is good enough. However, finer time discretization is also possible at the expense of additional hardware resource in the form of a deeper shift register. Input pulses and output pulses of the shift register block are counted by two separate 64-bit up-counters. By subtraction of the counts (counted by the two counter blocks), the number of pulses within the last millisecond of time is calculated. The result is compared with a pre-set threshold value for triggering the MCS block. In Fig. 2, a general schematic diagram of the system is presented. Except for the starting channel of the MCS from which its data are supplied by the circuit shown in Fig. 1, the up-counter block provides neutron counts in every millisecond after triggering. Any trigger signal starts the recording process by Nios II CPU interruption [35]. Communication with the computer as well as internal settings of the system are accomplished by the soft core processing unit. More details are shown in Figs. 1 and 2.

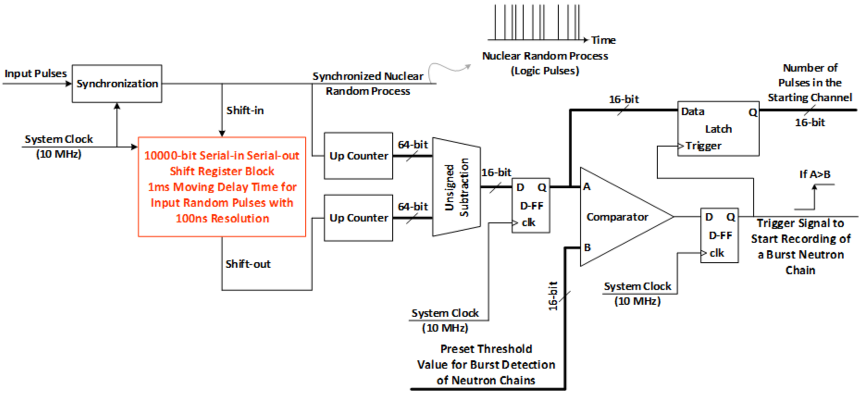

Fig. 1. The digital circuit for detection of positive fluctuations of neutron noise, generated by bursts of neutron chains.

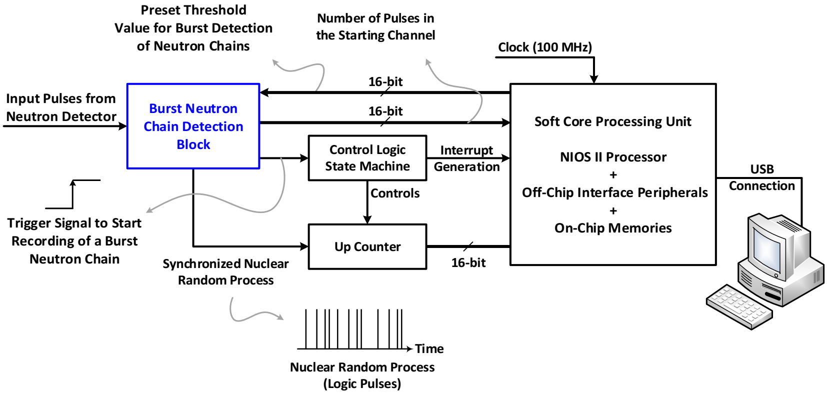

Fig. 2. A general block diagram of the correlation monitor for endogenous pulsed neutron source experiment, the system proposed in the present work.

4. Esfahan heavy-water zero power reactor (EHWZPR)

A very useful thermal system for experimental research on neutron physics in heavy-water moderated systems is EHWZPR, a heavy-water moderated nuclear research reactor. In this system, natural metallic uranium fuel elements are arranged in a 20 cm lattice pitch. The periphery of the core is filled with graphite as a reflector blanket. The present configuration includes 112 fuel elements. The structural materials including clad, top and bottom grid plates and reactor tank are made of nuclear-grade aluminium alloy. The cylindrical reactor tank dimensions are around 240 cm in diameter and 250 cm in height. A typical thermal power of the reactor is equal to 10 W. It is also possible for the reactor to operate at 100 W based on ratified experimental procedures approved by the reactor safety committee. The main actuator for reactor control is a precise water level adjusting system.

Two independent and diverse safety systems are designed as the reactor protection system (two safety rods and three dumping moderator valves). As a design basis accident, in the case of loss of electrical power, the safety rods drop into the core by the gravity and within less than three seconds, 80 cm decrease in water level is guaranteed by three normally open valves of the dumping system. As the moderator is heavy-water, the reactor core's size is big. No fuel depletion calculation is needed, as this is a zero power reactor. Therefore, this is an ideal case study for research purposes on reactor physics. The average prompt neutron lifetime is around 944 ± 10 µs [13] defining the reactor as a markedly thermal system. The present core configuration of the reactor is shown in Fig. 3. Elements of the core are demonstrated graphically. Some general specifications are given in Table 1 [36].

The system can function as a useful facility for research on physical properties of heavy-water natural uranium reactors. Also, training of the experimenters and academic teaching, as well as providing a useful tool for verifying and improving theoretical calculations are other major responsibilities of the facility.

The experiment performed in the present work in EHWZPR uses a Helium-3 in-core neutron detector. The position of the detector is located in the physical mid-height of the core. The top view of the location is shown in Fig. 3.

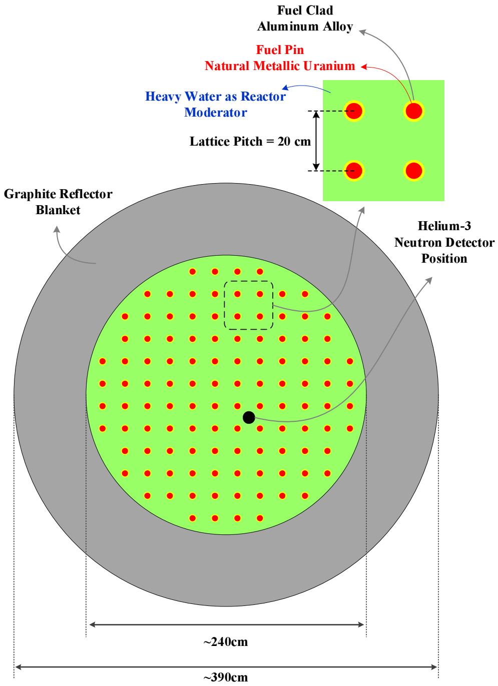

Fig. 3. EHWZPR core configuration; 112 fuel elements are loaded.
The location of the in-core neutron detector is also shown.

5. Experimental set-up

Figure 4 shows the experimental set-up employed in this work. To achieve the best timing features, the Helium-3 neutron detector and its preamplifier are assembled in a stainless steel housing. Note that the dead time of the detector used in the present work has been recently studied [32]. The location of the in-core neutron detector is shown in this figure. The preamplifier performs impedance matching as well as amplification of a micro-scale signal provided by the neutron detector. A coaxial cable connects the neutron detector to the amplifier and other nuclear electronic modules located in the laboratory room. Note that when EHWZPR is in operation, the radiation dose level of the reactor hall is increased. Therefore, no operating personnel is allowed to stay in the radiation area. As a result, the remote location of the measuring equipment is obligatory. In the laboratory room, the signal is first amplified and then converted to the logic pulses by a time pick-off module. Three different data acquisition systems are connected in parallel to collect the counting rate of pulses, to perform the Feynman-α analysis, and to measure the correlation of sequences using the endogenous pulsed neutron source *data acquisition* (DAQ) system. The data collected by each DAQ system are sent to an independent computer located in the laboratory room.

Table 1. A summary of important specifications of EHWZPR.

Item	Specification
Fuel Elements	Natural Metal Uranium Fuel Rods: Diameter: ~3.5 cm Height: ~200 cm
Moderator	Heavy-water
Lattice Pitch	20 cm (Can be changed in four different lattice pitches)
Reactor Tank	Made of Aluminium Alloy: Diameter: ~ 240 cm Height:~ 250 cm
Reflector	~75 cm Graphite Thickness at the periphery of the core
Reactor Thermal Power	Lower than 10 W (maximum operation time is about half an hour a day) Lower than 100 W (must be permitted by the reactor safety committee)
Safety Systems	Two diverse and redundant safety systems: - Two Safety Rods - Emergency Dumping System (Three normally open valves)
Reactor Control	Water level adjustment and two control rods
ℓ (Prompt neutron lifetime)	944 ± 10 [μs]
β_{eff} [pcm] (Effective delayed neutron fraction)	665.1

6. Results and discussion

In Fig. 5, counting rates of the neutron detector after reactor start-up are shown. During the first 6500 s, heavy water was injected into the core. A multiplication factor of EHWZPR core was controlled by a precise adjustment of the heavy-water level. The injection of the moderator was carried out through six stages in a safe and careful manner; every increase of the water level took about 15 minutes. Water levels are shown in the figure. Around 15 minutes after the water level had been adjusted at 1773.4 mm (to reach the steady state conditions of the system statistics), the data collection for Feynman-α and endogenous pulsed neutron source experiments was started. The data were acquired by the systems in an interval between 7500 s and 12500 s (5000 s data collection time). During the experiments, the mean value of neutron counts was about 30000 cps. The heavy-water critical level was about 1800 mm. Based on the reactivity value of the moderator (13.7 ± 0.41 pcm per millimetre of the heavy-water level of the moderator), an approximate multiplication factor at 1773.4 mm was estimated to be 0.9963. During the experiment, the reactor was held in the subcritical state. No external neutron source was employed as background neutrons in the heavy-water moderated system are strongly generated by the photoneutron production.

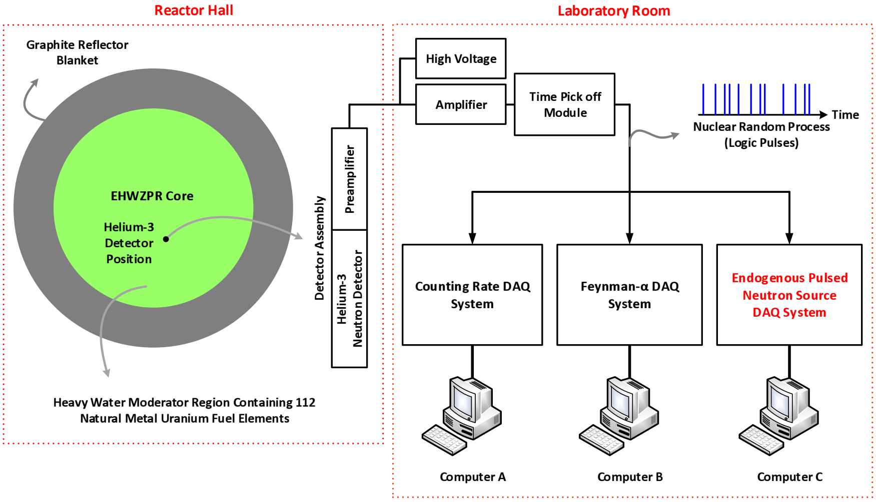

Fig. 4. The set-up of the experiment performed in EHWZPR. A Helium-3 in-core neutron detector is employed. A DAQ system for measurement of counting rates of the detector is used. Also, two isolated DAQ systems for the Feynman-α and endogenous pulsed neutron source (the system developed in the present work) experiments are specified.

6.1. Neutron statistics in EHWZPR

The neutron counts can be considered to have a Gaussian distribution [37]. But in the present case, they have a larger standard deviation than the ones in a non-multiplying medium, when both outputs are of the same mean value. A large value of standard deviation means that there is a high probability for the variable to deviate from its mean value. This large standard deviation becomes noticeable when the reactivity in the multiplying medium approaches the critical state. In the neighbourhood of such data, there are relatively more neutrons that correlate in time with each other.

During the data collection period, one million of 5 ms samples of integral counts was acquired. A 25 s interval (5000 data points) of the recorded data is shown in Fig. 6 Part-B. The mean count is about 149.8, and its standard deviation is 17.1. In Part-A, a pseudorandom pure Poisson process (the process usually seen in non-multiplying mediums) is shown. Note that in a Poisson process the standard deviation of the counts is equal to the square root of the mean value. A moving average filter is applied to both processes, and the results are illustrated by the red lines. Paroxysmal pulses are clearly seen in Part-B which is labelled as neutron noise fluctuations. Therefore, it is visually confirmed that σ_{ZPRN} is greater than $\sigma_{Poisson}$.

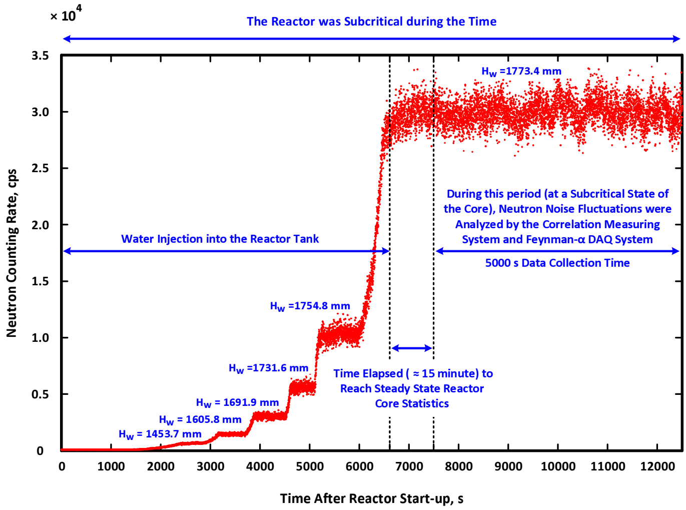

Fig. 5. Neutron counting rates in EHWZPR core after the reactor start-up. From 7500 s to 12500 s the data was acquired (around 5000 s data collection time). During the period, the data on neutron noise fluctuations were collected by the Feynman-α and endogenous pulsed neutron source data acquisition systems.

Figure 7 compares the experimental *probability density function* (pdf) of the counts with a Gaussian pdf. Accordingly, around the mean value, the probability is more intensive than the experimental pdf. Nonetheless, the distribution measured in EHWZPR shows extra fluctuations around the mean neutron counts. The Gaussian distribution is also fitted to the experimental data. The parameter values are shown in the figure. Now, assume that the Gaussian pdf is the distribution of the background radiation. It is obvious that the experimental pdf is the summation of correlated and background portions. Therefore, the ratio of these functions might be useful to be studied to gain knowledge about a conditional probability of the process. (10) shows the relation between the mentioned *SBR* parameter and the ratio of the pdfs:

$$\xi(n)=\frac{PDF_E(n)}{PDF_P(n)}=\frac{C_C+U_C}{U_C}=SBR(n)+1. \tag{10}$$

In this equation n is a neutron count; PDF_E is an experimental pdf of the count and PDF_P is a Gaussian pdf. The nominator of (10) is the neutron count affected by the neutron noise fluctuations. Comparing the experimental distribution of neutron statistics in EHWZPR with a pure Poisson distribution as shown in Fig. 7, (with the same average counting rates) a clear deviation from the Poisson distribution occurs due to the correlated chain neutrons. In Fig. 7, variations of the distributions are plotted. A systematic deviation between the experimental data points and the fitted Gaussian curve is obvious. In Fig. 8, the residues of the Gaussian curve fitted to the experimental data are displayed. Although the Gaussian curve is symmetric, the residues have an asymmetric distribution. Regardless of the fluctuations around the mean value $(\overline{C} \pm \sigma_{Exp})$, it is accepted that an observed burst of neutron chains causes a higher abundance on the right-hand side of the curve $(C > (\overline{C} + \sigma_{Exp}))$, which naturally reduces the probability of abundance of neutron counts on the left-hand side $(C < (\overline{C} - \sigma_{Exp}))$.

In Fig. 9, on the left axis in a logarithmic scale, ξ is demonstrated. In Region-A, $\xi < 1$, that means that the background term is the dominant portion of the process. Therefore, no information can be obtained by the experiments in this region. In regions B and C, the values of ξ are greater than one. But the desired region in the endogenous pulsed neutron source method is Region-C as the system is looking forward to detecting a burst of neutron chains.

Due to the neutron background, any increase of the threshold level leads to a better selection of the correlated portion of the process (a larger value of ξ). Therefore, the repetition rate is decreased and a longer collection time is required (refer to the experimental pdf of the counts in EHWZPR, shown in Fig. 7).

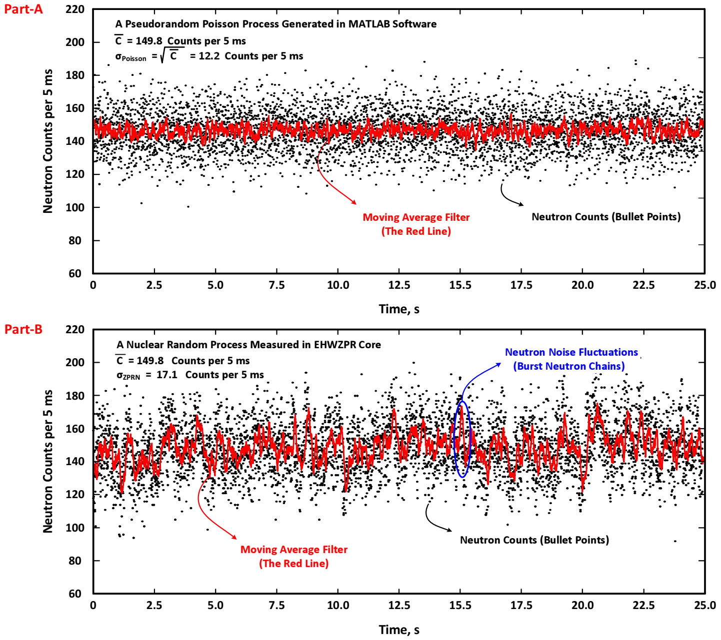

Fig. 6. Part-A: A pseudorandom Poisson process generated in MATLAB software [38]. The mean value of the counts is equal to the mean value of the counts measured in EHWZPR core. Part-B: Neutron counts within a 5 ms period, measured in EHWZPR. The mean value of the counts is 149.8, while the standard deviation is 17.1 (noted as σ_{ZPRN} in the figure). The measured standard deviation is larger than the standard deviation in the process with a Poisson statistics ($\sigma_{ZPRN} > \sigma_{Poisson}$). A moving average filteris applied to the data (the red lines) to show neutron noise fluctuations visually.

It is noticeable that there is an inverse relationship between the collection time in the endogenous pulsed neutron source experiment and the parameter θ value, according to (3) and (4). Combining (4), (5), (6) and (10), and using the fitted Gaussian function to the experimental pdf of the counts (PDF_E, as shown in Fig. 7), θ can be expressed as:

$$\theta = \frac{\xi - 1}{T} \int_{\gamma}^{\infty} PDF_E(C)\, dC = \frac{\xi - 1}{T} \int_{\gamma}^{\infty} C_1 \exp\left(- \left(\frac{C - C_2}{C_3} \right)^2 \right) dC\,, \tag{11}$$

where: C_1 to C_3 are constants which are given in Fig. 7 and C, a variable of integration, is the number of neutron counts. As the Gaussian fitted curve contains a systematic error shown in Fig. 8, applying the experimental data results in a more accurate definition of the parameter. Using (6), the definition of θ can be rewritten as:

$$\theta = \frac{\xi - 1}{T} \sum_{i=\gamma}^{\infty} P_i\,. \tag{12}$$

The values of parameter θ defined by (12) are calculated at different possible values of γ, and are plotted in Fig. 10. The optimum selection for γ is a range in which θ is maximized. According to the results shown in Fig. 10, at $T = 5$ ms, the best choice for γ ranges from 184 to 194.

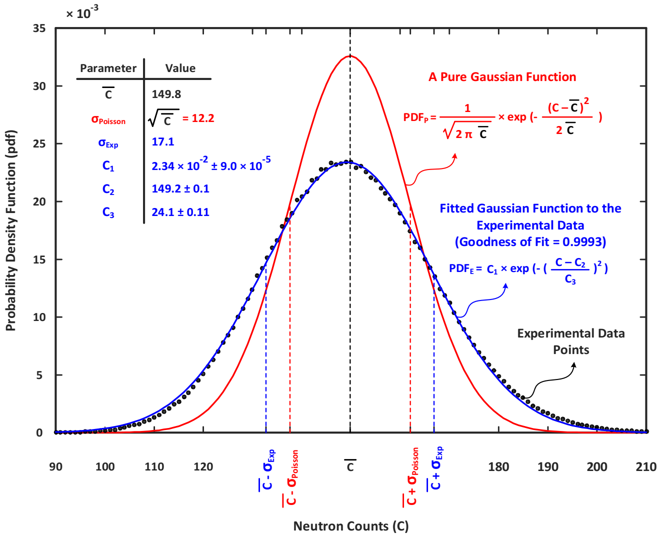

Fig. 7. Comparison of experimental neutron statistics in EHWZPR with a Gaussian pdf of the same mean value.

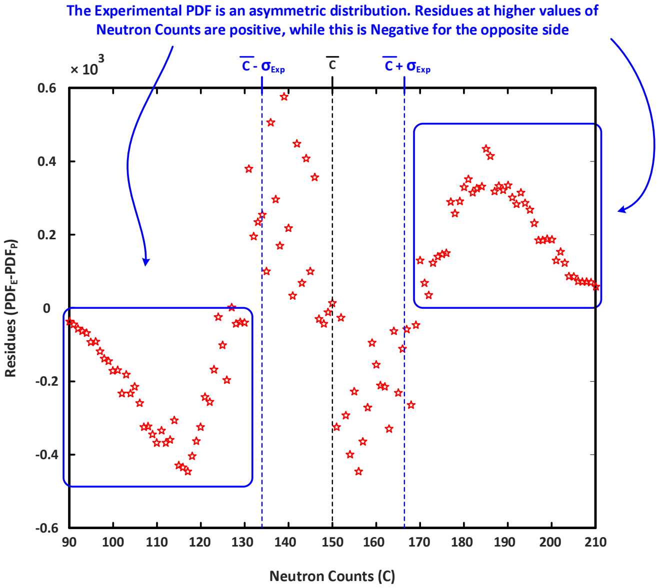

Fig. 8. Residues of the Gaussian function fitted to the experimental data. The results show that the experimental distribution is asymmetric. At higher values of neutron counts (> 170), the residues are positive.
On the other side of the distribution, there are negative residues.

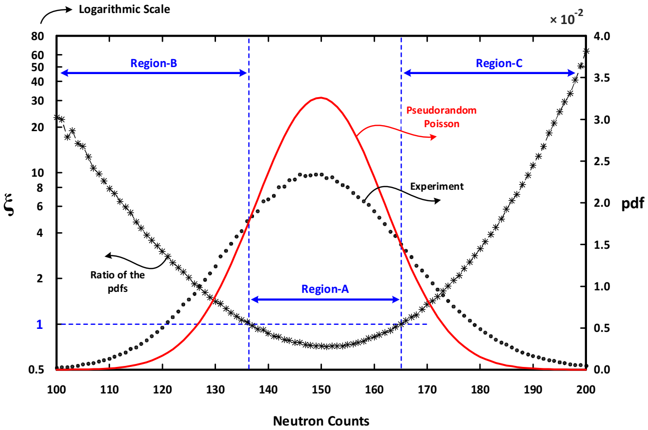

Fig. 9. Values of ξ at different neutron counts. In Region-A, the ratio is smaller than one, therefore the extraction of correlation data is less probable. In Region-B and Region-C, the ratio is larger than one. Since the endogenous pulsed neutron source experiment is sensitive to positive neutron noise fluctuations, a threshold level must be adjusted in Region-C for neutron burst detection.

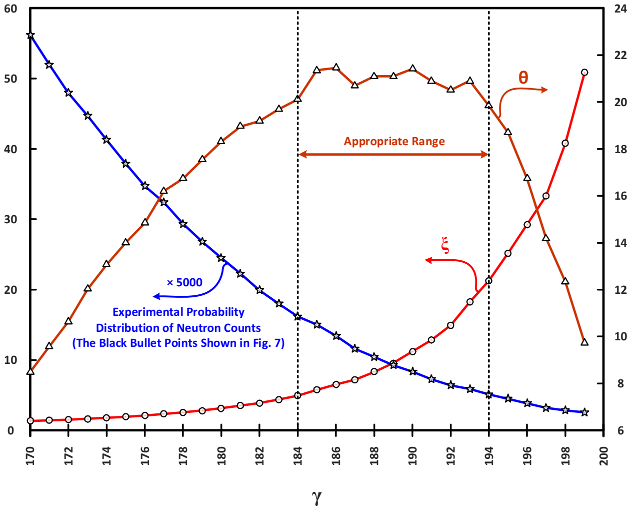

Fig. 10. Values of θ at different values of γ. The curves of ξ and PDF_E have increasing and decreasing trends, respectively. Therefore, θ is maximized for some values of γ.

6.2. Endogenous pulsed neutron source experiment

The endogenous pulsed neutron source experiment is carried out in EHWZPR. The EHWZPR core configuration and the experimental set-up are shown in Figs. 3 and 4, respectively. The accuracy of the results is directly related to the number of iterations on the occurrences of neutron bursts applied for the analysis. Therefore, at different numbers of iterations performed by the equipment, the collected data were stored in the memory for post-analysis examinations. In Fig. 11, a few of the results are demonstrated. It is obvious that any increase of the number of iterations improves the statistical accuracy of the results. Note that in EHWZPR the prompt neutron decay constant ranges from 7 s^{-1} to 20 s^{-1} based on a subcriticality level of the core. That is why the time domain of the total scanning time of the MCS is set to one second. For the most accurate result (item 6 in Fig. 11), the detailed calculation of the neutron decay constant (fitting (1) to the results) is shown in Fig. 12. The lower x-axis represents the time (in seconds) after the triggering pulse, while the upper x-axis – the corresponding MCS channel number. Some selected data at different numbers of iterations are presented in Table 2 in detail. It is clear that an increase of the number of iterations leads to a tighter standard deviation uncertainty of the results, which is confirmed by a better goodness of fit of the curve fittings. The most accurate result for the prompt neutron decay constant is estimated as 8.348 ± 0.376 s^{-1}. Also, the SBR parameter value of the experiment in EHWZPR is estimated as (6.04 ± 0.16) $\times 10^{-2}$ (item 14 in Table 2).

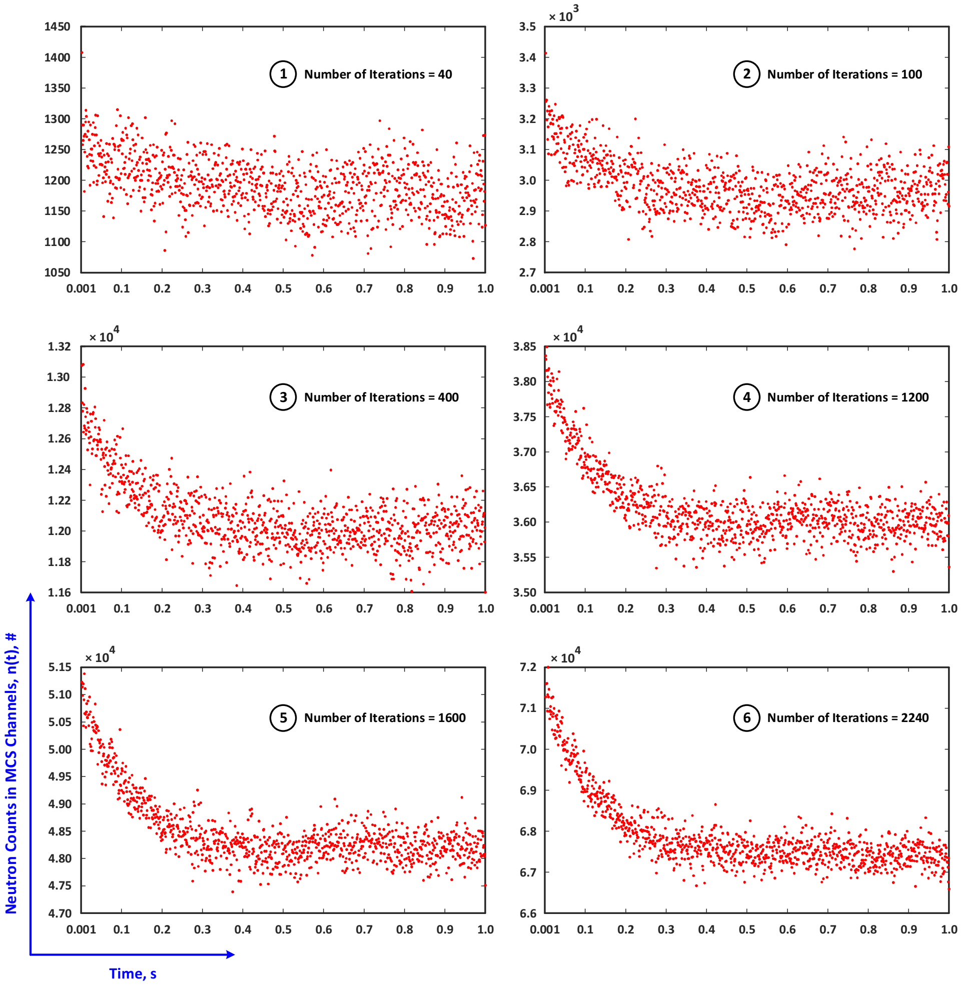

Fig. 11. Results of the endogenous pulsed neutron source experiment at different numbers of iterations on a burst of neutron chains. The item with the least scattered data belongs to the results with the largest number of iterations (item 6).

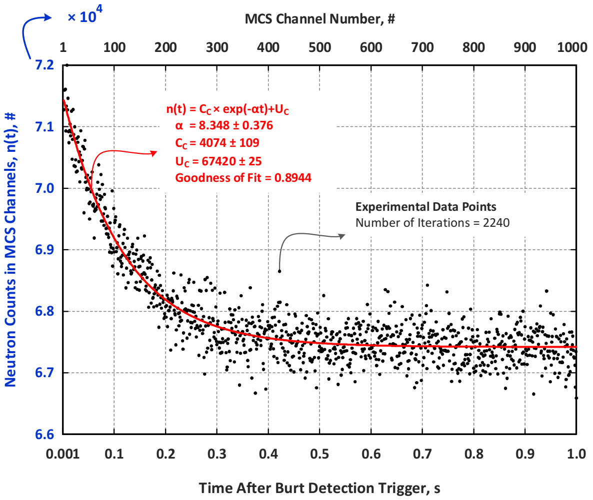

Fig. 12. Results of the endogenous pulsed neutron source experiment in EHWZPR. 2240 iterations on bursts of neutron chains are performed. (1) is fitted to the data and the fitting parameters are shown in the figure. The lower x-axis is time after the triggering pulse, while the upper x-axis is the corresponding MCS channel number.

6.2.1. Uncertainty analysis of results

The system was set to store the data collected in MCS channels every 20 iterations performed on the neutron noise fluctuations in the computer memory. Total of 2240 iterations were performed on the results which led to obtaining a 112 × 2 × 1000 data matrix. Cubic interpolations were carried out between the data points to generate finer experimental information. After analysing, the obtained results are presented in Figs. 13 to 15.

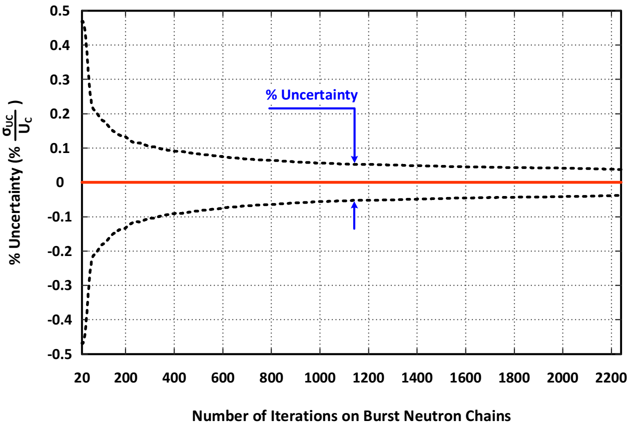

Fig. 13. The experimental uncertainty of *uncorrelated counts* (UC) at different numbers of iterations on a burst of neutron chains.

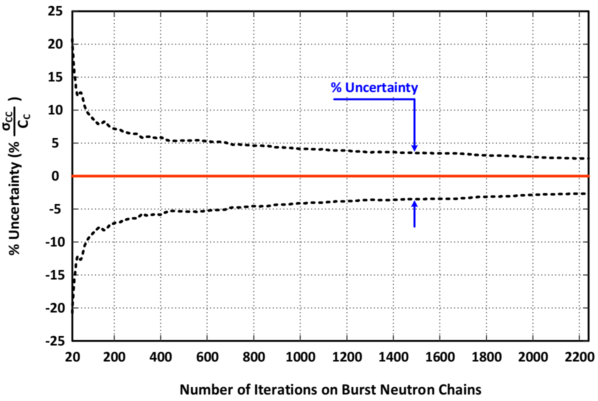

Fig. 14. The experimental uncertainty of *correlated counts* (CC) at different numbers of iterations on bursts of neutron chains.

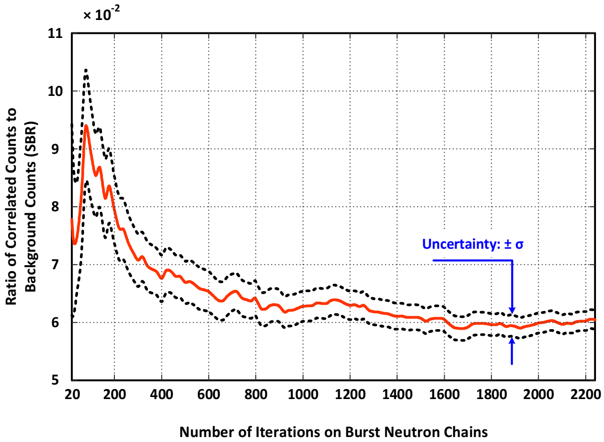

Fig. 15. The ratio of correlated counts and *background counts* (SBR) measured at different numbers of iterations on bursts of neutron chains.

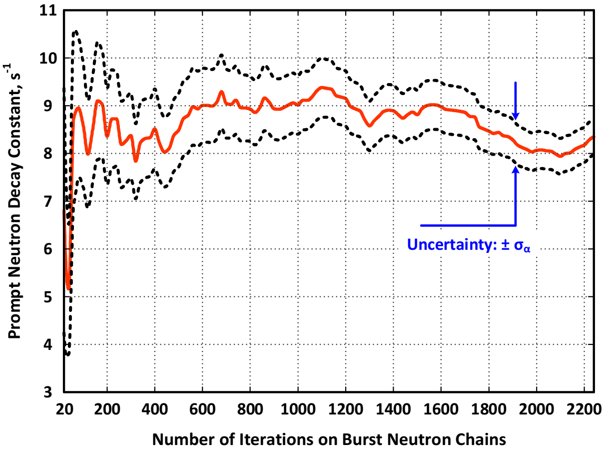

Fig. 16. The experimental results for the prompt neutron decay constant (its mean and its uncertainty boundaries) achieved at different numbers of iterations on the bursts of neutron chains.

The uncertainty bands, as well as the mean values, are also plotted. The most accurate result is related to the background counts (≈ ± 0.03%) (Fig. 13). The uncertainty of the correlated counts (for 2240 iterations) is ± 2.68%. After 600 iterations, the uncertainty was bounded within ± 5%, and further iterations led to tighter statistical uncertainties with a short negative slope. The SBR parameter value was also calculated at different numbers of iterations, and the results are shown in Fig. 15. After 1800 iterations, the result was quasi-stable within ± 3.2% of a statistical uncertainty. The error in SBR is mostly originated from the uncertainty of the correlated counts. The most important result, i.e. the prompt neutron decay constant of the core, is shown in Fig. 16. Within up to 1600 iterations, the fluctuating behaviour of the parameter is seen due to the lack of enough collected data on the physical parameter. After that, downward and then upward drifts of the mean value are seen within the statistical uncertainty of the parameter.

Table 2. Parameter values fitted to the experimental data obtained by the endogenous pulsed neutron source experiment for some selected different numbers of iterations on bursts of neutron chains.

Index	**Number of Iterations**	**Curve Fitting Parameters**				**SBR×10²** Dimensionless
		Prompt Neutron Decay Constant [s^{-1}] $\alpha \pm {}^{*}\sigma_{\alpha}$	Correlated Count [#] $C_C \pm {}^{*}\sigma_{Cc}$	Uncorrelated Count [#] $U_C \pm {}^{*}\sigma_{Uc}$	Goodness of Fit	
1	**40**	5.160 ± 1.359	88 ± 11	1176 ± 5	0.2355	7.48 ± 0.96
2	**100**	8.585 ± 1.294	264 ± 24	2953 ± 6	0.4278	8.94 ± 0.82
3	**200**	8.354 ± 1.001	476 ± 34	5989 ± 8	0.5403	7.95 ± 0.58
4	**300**	8.378 ± 0.894	638 ± 40	9010 ± 10	0.6005	7.08 ± 0.46
5	**400**	8.513 ± 0.835	811 ± 48	12000 ± 10	0.6388	6.76 ± 0.40
6	**600**	9.005 ± 0.783	1172 ± 67	17940 ± 10	0.6898	6.53 ± 0.35
7	**800**	8.929 ± 0.676	1536 ± 70	23970 ± 15	0.7460	6.41 ± 0.30
8	**1000**	9.016 ± 0.612	1879 ± 28	29940 ± 15	0.7851	6.28 ± 0.26
9	**1200**	9.148 ± 0.578	2264 ± 87	35980 ± 15	0.8074	6.29 ± 0.25
10	**1400**	8.890 ± 0.533	2571 ± 93	42120 ± 20	0.8240	6.10 ± 0.22
11	**1600**	8.974 ± 0.510	2915 ± 100	48180 ± 20	0.8390	6.05 ± 0.21
12	**1800**	8.466 ± 0.446	3232 ± 102	54230 ± 25	0.8597	5.96 ± 0.19
13	**2000**	8.063 ± 0.394	3607 ± 104	60210 ± 25	0.8790	5.99 ± 0.17
14	**2240**	8.348 ± 0.376	4074 ± 109	67420 ± 25	0.8944	6.04 ± 0.16

6.3. Feynman-α experiment

Within a 5 ms time window, one million data on neutron noise fluctuations in the EHWZPR core were measured during a 5000 s period of data collection in the experiment. The bunching method is employed for data analysis. In this method, the time series of data on neutron counts are measured by a MCS with a fundamental gate time channel width. Fig. 17 shows the algorithm of bunching method graphically. Twelve data channels of neutron counts are measured within a gate time of T, the basic gate time. The summation of data from every two consecutive channels produces the neutron counts within a gate time of $2T$. Executing the same operation on three consecutive data channels produces the channel data with a $3T$ gate time width. The same method can be applied for generation of greater values of gate times. The parameter k is called a combination coefficient, which is an integer number. The post-analysis of the data is performed using the MATLAB software [38]. The bunching method has been widely applied to various research reactors or critical assemblies [13]. The variance to mean ratios of the counts were analysed in time windows of up to one-second widths. The result is shown in Fig. 18; the detailed information estimated by the curve fitting method is also shown in the figure. In Table 3, the Feynman-α result is compared with the data measured by the endogenous pulsed neutron source experiment in EHWZPR . Although the data collection time for both methods is the same, the endogenous pulsed neutron source experiment shows the larger standard deviation error. However, the mean values of the results have a relatively good agreement within the statistical uncertainties. Performing the endogenous pulsed neutron source experiment during a longer data collection period can reduce the uncertainty, as the experiment is a stochastic method of reactor diagnosis.

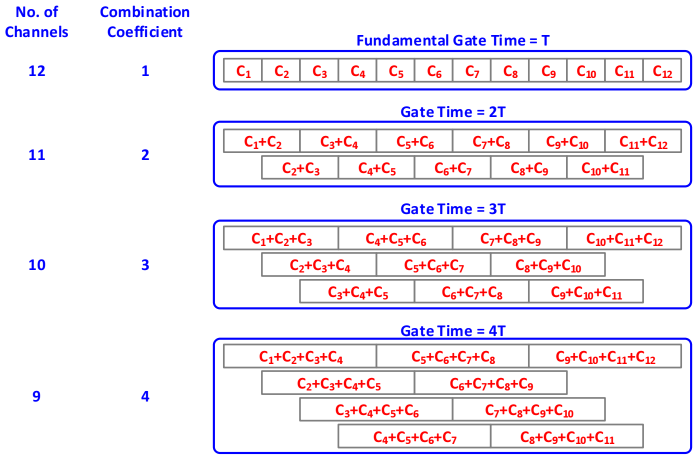

Fig. 17. The concept of bunching method.

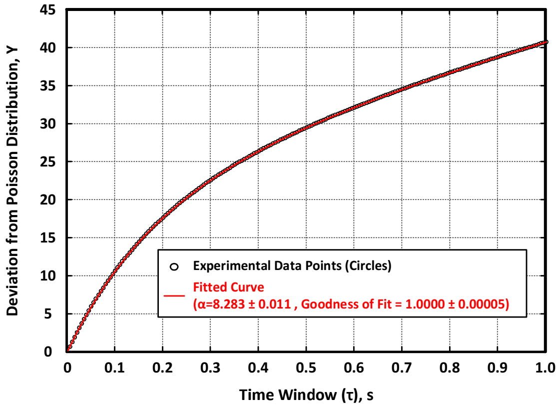

Fig. 18. The Feynman-α results measured in EHWZPR. Fitting parameters are shown in the figure.

Table 3. Comparison of the prompt neutron decay constant measured in EHWZPR using the Feynman-α and endogenous pulsed neutron source experiments.

Experimental Method	**Prompt Neutron Decay Constant [s^{-1}]**	**Goodness of Fit**	**Data Collection Parameter**
Feynman-α	8.283 ± 0.011*	1.0000 ± 0.00005*	One-million Integral Counts in 5ms Time Windows was Collected
Endogenous Pulsed Neutron Source	8.348 ± 0.376*	0.8944 ± 0.00005*	2240 Iterations on Burst Neutron Chains within 5000 s were Performed

*Standard Deviation

7. Conclusion

The reactor noise experiments have been made as standard methods of reactor diagnosis. A practical alternative method for the Rossi-α experiment in thermal systems is the endogenous pulsed neutron source experiment. The method does not need any special facility. Unlike the pulsed neutron source method, the endogenous pulsed neutron source experiment needs a simple system set-up and reactor operation. The endogenous pulsed neutron source experiment is an efficient method in markedly thermal systems like EHWZPR. In this work, a correlation measuring tool is developed which can detect bursts of neutron chains accurately using a 10-kbit embedded shift register. An MCS module of the system is also included in the design. The system is compact, cost-effective, and uses the state-of-the-art electronic technology. With the aid of the equipment, the endogenous pulsed neutron source experiment was performed in EHWZPR. A prompt neutron decay constant, correlated and uncorrelated counts and SBR parameters were estimated for different numbers of iterations on a burst of neutron chains. A threshold parameter (γ) at is crucial for the neutron bursts detection, which is in inverse relation to the collection time required for reaching an acceptable statistical accuracy. An appropriate range of γ parameter as well as an uncertainty of the results have been studied. To validate the results, we also performed the Feynman-α experiment. The results obtained by the endogenous pulsed neutron source and Feynman-α experiments have been compared and a good agreement is seen within the statistical uncertainties. The following conclusions are derived:

- An appropriate range of γ parameter can be determined using the relation between θ and γ. The optimal range of γ parameter is obtained for the maximum θ.
- The endogenous pulsed neutron source experiment is a useful and alternative method to be employed in EHWZPR and similar multiplying systems. In such multiplying mediums, the Rossi-α experiment cannot be applied, but the endogenous pulsed neutron source method is applicable.
- The results obtained by the endogenous pulse neutron source experiment are confirmed by the Feynman-α experiment in EHWZPR. Based on the same data collection time (5000 s), the uncertainty of Feynman-α method is tighter than that of the endogenous pulsed neutron source experiment. The endogenous pulsed neutron source method is a stochastic method of reactor analysis. Therefore, if the experiment duration is extended to several hours, better results with a tighter uncertainty might be achieved. For the same data collection time, the results achieved by the Feynman-α method are more accurate than those obtained by the endogenous pulsed neutron source experiment regarding the statistical uncertainty of the results.
- The neutron noise characteristics of the facility was examined with the proposed measuring tool.

- The system developed in this work is compact, cost-effective, easily adaptable with any special case study, reprogrammable, integrated in a single device, and uses the state-of-the-art digital electronic technology.
- A moving time window is designed with a 100 ns time resolution (described in Section 3) using a 10-kbit shift register. Therefore, bursts of neutron chains are detected accurately in time.

References

[1] Arkani, M., Hassanzadeh, M., Khakshournia, S. (2016). Calculation of six-group importance weighted delayed neutron fractions and prompt neutron lifetime of MTR research reactors based on Monte Carlo method. *Progress in Nuclear Energy*, (88), 352–363.

[2] Thie, J.A. (1963). *Reactor Noise*. New York: Rowman and Littlefield Inc.

[3] Uhrig, R.E. (1970). *Random Noise Techniques in Nuclear Reactor Systems*. New York: The Ronald Press Company.

[4] Williams, M.M.R. (1974). *Random Process in Nuclear Reactors*. Pergamon Press.

[5] Pázsit, I., Demazière, C. (2010). *Noise Techniques in Nuclear Systems*. Handbook of Nuclear Engineering. D. Cacuci, Springer US, 1629–1737.

[6] Pázsit, I., Pál, L. (2008). *Neutron fluctuations: A treatise on the physics on branching processes*. Amsterdam: Elsevier.

[7] Pacilio, N. (1966). Neutron statistics techniques applied to the ROSPO reactor. *Proc.s of the Karlsruhe EAES Symposium III*, European Atomic Energy Society.

[8] Pacilio, N. (1967–1969). Survey of Advancements in Neutron-Statistics and Reactor-Kinetics Techniques at LFCR. *CNEN-RT/FI*, (70)29, 1967–1969.

[9] Orndroff, J.D. (1957). Prompt Neutron Periods of Metal Critical Assemblies. *Nuclear Science and Engineering*, (2), 450–460.

[10] Kitamura, Y., Matoba, M., Misavita, T., Unesaki, H., Shiroya, S. (1999). Reactor Noise Experiments by using Acquisition System for Time Series Data of Pulse Train. *Nuclear Science and Technology*, (36)8, 653–660.

[11] Arkani, M., Mataji-Kojouri, N. (2016). A Newly Designed Multichannel Scaling System: Validated by Feynman-α Experiment in EHWZPR. *Nuclear Engineering and Design*, (305) 213–221.

[12] Arkani, M. (2015). A high performance digital time interval spectrometer: an embedded, FPGA-based system with reduced dead time behaviour. *Metrol. Meas. Syst.*, 22(4), 601–619.

[13] Arkani, M. (2015). *Measurement of Tehran and Esfahan Research Reactors Kinetic Parameters Using Reactor Noise Diagnostic Methods*. Amirkabir University of Technology (formerly called the Tehran Polytechnic), Nuclear Physics Department, Ph.D. Thesis.

[14] Arkani, M., Khalafi, H., Vosoughi, N. (2014). Development of an embedded FPGA-based data acquisition system dedicated to zero power reactor noise experiments. *Metrol. Meas. Syst.*, 22(3), 433–446.

[15] Arkani, M., Khalafi, H., Vosoughi, N., Khakshournia, S. (2015). A FPGA based Time Analyser for Stochastic Methods in Experimental Physics. *Instruments and Experimental Techniques*, 58(3), 350–358.

[16] Pacilio, N., *et al.* (1971). A micrologic integrated circuit for monitoring correlation in pulse sequences. *Nuclear Instruments and Methods*, 92, 13–17.

[17] International Atomic Energy Agency. (1972). *Kinetics and Noise Analysis of Zero-Power Reactors: An NPY-Project Report*, Technical reports series No. 138, Vienna.

[18] Rajeev, K., *et al.* (2015). Development and testing of neutron pulse time stamping data acquisition system for neutron noise experiment. *Nuclear Instruments and Methods in Physics Research Section A: Accelerators, Spectrometers, Detectors and Associated Equipment*, 770, 8–13.

[19] Cox, D.R. (1962). *Renewal Theory*. London: Methuen.

[20] Smith, W.L. (1957). On renewal theory, counter problems, and quasi-Poisson processes. *Mathematical Proceedings of the Cambridge Philosophical Society*, 53, 175–193.

[21] Hanus, R., *et al.* (2014). Velocity measurement of the liquid–solid flow in a vertical pipeline using gamma-ray absorption and weighted cross-correlation. *Flow Measurement and Instrumentation*, 40, 58–63.

[22] Zieliński, M., *et al.* (2009). Accumulated Jitter Measurement of Standard Clock Oscillators. *Metrol. Meas. Syst.*, 16(2), 259–266.

[23] Chwaszczewski, S., *et al.* (1966). Improved Method for Prompt Neutron Period Measurement. *Nuclear Science and Engineering*, 25(2), 201–202.

[24] Choithramani, S.J. (1981). A comparative study of the shift register and conventional coincidence methods for neutron coincidence counting. *Nuclear Instruments and Methods*, 180, 189–193.

[25] Murata, Y. (1970). An instrument for analysis of neutron correlation with shift registers. *Nuclear Instruments and Methods*, 87, 261–272.

[26] Hazama, T. (2003). Practical correction of dead time effect in variance-to-mean ratio measurement. *Annals of Nuclear Energy*, 30(5), 615–631.

[27] Szappanos, D.G., Por, G., Do, Q.B. (1998). Feynman-alpha measurement in a 100kW research reactor. *Progress in Nuclear Energy*, 33(4), 439–455.

[28] Kloosterman, J.L., Rugama, Y. (2005). Feynman-α measurements on the fast critical zero-power reactor MASURCA. *Progress in Nuclear Energy*, 46(2), 111–125.

[29] Spriggs, G.D., Sakurai, T., Okajima, S. (1999). Rossi-α and βeff measurements in a fast critical assembly. *Progress in Nuclear Energy*, 35(2), 169–181.

[30] Szieberth, M., Klujber, G., Kloosterman, J.L., Haas, D.H. (2015). Measurement of multiple α-modes at the Delphi subcritical assembly by neutron noise techniques. *Annals of Nuclear Energy*, 75, 146–157.

[31] Garelis, E., Jr. Russell, J.L. (1963).Theory of pulsed neutron source measurements. *Nuclear Science and Engineering*, 16(3), 263–270.

[32] Arkani, M., Raisali, G. (2015). Measurement of dead time by time interval distribution method. *Nuclear Instruments and Methods in Physics Research, Section A: Accelerators, Spectrometers, Detectors and Associated Equipment*, 774, 151–158.

[33] Misawa, T., Shiroya, S., Kanda, K. (1990). Measurement of prompt neutron decay constant and large subcriticality by the Feynman-α method. *Nuclear Science and Engineering*, 104(1), 53–65.

[34] Keiichi, S. (1979). Source papers in reactor noise. *Progress in Nuclear Energy*, 3(3), 157–218.

[35] *NIOS II Software Developer's Handbook Version 11.1*, ALTERA Corporation, 2011.

[36] AEOI, *Safety analysis report for Esfahan Heavy Water Zero Power Reactor* (EHWZPR), 2013.

[37] Yasuda, H. (1972). Some Remarks on the Endogenous Pulsed Source Technique in Reactor Noise Analysis. *Nuclear Science and Technology*, 9(8), 501–503.

[38] Mathworks. (2014). *MATLAB Reference Guide*. The Math Works Inc.

Metrol. Meas. Syst., Vol. 24 (2017), No. 3, pp. 463–471.

PAN
POLSKA AKADEMIA NAUK

METROLOGY AND MEASUREMENT SYSTEMS
Index 330930, ISSN 0860-8229
www.metrology.pg.gda.pl

M&MS

DESIGN OPTIMIZATION AND TRADE-OFFS OF MINIATURIZED WIDEBAND ANTENNA FOR INTERNET OF THINGS APPLICATIONS

Muhammad Aziz ul Haq, Sławomir Kozieł

Reykjavik University, School of Science and Engineering, 101 Reykjavik, Iceland
(✉ *koziel@ru.is,* +354 599 6376, *muhammadu16@ru.is)*

Abstract

Internet of Things (IoT) will play an important role in modern communication systems. Thousands of devices will talk to each other at the same time. Clearly, smart and efficient hardware will play a vital role in the development of IoT. In this context, the importance of antennas increases due to them being essential parts of communication networks. For IoT applications, a small size with good matching and over a wide frequency range is preferred to ensure reduced size of communication devices. In this paper, we propose a structure and discuss design optimization of a wideband antenna for IoT applications. The antenna consists of a stepped-impedance feed line, a rectangular radiator and a ground plane. The objective is to minimize the antenna footprint by simultaneously adjusting all geometry parameters and to maintain the electrical characteristic of antenna at an acceptable level. The obtained design exhibits dimensions of only 3.7 mm × 11.8 mm and a footprint of 44 mm^2, an omnidirectional radiation pattern, and an excellent pattern stability. The proposed antenna can be easily handled within compact communication devices. The simulation results are validated through measurements of the fabricated antenna prototype.

Keywords: compact antennas, Internet of Things, communication devices, numerical optimization, footprint-reduction-oriented design.

1. Introduction

In the modern era, the internet has revolutionized the way of gathering and processing information. An increasing number of communication devices are connected to the internet owing to their compact size and cost effectiveness. Hence, the concept of *Internet of Things* (IoT) has been introduced. A widespread use of wireless networks also promotes shift towards modern communication devices rather than traditional ones such as desktop computers, tablets, *etc*. According to the recent survey, over 50 million such devices will be interconnected with each other via internet by the end of this decade [1–3]. The required hardware structure for IoT devices is different from that for traditional communication networks. Therefore, design and manufacturing processes of these devices should account for their role in the future communication systems and their specific applications. In particular, the advent of IoT calls for new wireless microwave systems which are cost-effective and compact by design, offer high data transmission rates, a low power consumption, so that they could be used in wearable devices [4].

In recent years, there have been research efforts observed towards designing specific antennas for IoT applications with a narrow bandwidth, such as a miniature antenna for IoT [5], a dual band antenna [6], or a compact reconfigurable antenna [7]. However, the selection of a specific antenna for any application may be a real challenge. Some of research efforts are focused on identifying suitable technologies for fifth-generation communication and IoT applications, especially to enable handling all devices by one system [8]. Hence, it is actually

---

Article history: received on Mar. 17, 2017; accepted on May 17, 2017; available online on Sep. 01,2017; DOI: 10.1515/mms-2017-0047.

more important to design antennas which offer a wide frequency range of operation [9]. On the other hand, design of compact antennas for any wireless system is a non-trivial task due to fundamental limitations pertinent to electrically small antennas [10].

In this paper, we propose a structure of a compact monopole antenna for IoT applications. Numerical optimization is performed to minimize the antenna size and to ensure its acceptable matching. The selected frequency range of interest is 5 GHz to 10 GHz, important for 5G technology [11–13]. The selection of the frequency is made due to the advancement in technologies such as 4G and 5G. The footprint of the optimized antenna is only 44 mm^2. Due to its small size and good electrical performance, the proposed antenna can be a good candidate for various IoT applications; in particular, it can be easily mounted on small wireless devices. An alternative version of the antenna with improved matching obtained at the cost of a slight size increase is also considered. The simulation and measurement results confirm good electrical and field properties of both structures.

2. Antenna structure

The antenna geometry is shown in Fig. 1. The structure is a modification of a basic rectangular monopole antenna with an additional micro-strip section (parameters L_2, w_2) added to serve as an impedance transformer to facilitate wideband matching. The antenna is implemented on Taconic RF-35 substrate ($\varepsilon_r = 3.5$, $h = 0.762$ mm, $\tan\delta = 0.0018$). The design variables are $x = [L_1\ L_2\ L_3\ w_1\ w_2\ L_g\ w_g\ d_L\ d_w]^T$; $w_s = w_2 + 2.d_w$; $w_0 = 2$ mm is fixed to ensure 50-ohm input impedance. The computational model is implemented in CST Microwave Studio [14] (~200,000 mesh cells, simulation time 2 minutes). The EM model is equipped with an SMA connector in order to enable reliable experimental validation of the design. The antenna is supposed to operate in a frequency range from 5 GHz to 10 GHz.

3. Design optimization

Our primary goal is to reduce the antenna size while maintaining acceptable matching within a 5 GHz to 10 GHz frequency range. To achieve this, all geometry parameters of the antenna have been adjusted simultaneously through numerical optimization. Let $A(x) = (L_1 + L_2 + L_3 + d_L)$. w_s and $S(x) = \max\{|S11(x)|_{5\text{ GHz to }10\text{ GHz}}\}$ be the antenna footprint and EM-simulated maximum in-band reflection level, respectively. In rigorous terms, the objective is to reduce $A(x)$ and ensure $S(x) \le -10$ dB. Thus, the task is to solve (*cf.* [15]):

$$\boldsymbol{x}^* = \arg\min_{\boldsymbol{x}} \{A(\boldsymbol{x}) + \beta \cdot c(S(\boldsymbol{x}))^2\}, \qquad (1)$$

where: β is a penalty factor (here, $\beta = 1000$), whereas c is a penalty function defined as $c(S(x)) = \max\{S(x)+10)/10, 0\}$. The penalty term enforces $S(x^*)$ to satisfy the –10 dB threshold [15]. In this work, the problem (1) is solved using the trust-region-based [16] gradient search. The finite differentiation is used to estimate the reflection response Jacobian.

For the sake of comparison, the antenna will be also designed for the best possible matching within the frequency range of interest (5 GHz to 10 GHz). In this case, we use a simpler formulation of the following form:

$$\boldsymbol{x}^* = \arg\min_{\boldsymbol{x}} \{S(\boldsymbol{x})\}. \qquad (2)$$

The optimization engine is the same as before (TR-based gradient search with numerical derivatives).

4. Results and experimental verification

In this section we provide the results of antenna optimization. We consider two cases: (i) the miniaturization-oriented optimization, and (ii) the matching-oriented design. The reason for considering the alternative design is to identify the benefits of miniaturization-oriented design in terms of an additional size reduction achieved but also to examine the electrical and field performance differences between the two structures.

The antenna of Fig. 1 has been optimized using the approach described in Section 3. We will refer to the antenna optimized for the minimum size as Antenna I, and to the antenna optimized for the best matching as Antenna II. The detailed antenna dimensions are shown in Tables 1 and 2, respectively. The footprint area of Antenna I is only 44 mm^2, whereas the footprint of Antenna II is 69 mm^2. Fig. 2 shows photographs of the fabricated antenna prototypes. The simulated and measured reflection responses are shown in Fig. 3, whereas Figs. 4 through 7 show the simulated and measured radiation patterns. Finally, Fig. 8 shows the simulated and measured achieved gain of both antennas. It can be observed that an agreement between the simulation and measurement results is very good. Relatively large discrepancies of E-plane radiation patterns for certain directions are due to the shadowing effect of the 90-degree bend the antenna was mounted on during the measurement process.

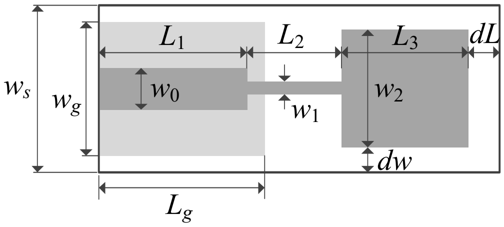

Fig. 1. Geometry of the considered compact antenna. The ground plane is shown using a light grey shade.

a)

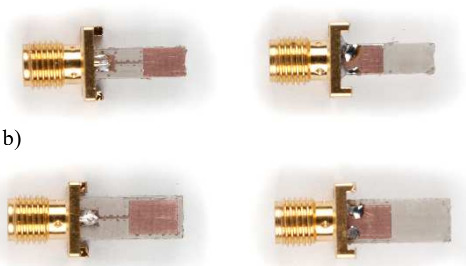

Fig. 2. Photographs of the fabricated antenna prototypes: the antenna optimized for the minimum size (Antenna I) (a); the antenna optimized for the best matching (Antenna II) (b). The antenna fronts and backs are shown on the left- and right-hand sides, respectively.

Formulating the design problem as described in Section 3 enables to ensure that the optimized design exhibit the smallest size while still satisfying the matching requirements at the prescribed frequency range of 5 GHz to 10 GHz. The simulated maximum in-band reflection for Antenna II was about –14 dB which leaves a sufficient margin to accommodate such effects as fabrication and assembly tolerances or inaccuracy of the computational model, and still to obtain acceptable matching for the measured prototype. This can indeed be observed in Fig. 3b. On the other hand, Antenna I exhibits a slight violation from the –10 dB threshold for frequencies between 9 GHz and 10 GHz.

The H-plane radiation patterns of both antennas are omnidirectional throughout the entire frequency range. For E-plane patterns, as mentioned before, a noticeable difference between the simulation and measurement results can be identified which is a result of the aforementioned shadowing effect. The achieved gain of both antennas is almost linear from 5 GHz to 10 GHz. The gain performance is excellent, given a very small footprint size.

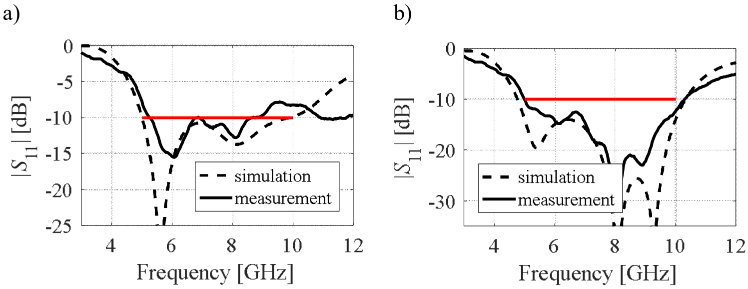

Fig. 3. The simulated and measured reflection characteristics: Antenna I (a); Antenna II (b). The frequency range of operation (5 GHz to 10 GHz) is marked using a horizontal line.

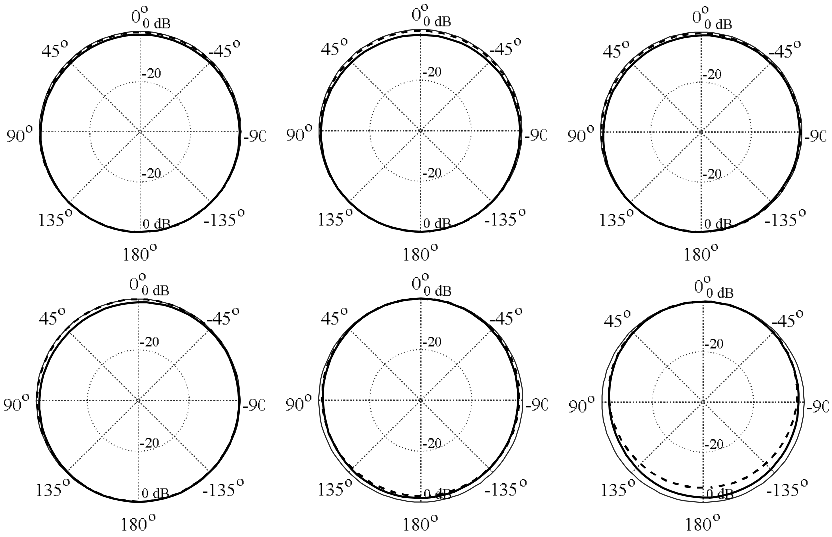

Fig. 4. The simulated and measured H-plane radiation patterns (E field) for the antenna optimized for the minimum size (Antenna I). From left top to bottom right: 5 GHz, 6 GHz, 7 GHz, 8 GHz, 9 GHz, and 10 GHz.

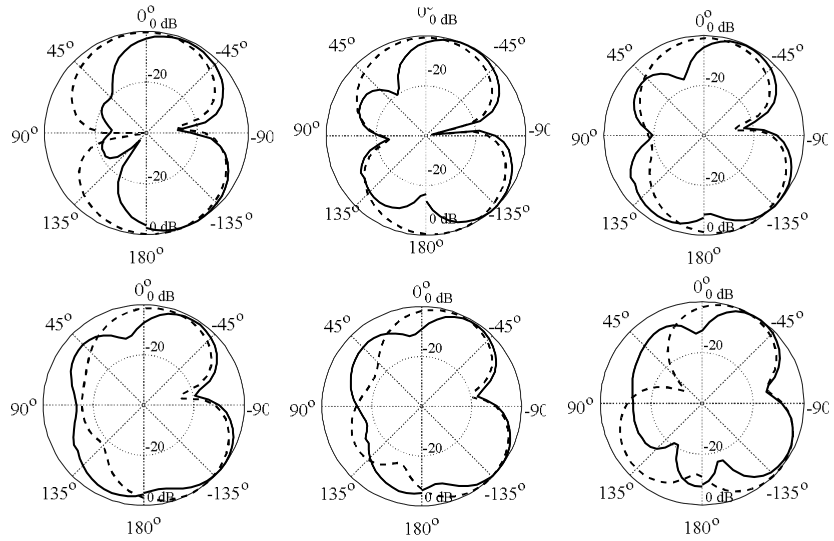

Fig. 5. The simulated and measured E-plane radiation patterns (E field) for the antenna optimized for the minimum size (Antenna I). From left top to bottom right: 5 GHz, 6 GHz, 7 GHz, 8 GHz, 9 GHz, and 10 GHz.

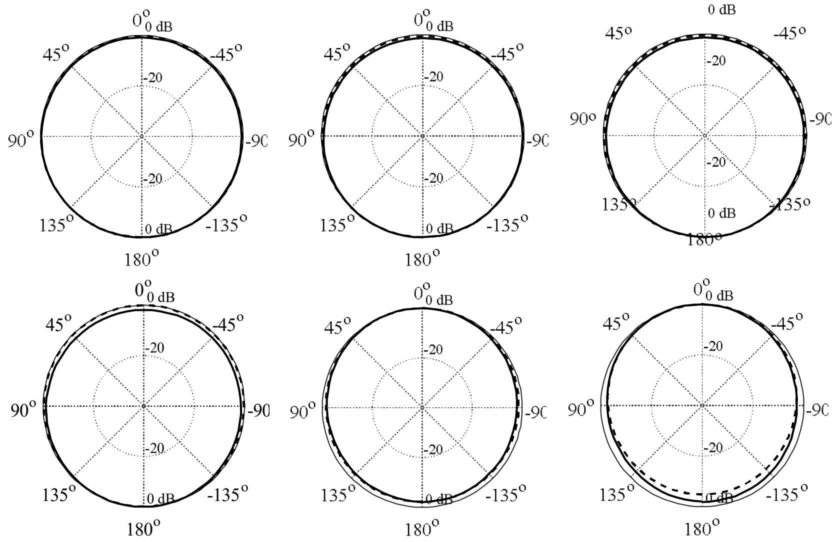

Fig. 6. The simulated and measured H-plane radiation patterns (E field) for the antenna optimized for the best matching (Antenna II). From left top to bottom right: 5 GHz, 6 GHz, 7 GHz, 8 GHz, 9 GHz, and 10 GHz.

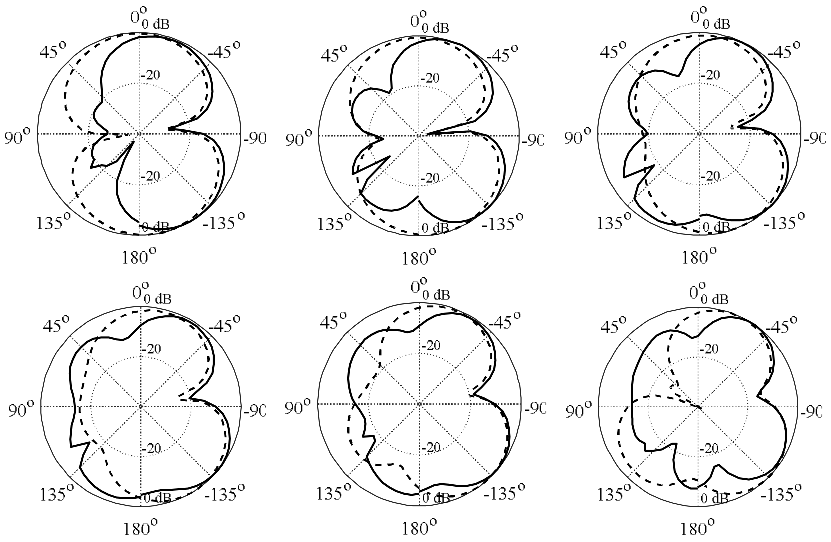

Fig. 7. The simulated and measured E-plane radiation patterns (E field) for the antenna optimized for the best matching (Antenna II). From left top to bottom right: 5 GHz, 6 GHz, 7 GHz, 8 GHz, 9 GHz, and 10 GHz.

Table 1. Optimized Dimensions (Antenna I).

Variable	L_1	L_2	L_3	w_1	w_2	L_g	w_g	dL	dw
Value [mm]	2.70	3.74	5.36	0.20	3.74	5.45	3.73	0.00	0.00

Table 2. Optimized Dimensions (Antenna II).

Variable	L_1	L_2	L_3	w_1	w_2	L_g	w_g	dL	dw
Value [mm]	2.43	3.91	6.05	0.28	4.24	5.63	4.17	0.63	0.54

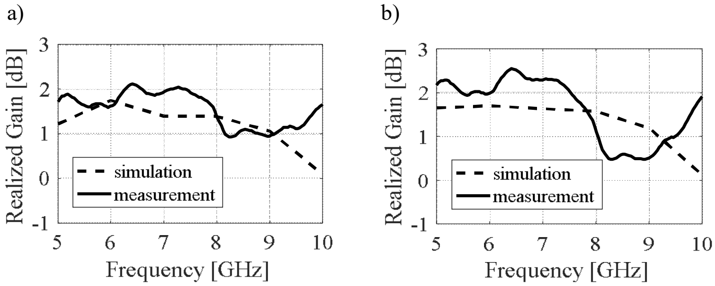

Fig. 8. The simulated and measured achieved gain: the antenna optimized for the minimum size (a); the antenna optimized for the best matching (b).

Figure 7 shows the simulated total efficiencies of the antennas. Clearly, the efficiency of Antenna II is higher than that of Antenna I. Nevertheless, the average in-band total efficiencies for both antennas are over 90% (92% for Antenna I and 96.5% for Antenna II).

The optimized antennas have been also compared in respect to the pattern stability, using the *pattern stability factor* (PSF) [17] that represents the relationship between radiation in a reference direction and radiation in all other directions over a specified bandwidth; here,

Metrol. Meas. Syst., Vol. 24 (2017), No. 3, pp. 463–471.

the operational bandwidth of the antenna. As indicated in [17], for a good performance of a UWB system, *PSF* of 0.95 or larger is desired. *PSF* is defined as:

$$PSF = \int_{\Omega} C(\vec{R})ds \Big/ \int_{\Omega} ds, \tag{3}$$

where: Ω is a range of operating directions (here, following [17], the H-plane is considered, so that the integral in (3) is reduced to a linear one); and $C(\vec{R})$ is a frequency-domain correlation pattern defined as [17]:

$$C(\vec{R}) = \int_{\Omega} F^2(\vec{R},\vec{r})ds \Big/ \int_{\Omega} ds \tag{4}$$

with

$$F^2(\vec{R},\vec{r}) = \left| \int_{BW} E(\vec{r},f)E^*(\vec{R},f)df \right| \Big/ \left[\int_{BW} |E(\vec{r},f)^2|\,df \int_{BW} |E^*(\vec{R},f)|^2\,df \right], \tag{5}$$

where: $E(\vec{r},f)$ is a far-field electric field in the direction $\vec{r}$; $\vec{R}$ is a reference direction; and * denotes a complex conjugate.

The PSF values for Antenna I and Antenna II are 0.956 and 0.962, respectively. This means that miniaturization of the antenna structure (specifically, Antenna I over Antenna II) has no negative effect on the pattern stability, similarly as concluded in [18].

Finally, in order to verify the robustness of the design, three copies of each antenna have been fabricated. The measured reflection responses have been shown in Fig. 8. It can be observed that the characteristics closely resemble each other, indicating that the designs are robust in respect to manufacturing and assembly tolerances.

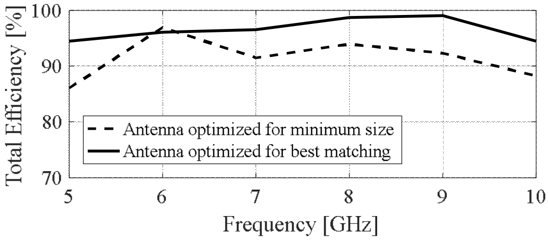

Fig. 9. Comparison of total efficiencies of Antenna I and Antenna II.

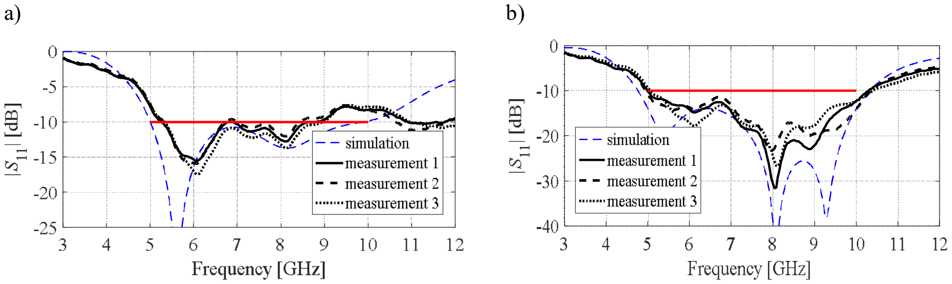

Fig. 10. The simulated and measured reflection characteristics: the antenna optimized for the minimum size (a); the antenna optimized for the best matching (b). The results of measurements 1 through 3 correspond to three copies of the fabricated antennas. The frequency range of operation (5 GHz to 10 GHz) is marked using a horizontal line.

5. Conclusion

In the paper, the structure and design optimization of a miniaturized wideband antenna for Internet of Things applications is presented. Simultaneous adjustment of all geometry parameters of the antenna enables to achieve a very small footprint of only 44 mm^2 and a good matching within the prescribed frequency range of 5 GHz to 10 GHz. At the cost of certain increase of its size (to 69 mm^2), the antenna matching can be improved by around 4 dB. The discussed structures exhibit a good electrical and field performance, including high efficiency, omnidirectional radiation pattern, high pattern stability, and almost linear gain.

Acknowledgment

The authors thank Computer Simulation Technology AG, Darmstad Germany for making CST Microwave Studio available. This work is partly supported by the Icelandic Centre for Research (RANNIS) Grant 163299051.

References

[1] Grau, A. (2016). How to Build a Safer Internet of Things: Todays IoT is full of security flaws. We must do better. *IEEE Spectrum*, *http://spectrum.ieee.org/telecom/security/how-tobuild-a-safer-internet-of-things*.

[2] Kamilaris, A., Pitsillides, A. (2016). Mobile Phone Computing and the Internet of Things: A Survey. *IEEE Internet of Things Journal*, 885–898.

[3] Jin, J., Gubbi, J., Marusic, S., Palaniswami, M. (2014). An Information framework for creating smart city through internet of things. *IEEE Internet of Things Journal*, 112–121.

[4] Moscato, S., Silvestri, L., Delmonte, N., Pasian, M., Bozzi, M., Perregrini, L. (2016). SIW components for the Internet of Things: Novel topologies, materials, and manufacturing techniques. *IEEE Topical Conference on Wireless Sensors and Sensor Networks (WiSNet)*, 78–80.

[5] Lizzi, L., Ferrero, F., Monin, P., Danchesi, C., Boudaud, S. (2016). Design of miniature antennas for IoT applications. *IEEE International Conference on Communications and Electronics*, 234–237.

[6] Katoch, S., Jotwani, H., Pani, S., Rajawat, A. (2015). A compact dual band antenna for IOT applications. *International Conference on Green Computing and Internet of Things*, 1594–1597.

[7] Mansour, A.M., Mokhtar, B., Gomah, K., Marghany, K., Abdelmonsef, A. Rizk, M.R.M., Shehata, N. (2016). Compact reconfigurable multi-size pixel antenna for cognitive radio networks and IoT environments. *Loughborough Antennas & Propagation Conference*, 1–5.

[8] Zanella, A., Bui, N., Castellani, A., Vangelista, L., Zorzi, M. (2014). Internet of things for smart cities. *IEEE Internet of Things Journal*, 22–32.

[9] Khan, M.A., ul Haq, M.A., ur Rehman, S. (2016). A practical miniature antenna design for future internet of things enabled smart devices. *Int. Conf. Signal Processing and Communication Systems*.

[10] Bekasiewicz, A., Koziel, S. (2016). Compact UWB monopole antenna for internet of things applications. *Electr. Lett.*, 52, 492–494.

[11] Livingston, V., Pearson, C., Svensson, A., Arefi, R. (2015). 4G Americas' vision for the americas: 5G spectrum recommendations. *http:// http://www.4gamericas.org /files /1914 / 41 2 2/0345 /5G_Spectrum_ Recommendations_Webinar_9.2.2015.pdf.*

[12] Lemey, S., Caytan, O., Vande Ginste, D., Demeester, P., Rogier, H., Bozzi, M. (2016). SIW cavity-backed slot (multi-)antenna systems for the next generation IoT applications. *IEEE Topical Conference on Wireless Sensors and Sensor Networks*, 75–77.

[13] Palattella, M.R., Dohler, M., Grieco, A., Rizzo, G., Torsner, J., Engel, T., Ladid, L. (2016). Internet of things in the 5G Era: enablers, architecture, and business models. *IEEE J. Selected Areas in Communications*, 510–527.

Metrol. Meas. Syst., Vol. 24 (2017), No. 3, pp. 463–471.

[14] CST Microwave Studio, ver. 2015. CST AG, Bad Nauheimer Str. 19, D-64289 Darmstadt, Germany, 2015.

[15] Bekasiewicz, A., Koziel, S. (2015). Structure and computationally-efficient simulation-driven design of compact UWB monopole antenna. *IEEE Ant. Wireless Prop. Lett*., 14, 1282–1285.

[16] Conn, A.R., Gould, N.I.M., Toint, P.L. (2000). Trust Region Methods. *MPS-SIAM Series on Optimization.*

[17] Dissanayake, T., Esselle, K.P. (2006). Correlation-based pattern stability analysis and a figure of merit for UWB antennas. *IEEE Trans. Ant. Prop*., 54(11), 3184–3191.

[18] Liu, J., Esselle, K.P., Hay, S.G., Zhong, S. (2014). Effects of printed UWB antenna miniaturization on pulse fidelity and pattern stability. *IEEE Trans. Ant. Prop*., 62(8), 3903–3910.

www.czasopisma.pan.pl PAN www.journals.pan.pl

Metrol. Meas. Syst., Vol. 24 (2017), No. 3, pp. 473–488.

METROLOGY AND MEASUREMENT SYSTEMS

Index 330930, ISSN 0860-8229

www.metrology.pg.gda.pl

ANALYSIS OF ECONOMICAL LIGHTING OF HIGHWAYS IN THE ENVIRONMENT OF SMOL LANGUAGE

Zdzisław Kowalczuk, Jakub Wszołek

Gdańsk University of Technology, Faculty of Electronics, Telecommunications and Informatics, G. Narutowicza 11/12, 80-233 Gdańsk, Poland (✉ *kova@pg.gda.pl*, +48 58 347 2018, *jwszolek@eti.pg.gda.pl)*

Abstract

The paper puts forward and implements a method of designing and creating a modelling simulation environment for extensive and complete analysis of economical lighting on highways. From a general design viewpoint, the proposed solution explores the concept of a network description language (SMOL), which has been designed to describe the necessary network functions, mechanisms, and devices for the purpose of their computer simulation and verification. The presented results of the performed research confirm the usability of intelligent lighting on highways, both in the sense of the design concept and in the aspect of saving energy.

Keywords: lighting systems, economical factors, engineering systems, monitoring, domain language, modelling and simulation environment.

1. Introduction

Economic issues encourage us to look for new opportunities of better solving specific technical problems. Thanks to knowledge, technology, and experience we can obtain higher optimality (reliability and effectiveness) of the designed systems.

The modern automatic control systems are to a great extent founded on measurement networks. Current monitoring gives us the possibility of verifying the correctness of a system's operation. The observed dynamic development of technology causes that computer-based automatic control systems have growing possibilities of analysing and using measurement data (and often saving them in a central place). The current techniques of data analysis (data mining – a data exploration process) enable us to develop useful mechanisms of detection or prediction of failures on the basis of symptoms hidden in the measurement data. Failure of a large management or automatic control system usually means a complete or partial stopping of the process (and financial losses). Therefore, tools for modelling and simulating such systems are significant in the analysis aiming at identification of weak points of the developed control solutions.

Within the research, a system [7–10] was developed in order to enable description of network structures of interconnected devices in SMOL (a language (…L) for describing networked *Systems for Monitoring Objects* (SMO); an original, dedicated domain language, and to run appropriate simulations.

Our study is a direct response to the research needs of one of Polish companies, specializing in the production of electronics. Since the presented model of SMO can easily map specific conditions of the measurement environment, we can consider all most essential cases and examine them in terms of cost-effectiveness of the intended intelligent system for measuring and controlling lighting on highways.

To perform this kind of detailed simulation studies, the SMO project has been expanded to

Article history: received on Oct. 10, 2016; accepted on Mar. 28, 2017; available online on Sep. 01, 2017; DOI: 10.1515/mms-2017-0041.

its branch of the description programming language SMOL (suitable also for implemental issues), and next to the complete system SMOLsim of modelling and simulation.

This paper briefly presents the concept of the language and a practical example demonstrating the possibilities of the developed simulation environment. Technical details related to the way of using this system in relation to the requirements of the considered application, are also included.

2. Modelling network structures using SMOL language

Development of measurement techniques resulted in the formation of a new branch of distributed measurement, which is currently used to engineer intelligent management and control of objects. The dynamic development of this branch of science was also an important incentive for the authors to develop an original mechanism for modelling structures for *measurement-diagnostics-control* (MDC) and the related MDC computer networks discussed here. In effect, in this paper, we first focus our attention on a method of describing the MDC networks in the dedicated language, SMOL. Proper description of a network structure, by means of SMOL, lays down the foundations for further analysis of the network and its optimisation.

2.1. Language concept

SMOL, a dedicated language of semantics enabling the designer to model measurement-diagnostics-control networks, is an example of a domain-specific tool, tailored to solve problems from a specific area [1].

Description of a network structure is an essential basis for representing the problems of configuration, re-structuring, and optimisation of network subsystems. In other words, SMOL is used to describe the components of a diagnostic network, and the accompanying connections, along with their appropriate parameterisation. Such a formal representation will also enable to verify the future process of implementing such a network with the use of a relevant parser, which is a software platform for analysing a programmed network structure and its parameters.

The *semantics of the language* (SMOL) are based on structures of hierarchical processing. It is assumed that all network signals are eventually bundled together in the Central Node, which is a central vertex of the analysed graph.

2.2. Components of network description

One of the best ways of modelling industrial computer networks is to use a directed flow graph as a tool suitable for describing relations occurring in a network. Such a model is represented by a triple of sets (vertices, edges, and mappings). By defining these sets, we can precisely present an information flowchart in MDC networks.

Below, we introduce the basic types of nodes used in graphs to properly represent network relations. The main division concerns the use of static and dynamic nodes implementing transforming functions [10].

2.3. Central node

In general, the *central node* (CN component) is an object of MIMO (*Multiple-Input Muliple-Output*) type (with multiple inputs and outputs). It is a necessary component in defining practical MDC networks. In an actual computer connection network, such a component represents the centre for transmitted information that receives data from measuring gauges and transmits information or control signals to receivers or actuators. A general scheme of this node is shown in Fig. 1.

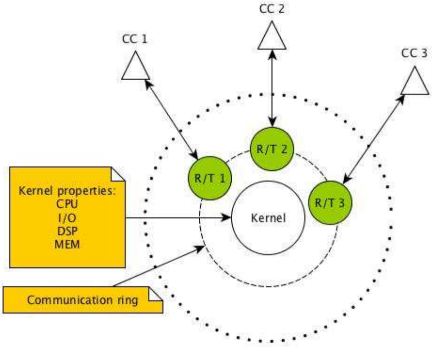

Fig. 1. Central node representing a multidimensional (MIMO) object.

The central node has a set of *communication channels* (CC) and associated *Receiver/Transmitter* (R/T) modules, belonging to the communication layer referred to as the Communication Ring, used to exchange information between the Kernel and other nodes. The kernel of CN is implemented as a computer system defined through proper hardware resources and their parameters (CPU – *Central Processing Unit*, I/O *Input/Output*, DSP – *Digital Signal Processing* or MEM – *Memory*).

The central node is always required when we intend to practically verify feasibility of implementing a designed network.

2.4. Transferring node

Transferring node is a universal element of MIMO type, which functions as a transmitter (TN element) in the network; it has a structure shown in Fig. 2, where CC and R/T components function analogously to those described above for the central node.

The kernel of this node can perform all necessary T(**A**) functions transforming information **A**. The concept of using such "transformers" is presented in Subsection 2.6.

In an actual implementation of an MDC network, the TN components have specific inputs and outputs, and the desired methods of signal transmission assigned to them. In practice, transmitters are working in most universal contemporary wire and wireless standards (WiFi – *Wireless Fidelity*, ZigBee – IEEE *802.15 standard*, Switch – *http://en.wikipedia.org/wiki/Network_switch*, Modem).

2.5. Expander

In the real-world solutions, data buses are commonly applied as components specifically dedicated to transmitting measurement and control data. Therefore, such a function is implemented in the SMOL language intended to be a tool for designing industrial MDC network systems.

Expander, representing a specific transmission component of designed network, gives the possibility of exchanging information on the basis of buses (PROFIBUS – *https://en.wikipedia.org/wiki/Profibus*, CAN – *https://en.wikipedia.org/wiki/CAN_bus*, RS-232, RS-485, DSB – *Diagnostic Service Bus* and KNX/EIB – *https://en.wikipedia.org/wiki/KNX_(standard)*) commonly used in industrial measurement and automatic control systems. The type of the applied protocol is pre-defined by means of a list of the parameters available for this (Expander) object.

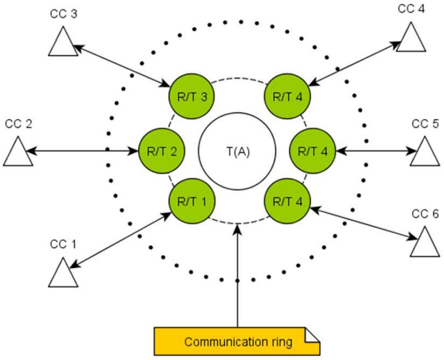

Fig. 2. Transferring node: a universal MIMO node.

2.6. Transformer – transforming function

MDC systems often require quick, and rather simple, modification of the transmitted data stream. Therefore, *transformers* (TRs) enable to implement a program of universal mathematical T(**A**) function (sum, difference, product, quotient, differentiation, integration, averaging, and some slightly more complex digital filters) operating on the input data. Currently, the possibility of using transformers is provided only for CN and TN nodes, described in Subsections 2.3 and 2.4.

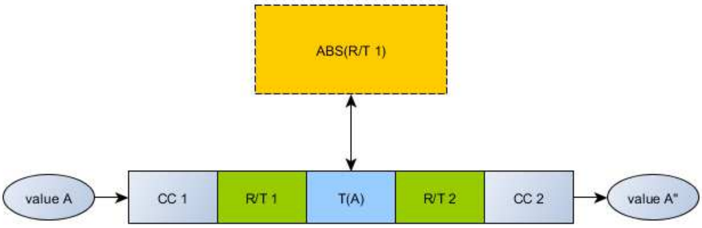

Fig. 3. TN node with a transforming function T(**A**) implemented as TR.

The mechanism of transformers' functioning comes down to operations on data **A** that flow into the node through the input communication port (CC_1) and are transferred outside through the output communication port (CC_2). Fig. 3 shows an approximate working diagram of a model transformer receiving data **A** through port CC_1, modifying them according to a selected function T(**A**) = A* **(**performing, for instance, a simple function T(**A**) = abs(**A**) = |**A**|), and using port CC_2 for displaying the results **A*** through.

2.7. Parameters of connections between nodes

By defining the parameters of direct connections between the system's nodes, that is, the parameters of *communication channels* (CC), one specifies the character of a medium used for transmission (*e.g.* Ethernet network). The designer can determine the necessary physical parameters of considered communication channel; for example, a length of physical medium, a type of it (air, copper cable, computer network, *etc*.), attenuation, and an estimated maximum data transfer speed.

2.8. Sensor/actuator node

It is a common type of node terminating the network structure in particular branches. In actual MDC networks this component usually represents a sensor and a measuring gauge, or display a gauge and (logical) states of control actuators.

2.9. Simulation environment

The concept of SMOL language has been based on solutions meeting the requirements of the object-oriented programming paradigm (namely, abstraction, polymorphism, encapsulation, and inheritance) [8]. This approach facilitates mapping of pertinent relations occurring in actual MDC systems.

A program written in the SMOL language describes a set of processes/objects communicating with each other in order to execute specific tasks. The proposed different types of nodes [10] enable us to implement objects having functions corresponding with devices commonly used in communications, diagnostics and automatic control engineering. These objects – represented according to the high-level programming language concept – have a structure defined by means of variable fields and behaviours. They are methods or functions embedded in the object (a function occurring independently in the code is considered to be a regular function). This enables the programmer to unequivocally define the roles performed by objects in the program, and organize the code structure. When programming in SMOL, the designer modelling a network structure does not have to limit himself to the use of the provided/implemented ready objects. Due to the application of open architecture, it is possible to add (with the use of the inheritance mechanisms and relevant interfaces) customized behaviours of the designed components of an MDC system. All this contributes to the ease of development of a SMOL environment, and enhances its universality.

As it has been mentioned, a SMOL environment contains many packages of ready objects and functions. To facilitate the designer's work, the objects are divided into two main groups.

SMOH is a group of objects referring to hardware components. The user can therefore employ ready-to-use objects, which are most frequently used in MDC networks. Examples of such objects are: a network switch, gauge, sensor or actuator. Each of the ready components has all mechanisms enabling to connect it with other network components. The connection of objects is performed through a specially defined interface (obviously, the objects which have no interface defined cannot be connected to other objects requiring an interface for communication). On the basis of the provided basic set of components and functions, the designer can customize objects with the use of the inheritance mechanism.

SMOF is a set of advanced functions useful in implementation of data flow and performing processes in MDC networks. Transforming functions are included in the system package. The SMOF package, among others, includes an implemented Dijkstra's algorithm for finding the shortest path between network nodes, and an Edmonds-Karp algorithm for computing the maximum flow either in the whole network or in a specific part of the network. Moreover, the SMOF package gives the possibility of generating a graphic representation of the modelled computer network environment. Displaying the structure of connections gives rise to better understanding of the network; the relations between its particular components have an impact on the final evaluation of the network's applicability, and facilitates network optimisation.

2.10. Simulation system architecture – SMOL platform

Once the language was developed, which enabled description of the network's connected measurement and automation devices, we began designing a corresponding tool for simulating the developed structures.

The intended SMOL simulation platform is composed of several interconnected modules. Each of the modules performs a specific function. The objective of implementation task was to develop a possibly general architecture enabling simple modification, redevelopment and integration of designed MDC networks.

The structure of software components included in this application is shown in Fig. 4.

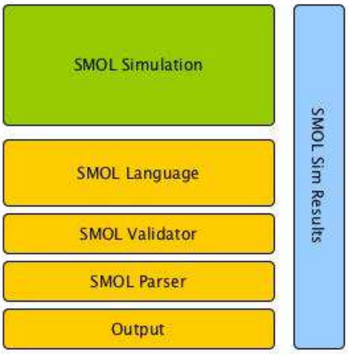

Fig. 4. A diagram of the SMOL architecture solution.

The SMOL platform is based on the Groovy technology (an object-oriented scripting language patterned on Java syntax, enriched with additional features such as closures; *http://www.groovy-lang.org/*) [2–3]. It is an object-oriented scripting language patterned on the Java syntax and run on a *Java Virtual Machine* (JVM) [4]. Due to its dynamic typing, closures, operator overloading and support for meta-programming (meta-classes, categories, AST (*https://sewiki.iai.uni-bonn.de/research/jtransformer/start*) transformations), SMOL is well suited for building customized domain-specific extensions. The applied technology enables simple integration of the languages, Groovy and SMOL. There is also the possibility of interlacing both languages, in order to achieve greater flexibility in programming using the SMOL platform. The system's designer can even implement a part of the functionalities developed in Java, and then embed it – through Groovy – directly in the SMOL language.

Such system functionality significantly enhances the capabilities of both the expansion and analysis of the discussed models of MDC networks. An unquestionable advantage of this solution is its openness to various modifications, enabling to use the environment in diverse industrial, engineering, and scientific applications, as well as in student projects.

2.11. SMOLsim codebase

The discrete simulation environment SMOLsim was implemented by using the Java and Python technologies. In the design work we aimed at developing a possibly universal software solution, which gives the ability to promptly implement different simulation scenarios and presents a great flexibility in the usage. Certainly, an important objective of the simulation module was also its full compatibility with the SMOL language.

In the developed simulation environment, we use discrete functions both in the formal description (characteristics of the state variables of the system) and in the description of dynamics (measurement of the elapsed time). Accordingly, in this event-driven simulation, changes (events) occur only at specific, discrete moments. This type of simulation can be implemented based on two methods: 1) planning events and 2) process interaction [14].

According to the design assumptions, a network description expressed in the SMOL language is transformed to a form compatible with the SMOLsim platform. The conversion performed using scripts written in the Python environment, yields a simulation project coded in the Java language. Thus, this project is also consistent with a commonly used tool – Apache Maven (*https://maven.apache.org/*), which automatizes building software for the Java platforms.

During the work on the simulation environment SMOLsim, we used common open-source third-party libraries. Such a solution enhances the versatility and flexibility of the environment. In addition, the generated Java code gives the opportunity to introduce modifications in the object's behaviour, what also extends the functionality of the simulator. A sample of Java code generated for one of the simulated objects (defined as a part of the description of the network of intelligent lamps modelled in SMOL) is attached in Appendix 3.

2.12. Examples of SMOL platform applications

In recent years, the development of smart buildings increased the possibilities of using the platform (SMOL) for modelling and simulating MDC networks. Smart buildings are currently a synonym for a productive and economically efficient environment, which enables to optimise various components: systems, structures, services, management, as well as the internal relations between them [16].

More and more complex systems of optimal management of heating systems, in buildings using passive heating and cooling, are nowadays being widely developed [5, 6]. Moreover, there are hybrid energy systems using renewable energy sources. Smart buildings also involve monitoring and alarm systems, fire systems and access control systems. These solutions use a common network for communication between particular modules. The leading aim of the work on the SMOL platform was the development of a tool for simulation and optimisation of operation of implemented MDC networks [9], with a particular emphasis on object-oriented and building automation systems.

Thus, apart from flexibly creating a description of general MDC structures and simulating them, the SMOL platform also offers the possibility of describing a structure of measurement, diagnostic and automation functionalities used in buildings, by means of a special domain-specific programming language. An unequivocal description of the network structure is the necessary basis for precise simulation and effective optimisation of the developed networks.

Recall that the architecture of SMOL, based on interfaces and abstract classes, enables to easily expand the functionalities. Also, the implemented basic classes open the possibility of creating customized node implementations using the provided methods of communication between objects and other libraries for free expansion of SMOL. An example of such expansion is the use of SMOL for simulating BAS (*Building Automation System*) and BMS (*Building Management System*) systems along with an expander simulating exchange of information between the devices by means of KNX/EIB bus (or other type). The communication media can be a twisted pair of cables, Ethernet network, energy cables, radio or infrared waves. The central part of the network is a line, which can have 64 bus devices connected to it. The information is sent asynchronously at a speed of 9600 bps [11–13].

KNX/EIB bus is one of the most frequently chosen solutions in implementing building automation systems.

The SMOL tool, matched for simulation of such building systems, suitably maps the specific mechanisms used in communication between building automation devices.

An example of creating an algorithm with the use of SMOL for modelling and simulating is presented in Figs. 5 and 6. The former shows the concept of a measurement network using a KNX/EIB interface for communication purposes, and the latter presents this network in a graphic form using the SMOL language, as a right solution for network representation, detailed modelling, and target optimisation.

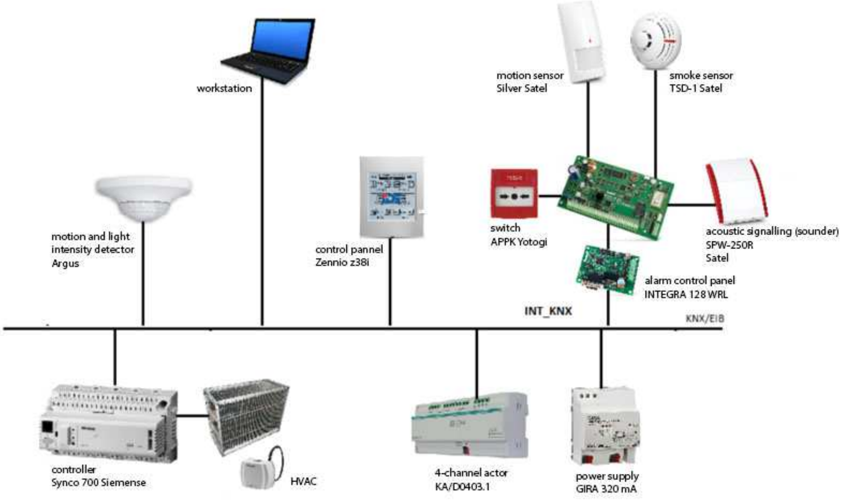

Fig. 5. The concept of a measurement network based on a KNX/EIB interface.

The software code in SMOL language describing the structure of presented MDC network is included in Appendix 1.

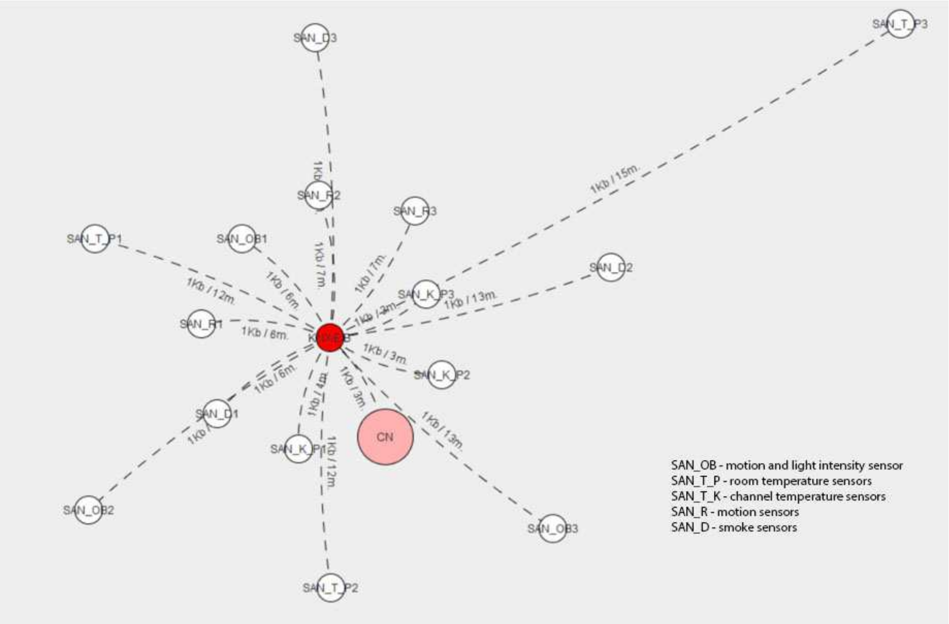

Fig. 6. A graphic representation of KNX/EIB network created with the use of SMOL environment.

3. Using SMOL environment in designing smart lighting

Let us now consider in a more detailed way an example, illustrating the working principle of the SMOL modelling and simulation system for distributed MDC network systems, and representing the concept of a road lighting system. In particular, in this section we present a practical application of the platform, SMOL, concerning the development and verification of a certain method of economical lighting of a highway. Below, we describe the subject of analysis, the simulation method, and the research results along with an assessment of suitability of the offered solution.

Figure 7 shows the resulting graph of the analysed network of the system, managing highway lighting, generated by means of a SMOL parser. The corresponding software code written in SMOL describing the structure of this MDC network is given in Appendix 2.

3.1. Object of analysis

In the analysed example shown in Fig. 7, as programmed and exercised in SMOL, the lamps communicate with each other and exchange information about detection of a moving vehicle.

The ultimate aim of this analysis is finding an answer to the question whether – from the viewpoint of possible savings – the designed MDC system is worth using for automatic management of road lighting. The presented test scenarios should also show the possibilities of effective implementation of different MDC lighting systems and (potential) verification of energy profitability of the offered solutions.

A situation diagram being the basis for scenarios of saving energy of the road lighting, as discussed here, is shown in Fig. 8.

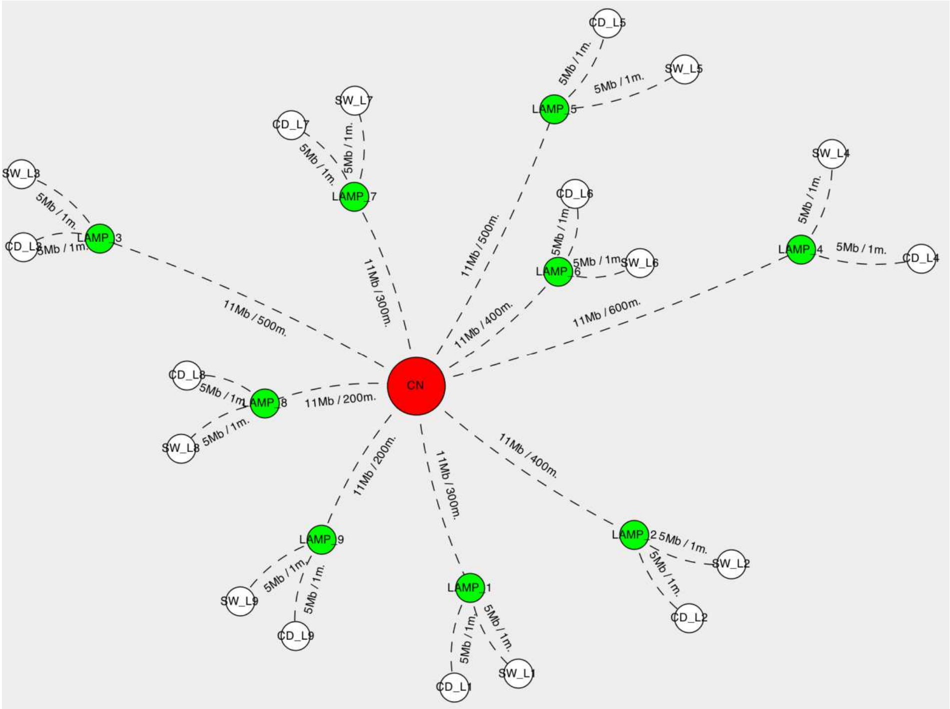

Fig. 7. A graphic representation of the network structure used in managing road lighting obtained as a result of SMOL parsing.

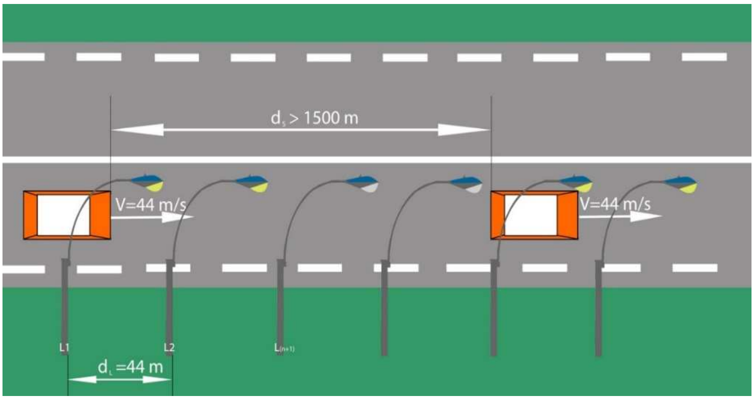

Fig. 8. A situation diagram of the analysed road simulation.

3.2. Research scenarios

We are going to present here two test scenarios. Through simulated testing of the designed network, we can spot and identify advantages and disadvantages of the discussed solution.

Before starting the experiments, let us make assumptions specifying simple and rational scenarios of simulations. Thus, we assume that all cars drive keeping the same distance from each other, at a constant speed of 160 km/h (44 m/s), and that the distance between each two successive road lamps is 44 m, and the period of a light's switching-on is 2 sec. The minimum period of a lamp being on is defined as 10 sec., and the period between switching-off and switching-on again is 5 sec. The technological requirements for the lamp operation cycle are explained in Fig. 9. Moreover, we determine how the lamps are switched on in relation to a moving car when a car is detected: a "current" lamp, which is the one whose sensor has just detected the presence of a car, is on and, by assumption, three lamps in the direction of the car movement are also on, which is shown in Fig. 10. For the safety of driving at a fixed speed of 160 km/h, we further assume that entering the road invokes initially switching on four lamps (obviously, one can use here also an adaptive algorithm, which adjusts the number of lights to the car's speed) at once.

The resulting diagram representing the hardware configuration of the analysed solution is shown in Fig. 7. In this study we consider the first 9 road lamps fitted with a sensor detecting a moving car (*CD_n – Car Detection*) and actuators responsible for switching lights on and off (*SW_n – Switch*).

1. **Off-wave OfW (switching off)**. The first experiment represents a situation where cars are driving in the same direction (one after another) at the same speed. Distances between cars are greater than 1500 metres. During this test we expected to observe the effect of automatic switching-off of the lights. Due to the lack of information about a new approaching car from the sensors, the lamps are switched-off, and lighting keeps up only to each single car, currently moving.
2. **On-wave OnW (switching on)**. The aim of this research scenario is to analyse a situation where cars are driving in the same direction (one after another) at the same speed, with a fixed distance between them, being smaller than 440 metres (10 × 44 m, the distance between the lighting posts). Due to this extremely high traffic volume, we expect the effect of constant lighting of the road lamps.

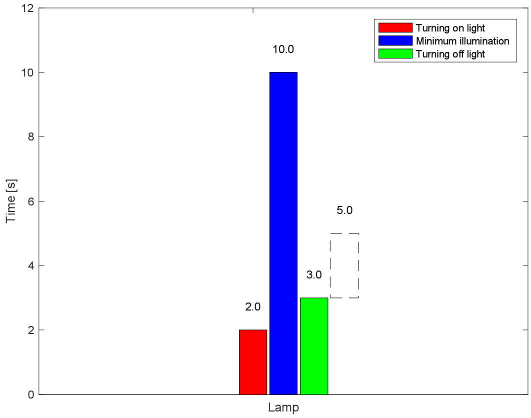

Fig. 9. A technological cycle of a single lamp's operation.

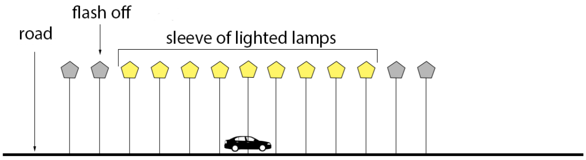

Fig. 10. A diagram of lighting "sleeve" diagram.

3.3. Simulation results

The results of the first simulated experiment with the lighting *on-off wave* (OfW) are shown in Fig. 11, where we can observe the effect of the implemented concept of a lighting "sleeve" (or tunnel), depicted in Fig. 10, which is:

$$R_S = \alpha V_S , \tag{1}$$

were: R_S – a length of the lighting sleeve (the number of lamps being simultaneously on); α – a quantity factor of 0.4318; V_S – a velocity of a moving car.

Within the first 396 metres each car is driving past 9 lamps, located every 44 metres (the lamps are turning on and off in pairs).

The obtained simulation results enable to state that after the car has driven 836 metres, the lamps, starting from the beginning of the road, reach the stable switch-off state. This means that a single car drives in the lighting sleeve of 836 metres (with 19 road lamps on). Four lamps are always on before the approaching car, while the rest (15 lamps) are on at the back of the car.

A length of the lighting sleeve, defined according to the relation (1) as the number of lamps being on at the same time, is dependent on a velocity of a driving car. The value of factor α is determined on the basis of data obtained during simulations, and it represents the ratio of 19 lamps being simultaneously on and the velocity of a driving car. This effective linear relation represents the rule that the higher the car's speed, the longer the lighting sleeve. The executive system coordinator (the central node) switches the lamps on and off in a proper mode, before and after a driving car.

The second experiment concerning the *on-wave* (OnW) has yielded the results, presented in Fig. 12, which show that gaps between the cars are short enough to not switch off the lamps. The lamps are on constantly, waiting for information from the sensors (related to the traffic volume reduction).

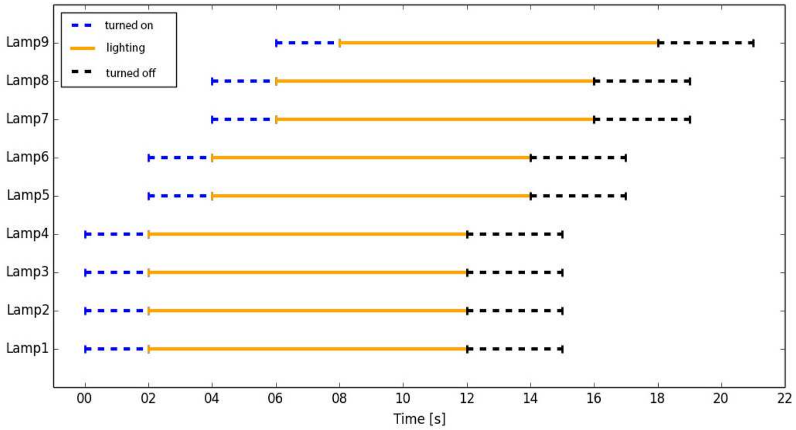

Fig. 11. An off-wave diagram for 9 lamps located along the 396 m distance of the road.

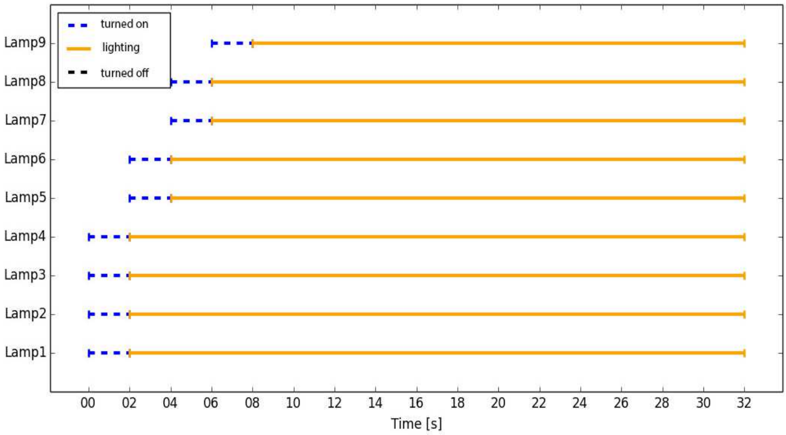

Fig. 12. An On-wave diagram of the lamps located along the 396 m distance of the road.

3.4. Aggregate observations

The simulated examination also covered an aggregated experiment concerning a distance of 10 000 metres (227 lamps). A car driving at a speed of 44 m/s covers this distance in 3 min and 47 sec. Assuming that the car is driving in a 19-second tunnel (836 m or 19 road lamps), the car uses only 8.37% of all available lamps. Obviously, for distances longer than 10 kilometres, the energy gain will be more considerable.

Figure 13 shows a simple impact of the distance on savings expressed in the percentage of lamps being simultaneously on. This impact is now considerable. Naturally, the biggest progress is reached for distances of up to 100 km.

On the basis of common experience, the following optimality criterion can be applied:

$$J = \overline{N}_{on} \cdot P_L \ , \tag{2}$$

were: J – a cost; $\overline{N}_{on}$ – a mean number of turned-on lamps; P_L – a mean power consumption of a single lamp (175 W). This criterion represents a simple function of cost, which is an average power along the highway for a given scenario. It is obvious that for a given lamp technology this criterion can be relatively represented by the average number of lamps turned on.

The criteria have been verified by driving a car at various speeds along the distance of 10 000 m, and the respective analytical data are listed in Table 1.

The results included in Table 1 are presented graphically in Fig. 14, which shows that the higher the speed of a driving car, the higher the number of simultaneously turned-on lamps.

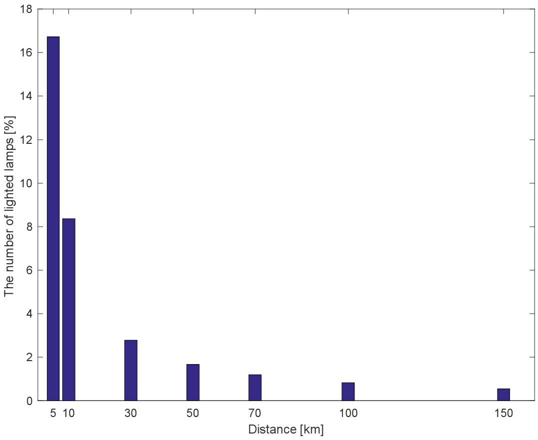

Fig. 13. A percentage of the number of lamps turned on in relation to the total length of the road.

Table 1. Data of the experiment for various speeds of cars along a distance of 10 000 m.

NO.	SPEED	SPEED	TIME OF TRAVEL	NUMBER OF LAMPS TURNED-ON	AVERAGE POWER (W)
1	18 km/h	5 m/s	33.3333 min	6	1 050
2	36 km/h	10 m/s	16.6667 min	7	1 225
3	54 km/h	15 m/s	11.1111 min	9	1 575
4	72 km/h	20 m/s	8.3333 min	11	1 925
5	90 km/h	25 m/s	6.6667 min	12	2 100
6	99.72 km/h	27.7 m/s	6.0168 min	13	2 275
7	104.4 km/h	29 m/s	5.7471 min	14	2 450
8	115.2 km/h	32 m/s	5.2083 min	15	2 625
9	126 km/h	35 m/s	4.7619 min	16	2 800
10	144 km/h	40 m/s	4.1667 min	18	3 150
11	158.4 km/h	44 m/s	3.7879 min	19	3 325
12	180 km/h	50 m/s	3.3333 min	21	3 675
13	198 km/h	55 m/s	3.0303 min	23	4 025
14	216 km/h	60 m/s	2.7778 min	24	4 200
15	234 km/h	65 m/s	2.5641 min	26	4 550

4. Summary

An advantage of the developed research modelling and simulation approach, based on both the SMOL language and the implemented simulation SMOL environment, is the possibility of a convenient description, visualisation and simulation of the analysed *measurement-diagnostics-control* (MDC) networks. It can be used for solving various problems connected with distributed computer systems. The designer of such networks receives a functional tool for an efficient description of the system's, or monitored object's, structures and associated parameters, limitations and relations, as well as for relevant simulations.

The SMOL platform has been developed in order to solve the design problems specific for the distributed network systems. In this paper we have presented an example of analysis of a specific adaptive highway system that proves the multi-purpose character of the SMOL platform. In particular, this platform has been used to analyse the profitability of introducing changes to a road lighting system, which – according to the demonstrated case – confirms the rationality of building suitable management systems for the lighting of highways used for long and fast driving.

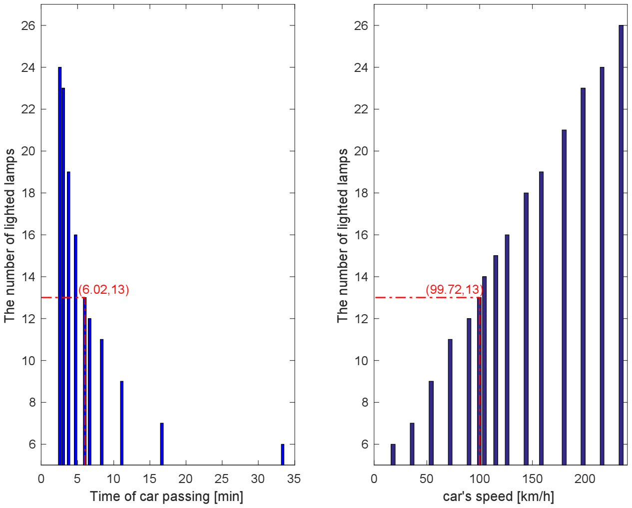

Fig. 14. A mean number of turned-on lamps in the lighting sleeve vs the period of car movement and the car's velocity.

References

[1] Chapman, T. (2008). *Network design language*. *http://www.johntchapman.com/NDL-1.0-WP-080520.pdf.*

[2] DAMADICS. (2004). Research training network on development and application of methods for actuator diagnosis in industrial control systems. *http://diag.mchtr.pw.edu.pl/damadics*.

[3] Dearle, F. (2010). *Groovy for Domain-Specific Languages*. Packt Publishing Ltd., Birmingham, UK.

[4] Doebelin, E. (2003). *Measurement Systems*. (5th ed.). McGraw-Hill Science.

[5] Eckel, B. (2006). *Thinking in Java*. (3rd ed.). Pearson Education, Inc, Upper Saddle River.

[6] Haasz, V. (2012). *Advanced Distributed Measuring Systems*. River Publishers.

[7] Krzaczek, M., Kowalczuk, Z. (2011). Thermal Barrier as a technique of indirect heating and cooling for residential buildings. *Energy and Buildings*. *www.elsevier.com/locate/enbuild*, 43(4), 823–837.

[8] Krzaczek, M., Kowalczuk, Z. (2012). Gain Scheduling control applied to Thermal Barrier in systems of indirect passive heating and cooling of buildings. *Control Engineering Practice*. *http://dx.doi.org/10.1016/ j.conengprac.2012.07.007*, 20(12), 1325–1336.

[9] Kowalczuk, Z., Wszołek, J. (2009). Monitoring objects over networks. *Systems Science*, 35(3), 49–53.

[10] Kowalczuk, Z., Wszołek, J. (2012). Networked Object Monitor – A distributed system for monitoring, diagnostics and control of complex industrial facilities. *Metrol. Meas. Syst*., 19(3), 521–530.

[11] Kowalczuk, Z., Wszołek, J. (2009). Network monitoring and diagnostics of buildings. *Detecting, Analysing and Fault-Tolerant Systems*, Z. Kowalczuk (ed.), PWNT, Gdańsk, 227–234.

[12] Kowalczuk, Z., Wszołek, J. (2014). Modeling of measurement and diagnostics using SMOL language. *Aktualne Problemy Automatyki i Robotyki*, AOW, Warszawa, 277–286.

[13] Nowacki, W. (2006). *Komputerowe Systemy Pomiarowe*. (wyd. II). Wydawnictwa Komunikacji i Łączności, Warszawa.

[14] Łatuszyńska, M. (2011). Computer Simulation Methods – an attempt of logical classification. *Studies & Proceedings of Polish Association for Knowledge Management*, Uniwersytet Szczeciński, Szczecin, 41.

[15] Ważna, W. (2015). Design of an intelligent office. Gdansk Univ. of Technology. Report No. 232 (BSc thesis; under prof. Z. Kowalczuk).

[16] *http://www.cs.put.poznan.pl/mnowak/IB/IB-2.pdf* (Sep. 2016).

Appendix 1: The software code in SMOL language describing the structure of an MDC network (KNX-EIB)

```
package UTest
import SMOH.*
import Utils.*
import com.SMOF.*
import com.UI.DrawSmolEngine;
import com.prototype.DrawSecond;
import com.sample.DrawFirst;
import com.utils.CustomEdge;
import com.utils.INode;
import com.utils.NodeBase;

DrawFirst df = new DrawFirst ()
HashMap<HBase> varList = new HashMap();

// central node definition
def(root) = [new MainNode("ROOT")]
varList.put("root",root);

// KNX/EIB bus definition
def (eib1) = [new EIBNode("KNX/EIB")]
eib1.connect(root ,1,SpeedUnit.Kb,3)
varList.put("KNX/EIB",eib1)

// temperature sensor
// room 1
def (sensor_temp_1) = [new SANode("SAN_T_P1")]
sensor_temp_1.connect(eib1,1,SpeedUnit.Kb,12)
varList.put("SAN_T_P1",sensor_temp_1)

// room 2
def (sensor_temp_2) = [new SANode("SAN_T_P2")]
sensor_temp_2.connect(eib1,1,SpeedUnit.Kb,12)
varList.put("SAN_T_P2",sensor_temp_2)

// room 3
def (sensor_temp_3) = [new SANode("SAN_T_P3")]
sensor_temp_3.connect(eib1,1,SpeedUnit.Kb,15)
varList.put("SAN_T_P3",sensor_temp_3)

// temperature sensor in the air duct
// outdoor temperature
def (sensor_temp_4) = [new SANode("SAN_K_P1")]
sensor_temp_4.connect(eib1,1,SpeedUnit.Kb,4)
varList.put("SAN_K_P1",sensor_temp_4)

// air temp - IN
def (sensor_temp_5) = [new SANode("SAN_K_P2")]
sensor_temp_5.connect(eib1,1,SpeedUnit.Kb,3)
varList.put("SAN_K_P2",sensor_temp_5)

// air temp - OUT
def (sensor_temp_6) = [new SANode("SAN_K_P3")]
sensor_temp_6.connect(eib1,1,SpeedUnit.Kb,3)
varList.put("SAN_K_P3",sensor_temp_6)

// presence detector and light sensor
// room 1
def (sensor_presence_1) = [new SANode("SAN_OB1")]
sensor_presence_1.connect(eib1,1,SpeedUnit.Kb,6)
varList.put("SAN_OB1",sensor_presence_1)

// room 2
def (sensor_presence_2) = [new SANode("SAN_OB2")]
sensor_presence_2.connect(eib1,1,SpeedUnit.Kb,13)
varList.put("SAN_OB2",sensor_presence_2)

// room 3
def (sensor_presence_3) = [new SANode("SAN_OB3")]
sensor_presence_3.connect(eib1,1,SpeedUnit.Kb,13)
varList.put("SAN_OB3",sensor_presence_3)

// motion sensor
// room 1
def (sensor_presence_1) = [new SANode("SAN_OB1")]
sensor_presence_1.connect(eib1,1,SpeedUnit.Kb,6)
varList.put("SAN_OB1",sensor_presence_1)

// room 2
def (sensor_presence_2) = [new SANode("SAN_OB2")]
sensor_presence_2.connect(eib1,1,SpeedUnit.Kb,7)
varList.put("SAN_OB2",sensor_presence_2)

// room 3
def (sensor_presence_3) = [new SANode("SAN_OB3")]
sensor_presence_3.connect(eib1,1,SpeedUnit.Kb,7)
varList.put("SAN_OB3",sensor_presence_3)

// smoke sensor
// room 1
def (sensor_smoke_1) = [new SANode("SAN_D1")]
sensor_smoke_1.connect(eib1,1,SpeedUnit.Kb,6)
varList.put("SAN_D1",sensor_smoke_1)

// room 2
def (sensor_smoke_2) = [new SANode("SAN_D2")]
sensor_smoke_2.connect(eib1,1,SpeedUnit.Kb,13)
varList.put("SAN_D1",sensor_smoke_2)

// room 3
def (sensor_smoke_3) = [new SANode("SAN_D3")]
sensor_smoke_3.connect(eib1,1,SpeedUnit.Kb,13)
varList.put("SAN_D1",sensor_smoke_3)

List<NodeBase> lstBase = Helper.GenerateVertexList(varList);
List<CustomEdge> lstLink =
Helper.GenerateEdgeList(lstBase,varList);
DrawSmolEngine dse = new
DrawSmolEngine(DrawSecond.DrawDiagram(lstBase,lstLink));
dse.DrawUIGraph();
```

Appendix 2: The software code written in SMOL describing the structure of a highway lighting model

```
package UTest
import SMOH.*
import Utils.*
import com.SMOF.*
import com.UI.DrawSmolEngine;
import com.prototype.DrawSecond;
import com.sample.DrawFirst
import com.utils.CustomEdge
import com.utils.INode
import com.utils.NodeBase

DrawFirst df = new DrawFirst();
HashMap<HBase> varList = new HashMap();

//define central node
def(root) = [new MainNode("ROOT")]
varList.put("root",root);

// LAMP 1
//define profibus node
def (can1) = [new CanNode("LAMP_1")]
can1.connect(root,11,SpeedUnit.Mb,300)
varList.put("can1",can1);

//define SA node
def (sa1) = [new SANode("CD_L1")]
sa1.connect(can1,5,SpeedUnit.Mb,1)
varList.put("sa1",sa1);

//define SA node
def (sa2) = [new SANode("SW_L1")]
sa2.connect(can1,5,SpeedUnit.Mb,1)
varList.put("sa2",sa2);
// End of LAMP 1

// LAMP 2
//define profibus node
def (can2) = [new CanNode("LAMP_2")]
can2.connect(root,11,SpeedUnit.Mb,400)
varList.put("can2",can2);

//define SA node
```

```
def (sa3) = [new SANode("CD_L2")]
sa3.connect(can2,5,SpeedUnit.Mb,1)
varList.put("sa3",sa3);

//define SA node
def (sa4) = [new SANode("SW_L2")]
sa4.connect(can2,5,SpeedUnit.Mb,1)
varList.put("sa4",sa4);
// End of LAMP 2

// LAMP 3
//define profibus node
def (can3) = [new CanNode("LAMP_3")]
can3.connect(root,11,SpeedUnit.Mb,500)
varList.put("can3",can3);

//define SA node
def (sa5) = [new SANode("CD_L3")]
sa5.connect(can3,5,SpeedUnit.Mb,1)
varList.put("sa5",sa5);

//define SA node
def (sa6) = [new SANode("SW_L3")]
sa6.connect(can3,5,SpeedUnit.Mb,1)
varList.put("sa6",sa6);
// End of LAMP 3

// LAMP 4
//define profibus node
def (can4) = [new CanNode("LAMP_4")]
can4.connect(root,11,SpeedUnit.Mb,600)
varList.put("can4",can4);

//define SA node
def (sa7) = [new SANode("CD_L4")]
sa7.connect(can4,5,SpeedUnit.Mb,1)
varList.put("sa7",sa7);

//define SA node
def (sa8) = [new SANode("SW_L4")]
sa8.connect(can4,5,SpeedUnit.Mb,1)
varList.put("sa8",sa8);
// End of LAMP 4

// LAMP 5
//define profibus node
def (can5) = [new CanNode("LAMP_5")]
can5.connect(root,11,SpeedUnit.Mb,500)
varList.put("can5",can5);

//define SA node
def (sa9) = [new SANode("CD_L5")]
sa9.connect(can5,5,SpeedUnit.Mb,1)
varList.put("sa9",sa9);

//define SA node
def (sa10) = [new SANode("SW_L5")]
sa10.connect(can5,5,SpeedUnit.Mb,1)
varList.put("sa10",sa10);
// End of LAMP 5

// LAMP 6
//define profibus node
def (can6) = [new CanNode("LAMP_6")]
can6.connect(root,11,SpeedUnit.Mb,400)
varList.put("can6",can6);

//define SA node
def (sa11) = [new SANode("CD_L6")]
sa11.connect(can6,5,SpeedUnit.Mb,1)
varList.put("sa11",sa11);

//define SA node
def (sa12) = [new SANode("SW_L6")]
sa12.connect(can6,5,SpeedUnit.Mb,1)
varList.put("sa12",sa12);
// End of LAMP 6

// LAMP 7
//define profibus node
def (can7) = [new CanNode("LAMP_7")]
can7.connect(root,11,SpeedUnit.Mb,300)
varList.put("can7",can7);

//define SA node
def (sa13) = [new SANode("CD_L7")]
sa13.connect(can7,5,SpeedUnit.Mb,1)
varList.put("sa13",sa13);

//define SA node
def (sa14) = [new SANode("SW_L7")]
sa14.connect(can7,5,SpeedUnit.Mb,1)
varList.put("sa14",sa14);
// End of LAMP 7

// LAMP 8
//define profibus node
def (can8) = [new CanNode("LAMP_8")]
can8.connect(root,11,SpeedUnit.Mb,200)
varList.put("can8",can8);
//
//define SA node
def (sa15) = [new SANode("CD_L8")]
sa15.connect(can8,5,SpeedUnit.Mb,1)
varList.put("sa15",sa15);
//
////define SA node
def (sa16) = [new SANode("SW_L8")]
sa16.connect(can8,5,SpeedUnit.Mb,1)
varList.put("sa16",sa16);
// End of LAMP 8

// LAMP 9
//define profibus node
def (can9) = [new CanNode("LAMP_9")]
can9.connect(root,11,SpeedUnit.Mb,200)
varList.put("can9",can9);

////define SA node
def (sa17) = [new SANode("CD_L9")]
sa17.connect(can9,5,SpeedUnit.Mb,1)
varList.put("sa17",sa17);
//
////define SA node
def (sa18) = [new SANode("SW_L9")]
sa18.connect(can9,5,SpeedUnit.Mb,1)
varList.put("sa18",sa18);
// End of LAMP 9

List<NodeBase> lstBase = Helper.GenerateVertexList(varList)
List<CustomEdge> lstLink = Helper.GenerateEdgeList(lstBase,
varList)
DrawSmolEngine dse = new
DrawSmolEngine(DrawSecond.DrawDiagram(lstBase, lstLink));
dse.DrawUIGraph();
```

Appendix 3: A Java code generated by the SMOLsim module

```
public class Lamp extends SimulationProcess {
        private LampProcess myModel;
        public boolean turningOnLight = false;
        public boolean minIllumination = false;
        public boolean turningOffLight = false;
        public Lamp(Model owner, String name, boolean
showInTrace) {super(owner, name, showInTrace);
            myModel = (LampProcess) owner;}
        @Override
        public void lifeCycle() {
                sendTraceNote("Lamp process started");
        }
}
```

Metrol. Meas. Syst., Vol. 24 (2017), No. 3, pp. 489–507.

PAN
POLSKA AKADEMIA NAUK
METROLOGY AND MEASUREMENT SYSTEMS
Index 330930, ISSN 0860-8229
www.metrology.pg.gda.pl
M&MS

INSTABILITY CHARACTERISTICS OF FREE-STANDING NANOWIRES BASED ON THE STRAIN GRADIENT THEORY WITH THE CONSIDERATION OF CASIMIR ATTRACTION AND SURFACE EFFECTS

Hamid M. Sedighi1), Hassen M. Ouakad2), Moosa Khooran1)

1) Shahid Chamran University of Ahvaz, Faculty of Engineering, Mechanical Engineering Department, Ahvaz 61357-43337, Iran
(✉ h.msedighi@scu.ac.ir, +98 61 33 330 010 5768, *moosakhooran@gmail.com)*
2) King Fahd University of Petroleum and Minerals, Department of Mechanical Engineering, Dhahran, 31261, KSA
(houakad@kfupm.edu.sa)

Abstract

Size-dependent dynamic instability of cylindrical nanowires incorporating the effects of Casimir attraction and surface energy is presented in this research work. To develop the attractive intermolecular force between the nanowire and its substrate, the *proximity force approximation* (PFA) for small separations, and the Dirichlet asymptotic approximation for large separations with a cylinder-plate geometry are employed. A nonlinear governing equation of motion for free-standing nanowires – based on the Gurtin-Murdoch model – and a strain gradient elasticity theory are derived. To overcome the complexity of the nonlinear problem in hand, a Garlerkin-based projection procedure for construction of a reduced-order model is implemented as a way of discretization of the governing differential equation. The effects of length-scale parameter, surface energy and vacuum fluctuations on the dynamic instability threshold and adhesion of nanowires are examined. It is demonstrated that in the absence of any actuation, a nanowire might behave unstably, due to the Casimir induction force.

Keywords: free-standing cylindrical nanowire, Casimir force, proximity force approximation, Dirichlet asymptotic approximation.

1. Introduction

In the last decades, the application of nanowire-based nanostructures is extensively growing because of their excellent physical properties such as their small size giving a large surface area-to-volume ratio. Due to their exciting properties, nanowires are promising candidates for detecting nano-objects with high sensitivity, and also they can be potentially employed in several fields, such as measurement systems [1, 2], *Micro/Nanoelectromechanical Systems* (M/NEMS) [3], biological or gas sensing devices [4], flexible electronics and renewable energy technologies [5], integrated *Shape Memory Alloy* (SMA) [6], resonators and actuators [7, 8] and multifunctional NEMSs.

Essentially, when the electronic and mechanical systems were successfully integrated in a nanoscale, some new phenomena originally governed by the nanoscale quantum effects have become more and more important. As an example, the motion of a nanowire-based structure is affected by the small-scale quantum electro-dynamical interactions, such as vacuum fluctuations. The van der Waals effect stems from the electrostatic interaction between a pair of magnetic poles at an atomic-order distance. The Casimir force stands for the attractive force between two flat parallel plates of solids that originates from quantum fluctuations in the ground state of the electromagnetic field [9].

The effect of vacuum fluctuation forces can be modelled by the Casimir attraction which is the dominant phenomenon in any sub-micron separation-based application [10–12]. Using experiments, Zou *et al.* [13] could demonstrate the Casimir effect between two micro-machined

Article history: received on Oct. 12, 2016; accepted on Mar. 28, 2017; available online on Sep. 01, 2017; DOI: 10.1515/mms-2017-0042.

silicon components on the same substrate. They achieved this result by integrating a force-sensing micromechanical beam and an electrostatic actuator on a single chip. Buks and Roukes [14] reported an experimental study of surface-surface interactions using micro-machined cantilevers fabricated from Au and focused on the extreme manifestation of Casimir interaction and the energy associated with this process.

The same effect is also numerically examined by Lombardo *et al.* [15], where the Casimir interaction energy is evaluated for configurations involving two perfectly conducting eccentric cylinders and a cylinder in front of a plane. The exact equation prescribing the Casimir force is analytically derived by Emig *et al*. [16] for a configuration involving a plate and a cylinder with the assumption of an intermediate geometry between the parallel plates and the plate-sphere configurations. Bordag *et al.* [17] published a review of some experimental and theoretical developments in the characterization of the Casimir effect in a nanoscale. They demonstrated that the Casimir force strongly depends on the shape, size, geometry and topology of boundaries. Therefore, many authors worked on computing the Casimir attraction assuming different geometries, *e.g*. parallel plates [18–20], plate-sphere [21], parallel cylinders [22] and plate-cylinder [23].

Also, many papers are concerned on studying the instability characteristics and nonlinear analysis of micro/nano-scale structures involving different assumptions and theories, such as the nonlocal elasticity theory [24–31], strain gradient theory [32–35], modified strain gradient theory [36, 37], strain-inertia gradient elasticity [38], nonlocal strain gradient theory [39] *etc.* It is worth mentioning that any nanoscale device might adhere to its actuating substrate under the effect of the Casimir attractive force, if a minimum gap between the flexible nanostructure and its substrate is not considered. Besides being one of the most effective ways of turning in the instability of freestanding nanostructures, the Casimir force can also induce undesired adhesion during the fabrication stages. Therefore, a fundamental understanding of the stability behaviour of free-standing nanowires is central to precise designing and mounting of these structures. All the previous works have studied the instability analysis of small-sized structures having planar or rectangular cross-sections. However, to the best of the authors' knowledge, no prior study considers the Casimir force while incorporating the surface effects with the application to dynamic instability characteristics of size-dependent nano-beams with a circular cross-section.

The experiments demonstrate that the surface layer plays an important role in the structural behaviour of nanoscale structures which is due to their surface-to-volume ratio [40]. Atoms in a free surface of nanostructures experience a local environment different from that met by atoms in any other bulk material. Consequently, these atoms have a different energy level than the atoms in the bulk pattern. The excess energy of surface atoms is called the surface free energy [41]. In the classical continuum mechanics, the effect of surface layer is typically ignored. However, for nanoscale devices, because of high surface-to-volume ratios, the influence of the surface layer on the overall dynamic behaviour of nanostructure could no longer be neglected. Gurtin and Murdoch [42] presented a surface elasticity theory to model the surface layer of a solid as a membrane with negligible thickness. In another study by Sedighi [43] the dynamic pull-in behaviour of an electrically actuated nano-bridge is studied, which features a rectangular cross-section incorporating the surface and intermolecular effects. Using a nonlocal finite element model, Eltaher *et al.* [44] examined the vibration characteristics of nano-beams accounting for the surface layer effects. Fu and Zhang [45] examined the pull-in behaviour of an electrically actuated nano-beam by incorporating the surface elasticity. They solved the complex mathematical problem by the *Analog Equation Method* (AEM). Their discussion considered the effects of surface energies on the static and dynamic responses, pull-in voltage and pull-in time. Koochi et al. [46] studied the influence of surface effect on the static instability behaviour of a cantilever nano-actuator in the presence of *van der Waals* force (vdW).

In the previous works, Sedighi and Bozorgmehri [47, 48] studied the dynamic behaviour of vibrating nanowires based on the non-local and modified couple stress theories. In the current paper, we examine the static and dynamic instability threshold of circular cross-section-based nano-systems (such as nanowires and nanotubes) by employing the *Strain Gradient Elasticity Theory* (SGET) which has three length-scale parameters to account for the size dependency of sub-micron structures. In addition, we use a new *Reduced-Order Method* (ROM) to capture the first three natural frequencies of nanowires. The main purpose of the present study is to examine the influence of Casimir attraction on the instability/adhesion characteristics of nano-bridges while addressing the size-dependency and surface layer effects. To serve this goal, the strain gradient elasticity theory together with the Euler-Bernoulli beam model are employed to derive a governing equation of nanowires accounting for the vacuum fluctuations and surface energy. To solve the nonlinear governing equation of motion, a reduced-order model, based on the so-called Galerkin expansion, is presented and performed. Finally, the effects of different parameters on the instability behaviour and adhesion time of Casimir-induced free-standing nanowires are studied.

2. Mathematical modelling

Figure 1 shows a schematic view and an SEM image of a free-standing doubly-clamped nanowire above a flat plate substrate. Influenced by the Casimir attractive force, the flexible cylinder can deform towards the fixed ground plane. The nanowire features an initial gap D, length L and radius R. Following, the governing equations of Casimir-induced nanowires are derived based on two different approaches: the PFA approach for small separation and the Dirichlet mode approach for large separation approximations.

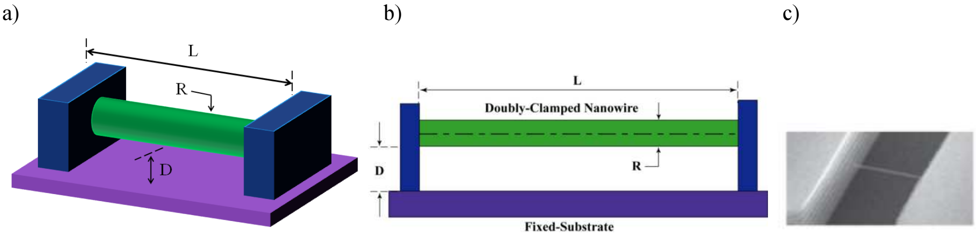

Fig. 1. A 3D schematic view (a); a 2D side view (b) and an SEM image of a doubly-clamped cylinder-plate based nanowire (c).

2.1. *Effect of surface stresses*

Figure 2 illustrates a doubly-clamped nanowire including a surface layer. Following the Gurtin-Murdoch approach [42], it is assumed that the nanowire has an elastic surface with zero thickness and specific material characteristics accounting for the surface energy effects.

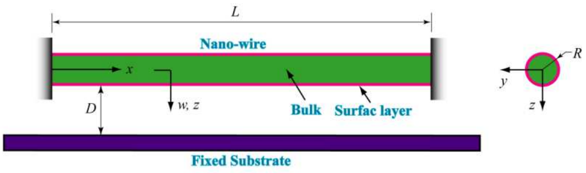

Fig. 2. A 2D schematic representation of a doubly-clamped nanowire.

To model the surface energy, the nano-bridge is split into two layers; a surface layer and a core (bulk) layer. The modulus of elasticity for the surface layer is represented by E_0 (determined from atomistic calculations). Assuming there is no residual stress in the bulk material due to surface tension, the corresponding bulk stress-strain relations of the beam may be written as [49]:

$$\sigma_{xx} = E\varepsilon_{xx} + v\sigma_{zz}, \tag{1}$$

where v is the Poisson's ratio of nano-beam. In the classical continuum mechanics theory, the stress component σ_{zz} is assumed zero. However, the equilibrium will not be satisfied with this assumption, if the surface stress is considered. In this case, the stress component σ_{zz} is expressed as follows [50]:

$$\sigma_{zz} = \frac{1}{2}\left(\sigma_{zz}^{+} + \sigma_{zz}^{-}\right) + \frac{z}{2R}\left(\sigma_{zz}^{+} - \sigma_{zz}^{-}\right), \tag{2}$$

where σ_{zz}^{+} and σ_{zz}^{-} are stresses at the top and bottom surface fibres, respectively. The stresses of the surface layer satisfy the following equilibrium relation [45]:

$$\sigma_{zz} = \frac{1}{2}\left[\left(\tau_0^{+} - \tau_0^{-}\right)\left(\frac{\partial^2 w}{\partial x^2}\right) - \left(\rho_0^{+} - \rho_0^{-}\right)\left(\frac{\partial^2 w}{\partial t^2}\right)\right] + \frac{z}{2R}\left[\left(\tau_0^{+} + \tau_0^{-}\right)\left(\frac{\partial^2 w}{\partial x^2}\right) - \left(\rho_0^{+} + \rho_0^{-}\right)\left(\frac{\partial^2 w}{\partial t^2}\right)\right]. \tag{3}$$

Moreover, Gurtin and Murdoch [42] developed the constitutive equations for the surface layers:

$$\tau_{xx} = \tau_0 + E_0\frac{\partial u}{\partial x}, \quad \tau_{zx} = \tau_0\frac{\partial w}{\partial x}, \tag{4}$$

where τ_{xx} and τ_{zx} are non-zero membrane stresses existing on the contact surfaces of the bulk material and surface layers. The following equilibrium relations must be satisfied by stresses of the surface layers [50]:

$$\left(\frac{\partial \tau_{\beta i}}{\partial \beta}\right)^{+} = \sigma_{iz}^{+} + \rho_0^{+}\left(\frac{\partial^2 u_i}{\partial t^2}\right)^{+}, \tag{5a}$$

$$\left(\frac{\partial \tau_{\beta i}}{\partial \beta}\right)^{-} = \sigma_{iz}^{-} + \rho_0^{-}\left(\frac{\partial^2 u_i}{\partial t^2}\right)^{-}, \tag{5b}$$

where $\beta = x, y$ and $i = x, y, z$, $u_i^{+} = u_i\left(z = +R\right)$ and $u_i^{-} = u_i\left(z = -R\right)$ denote a displacement of surface layers in the i-direction.

2.2. Effect of Casimir attractive force

For the case of conducting by flat parallel plates separated with a gap D, the Casimir energy per unit area is expressed as [51]:

$$E_{pp}(D) = -\frac{\pi^2 \bar{h} c}{720 D^3}, \tag{6}$$

where c is the light speed and $\bar{h}$ is Planck's constant [17]. It should be noted that this formula can be obtained while considering the electromagnetic mode structure between two plates in comparison with the free space by assigning a zero-point energy to each electromagnetic mode [52]. To predict the Casimir force in the case of a small gap, the *Proximity Force Approximation* (PFA) makes use of (6). The interaction between any other surfaces may be modelled by an extension of the PFA approach with the summation of infinitesimal parallel plates [17]. For small gaps, the correct zero$^{\text{th}}$-order approximation for the Casimir energy is given by [13]:

$$E^{PFA} = \int_{s} E_{PP}(D)dS = -\frac{\pi^2 \bar{h} C}{720}\iint \frac{dS}{D^3}, \tag{7}$$

where S is one of the two surfaces distanced by a gap. It should be emphasized that the PFA cannot be used in the case of large separation or non-smooth surfaces. Therefore, another approach should be then employed. A path integral representation [53] is used to properly model the Casimir energy for large separations. The electrodynamic Casimir energy of two parallel metallic surfaces assuming the Dirichlet mode definition at zero temperature can be expressed as [54, 55]:

$$E^{D} = \frac{\bar{h}c}{2\pi}\int_{0}^{\infty} Tr\ln(MM_{\infty}^{-1})dq_0, \tag{8}$$

where:

$$M_{12}\left(u,u';q_0\right)=G_0\left(s_1(u)-s_2(u');q_0\right),$$
$$G_0\left(x,x';q_0\right)=\frac{e^{-q_0\left|x-x'\right|}}{4\pi\left|x-x'\right|}, \tag{9}$$

where a matrix M_{12} denotes the geometry of surfaces 1 and 2, M_{∞}^{-1} is an inverse of matrix M at infinite surface separation, $s_i\left(u\right)$ represents a vector referring to the i-th surface parameterized by a surface vector u and G_0 is the free space Green function [56].

Based on the PFA approach (for small separations), the Casimir energy can be obtained as [13]:

$$E^{PFA} = -\frac{\pi^3 \bar{h} cL}{960}\sqrt{\frac{R}{2D^5}}, \tag{10}$$

where R denotes a radius of nanowire and D is a gap width. Therefore, the Casimir force for *Small Separation Approximation* (SSA) can be obtained by differentiating the energy in respect of D as:

$$f_{cas} = -\frac{\partial E(D)}{\partial D} = \frac{1}{768}\pi^3 \bar{h} cL\sqrt{\frac{2R}{D^7}}. \tag{11}$$

Otherwise, for the case of cylinder-plate geometry with a large separation gap, *i.e.* $D >> R$, the approximate expression for the attractive Casimir energy is written as [57]:

$$E^{D} = -\frac{\bar{h}cL}{D^2}\frac{1}{16\pi\ln(\frac{D}{R})}. \tag{12}$$

Therefore, the Casimir force for *large separation approximation* (LSA) can be expressed as:

$$f_{cas} = \frac{\bar{h}cL}{D^3}\frac{1}{8\pi\ln(\frac{D}{R})} + \frac{\bar{h}cL}{D^3}\frac{1}{16\pi\ln^2(\frac{D}{R})}. \tag{13}$$

2.3. Strain Gradient Elasticity Theory (SGET)

It is well-known that size has a strong impact on the mechanical behaviour of micro- and nanostructures. For instance, the bending rigidity of silica and polythene beams can increase substantially when the breadth of the beam reduces to several tens of nanometres. It should be noted that the classical continuum theories fail to predict and interpret the size effect phenomena. To address this issue, the size-dependent continuum theories (such as SGET) have been developed, which introduce additional material length-scale parameters as well as the Lame constants. In the strain gradient theory, the strain energy density with small deformation may be expressed as [58]:

$$\bar{U}=\frac{1}{2}\left(\sigma_{ij}\varepsilon_{ij}+p_i\gamma_i+\tau_{ijk}^{(1)}\eta_{ijk}^{(1)}+m_{ij}^s\chi_{ij}^s\right), \tag{14}$$

where:

$$\varepsilon_{ij}=\frac{1}{2}\left(u_{i,j}+u_{j,i}\right), \tag{15}$$

$$\gamma_i=\varepsilon_{mm,i}, \tag{16}$$

$$\eta_{ijk}^{(1)}=\frac{1}{3}\left(\varepsilon_{jk,i}+\varepsilon_{ki,j}+\varepsilon_{ij,k}\right)-\frac{1}{15}\delta_{ij}\left(\varepsilon_{mm,k}+2\varepsilon_{mk,m}\right)-\frac{1}{15}\left[\delta_{jk}\left(\varepsilon_{mm,i}+2\varepsilon_{mi,m}\right)+\delta_{ki}\left(\varepsilon_{mm,j}+2\varepsilon_{mj,m}\right)\right], \tag{17}$$

$$\chi_{ij}^s=\frac{1}{2}e_{jkl}u_{l,ki}. \tag{18}$$

In the above equations, u_i, γ_i, $\eta_{ijk}^{(1)}$, χ_{ij}^s, δ_{ij} and e_{ijk} indicate a displacement vector, a dilatation gradient vector, a deviatory stretch gradient tensor, a symmetric rotation gradient tensor, Kronecker delta and permutation symbols, respectively. Also, ε_{ij}, σ_{ij}, p_i, $\tau_{ijk}^{(1)}$, m_{ij}^s, are a strain tensor, Cauchy's stress and high order stress tensors, respectively, and are expressed as [58]:

$$\sigma_{ij}=2\mu\left(\varepsilon_{ij}+\frac{\nu}{1-2\nu}\varepsilon_{mm}\delta_{ij}\right), \tag{19}$$

$$p_i=2\mu l_0^2\gamma_i, \tag{20}$$

$$\tau_{ijk}^{(1)}=2\mu l_1^2\eta_{ijk}^{(1)}, \tag{21}$$

$$m_{ij}^s=2\mu l_2^2\chi_{ij}^s, \tag{22}$$

where v and μ are Poisson's ratio and shear modulus, respectively. Also, l_0, l_1 and l_2 are additional material length-scale parameters in the constitutive equations of higher-order stresses.

2.4. Governing equation of motion

In this section, the governing equation for size-dependent vibration of Casimir-induced nanowires in the presence of surface effects is derived. Based on the Euler-Bernoulli beam theory, the displacement field can be expressed as follows:

$$u(x,z,t)=-z\theta(x,t)=-z\frac{\partial w}{\partial x}, \qquad w=w(x,t). \tag{23}$$

The strain of a material point located at a distance z from the top plane for a nano-beam is represented as:

$$\varepsilon_{xx}=\frac{\partial u}{\partial x}=-z\frac{\partial^2 w}{\partial x^2}. \tag{24}$$

Substituting the linear displacement field of (23) into (15) to (22), the total strain energy on the basis of SGET for a deformed Euler-Bernoulli beam is given by:

$$U_{SGET}=\frac{1}{2}\int_0^L\left[\left(2\mu Al_0^2+\frac{8}{15}\mu Al_1^2+\mu Al_2^2\right)\left(\frac{\partial^2 w}{\partial x^2}\right)^2+I\left(2\mu l_0^2+\frac{4}{5}\mu l_1^2\right)\left(\frac{\partial^3 w}{\partial x^3}\right)^2\right]dx. \tag{25}$$

In (25), I represents the second moment of inertia of the beam around its y-axis. Based on the surface elasticity theory, the strain energy in the surface layer with zero thickness can be expressed as [59]:

Metrol. Meas. Syst., Vol. 24 (2017), No. 3, pp. 489–507.

$$U_s = \frac{1}{2}\int_0^L \int_S \left(\tau_{\alpha\beta}\varepsilon_{\alpha\beta} + \tau_{k\alpha}u_{k,\alpha}\right) dS dx, \tag{26}$$

where α, β denote in-plane Cartesian coordinates of the surface and k is an out-plane Cartesian coordinate of the surface. Substituting (4) into (26) results in:

$$\begin{aligned} U_s &= \frac{1}{2}\int_0^L \int_S \left[\left(\tau_0 + E_0\frac{\partial u}{\partial x}\right)\varepsilon_{xx} + \tau_0\left(\frac{\partial w}{\partial x}\right)^2\right] dSdx \\ &= \frac{1}{2}\int_0^L \int_{S^+} \left[-\left(\tau_0^+ - E_0^+ z\frac{\partial^2 w}{\partial x^2}\right) z\frac{\partial^2 w}{\partial x^2} + \tau_0^+\left(\frac{\partial w}{\partial x}\right)^2\right] dS^+ dx \\ &+ \frac{1}{2}\int_0^L \int_{S^-} \left[-\left(\tau_0^- - E_0^- z\frac{\partial^2 w}{\partial x^2}\right) z\frac{\partial^2 w}{\partial x^2} + \tau_0^-\left(\frac{\partial w}{\partial x}\right)^2\right] dS^- dx. \end{aligned} \tag{27}$$

Simplifying the surface energy described in (27) yields:

$$U_s = \frac{1}{2}\int_0^L \left[\left(\tau_0^+ + \tau_0^-\right) S_0^* \left(\frac{\partial w}{\partial x}\right)^2 + \left(E_0^+ + E_0^-\right) I_0^* \left(\frac{\partial^2 w}{\partial x^2}\right)^2\right] dx. \tag{28}$$

In addition, the virtual work $\tilde{W}$ induced by the axial and Casimir forces incorporating the von-Kármán type nonlinear strain can be written as [60]:

$$\tilde{W} = -\frac{1}{2}\int_0^L \left(N_0 + \frac{EA}{2L}\int_0^l \left(\frac{\partial w}{\partial x}\right)^2 dx\right)\left(\frac{\partial w}{\partial x}\right)^2 dx + \int_0^L f_{cas} w\, dx. \tag{29}$$

The kinetic energies for the bulk material and surface layer are obtained as follows:

$$\begin{aligned} T &= \frac{1}{2}\int_0^L \int_A \rho\left(\frac{\partial w}{\partial t}\right)^2 dAdx + \frac{1}{2}\int_0^L \int_{S^+} \rho_0^+\left(\frac{\partial w}{\partial t}\right)^2 dS^+ dx + \frac{1}{2}\int_0^L \int_{S^-} \rho_0^-\left(\frac{\partial w}{\partial t}\right)^2 dS^- dx \\ &= \frac{1}{2}\left(\rho A + \left(\rho_0^+ + \rho_0^-\right) S_0^*\right)\int_0^L \left(\frac{\partial w}{\partial t}\right)^2 dx. \end{aligned} \tag{30}$$

The first variation of the strain energy function is obtained as [61, 62]:

$$\delta U_b = \int_0^L \int_A \sigma_{ij}\delta\varepsilon_{ij} dAdx, \tag{31}$$

where A is an area of the cross-section of nano-beam.

Substituting (15) into (22), the variation of the strain energy function can be obtained as:

$$\delta U_b = -\int_0^l \int_A z\sigma_{xx}\frac{\partial^2 \delta w}{\partial x^2} dAdx = \int_0^l M(x,t)\left(\frac{\partial^2 \delta w}{\partial x^2}\right) dx, \tag{32}$$

where $M(x,t) = -\int_A \sigma_{xx} z dA$ is a resultant bending moment of the nanowire. Applying the Hamilton's principle results in:

$$\int_{t_1}^{t_2} \left(\delta T - \left[\delta U_b + \delta U_s\right] + \delta W\right) dt = 0. \tag{33}$$

Subsequently, while assuming some mathematical simplifications, the nonlinear governing equation of motion can be written as follows:

$$\begin{aligned}\frac{\partial^2 M}{\partial x^2} &= -\left(\rho A+\left(\rho_0^+ + \rho_0^-\right)S_0^*\right)\frac{\partial^2 w}{\partial t^2} - \left(E_0^+ + E_0^-\right)I_0^*\frac{\partial^4 w}{\partial x^4} + \left(\tau_0^+ + \tau_0^-\right)S_0^*\frac{\partial^2 w}{\partial x^2}\\ &+\left(2\mu A l_0^2 + \frac{8}{15}\mu A l_1^2 + \mu A l_2^2\right)\frac{\partial^4 w}{\partial x^4} - I\left(2\mu l_0^2 + \frac{4}{5}\mu l_1^2\right)\frac{\partial^6 w}{\partial x^6}\\ &+\left(N_0 + \frac{EA}{2L}\int_0^L\left(\frac{\partial w}{\partial x}\right)^2 dx\right)\frac{\partial^2 w}{\partial x^2} + f_{cas},\end{aligned} \tag{34}$$

and the corresponding boundary conditions at the ends of the nano-bridge can be written as follows:

$$w\left(x=0\right)=0,\ \frac{\partial w}{\partial x}\left(x=0\right)=0,\ \ w\left(x=L\right)=0,\ \frac{\partial w}{\partial x}\left(x=L\right)=0, \tag{35}$$

Using the relation of normal stress described in the equation (1), a resultant bending moment of nanowire can be expressed as:

$$\begin{aligned}M\left(x,t\right) &= -\int_A \sigma_{xx} z dA = -\int_A\left(Ez\varepsilon_{xx} + v\left\{\frac{z}{2}\left[\left(\tau_0^+ - \tau_0^-\right)\left(\frac{\partial^2 w}{\partial x^2}\right) - \left(\rho_0^+ - \rho_0^-\right)\left(\frac{\partial^2 w}{\partial t^2}\right)\right]\right.\right.\\ &\left.\left.+\frac{z^2}{h}\left[\left(\tau_0^+ + \tau_0^-\right)\left(\frac{\partial^2 w}{\partial x^2}\right) - \left(\rho_0^+ + \rho_0^-\right)\left(\frac{\partial^2 w}{\partial t^2}\right)\right]\right\}\right)dA\\ &= EI\frac{\partial^2 w}{\partial x^2} - \frac{vAR}{2}\left(\left(\tau_0^+ - \tau_0^-\right)\frac{\partial^2 w}{\partial x^2} - \left(\rho_0^+ - \rho_0^-\right)\frac{\partial^2 w}{\partial t^2}\right) - \frac{vI}{2R}\left(\left(\tau_0^+ + \tau_0^-\right)\frac{\partial^2 w}{\partial x^2} - \left(\rho_0^+ + \rho_0^-\right)\frac{\partial^2 w}{\partial t^2}\right).\end{aligned} \tag{36}$$

Therefore, the governing equation of motion for nanowires can be obtained by inserting (27) into (25) as follows:

$$\begin{aligned}&EI\frac{\partial^4 w}{\partial x^4} + \left(2\mu A l_0^2 + \frac{8}{15}\mu A l_1^2 + \mu A l_2^2\right)\frac{\partial^4 w}{\partial x^4} - I\left(2\mu l_0^2 + \frac{4}{5}\mu l_1^2\right)\frac{\partial^6 w}{\partial x^6}\\ &-\frac{vI}{2R}\left(\left(\tau_0^+ + \tau_0^-\right)\frac{\partial^4 w}{\partial x^4} - \left(\rho_0^+ + \rho_0^-\right)\frac{\partial^4 w}{\partial x^2 \partial t^2}\right) - \frac{vAR}{2}\left(\left(\tau_0^+ - \tau_0^-\right)\frac{\partial^4 w}{\partial x^4} - \left(\rho_0^+ - \rho_0^-\right)\frac{\partial^4 w}{\partial x^2 \partial t^2}\right)\\ &+\left(E_0^+ + E_0^-\right)I_0^*\frac{\partial^4 w}{\partial x^4} - \left(\tau_0^+ + \tau_0^-\right)S_0^*\frac{\partial^2 w}{\partial x^2} = \left[-\left(\rho A + \left(\rho_0^+ + \rho_0^-\right)S_0^*\right)\frac{\partial^2 w}{\partial t^2}\right.\\ &\left.\qquad+\left(N_0 + \frac{EA}{2L}\int_0^l\left(\frac{\partial w}{\partial x}\right)^2 dx\right)\frac{\partial^2 w}{\partial x^2} + f_{cas}\right].\end{aligned} \tag{37}$$

2.5. Normalization of governing equation of motion

In order to describe the governing equation in a non-dimensional from, the following variables are introduced:

$$\begin{aligned}&W = \frac{w}{D},\ \xi = \frac{x}{L},\ \alpha = \frac{EAD^2}{2EI},\ \tau = \sqrt{\frac{E^+ h^2}{12\rho^+ L^4}}\,t,\ f_i = \frac{N_0 L^2}{EI},\ k = \frac{D}{R},\ \mu_l = \frac{12\mu}{E\left(h/l\right)^2}\\ &\mu = \frac{\left(E_0^+ + E_0^-\right)I_0^*}{E^+ I},\ \ \sigma_1 = \frac{-12ARv\left(\tau_0^+ + \tau_0^-\right) - 36vAR\left(\tau_0^+ - \tau_0^-\right)}{E^+ I}\ \ \sigma_2 = \frac{\left(\tau_0^+ + \tau_0^-\right)S_0^* l^2}{E^+ I},\\ &\kappa_1 = \frac{2v\left(\rho_0^+ + \rho_0^-\right)R + 3\left(\rho_0^+ - \rho_0^-\right)}{12\rho^+ L^2},\ \ \kappa_2 = \frac{\left(\rho_0^+ + \rho_0^-\right)S_0^*}{\rho^+ A},\ \gamma = \frac{\bar{h} c L^4}{8\pi D^4 EI}\\ &\alpha_4 = \left(1 + \frac{\mu_l}{15}\left(30\left(\frac{l_0}{l_2}\right)^2 + 8\left(\frac{l_1}{l_2}\right)^2 + 15\right) + \mu - \sigma_1\right),\ \ \alpha_6 = \frac{\mu_l}{30\left(L/h\right)^2}\left[5\left(\frac{l_0}{l_2}\right)^2 + 2\left(\frac{l_1}{l_2}\right)^2\right]\end{aligned} \tag{38}$$

Thus, the non-dimensional equation of motion for size-dependent nanowires incorporating the surface effects and the Casimir force can be written as:

$$\alpha_4 \frac{\partial^4 W}{\partial \xi^4} - \alpha_6 \frac{\partial^6 W}{\partial \xi^6} + \kappa_1 \frac{\partial^4 W}{\partial \xi^2 \partial \overline{\tau}^2} - \sigma_2 \frac{\partial^2 W}{\partial \xi^2} = \left[\frac{\pi^4 \gamma}{96} \sqrt{\frac{2}{k\left(1-W\right)^7}} + \alpha \frac{\partial^2 W}{\partial \xi^2} \int_0^1 \left(\frac{\partial W}{\partial \xi} \right)^2 d\xi - \left(1+\kappa_2\right) \frac{\partial^2 W}{\partial \overline{\tau}^2} \right], \tag{39a}$$

for the SSA approximation and:

$$\begin{gathered} W = \frac{w}{D},\ \ \xi = \frac{x}{L},\ \alpha = \frac{EAD^2}{2EI},\ \tau = \sqrt{\frac{E^+ h^2}{12\rho^+ L^4}}\, t,\ f_i = \frac{N_0 L^2}{EI},\ k = \frac{D}{R},\ \ \mu_l = \frac{12\mu}{E\left(h/l\right)^2} \\ \mu = \frac{\left(E_0^+ + E_0^-\right) I_0^*}{E^+ I},\ \ \sigma_1 = \frac{-12ARv\left(\tau_0^+ + \tau_0^-\right) - 36vAR\left(\tau_0^+ - \tau_0^-\right)}{E^+ I}\ \ \sigma_2 = \frac{\left(\tau_0^+ + \tau_0^-\right) S_0^* l^2}{E^+ I}, \\ \kappa_1 = \frac{2v\left(\rho_0^+ + \rho_0^-\right) R + 3\left(\rho_0^+ - \rho_0^-\right)}{12\rho^+ L^2},\ \ \ \kappa_2 = \frac{\left(\rho_0^+ + \rho_0^-\right) S_0^*}{\rho^+ A},\ \ \gamma = \frac{\overline{h} c L^4}{8\pi D^4 EI} \\ \alpha_4 = \left(1 + \frac{\mu_l}{15} \left(30 \left(\frac{l_0}{l_2} \right)^2 + 8 \left(\frac{l_1}{l_2} \right)^2 + 15 \right) + \mu - \sigma_1 \right),\ \ \ \alpha_6 = \frac{\mu_l}{30\left(L/h\right)^2} \left[5 \left(\frac{l_0}{l_2} \right)^2 + 2 \left(\frac{l_1}{l_2} \right)^2 \right] \\ \alpha_4 \frac{\partial^4 W}{\partial \xi^4} - \alpha_6 \frac{\partial^6 W}{\partial \xi^6} + \kappa_1 \frac{\partial^4 W}{\partial \xi^2 \partial \overline{\tau}^2} - \sigma_2 \frac{\partial^2 W}{\partial \xi^2} = \\ \left[\frac{\gamma}{(1-W)^3} \left(\frac{1}{\ln\left(k(1-W)\right)} + \frac{1}{2\left(\ln\left(k(1-W)\right)\right)^2} \right) + \alpha \frac{\partial^2 W}{\partial \xi^2} \int_0^1 \left(\frac{\partial W}{\partial \xi} \right)^2 d\xi - \left(1+\kappa_2\right) \frac{\partial^2 W}{\partial \overline{\tau}^2} \right] \end{gathered} \tag{39b}$$

for the LSA approach. It is worth mentioning that, due to the nanowire deflection $W\left(x,t\right)$, a distance D assumed in the Casimir force is replaced by $D-W$. Moreover, in the case of a large separation gap, it is assumed that $D+R \approx D$.

3. Solution methodology

3.1. Reduced-order modelling

To simulate the total response of a nanowire, (39a) and (39b) are discretized using a so-called Galerkin procedure to yield a Reduced-Order Model (ROM). Hence, the deflection of nanowire is approximated as:

$$W\left(x,t\right) = \sum_{i=1}^{n} u_i\left(t\right) \phi_i\left(x\right), \tag{40}$$

where $\phi_i\left(x\right)$ are normalized linear undamped mode shapes of a perfectly straight clamped beam, and $u_i(t)$ are non-dimensional modal coordinates. It is worth mentioning here that, because of a nonlinear nature of the Casimir attractive force, symmetric (odd) and anti-symmetric (even) mode shapes are assumed in this work. To obtain the ROM, we substitute the equation (40) into (39a) and (39b), multiply by $\phi_i\left(x\right)$, use the orthogonality conditions of the mode shapes, and then integrate the outcome from 0 to 1. The results are differential equations in terms of the modal coordinates $u_i(t)$ that can be integrated and the total response of nanowire can be obtained from (40).

Several issues need to be clarified about the developed ROM. Unlike the case of rectangular micro-beams [63], here there is no numerical advantage of multiplying (39a) or (39b) by the denominator of Casimir force term, since the mode shape $\phi_i\left(x\right)$ will remain embedded in the nonlinear terms even after imposing the orthogonality of the mode shapes. To deal with the complicated integral terms due to the nonlinear Casimir attractive force, we evaluated the spatial integrals containing the $\phi_i(x)$ terms numerically, using a trapezoidal method, while simultaneously integrating the differential equations of the modal coordinates $u_i(t)$.

3.2. Static response

To simulate the static response, all time-dependent terms in the governing differential equations of nanowire in (39a) and (39b) are set equal to zero. Then, the modal coordinates $u_i(t)$ are replaced by unknown constant coefficients a_i ($i = 1,2,\dots,n$). This results in a system of nonlinear algebraic equations in terms of coefficients a_i. The system is then solved numerically using the Newton-Raphson method [64] to obtain the static deflection of nanowire.

3.3. Eigen-value problem

In this work, we propose to examine the variation of fundamental natural frequency of a nanowire under the effect of the attractive force. Toward this, we consider the ROM obtained in Subsection 3.1, which can be re-written in a matrix form as:

$$M(U)\dot{U} = R(U), \tag{41}$$

where:

$$U = [u_1, u_2, u_3, \dots, u_n], \tag{42}$$

is a modal vector of amplitudes, $M(U)$ is a nonlinear matrix representing the coefficients of $\dot{U}$, and $R(U)$ is a right-hand side vector representing the forcing, stiffness, and damping coefficients. Both $M(U)$ and $R(U)$ are nonlinear functions of the modal coordinates $u_i(t)$. Note here that we consider the symmetric and anti-symmetric mode shapes in the ROM to get all the possible natural frequencies and mode shapes of the nanowire.

Next, we split U into a static component X_s, representing the equilibrium position due to the applied Casimir force, and a dynamic component $\eta(t)$ representing the perturbation around the equilibrium position, that is:

$$U = X_s + \eta(t). \tag{43}$$

Then, substituting (43) into (41), using the Taylor series expansion assuming small η, eliminating the quadratic terms, and using the fact that $R(X_s) = 0$, we obtain the following:

$$M(X_s)\dot{\eta} = J(X_s)\eta, \tag{44}$$

where $J(X_s)$ is a Jacobian matrix calculated at the equilibrium points [65].

To calculate the natural frequencies of nanowire for the applied attractive force, we substitute the stable static solution, X_s, into the matrix $M^{-1}J$ and then find its corresponding eigenvalues. The eigenvalues are calculated by solving the below equation, which gives a characteristic algebraic equation for an eigenvalue λ:

$$det\left(M^{-1}(X_s)J(X_s) - \lambda I\right) = 0, \tag{45}$$

where I symbolizes an identity matrix. Finally, by taking the square root of each individual eigenvalue, we obtain the natural frequencies of the system.

4. Results and discussion

This work attempts to examine the influence of vacuum fluctuations and size-dependency on the nonlinear dynamic behaviour of freestanding nanowires. In order to endorse the accuracy of present ROM simulations, the static deflection of nanowire versus the Casimir force for SSA and LSA models are plotted and compared with the results of Farrokhabadi *et al.* [66] (see Fig. 3). One can clearly observe that the results of our modelling are in a good agreement with those reported in the literature.

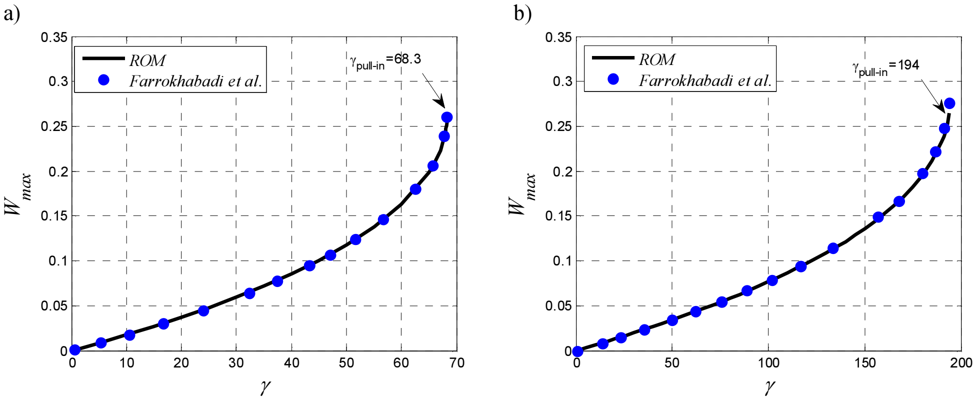

Fig. 3. Variations of the static deflection vs the Casimir force for (a) SSA approximation ($k = 5$) and (b) LSA approximation ($k = 100$), and for $\alpha_4 = 1$, $\alpha_6, \kappa_1, \sigma_2, \alpha, \kappa_2 = 0$.

To show the instability behaviour of a nano-fabricated system by varying the Casimir parameter, Fig. 4 displays variations of the static deflection and the fundamental frequency of nanowire versus the Casimir force parameter γ for the following system parameters: $\alpha_1 = 6$; $\kappa_1 = 0$; $\kappa_2 = 0.2$. It is worth mentioning that, when the geometry parameter k takes rather large values (here $k = 100$), the LSA approximations should be employed to take the Casimir induction force into account. One can observe that any increase in the Casimir induction force leads to reduction of the initial gap and natural frequency of nanowire up to the critical point ($\gamma = 216$) beyond which the nanowire becomes unstable and consequently it collapses onto the fixed substrate. Moreover, Fig. 5 indicates the same behaviour when the geometry parameter is considered small, in which we have to assume the SSA approximation to account for the vacuum fluctuations. It is demonstrated that, for SSA approximation, the nanowire falls to the fixed plate at lower values of the Casimir parameter γ.

In order to examine the influence of geometry ratio k on the predicted critical Casimir value of induced nanowires, variations of $\gamma_{pull\text{-}in}$ as functions of the geometry parameter for two different models, *i.e.* LSA and SSA, are displayed in Fig. 6. One can observe that $\gamma_{pull\text{-}in}$ is remarkably affected by this parameter. It is shown that the Casimir critical value increases continuously with increasing the geometry ratio k. This reveals that, as the initial gap D increases and/or the radius of nanowire decreases, the free-standing nanowire diverges to the bottom plate at higher values of the Casimir parameter.

Due to a high surface-to-volume ratio of several nano-fabricated structures, it was empirically showed that the surface stress plays a significant role in the static and dynamic behaviour of such devices. To show the impact of surface stress σ_2 on the instability characteristics of Casimir-induced nanowires, variations of the static deflection and the first natural frequency are presented in Figs. 7 and 8 for both LSA and SSA approximations, respectively.

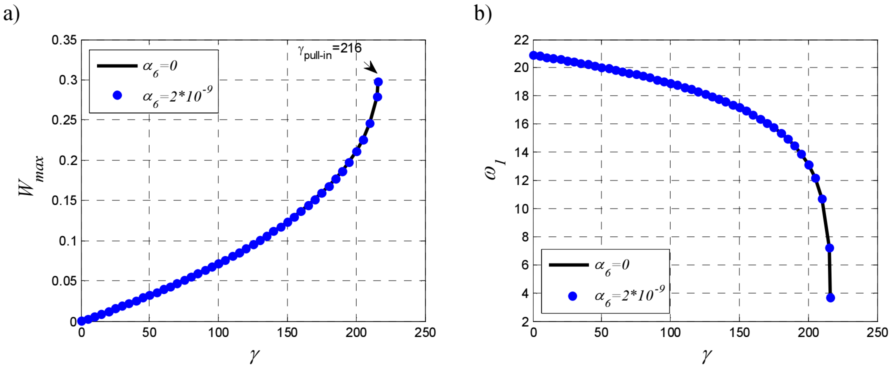

Fig. 4. Variations of (a) the static deflection and (b) the natural frequency vs the Casimir force for LSA approximation and $k = 100$, $\alpha_4 = 1, \sigma_2 = 2$.

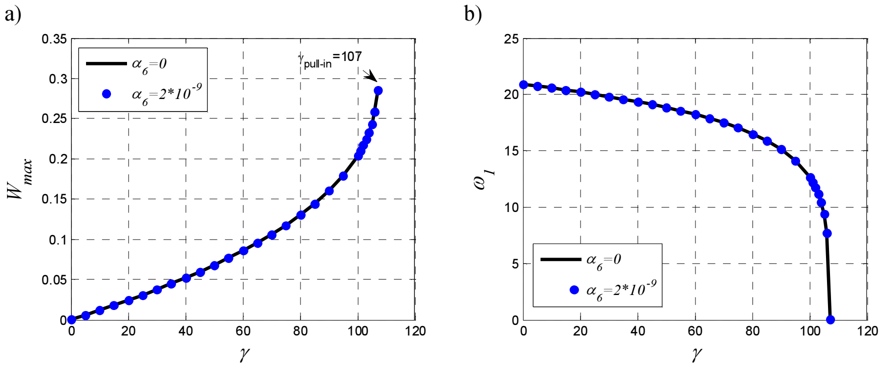

Fig. 5. Variations of (a) the static deflection and (b) the natural frequency vs the Casimir force for SSA approximation and $k = 10$, $\alpha_4 = 1, \sigma_2 = 2$

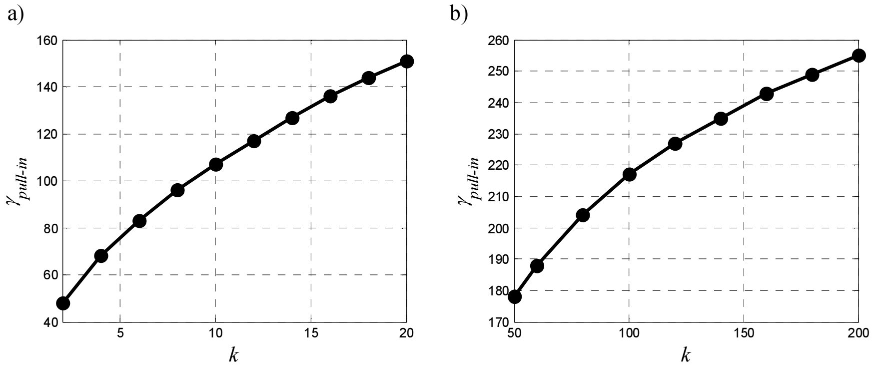

Fig. 6. Variations of the critical Casimir value vs the geometry ratio for (a) SSA and (b) LSA approximations.

It is illustrated that the critical values of Casimir parameter, predicted by both LSA and SSA models, increase as the parameter σ_2 varies from negative to positive values. In addition, one can infer that in the absence of any Casimir attraction, the fundamental frequency of nanowire shifts upward by increasing the surface stress values.

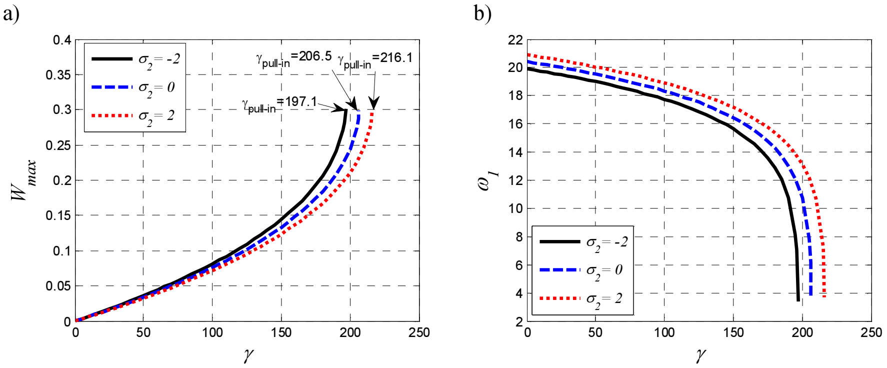

Fig. 7. Variations of (a) the static deflection and (b) the natural frequency vs the Casimir force for LSA approximation and some assigned values of σ_2 and $\alpha_4 = 1$.

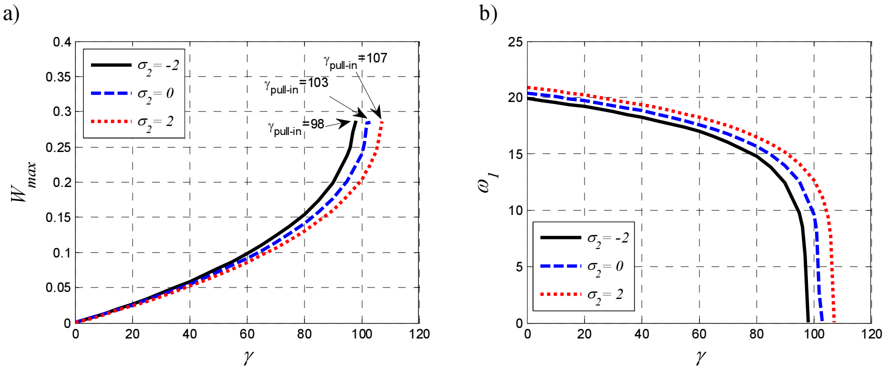

Fig. 8. Variations of (a) the static deflection and (b) the natural frequency vs the Casimir force for SSA approximation and some assigned values of σ_2 and $\alpha_4 = 1$.

As mentioned earlier, it has been validated that the mechanical behaviour of miniature-sized structures are size-dependent and the classical theories may not predict the instability threshold of nano-beams precisely. To this end, the *strain gradient elasticity theory* (SGET) including three material length-scale parameters has been employed to capture the micro-structure size-dependency. In this paper, the non-dimensional parameter α_4 accounts for the length-scale parameters. Figs. 9 and 10 depict variations of the initial gap between the nanowire and substrate as well as the first natural frequency of induced nanowire as functions of the Casimir parameter γ for three values of parameter α_4. One can conclude that the instability occurs at higher values of Casimir parameter by increasing the size parameter α_4. Moreover, according to Figs. 9b and 10b, it is clearly shown that the fundamental frequency of nanowire increases when the length-scale parameter increases.

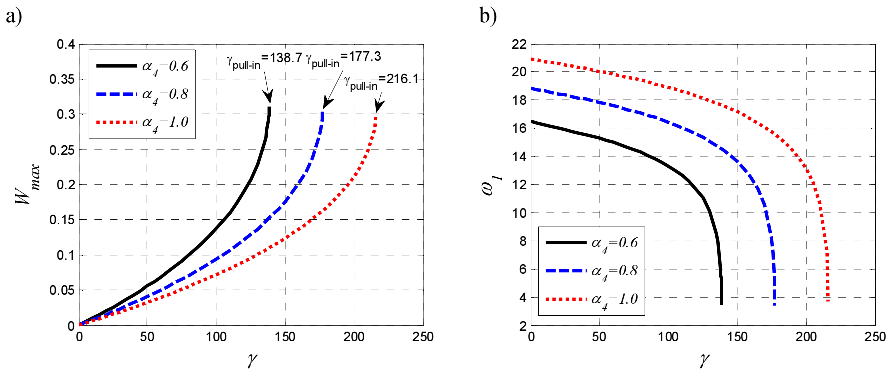

Fig. 9. Variations of (a) the static deflection and (b) the natural frequency vs the Casimir force for LSA approximation and $\sigma_2 = 2$.

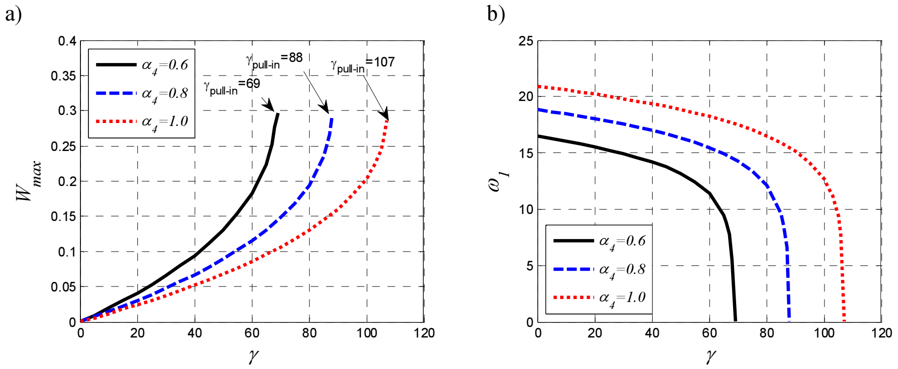

Fig. 10. Variations of (a) the static deflection and (b) the natural frequency vs the Casimir force for SSA approximation and $\sigma_2 = 2$.

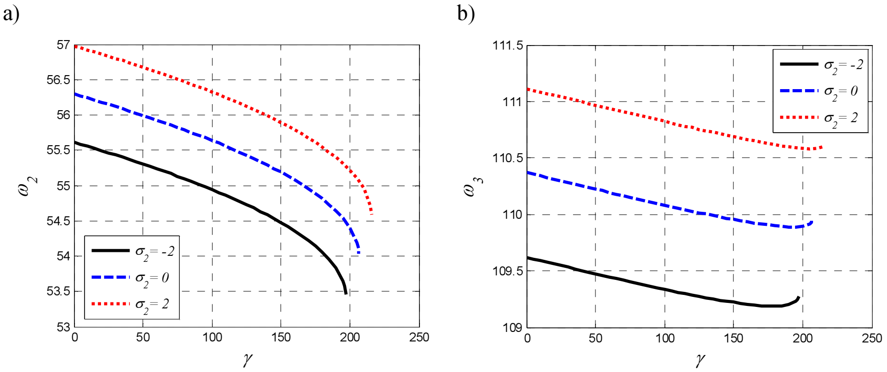

Fig. 11. Variations of (a) the second and (b) the third natural frequencies vs the Casimir force for LSA approximation and some assigned values of σ_2 and $\alpha_4 = 1$.

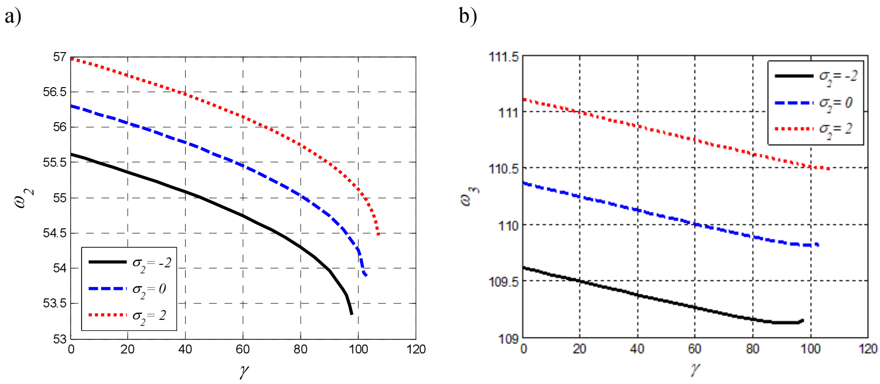

Fig. 12. Variations of (a) the second and (b) the third natural frequencies vs the Casimir force for SSA approximation and some assigned values of σ_2 and $\alpha_4 = 1$.

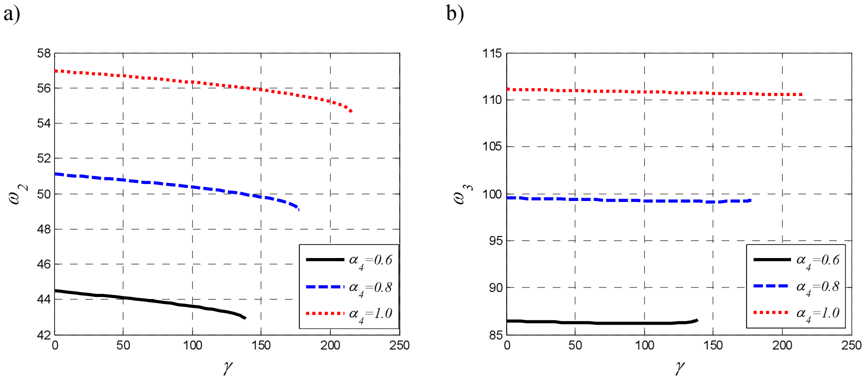

Fig. 13. Variations of (a) the second and (b) the third natural frequencies vs the Casimir force for LSA approximation and $\sigma_2 = 2$.

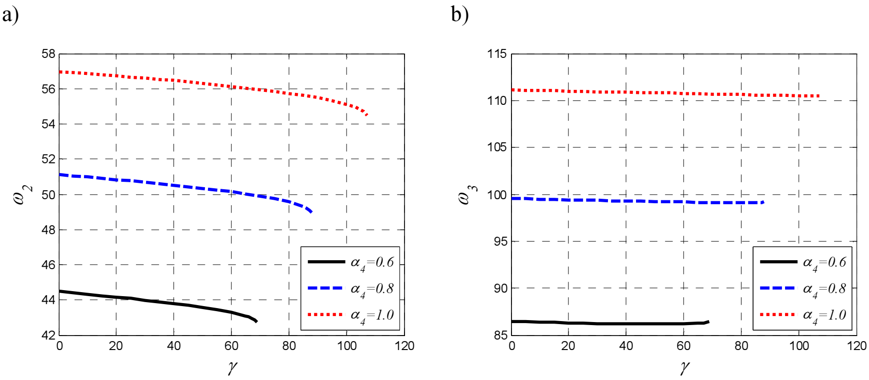

Fig. 14. Variations of (a) the second and (b) the third natural frequencies vs the Casimir force for SSA approximation and $\sigma_2 = 2$.

Finally, to examine the effect of Casimir attraction force on the higher frequencies of nanowires, variations of the second and third natural frequencies for LSA and SSA models are shown in Figs. 11 to 14, for some values of surface stress parameter σ_2 and size-effect parameter α_4. As can be seen, the second natural frequency is more sensitive to the variation of Casimir parameter in comparison with the third one. In addition, one can infer that the slope of the second natural frequency increases with increasing the Casimir force, whereas the slope of the third one decreases as the Casimir force increases.

According to the illustrated results in Figs. 13 and 14, it is concluded that, when the surface stress σ_2 keeps constant, the second and third natural frequencies are very sensitive to variation of the scale parameter α_4. Furthermore, Figs. 13b and 14b exhibit that the third natural frequency does not show a noticeable change when the surface stress is constant.

5. Conclusions

In this work we have studied the instability characteristics of Casimir-induced nanowires in the presence of microstructure size-dependency and surface effects. A non-linear governing equation of nanowires for both small and large separation gaps has been developed and the static response as well as eigenvalue problems have been presented to examine the mechanical behaviour of a considered nano-beam. It is concluded that:

1. Increasing the geometry ratio k increases the instability threshold of Casimir-induced nanowires for both SSA and LSA models.
2. Increasing the surface stress parameter from negative to positive values, raises the critical Casimir value and the fundamental frequency of nanowires.
3. The fundamental frequency of nanowires increases with increasing the size-dependency parameter and the nanowire collapses onto the fixed substrate at higher values of the Casimir parameter.
4. It has been shown that the second natural frequency is more sensitive to variations of the Casimir parameter in comparison with the third one.

Acknowledgment

Dr. Hassen M. OUAKAD is grateful for the support of his funding body supported by the Deanship of Scientific Research (DSR) at King Fahd University of Petroleum and Minerals (KFUPM) (grant number SB151004).

References

[1] Cuesta, E., Mantaras, D.A., Luque, P., Alvarez, B.J., Muina, D. (2015). Dynamic Deformations in Coordinate Measuring Arms Using Virtual Simulation. *International Journal of Simulation Modelling*, 14(4), 609–620.

[2] Herzog, V., Zavec Pavlinic, N., Kuzmanovic, D., Buchmeister, B. (2016). Thermal Manikin and Its Stability for Accurate and Repeatable Measurements. *International Journal of Simulation Modelling*, 15(4), 676–687.

[3] Craighead, H.G. (2000). Nanoelectromechanical systems. *Science*, 290, 1532–1535.

[4] Wang, M.C.P., Gates, B.D. (2009). Directed assembly of nanowires. *Materials Today*, 12, 34–43.

[5] Khajeansari, A., Baradaran, G.H., Yvonnet, J. (2012). An explicit solution for bending of nanowires lying on Winkler-Pasternak elastic substrate medium based on the Euler–Bernoulli beam theory. *International Journal of Engineering Science*, 52, 115–128.

[6] Ternik, P., Rudolf, R. (2016). Numerical Analysis of Continuous Casting of NiTi Shape Memory Alloy. *International Journal of Simulation Modelling*, 15(3), 522–531.

[7] Komeili, M., Menon, C. (2016). Robust Design of Thermally Actuated Micro-Cantilever Using Numerical Simulations. *International Journal of Simulation Modelling*, 15(3), 409–422.

[8] Feng, X.L., He, R., Yang, P., Roukes, M.L. (2007). Very High Frequency Silicon Nanowire Electromechanical Resonators. *Nano Letters*, 7(7), 1953–1959.

[9] Sedighi, H.M., Daneshmand, F., Zare, J. (2014). The influence of dispersion forces on the dynamic pull-in behavior of vibrating nano-cantilever based NEMS including fringing field effect. *Archives of Civil and Mechanical Engineering*, 14(4), 766–775.

[10] Farrokhabadi, A., Abadian, N., Rach, R., Abadyan, M. (2014). Theoretical modelling of the Casimir force-induced instability in freestanding nanowires with circular cross-section. *Physica E*, 63, 67–80.

[11] Buks, E., Roukes, M.L. (2002). Quantum physics: Casimir force changes sign. *Nature*, 419, 119–120.

[12] Buks, E., Roukes, M.L. (2001). Metastability and the Casimir effect in micromechanical systems. *Europhysics Letters*, 54(2), 220.

[13] Zou, J., Marcet, Z., Rodriguez, A.W., Reid, M.T.H., McCauley, A.P., Kravchenko, I.I., Lu, T., Bao, Y., Johnson, S.G., Chan, H.B., (2013). Casimir forces on a silicon micromechanical chip. *Nature Communications*, 4, 1845.

[14] Buks, E., Roukes, M.L. (2001). Stiction, adhesion energy, and the Casimir effect in micromechanical systems. *Phys. Rev. B*, 63, 033402.

[15] Lombardo, F.C., Mazzitelli, F.D., Villar, P.I., (2008). Numerical evaluation of the Casimir interaction between cylinders. *Physical Review D*, 78, 085009.

[16] Emig, T., Jaffe, R.L., Kardar, M., Scardicchio, A. (2006). Casimir interaction between a plate and a cylinder. *Physical Review Letters*. 96, 080403.

[17] Bordag, M., Mohideen, U., Mostepanenko, V.M. (2001). New developments in the Casimir effect. *Physics Reports*, 353, 1–205.

[18] Casimir, H.B.G. (1948). On the attraction between two perfectly conducting plates. *Proc. of the Koninklijke Nederlandse Akademie van Wetenschappen*, 51, 793.

[19] Guo, J.G., Zhao, Y.P. (2004). Influence of van der Waals and Casimir Forces on Electrostatic Torsional Actuators. *Journal of Microelectromechanical System*s, 13(6), 1027.

[20] Lin, W.H., Zhao, Y.P., (2005). Nonlinear behavior for nanoscales electrostatic actuators with Casimir force. *Chaos, Solitons & Fractals*, 23, 1777.

[21] Casimir, H.B.G., Polder, D. (1948). The influence of retardation of the London-van der Waals forces. *Physical Review Letters*, 73, 360.

[22] Teo, L.P. (2011). First analytic correction to the proximity force approximation in the Casimir effect between two parallel cylinders. *Physical Review D*, 84, 065027.

[23] Teo, L.P. (2011). Casimir, interaction between a cylinder and a plate at finite temperature: Exact results and comparison to proximity force approximation. *Physical Review D*, 84, 025022.

[24] Barretta, R., Čanađija, M., Marotti de Sciarra, F. (2016). A higher-order Eringen model for BernoulliEuler nanobeams. *Archive of Applied Mechanics*, 86(3), 483–495.

[25] Barretta, R., Feo, L., Luciano, R., Marotti de Sciarra, F. (2015). Variational formulations for functionally graded nonlocal Bernoulli-Euler nanobeams. *Composite Structures*, 129, 80–89.

[26] Romano, G., Barretta, R., Diaco, M., Marotti de Sciarra, F. (2017). Constitutive boundary conditions and paradoxes in nonlocal elastic nano-beams. *Int. J. Mech. Sciences.*, 121, 151–156.

[27] Romano, G., Barretta, R. (2017). Stress-driven versus strain-driven nonlocal integral model for elastic nano-beams, *Composites Part B*, DOI: 10.1016/j.compositesb.2017.01.008

[28] Čanađija, M., Barretta, R., Marotti de Sciarra, F. (2016). A gradient elasticity model of Bernoulli-Euler nanobeams in nonisothermal environments. *European Journal of Mechanics – A/Solids*, 55, 243–255.

[29] Sari, M., Shaat, M., Abdelkefi, A. (2017). Frequency and mode veering phenomena of axially functionally graded non-uniform beams with nonlocal residuals. *Composite Structures*, 163, 280–292.

[30] Civalek, O., Demir, C, Akgöz, B. (2009). Static analysis of single walled carbon nanotubes (SWCNT) based on Eringen's nonlocal elasticity theory. *Inter. J. Eng. App. Sci.*, 2, 47–56.

[31] Civalek, O., Demir, C. (2016). A simple mathematical model of microtubules surrounded by an elastic matrix by nonlocal finite element method. *Applied Mathematics and Computation*, 289, 335–352.

[32] Sedighi, H.M. (2014). Size-dependent dynamic pull-in instability of vibrating electrically actuated micro-beams based on the strain gradient elasticity theory. *Acta Astronautica*, 95, 111–123.

[33] Shaat, M., Abdelkefi, M. (2016). On a second-order rotation gradient theory for linear elastic continua. *International Journal of Engineering Science*, 100, 74–98.

[34] Keivani, M., Koochi, A., Kanani, A., Mardaneh, M.R., Sedighi, H.M., Abadyan, M. (2016). Using strain gradient elasticity in conjunction with Gurtin-Murdoch theory for modeling the coupled effects of surface and size phenomena on the instability of narrow nano-switch. *Proc.of the Institution of Mechanical Engineers, Part C: Journal of Mechanical Engineering Science*, DOI:10.1177/0954406216642475.

[35] Akgoz, B., Civalek, O. (2013). Buckling analysis of linearly tapered micro-columns based on strain gradient elasticity. *Structural Engineering and Mechanics*, 48(2), 195–205.

[36] Ansari, R., Gholami, R., Sahmani, S. (2013). Size-dependent vibration of functionally graded curved microbeams based on the modified strain gradient elasticity theory. *Archive of Applied Mec*hanics, 83(10), 1439–1449.

[37] Akgoz, B, Civalek, O. (2015). A novel microstructure-dependent shear deformable beam model. *International Journal of Mechanical Sciences*, 99, 10–20.

[38] Daneshmand, F. (2014). Combined strain-inertia gradient elasticity in free vibration shell analysis of single walled carbon nanotubes using shell theory. *Applied Mathematics and Computation*, 243, 856–869.

[39] Li, L., Hu, Y., Ling, L. (2016). Wave propagation in viscoelastic single-walled carbon nanotubes with surface effect under magnetic field based on nonlocal strain gradient theory. *Physica E: Low-dimensional Systems and Nanostructures*, 75, 118–124.

[40] Wang, Z.Q., Zhao, Y.P., Huang, Z.P. (2010). The effects of surface tension on the elastic properties of nano structures. *International Journal of Engineering Science*, 48, 140–150.

[41] Dingrevillea, R., Qua, J., Cherkaoui, M. (2005). Surface free energy and its effect on the elastic behavior of nano-sized particles, wires and films. *Journal of the Mechanics and Physics of Solids*, 53(8), 1827–1854.

[42] Gurtin, M.E., Murdoch, A.I. (1978). Surface stress in solids. *International Journal of Solids and Structures*. 14, 431–440.

[43] Sedighi, H.M. (2014). The influence of small scale on the pull-in behavior of nonlocal nano-bridges considering surface effect, Casimir and van der Waals attractions. *International Journal of Applied Mechanics*, 6(3), 22.

[44] Eltaher, M.A., Mahmoud, F.F., Assie, A.E., Meletis, E.I. (2013). Coupling effects of nonlocal and surface energy on vibration analysis of nanobeams. *Applied Mathematics and Computation*, 224, 760–774.

[45] Fu, Y., Zhang, J. (2011). Size-dependent pull-in phenomena in electrically actuated nanobeams incorporating surface energies. *Applied Mathematical Modelling*, 35(2), 941–951.

[46] Koochi, A., Hosseini-Toudeshky, H., Ovesy, H.R., Abadyan, M. (2013). Modeling the influence of surface effect on instability of nano-cantilever in presence of Van der Waals force. *International Journal of Structural Stability and Dynamics*, 13, 1250072.

[47] Sedighi, H.M., Bozorgmehri, A. (2016). Dynamic instability analysis of doubly clamped cylindrical nanowires in the presence of Casimir attraction and surface effects using modified couple stress theory. *Acta Mechanica*, 227(6), 1575–1591.

[48] Sedighi, H.M., Bozorgmehri, A. (2017). Nonlinear vibration and adhesion instability of Casimir-induced nonlocal nanowires with the consideration of surface energy. *Journal of the Brazilian Society of Mechanical Sciences and Engineering*, 39(2), 427–442.

[49] Beer, FP., Johnston Jr., E.R., DeWolf, J.T. (1981). *Mechanics of Materials*. New York: McGraw-Hill.

[50] Lu, P., He, L.H., Lee, H.P., Lu, C. (2006). Thin plate theory including surface effects. *International Journal of Solids and Structures*, 44, 4631–4647.

[51] Yekrangi, A., Soroush, R. (2016). Modeling of the intermolecular Force-Induced Adhesion in Freestanding Nanostructures Made of Nano-beams. *Journal of Applied and Computational Mechanics*, 2(1), 1–7.

[52] Lamoreaux, S.K. (2005). The Casimir force: background, experiments, and applications. *Reports on Progress in Physics*, 68, 201–236.

[53] Chan, H.B., Bao, Y., Zou, J., Cirelli, R.A., Klemens, F., Mansfield, W.M., Pai, C.S. (2008). Measurements of the Casimir Force between a Gold Sphere and a Silicon Surface with Nanoscale v Trench Arrays. *Physical Review Letters*, 101, 030401.

[54] Li, H., Kardar, M. Fluctuation-induced forces between rough surfaces. *Physical Review Letters*, 67, 3275.

[55] Buscher, R., Emig, T. (2005). Geometry and Spectrum of Casimir Forces. *Physical Review Letters*, 94, 133901.

[56] Rahi, S.J., Emig, T., Jaffe, R.L., Kardar, M. (2008). Casimir forces between cylinders and plates. *Physical Review A*, 78, 012104.

[57] Bulgac, A., Magierski, P., Wirzba, A. (2006). Scalar Casimir effect between Dirichlet spheres or a plate and a sphere. *Physical Review D*, 73, 025007.

[58] Lam, D.C.C., Yang, F., Chong, A.C.M., *et al.* (2003). Experiments and theory in strain gradient elasticity. *Journal of the Mechanics and Physics of Solids*, 51(1), 477–508.

[59] Shaat, M., Mohamed, S.A. (2014). Nonlinear-electrostatic analysis of micro-actuated beams based on couple stress and surface elasticity theories. *International Journal of Mechanical Sciences*, 84, 208–217.

[60] Batra, R.C., Porfiri, M., Spinello, D. (2008). Vibrations of narrow microbeams predeformed by an electric field. *Journal of Sound and Vibration*, 309, 600–612.

[61] Soltani, P., Kassaei, A., Taherian, M.M. (2014). Nonlinear and quasi-linear behavior of a curved carbon nanotube vibrating in an electric force field; an analytical approach. *Acta Mechanica Solida Sinica*, 27(1), 97–110.

[62] Rahmani, O., Pedram, O. (2014). Analysis and modeling the size effect on vibration of functionally graded nanobeams based on nonlocal Timoshenko beam theory. *International Journal of Engineering Science*, 77, 55–70.

[63] Younis, M.I., Abdel-Rahman, E.M., Nayfeh, A.H. (2003). A Reduced-order model for electrically actuated microbeam-based MEMS. *J. Microelectromech. Syst.*, 12, 672–680.

[64] Whittaker, E.T., Robinson, G. (1967). The Newton-Raphson Method, §44 in the Calculus of Observations: A Treatise on Numerical Mathematics, (4th ed.), NY: Dover, 84–87.

[65] Nayfeh, A.H., Balachandran, B. (1995). *Applied Nonlinear Dynamics*. Wiley, New York.

[66] Farrokhabadi, A., *et al*. (2014). Theoretical modeling of the Casimir force-induced instability in freestanding nanowires with circular cross-section. *Physica E: Low-dimensional Systems and Nanostructures*, 63, 67–80.

Metrol. Meas. Syst., Vol. 24 (2017), No. 3, pp. 509–514.

PAN
POLSKA AKADEMIA NAUK

METROLOGY AND MEASUREMENT SYSTEMS
Index 330930, ISSN 0860-8229
www.metrology.pg.gda.pl

M&MS

FAST RESPONSE HOT (111) HGCDTE MWIR DETECTORS

Kacper Grodecki1), Piotr Martyniuk1), Małgorzata Kopytko1), Andrzej Kowalewski1), Dawid Stępień1,2), Artur Kębłowski2), Adam Piotrowski2), Józef Piotrowski2), Waldemar Gawron2), Antoni Rogalski1)

1) Military University of Technology, Institute of Applied Physics, Gen. S. Kaliskiego 2, 00-908 Warsaw, Poland
(✉ kacper.grodecki@wat.edu.pl, +48 261 839 374, piotr.martyniuk@wat.edu.pl, malgorzata.kopytko@wat.edu.pl, andrzej.kowalewski@wat.edu.pl, dawid.stepien@wat.edu.pl, antoni.rogalski@wat.edu.pl)
2) Vigo System S.A., Poznańska 129/133, 05-850 Ożarow Mazowiecki, Poland
(akeblowski@vigo.com.pl, apiotrowski@vigo.com.pl, jpiotrowski@vigo.com.pl, wgawron@vigo.com.pl)

Abstract

In this work we report simulation and experimental results for an MWIR HgCdTe photodetector designed by computer simulation and fabricated in a joint laboratory run by VIGO Sytems S.A. and Military University of Technology. The device is based on a modified N^+pP^+ heterostructure grown on 2”., epiready, semi-insulating (100) GaAs substrates in a horizontal MOCVD AIX 200 reactor.

The devices were examined by measurements of spectral and time responses as a function of a bias voltage and operating temperatures. The time response was measured with an *Optical Parametric Oscillator* (OPO) as the source of ~25 ps pulses of infrared radiation, tuneable in a 1.55–16 µm spectral range. Two-stage Peltier cooled devices (230 K) with a 4.1 µm cut-off wavelength were characterized by 1.6×10^{12} cm $Hz^{1/2}$/W peak detectivity and < 1 ns time constant for $V > 500$ mV.

Keywords: HgCdTe, MWIR, photodetector, response time.

1. Introduction

The sensitive and fast response *mid-IR photodetectors* (MWIR) working at *high operating temperature* (HOT) are of increasing demand for numerous applications in the infrared technology [1]. But obtaining photodetectors of high detectivity and fast response at the same time stays in contradiction. An example is one of the first HOT detectors with narrow-band gap semiconductors used for uncooled detection of CO_2 laser radiation [2]. Much faster can be graphene devices [3]. Unfortunately, the devices based on a high recombination rate suffer from a low responsivity since most of the charge carriers recombine before reaching contacts. At the same time, they are noisy due to a statistical nature of the thermal generation-recombination processes. However, the time response of IR photodetectors can be improved by fast carrier collection [1, 4, 5]. For photodiodes the recombination mechanism is generally important at forward, zero and weak reverse bias when the recombination rate is large. The transport removal of charge carriers becomes the dominating mechanism for reverse bias voltages [4]. This can be easier to achieve with thin absorbers. Unfortunately, thin absorber devices will suffer from a low quantum efficiency. The issue is especially pronounced in detection of longer wavelength radiation, due to decreasing absorption. A possible way to solve the problem is to enhance absorption by the use of multi-junction detectors [6].

Hetero-structural HgCdTe photodiodes, due to the inherent flexibility of design, are very promising for using in sensitive and broadband HOT detectors [1]. Careful optimization of the devices’ architectures makes possible to achieve a near BLIP (*Background Limited*) performance at a GHz frequency range.

Article history: received on Dec. 01, 2016; accepted on Apr. 08, 2017; available online on Sep. 01, 2017; DOI: 10.1515/mms-2017-0044.

In this work we present the theoretical modelling and experimental results for 4.1 µm cut-off wavelength photodiodes at T = 230 K, based on epitaxial HgCdTe multi-layer-band gap engineered architecture.

2. Simulation procedure and experimental details

Numerical modelling of variable band gap and doping profile HgCdTe hetero-structures was based on the continuity equations for electrons and holes, Poisson and thermal conductivity equations [7, 8]. The following mechanisms of dark current generation were considered: the *Shockley-Read-Hall* (SHR) and Auger 7 (Auger) generation-recombination processes, *band-to-band* (BTB), *trap-assisted tunnelling* (TAT) and *dislocations-related generation* (Dis).

Densities of dislocations $D_D = 5 \times 10^6 \text{cm}^{-2}$ and traps $Nt = 1 \times 10^{14}$ cm^{-3} were assumed to fit to the experimental results. A detailed description of calculation methods is given in [9, 10]. The simulation results were used to select promising architectures, characterized by a low dark current, a high responsivity and minimized parasitic impedances.

The mid-IR HgCdTe photodiodes were fabricated in a joint laboratory run by VIGO System and Military University of Technology, Warsaw. The multilayer detector hetero-structures were grown on 2” semi-insulating, 2 deg disoriented (100) GaAs substrates in a horizontal MOCVD AIX 200 reactor. The *inter-diffused multilayer process* (IMP) technique was applied to the HgCdTe layer deposition. A detailed description of the implemented MOCVD growth procedure is presented in [12].

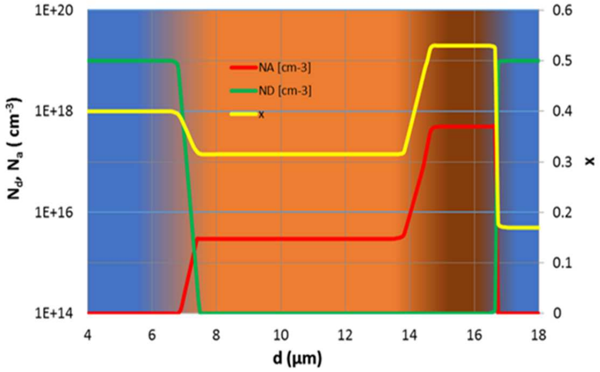

Fig. 1. A composition and doping profiles of the simulated HgCdTe hetero-structure.

An example of the photodiode structure is shown in Fig.1. The device consists of a p-type absorber, heavily doped wide-gap P^+ and N^+ hole and electron contacts and a heavily doped n^+ layer used to minimize the series resistance between P^+ layer and contact metallization. The four main layers are separated by interfaces with graded gap and doping profiles. The composition of the device is obtained by a programmed change of growth temperature, precursor fluxes, mercury pressure, duration of IMP stages and other growth parameters [5]. It should be noted that the CdTe/HgTe inter-diffusion and dopant diffusion processes were found to be slow for (100) growth compared with that for (111) orientation, so the interfaces were intentionally smoothed to prevent formation of dislocations by a suitable control of precursor fluxes.

The photodiodes were examined by measurements of a spectral responsivity, current voltage plots and a noise current. The time response was measured using an *optical parametric oscillator* (OPO) as the source of ~25 ps long, tuneable wavelength (1.55–16 µm) pulses of IR radiation, a broad-bandwidth preamplifier and an 8 GHz digital oscilloscope[12].

3. Results and discussion

Figure 2 shows simulated band structures. For the reverse bias electrons and holes are extracted from the absorber to N^+ and P^+ contacts, respectively. The carriers cannot be replenished by injection of minority carriers from the contact layer since their concentration there is very low. As a result, the absorber electrons are fully depleted while the hole concentration decreases to the extrinsic concentration, leading to suppression of Auger generation. To minimize the tunnel and generation-recombination in space charge regions, the device structure was designed for flat absorber bands and low electric fields (Fig. 2c) in the narrow gap part of absorber interfaces. In contrast, the P+n+ interface is made as sharp as possible to produce a low-resistance tunnelling contact.

Due to the flat band condition, the collection of photo-generated charge carriers mostly refers to diffusion rather than drift transport. The ambipolar diffusion coefficient in the depleted p-type absorber is large, making the collection fast.

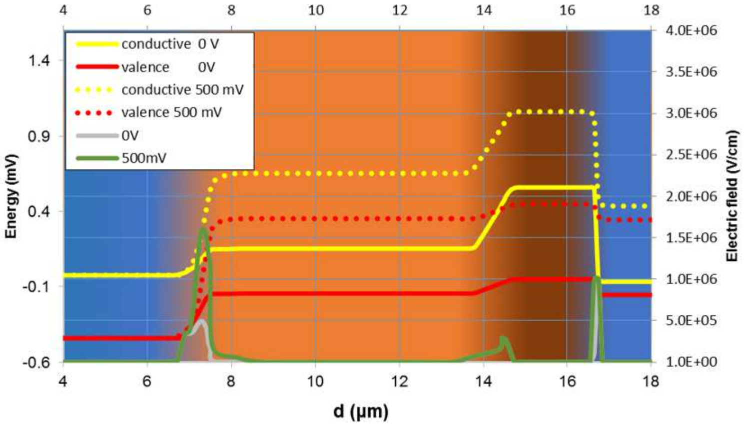

Fig. 2. The simulated band structure for 0 V and 500 mV(yellow and red lines) bias voltages and electric fields of 0 V (grey line) and 500 mV (green line).

Figure 3c shows the measured and calculated dark current-voltage plots. For the calculated dark current components – the Auger, SRH and Dis-related processes are shown. The first two mechanisms generate charge carriers mostly in the absorber region (Fig. 3a and 3 b). The carriers diffuse to the contact regions resulting in a diffusion current which saturates at a reverse bias > 50 mV. It is worth mentioning that, in contrast to the homo-junction pin photodiodes, the SRH generation at absorber interfaces was to a large degree suppressed by an increased band gap.

The generation rate of Auger is large in the heavily doped n^+ contact region, but the generation does not produce a dark current due to the high electron barrier in P^+n^+ interface.

In contrast, the dislocations-related current is generated mostly at interfaces with an increased dislocation density. The current increases with the bias voltage and dominates for large (> 700 mV) bias values.

Figure 4 shows the measured spectral responsivity and detectivity of optically immersed HgCdTe photodiode. The device is characterized by peak and cut-off wavelengths equal to 3.4 and 4.1 µm, respectively. The spectral current response remains nearly constant over a spectral range of 2.9 to 3.7 µm, with a high R_i~3A/W and $D^*{\sim}1.2\cdot10^{12}$ $\text{cmHz}^{1/2}/\text{W}$. It should be noted that the measured detectivity of the device is larger compared with the BLIP (300 K, 180°)

detectivity. This is due to the 36° acceptance angle, limited by the hyper-hemispherical immersion lens.

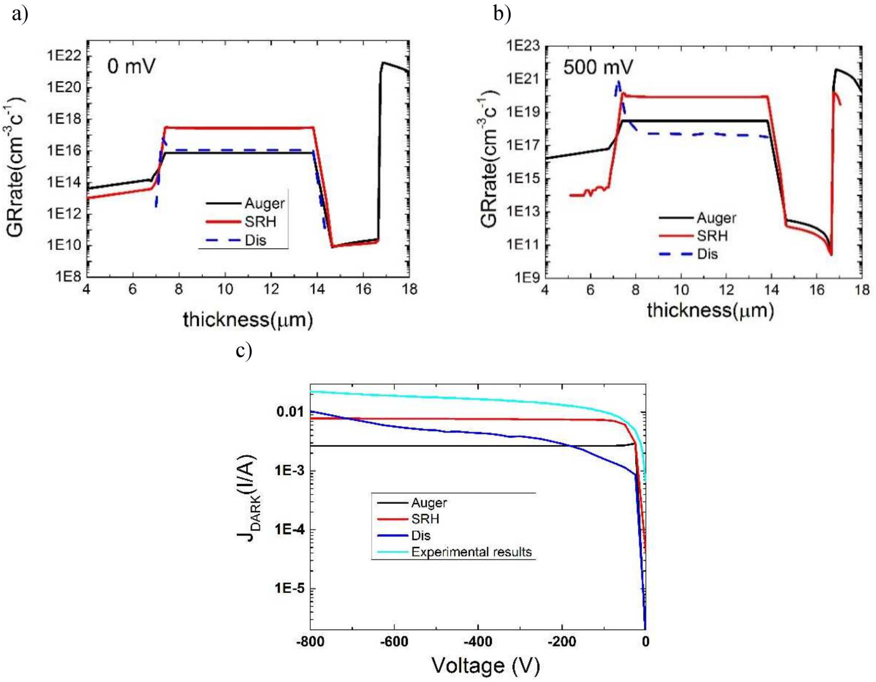
a) b) c)

Fig. 3. The calculated and measured dark currents: the distribution of calculated thermal generation rates along the sample for Auger, SRH and Dis mechanisms for bias voltages of 0 mV and 500 mV (a, b); respectively the calculated Auger, SRH, Dis and the experimental results of thermal generation rates in a function of bias voltage (c).

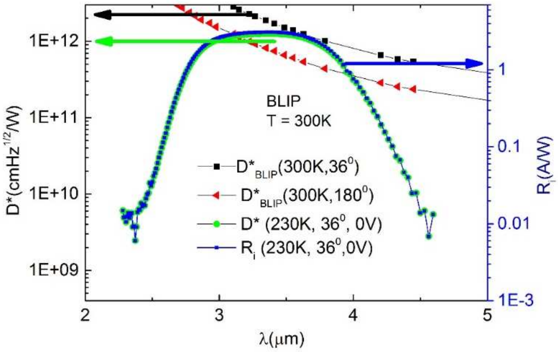

Fig. 4. The measured spectral current responsivity (blue curve), detectivity of the measured photodetector (green curve) and D*$_{BLIP}$ (black and red curve).

Figure 5 shows the simulated and measured response time as a function of bias voltage. The response is quite slow in unbiased devices and voltage signal readout conditions. This is due to a large diffusion capacitance for zero or small bias voltages, resulting in a large RC time constant.

The response highly improves with increasing the bias voltage and the current mode readout. Picosecond-range time constants are easily achievable for small area devices operating with low (< 50 ohms) input resistance amplifiers.

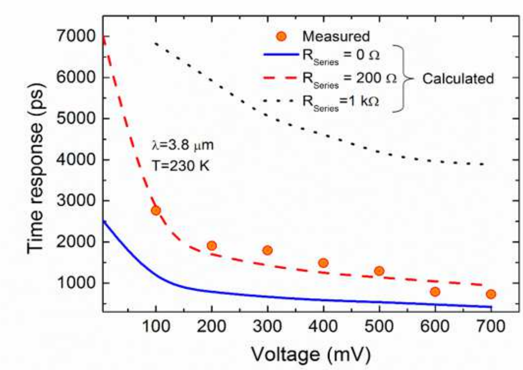

Fig. 5. The simulated and measured response time as a function of bias voltage.

4. Summary and conclusions

Fast response HOT MWIR optically immersed 4.1 μm cutoff photodiodes operating at 230 K have been designed by computer simulation of modified N^+pP^+ HgCdTe heterostructures. The devices were implemented by MOCVD growth on GaAs substrate and examined by the current–voltage, noise and spectral measurements. Comparison of the calculated and measured J-V characteristics revealed the Auger and SRH mechanisms in the absorber to be responsible for the diffusion component of dark current, dominating at a weak (< 0.3 V) reverse bias. Another important mechanism, significant at > 0.3 V and dominating at > 0.7 V bias, is the dislocation-related generation in absorber interfaces.

The optically immersed devices are characterized by a high ($1 \cdot 10^{12}$ cmHz$^{1/2}$/W for 3 μm < λ < 3.7 μm) detectivity, exceeding the 300 K, 180° BLIP limit. This was possible due to reduction of the device acceptance angle to ~36° by the hyper-hemispherical immersion lenses.

Measurements of the time response using OPO sources of a short radiation pulse revealed its strong dependence on the detector bias and the type of signal readout. The response is quite slow for an unbiased device and/or voltage mode signal readout. This is due to a large RC time constant, determined by the product of the diffusion and depletion layer capacitance of the load and the detector series resistance. The time response highly improves with a reverse bias and a low resistance of signal readout electronics, that makes possible to obtain a picosecond-range response, eventually limited by the detector series resistance.

Acknowledgments:

This work was supported by Polish National Science Centre in the frame of the project NO. UMO-2013/08/A/ST5/00773

References

[1] Piotrowski, J., Rogalski, A. (2007). *High-Operating-Temperature Infrared Photodetectors*. SPIE, Bellingham.

[2] Piotrowski, J., Galus, M., Grudzien, M. (1991). Near room-temperature IR photo-detectors. *Infrared Phys.*, 31(1), 1–48.

[3] Hunter, N., Mayorov, A.S., Wood, C.D., Russell, C., Li, L., Linfield, E.H., Davies, A.G., Cunningham, J.E. (2015). On-Chip Picosecond Pulse Detection and Generation Using Graphene Photoconductive Switches. *Nano Lett.*, 15(3), 1591–1596.

[4] Newman, A.K., Liu, J.M. (1997). Physical characteristics of band-gap engineered, photovoltaic detectors. *Journal of Applied Physics*, 82(9), 4637–4646.

[5] Piotrowski, J., Gawron, W., Orman, Z., Pawluczyk, J., Kłos, K., Stępień, D., Piotrowski, A. (2010). Dark currents, responsivity, and response time in graded gap HgCdTe structures. *Proc. SPIE*, 7660, 766031.

[6] Spears, D.L. (1984). 10.6 micron photomixer arrays at 195. *Proc. IRIS Active Systems*, 331–349.

[7] Van Roosbroeck, W. (1950). Theory of the flow of electrons and holes in germanium and other semiconductors. *Bell Syst. Tech. J.*, 29(4), 560–607.

[8] Kurata, M. (1982). *Numerical Analysis for Semiconductor Devices.* Lexington Books.

[9] Kopytko, M., Jóźwikowski, K., Jóźwikowska, A., Rogalski, A. (2010). High frequency response of near-room temperature LWIR HgCdTe heterostructure photodiodes. *Opto-Electronics Rev.*, 18(3), 277–283.

[10] Jóźwikowski, K., Jóźwikowska, A., Kopytko, M., Rogalski, A., Jaroszewicz, L.R. (2012). Simplified model of dislocations as a SRH recombination channel in the HgCdTe heterostructures. *Infrared Physics & Technology*, 55(1), 98–107.

[11] Piotrowski, A., Madejczyk, P., Gawron, W., Kłos, K., Pawluczyk, J., Rutkowski, J., Piotrowski, J., Rogalski, A. (2007). Progress in MOCVD growth of HgCdTe heterostructures for uncooled infrared photodetectors. *Infrared Phys. Technol.*, 49(3), 173–326

[12] Stanaszek, D., Piotrowski, J., Piotrowski, A., Gawron, W., Orman, Z., Paliwoda, R., Brudnowski, M., Pawluczyk, J., Pedzinska, M. (2009). Mid and long infrared detection modules for picosecond range measurements. *Proc. SPIE*, 7482, 74820, M–74820, M–11.

Metrol. Meas. Syst., Vol. 24 (2017), No. 3, pp. 515–524.

METROLOGY AND MEASUREMENT SYSTEMS
Index 330930, ISSN 0860-8229
www.metrology.pg.gda.pl

MEASUREMENT AND ANALYSIS OF PARTIAL DISCHARGE USING AN ULTRA-HIGH FREQUENCY SENSOR FOR GAS INSULATED STRUCTURES

Guoming Wang, Gyung-Suk Kil

Korea Maritime and Ocean University, Department of Electrical and Electronics Engineering, 727, Taejong-ro, Yeongdo-gu, Busan, Korea (journey@kmou.ac.kr, ✉ kilgs@kmou.ac.kr, +82 51 410 4414*)*

Abstract

Although the gas insulated structures have a high degree of reliability, the unavoidable defects are primary reason of their failures. *Partial discharge* (PD) has been regarded as an effective indication for condition monitoring and diagnosis of *gas insulated switchgears* (GISs) to ensure their reliable and stable operation. Among various PD detection methods, the *ultra-high frequency* (UHF) technique has the advantages of on-line motoring and defect classification. In this paper, there are presented 7 types of artificial electrode systems fabricated for simulation of real insulation defects in gas insulated structures. A real-time measurement system was developed to acquire defect patterns in a form of *phase-resolve partial discharge* (PRPD) intensity graph, using a UHF sensor. Further, the discharge distribution and statistical characteristics were extracted for defect identification using a neural network algorithm. In addition, a conversion experiment was proposed by detecting the PD pulse simultaneously using a non-induction resistor and a UHF sensor. A relationship between the magnitude of UHF signal and the amplitude of apparent charge was established, which was used for evaluation of PD using the UHF sensor.

Keywords: gas insulated structures, partial discharge, ultra-high frequency sensor, conversion.

1. Introduction

The gas insulated structures that are filled with sulphur hexafluoride (SF_6) gas, such as switchgears and transmission lines, have a high insulation and arc-extinguishing capability, ensuring their high reliability, compact size, and economical efficiency. As a result, they are widely employed in space-limited locations, such as city substations, offshore plants, and electric railway systems. The *gas insulated switchgears* (GISs), which are composed of a circuit breaker, disconnect and grounding switches and other high voltage components, have been used for power transmission and distribution sine 1960s. In addition, a *gas insulated transmission line* (GIL) is regarded as a safe and flexible alternative to an overhead line. However, insulation defects generated during the manufacture, assembly, transportation and operation are one of the primary causes of GIS and GIL failures [1−4]. Owing to the large power supply capacity, the failures result in enormous economic losses and serious human injuries. It is therefore necessary to monitor and diagnose the condition of gas insulated structures to work out proper maintenance schedules and to ensure their reliable and stable operation [5−6].

The maintenance strategy for power facilities has developed from the run-to-failure, through the maintenance as necessary, time-based and condition-based maintenance, to the *reliability-centred maintenance* (RCM) that is proposed nowadays. The RCM strategy is a combination of the reactive, preventive, predictive, and proactive maintenance to maximise the reliability and availability of power apparatus [7−8]. The *partial discharge* (PD) is defined as a localized electrical discharge that partially bridges the insulation [9−10]. It causes progressive deterioration and the final failure of equipment. Therefore, monitoring and analysis of PD are important parts of RCM. The study of PD consists of four parts: detection, analysis,

Article history: received on Dec. 03, 2016; accepted on Feb. 26, 2017; available online on Sep. 01, 2017; DOI: 10.1515/mms-2017-0045.

classification, and localization [11]. PD detection methods are categorized into the conventional and non-conventional ones. A conventional method is a means of measuring the electrical discharge pulse, complying with IEC 60270 [9]. Non-conventional ways of detection include acoustic emission, dissolved gas analysis, and *ultra-high frequency* (UHF) methods [12–19]. Among various methods, UHF is the best choice including the four mentioned activities. In addition, it has obvious advantages of immunity against external noise and the capability of on-line monitoring [20–21].

This paper discusses the measurement and analysis of PD using a UHF sensor for condition monitoring and diagnosis of gas insulated structures. All of the possible insulation defects in GIS were simulated. A real-time analysis system was developed to extract *phase-resolved partial discharge* (PRPD) patterns and to identify a defect type using 17 proposed parameters. In addition, a conversion method was proposed to analyse the relationship between the magnitude of UHF signal and the amplitude of apparent charge, used for evaluation of PD with the non-conventional UHF method.

2. Experiment

2.1. Insulation defects

PD occurs in an insulation defect that is generated during the manufacture, assembly, and transportation procedures of gas insulated structures. Most of such defects can be detected in the factory and commissioning tests whereas there are still some micro ones hard to be found. Left without checking, those micro defects cause a progressive deterioration of the dielectric material even though power facilities operate at their rated voltage [22]. Fig. 1 shows 7 types of typical insulation defects in GIS and GIL, including *protrusion on conductor* (POC), *protrusion on enclosure* (POE), *void inside spacer* (VIS), *particle on spacer* (POS), *crack inside spacer* (CIS), *free particle* (FP), and floating. In this paper, they were simulated using artificial defects.

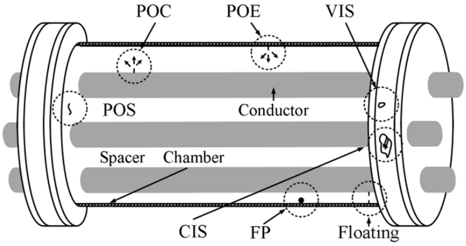

Fig. 1. Typical insulation defects in GIS and GIL.

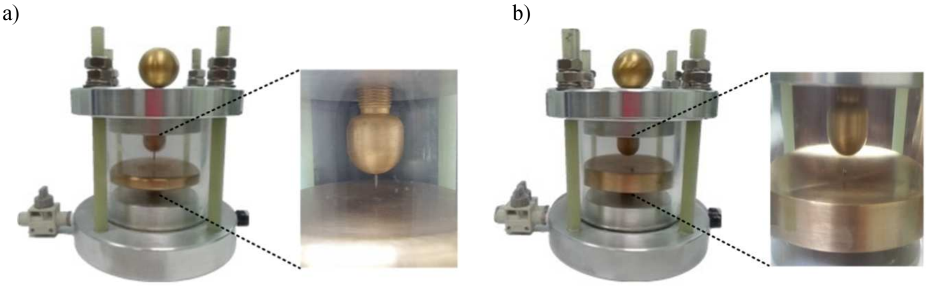

Fig. 2. Examples of artificial defects: protrusion on conductor (a); free particle (b).

Metrol. Meas. Syst., Vol. 24 (2017), No. 3, pp. 515–524.

Examples of the POC and FP defects are illustrated in Fig. 2. In the POC and POE, a needle electrode with a curvature radius of 5 µm representing a micro-size metallic protrusion, and a plane electrode with a diameter of 80 mm were used. A distance between the two electrodes was 3 mm. The edge of the plane electrode was rounded to prevent concentration of the electric field. The VIS, POS, and CIS were designed to simulate deficiencies in the spacer of GIS or GIL, representing an imperfection of product, attachment of a conductive particle, and a crack resulting from impact, respectively. The FP, which is the most common defect, was created as a 1 mm-diameter aluminium sphere to simulate a free moving metal in the chamber. All of the artificial defects were sealed with SF_6 gas with a pressure of 0.5 MPa.

2.2. Measurement system

The measurement program was developed using a real-time operation system based on LabVIEW. Fig. 3 demonstrates a flow chart of the measurement system. The virtual instruments (VI) were divided into HOST VI that runs on a personal computer, and RT VI that operates on a PXI. The shared variables were used for communication between those two VIs.

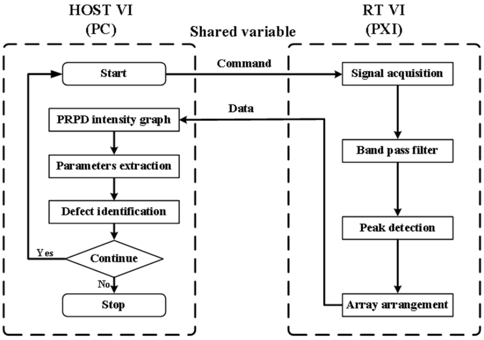

Fig. 3. A flow chart of the measurement system.

In the RT VI, a producer-consumer design pattern based on queue operation was applied, which is able to run the application with precise timing and a high degree of reliability. The acquired signal was then fed through a band-pass filter to suppress the mobile telephone interference at a frequency of 800−900 MHz. The peak point of UHF signal was captured by peak detection to be displayed in the PRPD intensity graph. The arranged data were sent to the personal computer for further analysis.

In the HOST VI, a standard state machine design pattern was built, which enabled distinct states to operate in a programmatically determined dynamic sequence. The following parameters: pulse distribution, skewness, kurtosis, and *correlation coefficient* (CC), were extracted.

The skewness and kurtosis are given by:

$$Skewness = \sum_{i=1}^{n} \frac{[X(i)-\mu]^3}{n \times \sigma^3}, \tag{1}$$

$$Kurtosis = \sum_{i=1}^{n} \frac{[X(i)-\mu]^4}{n \times \sigma^4}, \tag{2}$$

where: $X(i)(i = 1, 2,..,n)$ are data sets; μ and σ are their means and standard deviations, respectively. In the present study, $X(i)$ are the PRPD data in the positive or negative half of the applied voltage. Skewness is a measure of the symmetry of a distribution in respect of the normal distribution. The negative values of skewness indicate data that are left-skewed, whereas positive values indicate right-skewed data. The symmetric data which are called a normal distribution have a skewness value of zero. Kurtosis is an indicator of the steepness of a probability distribution. The normal distribution has a kurtosis value of 3. The data with a kurtosis value higher than 3 tend to be steeply distributed, whereas the data with a kurtosis value lower than 3 tend to be distributed evenly.

The correlation coefficient that is used to evaluate the similarity of two signals is calculated as follows:

$$CC = \frac{\sum_{i=0}^{n-1}\{[X(i)-\bar{X}]\times[Y(i)-\bar{Y}]\}}{\sqrt{\sum_{i=0}^{n-1}\{[X(i)-\bar{X}]^2\times[Y(i)-\bar{Y}]^2\}}}, \tag{3}$$

where: $X(i)$ and $Y(i)$ are two data sets; and $\bar{X}$ and $\bar{Y}$ are their average values. To be specific, $X(i)$ and $Y(i)$ are the PRPD data in the positive and negative halves of applied voltage, respectively. A value of CC is between 0 and 1. A large value indicates a high similarity of two signals [23–24]. Finally, the extracted parameters were input into a neural network for classifying the type of defect.

2.3. Experimental setup

The experimental setup is shown in Fig. 4. A dry-type transformer with a maximum output of 50 kV was immersed in insulation oil to avoid the occurrence of corona. The applied voltage was measured by a high voltage capacitive divider. Its capacitance and ratio were 25 pF and 10,000:1, respectively. An artificial defect was placed inside a GIS chamber to generate PD pulses. A UHF sensor with a frequency range of 0.5−1.5 GHz was mounted in a window of GIS. It is a semi-circular dipole antenna with a minimum detection sensitivity of 1 *pico-coulombs* (pC). To verify the validity of the developed measurement system and to run the conversion experiment, a 50 Ω non-inductive resistor was connected to detect a PD pulse. The signal was acquired using a *digital storage oscilloscope* (DSO) with a sampling rate of 5 GS/s and a *data acquisition* (DAQ) unit with a sampling rate of 250 MS/s.

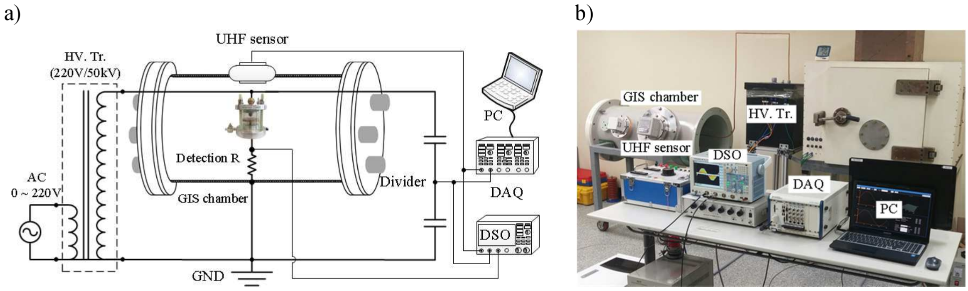

Fig. 4. The experimental setup: a configuration (a); a photograph (b).

3. PRPD and defect classification

Depending on the types of defects, PD presents different patterns. The parameters extracted from PD patterns are used for identification of defects; basing on these parameters the operating personnel can work out a proper maintenance schedule for the in-service equipment. In this section, the PRPD intensity graphs that feature the φ-q-n pattern were acquired from seven types of artificial defects, where φ is a phase position, q is a discharge magnitude, and n is a count of PD events. An intensity graph was acquired from the PXI using the UHF sensor and was simultaneously collected by the DSO through the resistor. These two graphs were compared to verify the validity of the proposed measurement system. To reduce the complexity of PD patterns, characteristic properties were analysed regarding distribution of pulses and statistical features. For the distribution of pulses, a PRPD intensity graph was divided into 12 windows and percentages of PD pulses in each window were calculated, named P1, P2,…, P12, as illustrated later. The statistical features include the skewness and kurtosis of the phase spectra in the positive and negative halves of applied voltage, as well as the *CC* value between the phase spectra in the positive and negative halves. Finally, the 17 extracted parameters were input into the artificial neural network for classifying the type of defect.

The PRPD intensity graphs of POC acquired from the DSO and the measurement system are shown in Fig. 5. It can be seen that the same pattern was obtained. PD pulses are distributed in 33−108° in the positive half of applied voltage and in 140−305° in the negative half. The magnitudes of pulses in the positive half were higher than those in the negative half. In addition, the counts of pulses in the positive and negative halves were 509 and 253, respectively. Fig. 6 demonstrates the PRPD distribution as well as the phase spectrum. 99.5% of PD pulses are in the positive half. Especially, 51.69% of pulses are clustered in the window of 90−180° and −60 – −80 dBm. Further, the statistical parameters were extracted from the phase spectrum.

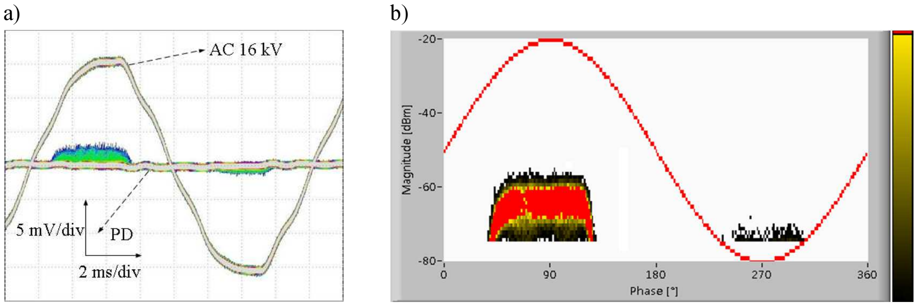

Fig. 5. A PRPD intensity graph of POC: DSO (a); the measurement system (b).

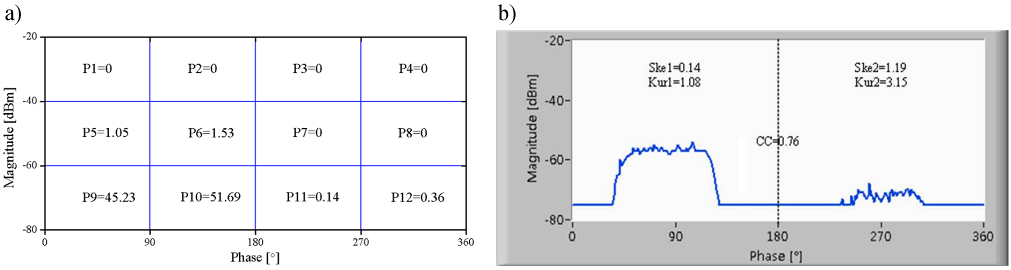

Fig. 6. Parameters of POC: a PRPD distribution (a); a phase spectrum (b).

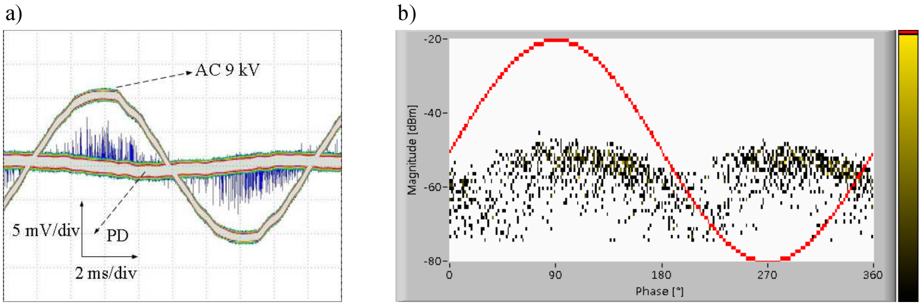

Fig. 7. A PRPD intensity graph of FP: DSO (a); the measurement system (b).

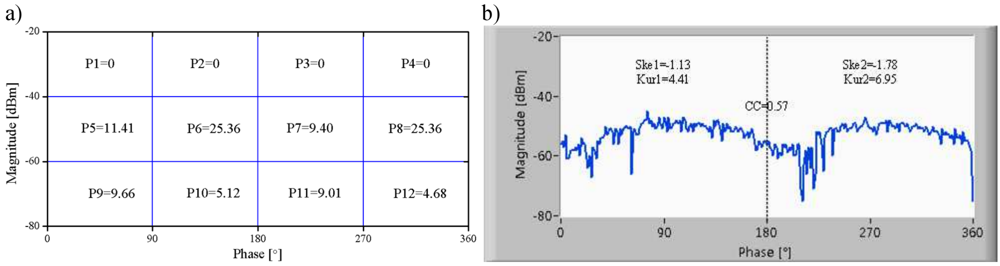

Fig. 8. Parameters of FP: a PRPD distribution (a); a phase spectrum (b).

Figures 7 and 8 illustrate the PRPD intensity graph and parameters of FP, respectively. Pulses scattered over all of the phase and the discharge magnitude varied with the amplitude of applied voltage. The discharge patterns were similar in the positive and negative halves.

The PRPD intensity graphs and parameters of other five types of defects are appended. In the POE, most of PD pulses are distributed in the negative half of applied voltage, and the magnitudes of pulses in the negative half are higher than those in the positive half. Similar patterns in the positive and negative halves were acquired in the VIS, where pulses are distributed within 30°–90° and 210°–270°. In the POS, PDs occurred with a magnitude lower than −62 dBm, whereas PD pulses with a magnitude higher than −30 dBm were detected in the floating. In the CIS, most of pulses are distributed in the P9 and P11 windows.

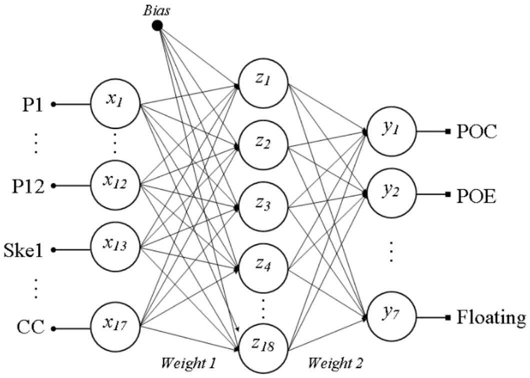

Fig. 9. A structure of artificial neural network.

A structure of artificial neural network is demonstrated in Fig. 9. There are 17 neurons – as many as the number of extracted parameters in the input layer. One hidden layer with 18 neurons was used to connect the neurons in the input and output layers. The number of neurons in the output layer is the same as that of the typical insulation defects, which is set to 7. In addition, a sigmoid function is selected to determine the activation function. During the training procedure, the PRPD intensity graphs had been extracted for 20 times from each defect and a back propagation algorithm was applied to update the weights and biases until the allowable error was less than 0.0001. Then, the updated weights and biases were written into the measurement system to replace their initial values; they were finally used for real-time defect identification. To verify the accuracy of the developed system, another 20 groups were acquired for each of 7 defects, and then identified. As a result, 134 of 140 data were accurately identified. Therefore, the proposed system can classify a defect type with an average accuracy of 95.7%.

4. Apparent charge calculation

In IEC 60270, PD is evaluated using an apparent charge (q), whose unit is pC [9]. The apparent charge is an integrated value of the detected pulse and can be calculated by:

$$q = \int_{t_1}^{t_2} i(t)dt = \int_{t_1}^{t_2} \frac{v(t)}{50} dt \ \ [\text{pC}], \tag{4}$$

where: $v(t)$ is a waveform of pulse detected by the non-inductive resistor. The accuracy was verified by injecting current pulses with specified apparent charges using a calibrator, and then comparing the injected values with the integrated ones. The magnitude of UHF signal is expressed in dBm. The conversion experiment was performed to analyse the relationship between the magnitude of UHF signal and the apparent charge, in order to evaluate PD with UHF sensors. Fig. 10 shows electrical PD pulses simultaneously measured with the UHF signals. Since a UHF pulse lasts only tens of nanoseconds, an extremely expensive acquisition device with a high sampling rate is needed to capture such a short signal. Therefore, an integral circuit was used in this sensor. As a result, the width of pulse detected with the UHF sensor (lower) was longer than that detected by the 50 Ω resistor (upper). It can be seen that PD pulses detected by the resistor and the UHF sensor matched very well, providing the evidence for a good conversion accuracy.

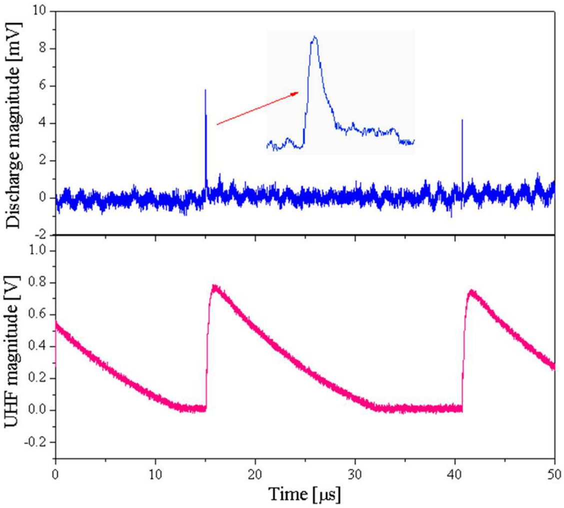

Fig. 10. PD pulses detected by the 50 Ω resistor (upper) and the UHF sensor (lower).

The conversion experiment was carried out for 7 defects. The results are shown in Fig. 11. Although obtained for different defect types, the relationships between the magnitude of UHF signal and the amplitude of discharge follow a single curve, which is given in (5). Therefore, the dBm can be converted into pC for evaluating PD by the UHF sensor during the on-line PD monitoring:

$$q = 10^{\frac{mangitude\ of\ UHF\ signal\ in\ dBm+81.31}{23.32}} \ \ [\text{pC}]\ . \tag{5}$$

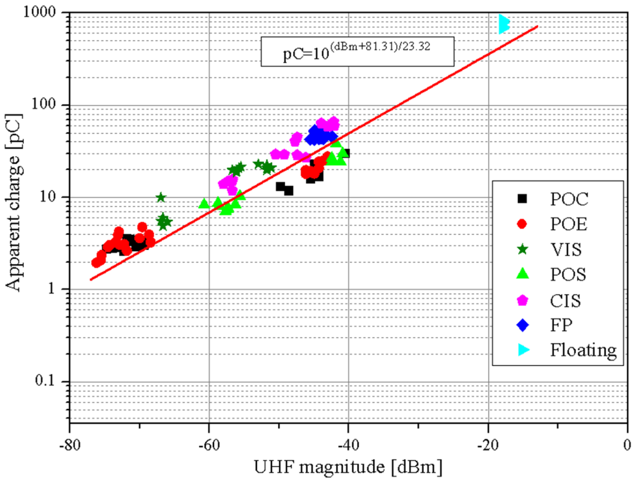

Fig. 11. The results of conversion.

5. Conclusions

This paper deals with the measurement and analysis of PD using a UHF sensor for the purpose of condition monitoring and diagnosis of gas insulated structures. A real-time measurement system that combined the signal acquisition, pattern generation, feature extraction and defect identification was developed. The PRPD intensity graphs were acquired from 7 types of artificial defects, which presented distinguishable patterns. Then, 17 parameters were extracted, including the distribution of PD pulses over 12 phase-magnitude windows, skewness and kurtosis of the phase spectra in the positive and negative halves of applied voltage, as well as the correlation coefficient between the phase spectra in the positive and negative halves. Using an artificial neural network, the defects were classified with a high accuracy of 95.7%. In addition, by using the proposed conversion method, the relationship between the magnitude of UHF signal and the amplitude of apparent charge was examined, even for different defects. Therefore, PD can be evaluated using a UHF sensor in the gas insulated structures in service.

References

[1] Haddad, A., Warne, D.F. (2004). *Advances in high voltage engineering*. The Institution of Engineering and Technology, 37–54.

[2] Ryan, H.M. (2013). *High-voltage engineering and testing*. The Institution of Engineering and Technology, 319–324.

[3] Neumann, C., Krampe, B., Feger, R., Feser, K., Knapp, M., Breuer, A., Rees, V. (2000). PD measurements on GIS of different designs by non-conventional UHF sensors. *CIGER session 15–305*, 1–9.

[4] ABB. (2009). Compact and reliable – Decades of benefits: Gas-insulated switchgear from 52 to 1100 kV (ABB Technology magazine), 1–7.

[5] Neumann, C., Rusek, B., Balzer, G., Jeromin, I. (2012). End of life estimation and optimisation of maintenance of HV switchgear and GIS substations. *CIGER session A3–202*, 1–12.

[6] Jo, H.E., Wang, G.M., Kim, S.J., Kil, G.S. (2015). Comparison of partial discharge characteristics in SF_6 gas under AC and DC. *Trans. Electr. Electron. Mater.*, 16(6), 323–327.

[7] Gill, P. (2008). *Electrical power equipment maintenance and testing*. CRC Press, 1–18.

[8] Balzer, G., Degen, W., Halfmann, M., Hartkopf, T., Neumann, C. (2004). Strategies for optimizing the use of substation assets. *CIGER session B3–101*, 1–8.

[9] IEC 60270. (2000). *High-voltage test techniques-Partial discharge measurement.*

[10] Tang, J., Xie, Y. (2011). Partial discharge location based on time difference of energy accumulation curve of multiple signals. *IET Electr. Power Appl.*, 5(1), 175–180.

[11] Kreuger, F.H. (1990). *Partial discharge detection in high-voltage equipment.* Butterworths, 29–48.

[12] Vedral. J., Kříž, M. (2010). Signal processing in partial discharge measurement. *Metrol. Meas. Syst.*, 31(6), 22–35.

[13] IEEE. (2007). IEEE guide for the detection and location of acoustic emission from partial discharges in oil-immersed power transformers and reactors.

[14] Hekmati, A. (2016). A novel acoustic method of partial discharge allocation considering structure-borne waves. *Int. J. Electr. Power Energy Syst.*, 77, 250–255.

[15] Kil, G.S., Kim, I.K., Park, D.W., Choi, S.Y., Park, C.Y., (2009). Measurements and analysis of the acoustic signals produced by partial discharge in insulation oil. *Curr. Appl. Phys.*, 9(2), 296–300.

[16] Kim, S.W., Kim, S.J., Seo, H.D., Jung, J.R., Yang, G.J., Duval, M. (2013). New methods of DGA diagnosis using IEC TC 10 and related databases part 1 application of gas-ratio combinations. *IEEE Trans. Dielect. Elect. Insul.*, 20(2), 685–690.

[17] Muhamad, N.A., Phung, B.T., Blackburn, T.R. (2011). Dissolved gas analysis for common transformer faults in soy seed-based oil. *IET Electr. Power Appl.*, 5(1), 133–142.

[18] Zhu, M.X., Xue, J.Y., Zhang, J.N., Li, Y., Deng, J.B., Mu, H.B., Zhang, G.J., Shao, X.J., Liu, X.W. (2016). Classification and separation of partial discharge ultra-high-frequency signals in a 252 kV gas insulated substation by using cumulative energy technique. *IET Sci. Meas. Technol.*, 10(4), 316–326.

[19] Raja, K., Devaux, F., Lelaidier, S. (2002). Recognition of discharge sources using UHF PD signatures. *IEEE Elect. Insul. Mag.*, 18(5), 8–14.

[20] Wang, Y.C., Wu, J.D., Li, Z., Yin, Y. (2014). Research on a practical de-nosing method and the characterization of partial discharge UHF signals. *IEEE Trans. Dielect. Elect. Insul.*, 21(5), 2206–2216.

[21] Okabe, S., Ueta, G., Hama, H., Ito. T., Hikita, M., Okubo, H. (2014). New aspects of UHF PD diagnostics on gas-insulated systems. *IEEE Trans. Dielect. Elect. Insul.*, 21(5), 2245–2258.

[22] CIGER. (2013). *Risk assessment on defects in GIS based on PD Diagnosis.*

[23] Sahoo, N.C., Salama, M.M.A., Bartnikas, R. (2005). Trends in partial discharge pattern classification: A survey. *IEEE Trans. Dielect. Elect. Insul.*, 12(2), 248–264.

[24] Masud, A.A., Stewart, B.G., Mcmeekin, S.G. (2014). Application of an ensemble neural network for classifying partial discharge patterns. *Electr. Power Syst. Res.*, 110, 154–162 .

Appendices

Figures 12–16 show the PRPD intensity graphs and parameters of five types of defects.

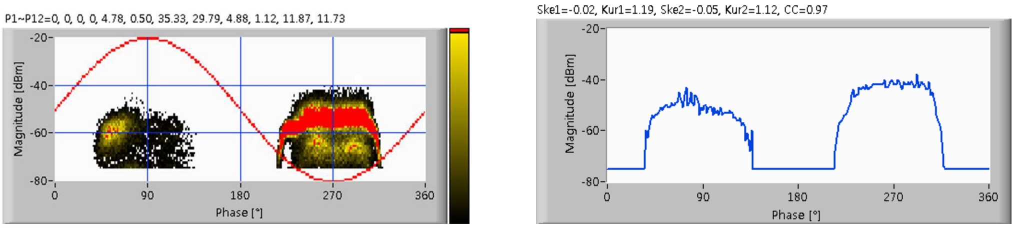

Fig. 12. PRPD intensity graph and parameter of protrusion on enclosure.

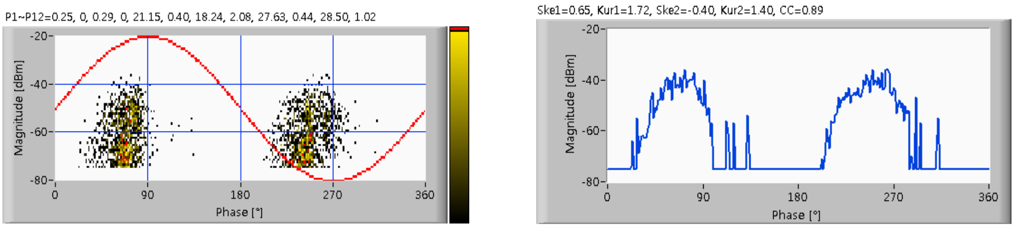

Fig. 13. PRPD intensity graph and parameter of void inside spacer.

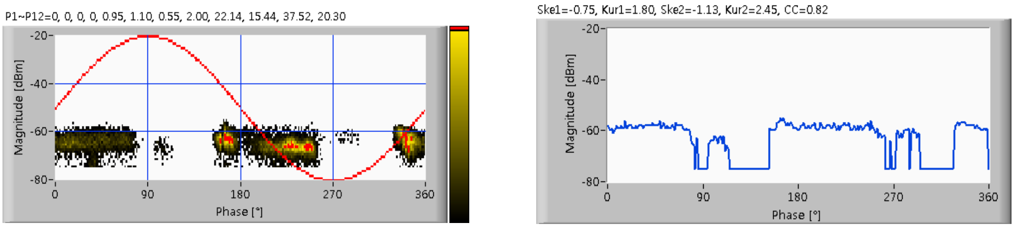

Fig. 14. PRPD intensity graph and parameter of particle on spacer.

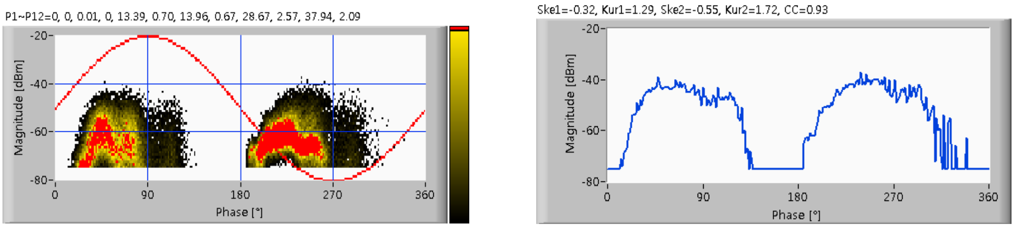

Fig. 15. PRPD intensity graph and parameter of crack inside spacer.

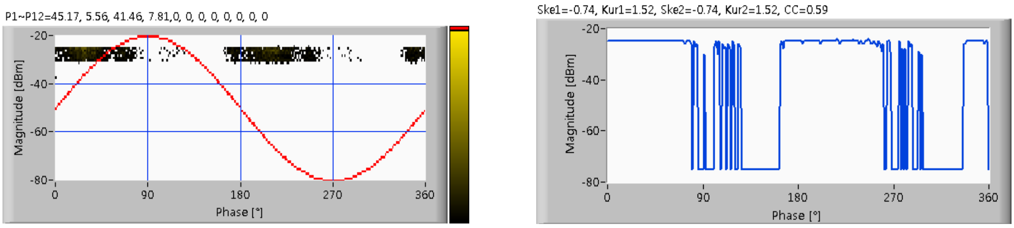

Fig. 16. PRPD intensity graph and parameter of floating.

www.czasopisma.pan.pl PAN www.journals.pan.pl

Metrol. Meas. Syst., Vol. 24 (2017), No. 3, pp. 525–536.

METROLOGY AND MEASUREMENT SYSTEMS

Index 330930, ISSN 0860-8229

www.metrology.pg.gda.pl

PROBLEM OF NON-MEASURED POINTS IN SURFACE TEXTURE MEASUREMENTS

Paweł Pawlus$^{1)}$, **Rafał Reizer**$^{2)}$, **Michał Wieczorowski**$^{3)}$

1) Rzeszow University of Technology, Faculty of Mechanical Engineering and Aeronautics, Al. Powstańcow Warszawy 12, 35-959 Rzeszów, Poland (ppawlus@prz.edu.pl)
2) University of Rzeszow, Faculty of Mathematics and Natural Sciences, Centre for Innovative Technologies, Al. Rejtana 16c, 35-959 Rzeszów, Poland (rreizer@ur.edu.pl)
3) Poznan University of Technology, Faculty of Mechanical Engineering and Management, Pl. Marii Sklodowskiej-Curie 5, 60-965 Poznań, Poland (✉ michal.wieczorowski@put.poznan.pl, +48 61 665 3567)

Abstract

This work is focused on the issue of non-measured points – one of the most important problems in surface texture measurements using optical methods. The fundamental aim of this research is to analyse errors of surface texture measurements caused by the presence of non-measured points. This study is divided into two parts. In the first part, circles with non-measured points were artificially created on peak portions of measured surfaces. In the second part – the results of measurement by a Talysurf CCI Lite interferometer were analysed. A measurement area of 3.3 × 3.3 mm contained 1024 × 1024 points. The measurements were performed with different intensity of light. Changes of parameters regarding the analysed errors depended on a surface type. The following parameters are susceptible to errors: skewness *Ssk*, areal material ratio *Smr,* as well as the following feature parameters: *Spd*, *Sda*, *Sdv*, *Sha* and *Shv*. Inaccuracies of measurement in valley parts of two-process textures led usually to larger errors of parameter computations compared with deviations in peak portions.

Keywords: surface texture measurements, optical method, non-measured points, white light interferometer.

1. Introduction

The manufacturing industry moves towards a higher degree of production acumen. Some properties, like materials' contact, sealing, friction, lubricant retention and wear resistance are related to the surface topography. The designer should decide on the number of surface topography parameters that will meet the functional demands of a product. The knowledge about the relationship between the product's surface texture and its function is still incomplete. The process of measuring the surface topography gives quantitative information about it. The surface texture is very important for many practical applications [1−8]. Many roughness measuring instruments give absolute measurement values of surface heights. The profile measurement is usually quick, simple and easy to interpret. However, most surface interactions are areal in nature. The areal (3D) texture parameters [9] are more reliable than the profile (2D) ones. Therefore the 3D measurement became popular. The assessment of surfaces using profiles has been employed since the early 1930's. The measurement systems basically involved the use of a mechanical stylus. There are a lot of factors affecting an uncertainty in surface geometry measurements using the stylus technique. The uncertainty is influenced by various environment, measuring equipment, measured objects, software, as well as tip shapes and sizes [10]. There are other methods for measuring roughness [11−13]. Some kinds of errors are common for various measuring techniques, for example errors caused by an improper digital filtration. It was found that for multi-process (stratified) surfaces having traces of more than one process, the application of a standardised Gaussian filter led to distortion of roughness

Article history: received on Dec. 22, 2016; accepted on Apr. 04, 2017; available online on Sep. 01, 2017; DOI: 10.1515/mms-2017-0046.

values. Cylinder textures after plateau honing are typical examples of two-process surfaces. Although the fine texture marks fall well within a bandwidth accepted for the cut-off, the scratches do not, since they are too wide. It was recommended that a standard cut-off should be increased to 2.5 mm for this application [14]. A double Gaussian filter (*Rk*) according to the ISO 13565-2 standard can be also applied [15]. An alternative approach is to use robust Gaussian filters, in which additional weights decreased in the places of valleys or peaks. As a result, textures having deep and wide valleys can be filtered properly [16–19].

The time required to collect real data for areal measurements using stylus instruments can appear excessively long compared with the operating time of the optical techniques [20– 23]. This could now become the most important disadvantage of the stylus methods. The optical methods are fast, but they are more sensitive to extraneous effects [24]. Among the optical methods, some of new advanced variants of confocal methods and white light interferometry are the most popular. The confocal optical systems are widely applied in engineering and biology because of very high clarity of obtained images, but when a range is increased the resolution tends to decrease; this factor does not occur when using the interferometric methods. The coherence scanning interferometry extends interferometric techniques to surfaces that are complex in terms of roughness, steps and discontinuities. Additional benefits include an equivalent of autofocus at every point in the field of view [24]. The environment can significantly contribute to measurement errors in the coherence scanning interferometer applications. Sharp edges can cause outliers called spikes in the topographic images [25]. If the light intensity received on a photodetector is too low, the surface height cannot be detected. A part of this image can be corrected using interpolation with an algorithm of determining areas with an ambiguous signal. Non-measured points exist also after the application of confocal optical systems. Non-measured points can result from many different causes, like high steepness of the slopes, surface absorbance or reflectivity. However, it is difficult to find in the accessible technical literature works dealing with the effect of errors caused by non-measured points on the distortion of surface texture parameter values. Nevertheless, this problem is one of the most important ones in the surface metrology. These errors may cause a false quality assessment of machined elements.

The fundamental aim of this research is to analyse errors of surface texture measurement of various machined surfaces caused by the presence of non-measured points. Another aim is to select the surface topography parameters that are the most and the least sensitive to the analysed errors.

2. Materials and methods

This study is divided into two parts. In the first part, circles with non-measured points were artificially created on peak parts of different measured surfaces, with the same measured areas and sampling intervals in perpendicular directions. The measuring area was 3.3 × 3.3 mm, the sampling interval in perpendicular directions was 5 μm. Ten samples with simulated errors were studied. A ratio of *non-measured* points (NM) was in each case 0.73%.

In the second part of this study the results of measurements by a Talysurf CCI Lite interferometer (produced by Taylor Hobson Ltd) with a 0.01 nm vertical resolution were analysed. A Nikon 5×/0.13 TI objective was used for all the measurements. The measuring area of 3.3 × 3.3 mm contained 1024 × 1024 measured points. The measurements were performed at a different intensity of light. The results of measurement with the smallest number of non-measured points were the reference (best) data. Fifteen surfaces (one- and two-process, isotropic and anisotropic, random and deterministic) were measured and analysed.

In both parts, TalyMap Gold version 6.1 software, copyright by Digital Surf, was used for filling in non-measured points. They were replaced by a smooth shape calculated from the neighbour points.

Before computations of parameters, flat surfaces were levelled using a least square plane, whereas curved forms of surfaces were removed using polynomials.

3. Study of surfaces with artificially created non-measured points

The aim of this part of research was to analyse the effect of surface type on the errors, because the NM ratio and shape of breaks were the same.

Ten surfaces were analysed; four of them were subjected to a detailed study. Fig. 1 shows examples of the analysed textures. The arrows indicate places where non-measured points are present after filling in. They indicate the effect of non-measured points on surface views. One can see that the corrected part of image is clearly visible on the surface after milling, as shown in Fig 1a, because the circle with non-measured points was located in a surface peak part. The modified circles on honed (Fig. 1b) and polished surfaces (Fig. 1d) are also visible. An anisotropic character of these textures is the most probably reason of visibility of the improved surface parts, because the corrected details are isotropic. However, it is difficult to find a circle with filled in non-measured points on the lapped surface with isolated oil pockets, created by the abrasive jet machining (Fig. 1c). The presence of dimples and an isotropic character of the peak surface part after lapping are the most probable reasons of a small visibility of the error.

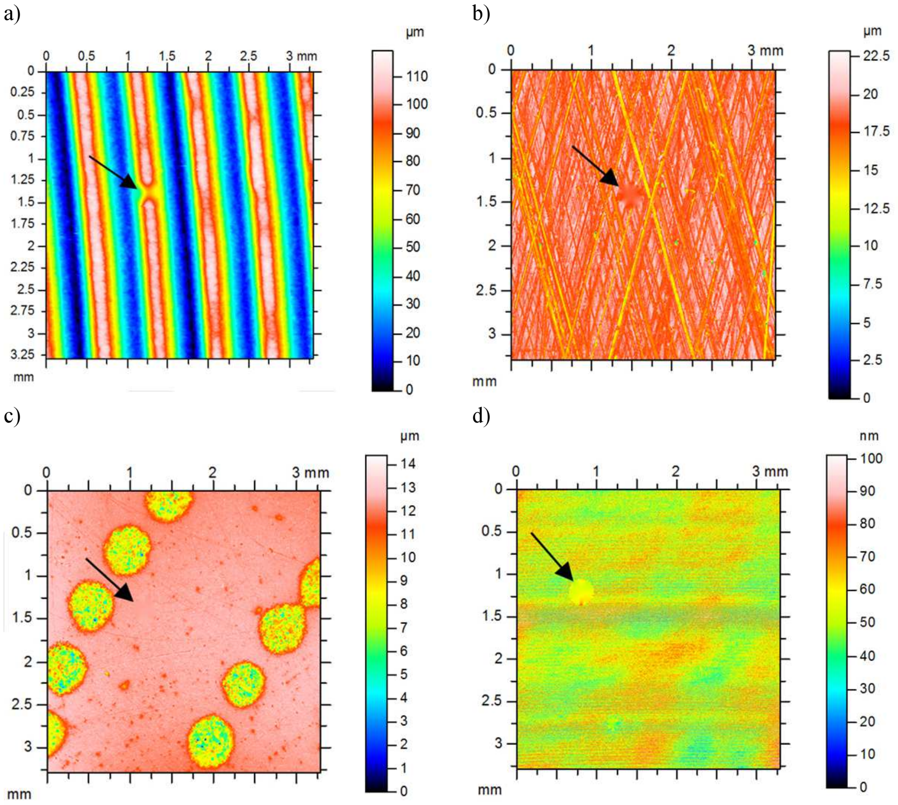

Fig. 1. Contour plots of surface points after milling (a); honing (b); texturing by the abrasive jet machining after initial lapping (c) and polishing (d) after filling in non-measured points.

Relative changes of the surface topography parameters defined according to the ISO 25178 standard due to disturbances were studied.

Although the error caused a change of the milled surface view (see Fig. 1a), the relative absolute changes of parameter values were not higher than 2%. A different tendency of changes of values for various height parameters was found: for statistical parameters *Sa* (arithmetic mean height) and *Sq* (root mean square height) as well as *Spk* (reduced summit height) and *Sv* (maximum valley height) they decreased, whereas for *Sk* (core roughness depth) and *Sp* (maximum peak height) parameters the changes increased. They were not higher than 0.7%. Due to a decrease of the *Spk* parameter as well as *Sr*1 ratio (upper bearing area) values, the *Sa*1 parameter value decreased; its changes were comparatively large (about 1.9%). The values of both skewness *Ssk* and kurtosis *Sku* increased. As a consequence of reduced statistical height parameter values, the values of hybrid parameters *Sdq* (root mean square slope) and *Sdr* (developed interfacial area ratio) decreased. The material volume *Vm* increased; its changes were the biggest of all the analysed parameters (about 2%). Among the feature parameters, *Spd* (peak density) and *Sda* (mean hill area) values increased. The spatial parameters were stable. Generally, it was found that the values of parameters related to a peak surface part (*Sa*1 and *Vm*) changed in the greatest degree.

It is interesting that – from the cylinder liner surface parameters – the closed dale volume *Sdv* value decreased the most (about 4%) (Fig. 1b). The maximum relative change of other parameter values was 1.7%. From the amplitude parameters only the value of *Sq* decreased, whereas *Spk* increased. Similarly to the milled surface, the *Ssk* and *Sku* parameter values increased, whereas those of *Sdq* and *Sdr* decreased. The functional parameter values from *V* family changed; those of *Vm* increased, whereas *Vmc* (core material volume) and *Vvc* (core void volume) decreased. The feature parameter values *Spd* and *Sdv* (mean dale volume) decreased while that of *Sda* increased. Generally, the same tendency of parameter value changes for the milled and honed surfaces was found.

The parameter values of textured surfaces shown in Fig. 1c changed marginally due to the presence of non-measured points. The maximum change of parameter values was 1% (*Spd* and *Sdv* values decreased). The values of the following parameters decreased: *Spk*, *Sa*1, *Sdr*, *Vvc* and *Sda*, whereas *Sxp* (extreme peak height) – increased.

The relative errors of parameters for the polished surface shown in Fig. 1d were comparatively large. Those for *Sdv* decreased by about 8%, for *Sr*1 increased by 2.4% and – consequently – for *Sa*1 increased by 3.5%, whereas for *Ssk* and *Sda* decreased by 3 and 1.6%, respectively. Changes for other parameters were smaller than 1%; for the following parameters they decreased: *Sk*, *Sr*2 (lower bearing area), *Sp*, *Sa*, *Std* (texture direction), *Sdq*, *Sdr*, *Vvc* and *Spd*, whereas for the following parameters they increased: *Spk*, *Sa*2 (oil capacity), *Sku* and *Vm*.

Generally, after analysis of parameter value changes for all ten tested surfaces it was found that deviations of the skewness *Ssk* and kurtosis *Sku* values occurred (up to 3%). The values of statistical amplitude parameters *Sa* and *Sq* typically decreased, whereas those of the parameters describing total height *Sz*, *Sp* and *Sv* were more stable. As a result of the amplitude reduction, the values of hybrid parameters also decreased. Since non-measured points were located in the peak regions of analysed surfaces, the values of parameters connected with a peak part: *Sr*1, *Spk*, sometimes *Sk* and consequently *Sa1* typically changed (up to 4%); in most cases the peak density *Spd* value marginally decreased. The spatial parameters were usually stable; the main directionality described by *Str*, changed only for the anisotropic one-directional texture (Fig. 1d). Large changes of the feature parameters: *Sdv* and *Sda* deserve attention. Changes of parameter values depend on a surface type. For example, maximum changes of parameter values shown in Fig. 1c was 1%; it is difficult to find filled-in non-measured points on this graph.

4. Study of surfaces measured in different conditions

It was found that improper measurement conditions might cause serious inaccuracies in the parameter calculations. High errors of parameter computations occurred even for very small ratios of *non-measured* points (NM). Fig. 2 presents an example. Non-measured points of a small ratio (0.0268%) located in a valley surface part caused a considerable increase of roughness height in this part (the *Sv* value increased by more than 20%). In addition, the spatial parameter values changed; the autocorrelation length *Sal* increased by more than 20%, whereas the texture parameter *Str* by more than 15%. The peak density decreased by about 25%, whereas the values of feature parameters: *Sda*, *Sha* (mean hill area), *Sdv* and *Shv* (mean hill volume) increased by more than 25%. These changes are large, therefore analysis of the surface distortion due to the presence of non-measured points deserves attention. However, the changes of parameter values characterizing the material ratio curve, from the *Sk* family: *Sk*, *Spk*, *Svk* (reduced valley depth), *Sr*1 and *Sr*2 were smaller than 5%. An increase of the NM ratio from 0.00935 to 0.0268% caused non-visible changes of the contour plot; therefore it was presented in Fig. 1 only for the reference surface.

From the analysis of several measured surfaces it was found that – due to a growth of relative light intensity from the initial small value - the NM ratio decreased, reached the smallest value and then increased.

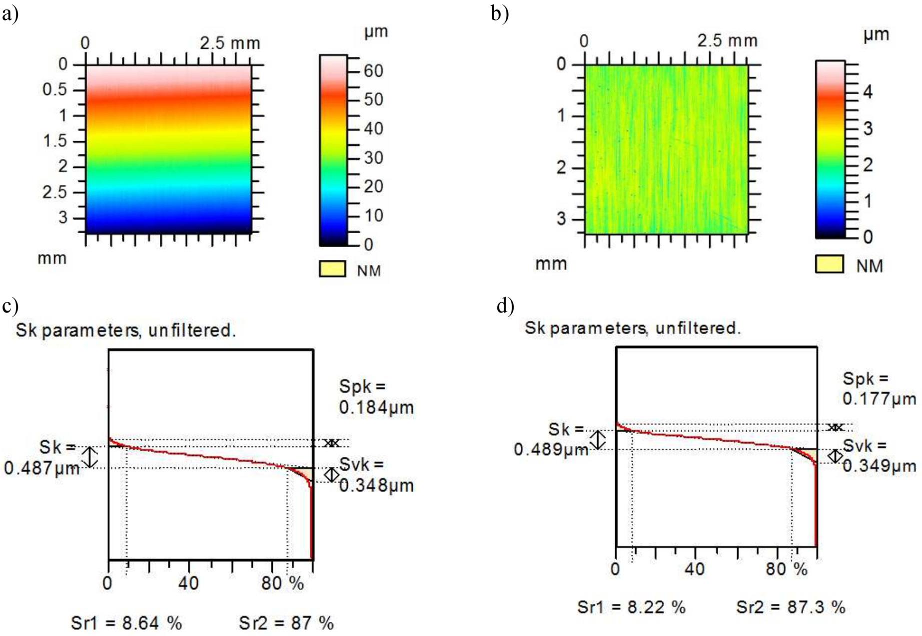

e)

Sv = 2.34 µm; *Sal* = 0.00965 mm
Str = 0.024; *Spd* = 887/mm^2

f)

Sv = 2.81 µm; *Sal* = 0.0116 mm
Str = 0.028; *Spd* = 669/mm^2

Fig. 2. Contour plots of the polished surface before (a) and after form removal (b) with material ratio curves (c, d) and selected parameters (e, f); graphs a, b, c, e correspond to NM ratio 0.00935%, but d and f – 0.0268%.

Too small a light intensity caused the presence of non-measured points in a valley region, whereas too high intensity – in a peak surface part. An increase of light intensity caused typically a growth of height, hybrid and functional (*V* family) parameter values as well as of oil capacity, however for very high NM ratios (larger than 40%) different tendencies of parameter changes were also possible. The spatial parameter *Sal* value mainly decreased due to an increase of light intensity. Its changes were higher for the anisotropic surface compared with the isotropic or mixed ones. The variability of *Sdq* parameter is smaller than that of *Sdr*. A similar finding was found in other research reports [22, 23] and in the first part of the present study.

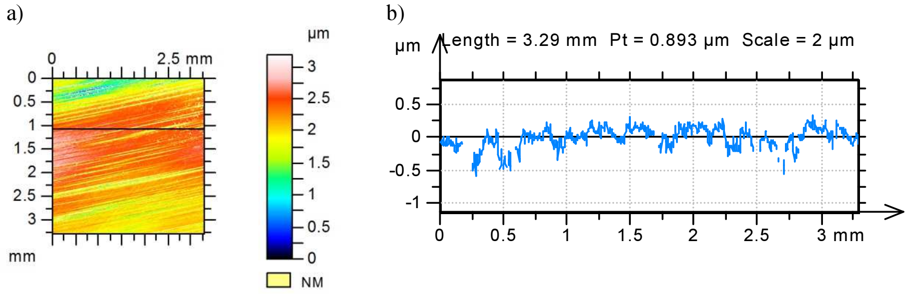

c)

Sq = 0.387 µm; *Sp* = 1.13 µm; *Sv* = 2.03 µm; *Ssk* = –0.76; *Smr* = 49.1%

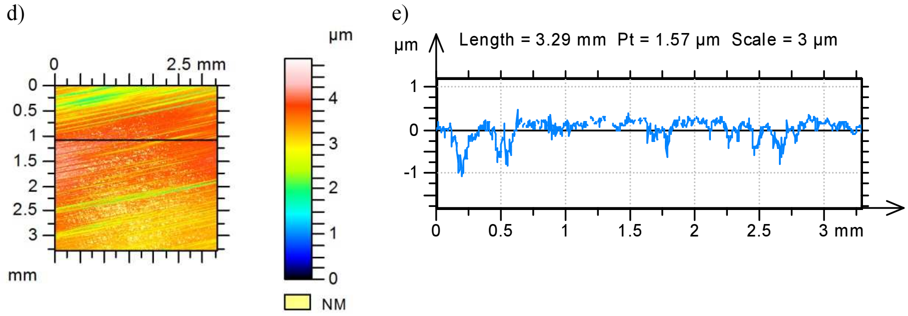

f)

Sq = 0.444 µm; *Sp* = 1.47 µm; *Sv* = 3.43 µm; *Ssk* = –0.78; *Smr* = 11.9%

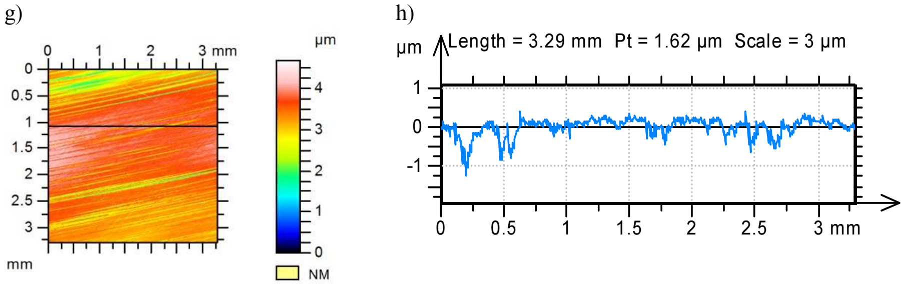

i)

Sq = 0.442 µm; *Sp* = 1.27 µm; *Sv* = 3.43 µm; *Ssk* = –0.81; *Smr* = 35.5%

Fig. 3. Contour plots (a, d, g); extracted profiles (b, e, h) and selected parameters (c, f, i) of the polished surface with non-measured points located in a valley part, NM ratio 10.1% (a, b, c) with non-measured points located in a peak part, NM ratio 9.3% (d, e, f) with the smallest number of non-measured points, NM ratio 0.1% (g, h, i).

The non-measured points caused typically an increase of the *Ssk* parameter and decrease of the *Sku* parameter values for one-process surfaces. The functional parameters *Smc* (inverse areal material ratio) and especially *Sxp* were more stable than the *Smr* parameter. A large variation of the *Smr* parameter value was found in other research reports [26, 27]. Typically, the changes of the values of spatial parameters *Str* and – especially – *Sal* were larger than those of height parameters, however a different situation was also possible. The main texture direction *Std* was constant for the anisotropic surface with the main directionality, contrary to the isotropic textures. It is difficult to find a tendency of changes of the peak density *Spd*, however variation of this parameter value was large. The following feature parameters: *Sda*, *Sdv*, *Sha* and *Shv* were also non-stable on the surface. The variability of *Sr*2 material ratio was lower than that of *Sr*1 ratio. Usually, a one-process surface with the highest NM ratio corresponded to maximum changes of parameters.

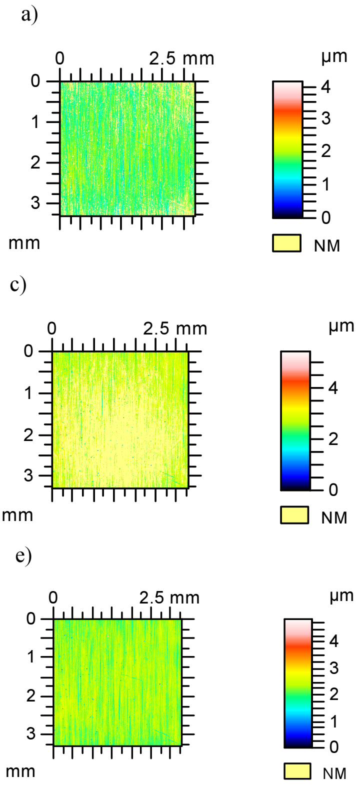

b)

Sq = 0.2 μm
Sp = 2.4 μm
Sv = 1.53 μm
Ssk = –0.42
Sal = 0.0193
Str = 0.042

d)

Sq = 0.24 μm
Sp = 6.82 μm
Sv = 1.81 μm
Ssk = –0.5
Sal = 0.0245
Str = 0.107

f)

Sq = 0.22 μm
Sp = 2.53 μm
Sv = 2.34 μm
Ssk = –0.68
Sal = 0.0096
Str = 0.024

Fig. 4. Contour plots (a, c, e) and selected parameters (b, d, f) of the polished surface with non-measured points located in a valley part, NM ratio 24.2% (a, b) with non-measured points located in a peak part, NM ratio 58% (c, d) with the smallest number of non-measured points, NM ratio 0.00935% (e, f).

Generally, the variability of statistical height parameters *Sa*, *Sq*, spatial parameter *Std*, slope *Sdq*, functional parameters from *V* family as well as material ratio *Sr*2 caused by the presence of non-measured points was relatively small. Large errors existed only for a high NM ratio. However the following parameters are susceptible to errors caused by high NM ratios: skewness *Ssk*, functional parameter *Smr* and the following feature parameters: *Spd*, *Sda*, *Sdv*, *Sha* and *Shv*.

The changes of parameters depend on a location of non-measured points. Fig. 3 presents an example. A surface of a little asymmetric distribution after polishing was studied. An NM ratio of a texture shown in Figs. 3a and 3b is similar to that presented in Figs. 3d and 3e, however one can see from both views of contour plots and extracted profiles that non-measured points are located in valley and peak parts, respectively. Due to the presence of non-measured points in a valley part the *Sv* parameter value decreased by about 40% and *Sq* – by nearly 12%. The presence of non-measured points in a peak surface part led to an increase of the *Sp* parameter value by more than 15% and a decrease of the *Smr* value by more than 60%. Due to the presence of non-measured points the *Ssk* parameter value increased. A change of *Sal* parameter value was smaller than 10%, which was probably related to the fact that a mixed surface (*Str* about 0.35) was analysed.

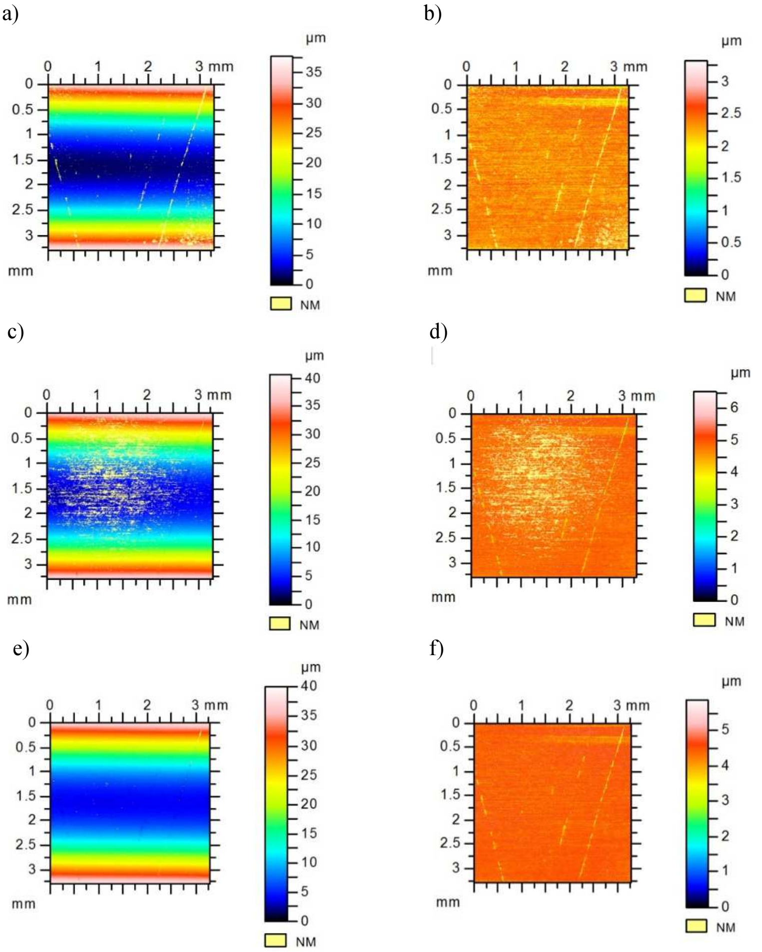

Fig. 5. Contour plots of a worn cylinder surface before (a, c, e) and after form removal (b, d, f) with non-measured points located in a valley region; NM ratio 4.31%(a, b), in a peak part; NM ratio 14.4% (c, d) and with their smallest number; NM ratio 0.102% (e, f).

The statistical parameters *Sq* and *Sa* are stable for an extremely high number of non-measured points. When these points are located in a peak surface part (NM ratio was 58% – see Figs. 4c, and 4d) the *Sq* parameter value was overestimated by 9%. A similar error was obtained when non-measured points were present in a valley part (NM ratio was 24.2% – see Figs. 4a and 4b). Similarly to Fig. 3, the presence of non-measured points in a valley surface part caused large changes of the *Sv* parameter value, but in a peak part – of the *Sp* parameter value. In both cases, errors led to an increase of the parameter values: *Sal*, *Str* and *Ssk*.

The presented above tendencies are concerned mainly with one-process surfaces. However similar trends were observed also for two-process textures characterized by a negative skewness (usually smaller than −1). An increase of light intensity led in most cases to a decrease of skewness *Ssk* and usually to an increase of kurtosis *Sku* values. This is reasonable because a small skewness corresponds to a large kurtosis. This tendency was probably caused by the presence of non-measured points in the bottom of valleys (Figs. 3a and 3b).

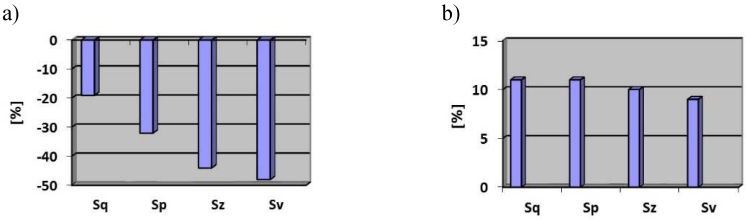

Fig. 6. Relative changes of parameters for the surface presented in Fig. 5a (a) and 5b (b).

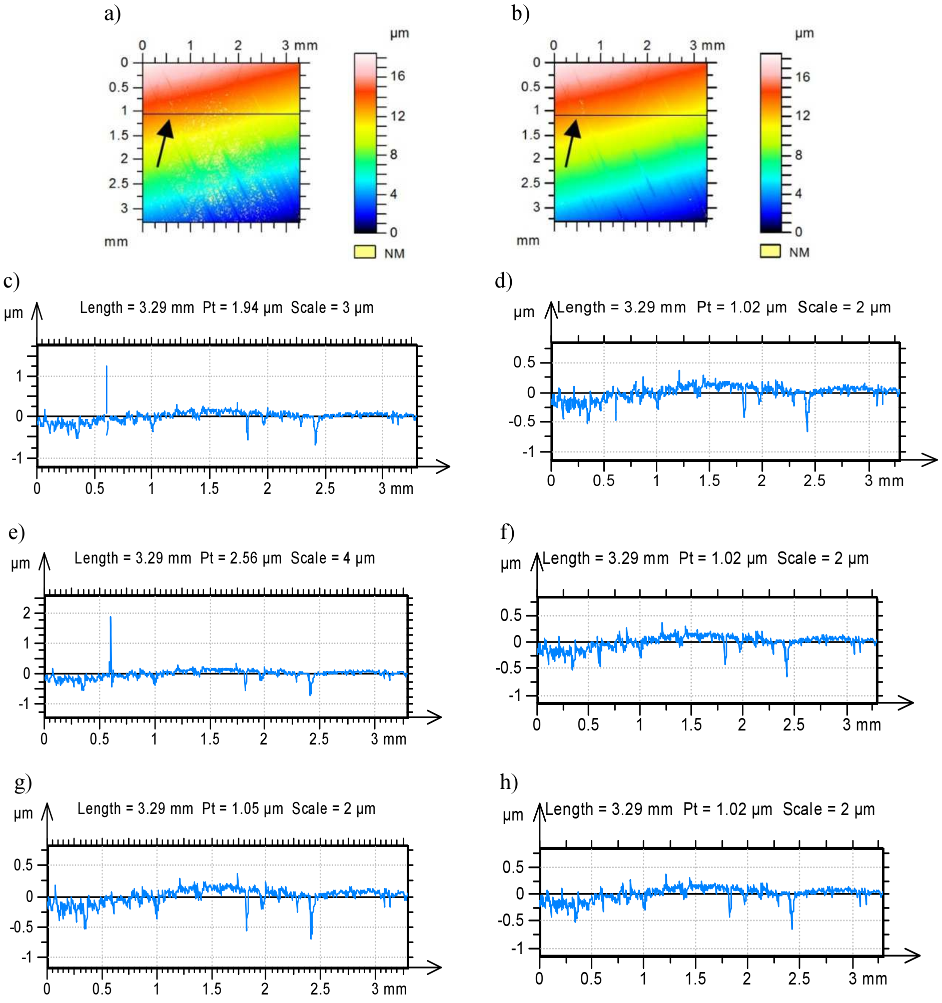

Fig.7. Contour plots (a, b), extracted profiles before correction – filling in (c, d), after correction of the whole surface (e, f) and after profile correction (g, h); NM ratio 6.68% (a, c, e, g) and 0.079% (b, d, f, h).

For the surface shown in Fig. 3 the change of *Ssk* parameter value is small, but high errors of this parameter calculation can occur for two-process textures. As a result of it a surface machined well looks like a one-process texture and can be classified as a spoilage. An increase of the *Ssk* parameter value is related to a decrease of the *Svk* parameter value. Errors of two-process surface topography parameter estimations are very important, because the functional properties of two-process surfaces are better than those of one-process textures [28–31]. An inaccuracy of a valley part measurement typically led to larger errors of parameter computations compared with a disturbance in a plateau region. For example, the relative errors of parameter values for the surface shown in Figs. 5a and 5b are higher than those for the surface presented in Figs. 5c and 5d, although the NM ratio of the latter is higher. Fig. 6 presents relative changes of typical parameters. Negative changes correspond to underestimation, while positive ones – to overestimation of amplitude parameters. The *Ssk* parameter values of the surface shown in Fig. 5 are: in 5a and 5b −0.34, 5c and 5d −1.26, 5e and 5f −1.25.

The other tendencies of parameter changes due to the presence of non-measured points found for a one-process surface were also confirmed for two-process textures. The texture direction was typically constant. The feature parameters, especially *Sda*, *Sha*, *Sdv* and *Shv* were non-stable on two-process surfaces.

An incorrect light intensity could lead to the presence of spikes (Fig. 6). However, erasing non-measured points from the whole honed surface can cause an increase of profile height (Fig. 7c and 7e), contrary to a similar correction of profile only (Fig. 7g). When the light intensity was smaller (Fig. 7b, 7d, 7f and 7h) the non-measured points appeared in the same place (see arrows), but without the presence of spikes. The same profile was obtained after correction of the whole surface or profile (see Fig. 7f and 7h). The *Sp* parameter value for the corrected surface after form removal with a smaller NM ratio was 1.21 µm, but with a higher one – 3.07 µm. The arrows indicate positions of errors.

5. Conclusions

The problem of non-measured points is one of the most important issues in surface texture measurements. The presence of even a small number of non-measured points can cause false estimation of surface texture parameters which can substantially affect the quality assessment of machined elements.

When non-measured points were located in one place of a peak surface part, the values of parameters describing this part changed more than the others. A character of parameter changes depends on a surface type.

An increase of light intensity caused typically an increase of the height, hybrid and functional parameter values; the spatial parameter *Sal* value mainly decreased. The following parameters are susceptible to errors caused by a high NM ratio: skewness *Ssk*, functional parameter *Smr* and feature parameters: *Spd*, *Sda*, *Sdv*, *Sha* and *Shv*.

For stratified surfaces, an increase of light intensity caused a decrease of skewness *Ssk* and an increase of kurtosis *Sku* values. These changes can be large. For this type of surface an inaccuracy of measurement in a valley part led usually to larger errors of parameter computations compared with disturbances in a plateau region.

Acknowledgements

Part of this work was supported by the Polish National Centre of Research and Development (the project contract No. PBS2/A6/20/2013/NCBiR/24/10/2013; “Research and evaluation of reliability of modern methods of surface topography measurements in micro and nano scale”).

References

[1] Wieczorowski, M., Mrozek, R., Andrałojć. P. (2010). The use of surface asperities analysis to investigate wear of bodies in contact on example of brake elements. *Metrol. Meas. Syst.*, 17(2), 271–278.

[2] Twardowski, P. (2011). Surface roughness analysis in milling tungsten carbide with CBN cutters. *Metrol. Meas. Syst.*, 18(1), 105–114.

[3] Wojciechowski, S., Twardowski, P., Wieczorowski, M. (2014). Surface texture analysis after ball end milling with various surface inclination of hardened steel. *Metrol. Meas. Syst.*, 21(1), 145–156.

[4] Krolczyk, G.M., Legutko, S. (2014). Experimental analysis by measurement of surface roughness variations in turning process of duplex stainless steel. *Metrol. Meas. Syst.*, 21(4), 759–770.

[5] Lipiński, D., Kacalak, W. (2016). Metrological aspects of abrasive tool active surface topography evaluation. *Metrol. Meas. Syst.*, 23(4), 567–577.

[6] Krolczyk, G.M., Krolczyk, J.B., Maruda, R.W., Legutko, S., Tomaszewski, M. (2016). Metrological Changes in Surface Morphology of High-Strength Steels in Manufacturing Processes. *Measurement*, 88, 176–185.

[7] Krolczyk, G.M., Maruda, R.W., Nieslony, P., Wieczorowski, M. (2016). Surface morphology analysis of Duplex Stainless Steel (DSS) in Clean Production using the Power Spectral Density. *Measurement*, 94, 464–470.

[8] Rosen, B.G., Anderberg, C., Ohlsson, R. (2008). Parameter correlation study of cylinder liner roughness for production and quality control. *Proc. of the Institution of Mechanical Engineers, Part B: Journal of Engineering Manufacture*, 222, 1475–1487.

[9] Blateyron, F. (2013). The areal field parameters. Leach, R.K. *Characterisation of Areal Surface Texture*, Springer, 15–43.

[10] Pawlus, P., Wieczorowski, M., Mathia, T. (2014). *The errors of stylus methods in surface topography measurements*. Zapol.

[11] Murugarajan, A., Samuel, G.L. (2011). Measurement, modelling and evaluation of surface parameter using capacitive-sensor-based measurement system. *Metrol. Meas. Syst.*, 18(3), 403–418.

[12] Zawada-Tomkiewicz, A. (2010). Estimation of surface roughness parameter based on machined surface image. *Metrol. Meas. Syst.*, 17(3), 493–504.

[13] Salazar, F., Belenguer, T., García, T., Ramos, T. (2012). On roughness measurement by angular speckle correlation. *Metrol. Meas. Syst.*, 19(2), 373–380.

[14] Whitehouse, D.J. (1983). Some theoretical aspects of a practical measurement problem in plateau honing. *Int. J. Prod. Res.*, 21(2), 215–221.

[15] Mummery, L. (1990). *Surface texture analysis, the handbook.* Hommelwerke GmbH.

[16] Brinkman, S., Bodschwinna, H. (2003). Advanced Gaussian filters. *Assessment surface topography*, Blunt, L., Jiang, X. (eds.). Kogan Page Science, London and Sterling, 62–89.

[17] Brinkman, S., Bodschwinna, H., Lemke, H.W. (2000). Development of a robust Gaussian regression filter for three-dimensional surface analysis. *X International Colloquium on Surfaces*. Chemnitz, Germany, 122–131.

[18] Li, H., Jiang, X., Li, Z. (2004). Robust estimation in gaussian filtering for engineering surface characterization. *Precis. Eng.*, 28(2), 186–193.

[19] Dobrzanski, P., Pawlus, P. (2010). Digital filtering of surface topography: Part II. Applications of robust and valley suppression filters. *Precis. Eng.*, 34 (3), 651–658.

[20] Whitehouse, D.J. (2011). Surface metrology today: complicated, confusing effective? *Proc. of the 13th International Conference on Metrology and properties of Engineering Surfaces*. Twickenham Stadium, UK, 1–10.

[21] Leach, R.K. (2011). *Optical measurement of surface topography*. Springer.

[22] Vorburger, T.V., Rhee, H.G., Renegar, T.B., Song, J.F., Zheng A. (2007). Comparison of optical and stylus methods for measurement of surface texture. *Int. J. Adv. Manuf. Tech.* 33(1), 110–118.

[23] De Groot, P. (2015). Principles of interference microscopy for the measurement of surface topography. *Adv. Opt. Photonics*, 7(1), 1–65.

[24] de Groot, P. (2011). Coherence scanning interferometry. *Optical Measurement of Surface Topography*, Leach, R. (ed.), Springer-Verlag, Berlin and Heidelberg.

[25] Podulka, P., Pawlus, P., Dobrzański. P., Lenart, A. (2014). Spikes removal in surface measurement. *J. Phys. Conf. Ser.*, 483(1), 012025.

[26] Pawlus, P., Grabon, W., Reizer, R., Gorka, S. (2015). A study of variations of areal parameters on machined surfaces. *Surf. Topog.: Metrol. Prop.*, 3(2), 025003.

[27] Dzierwa, A., Reizer, R., Pawlus, P., Grabon, W. (2014). Variability of areal surface topography parameters due to the change in surface orientation to measurement direction. *Scanning*, 36(1), 170–183.

[28] Grabon, W., Pawlus, P., Sep, J. (2010). Tribological characteristics of one-process and two-process cylinder liner honed surfaces under reciprocating sliding conditions. *Tribol. Int.*, 43(10), 1882–1892.

[29] Johansson, S., Nilsson, P.H., Ohlsson, R., Anderberg, C., Rosen, B.G. (2008). New cylinder liner surfaces for low oil consumption. *Tribol. Int.*, 41(9–10), 854–859.

[30] Yousfi, M., Mezghani, S., Demirci, I., El Mansori, M. (2015). Smoothness and plateauness contributions to the running-in friction and wear of stratified helical slide and plateau honed cylinder liners. *Wear*, 332–333, 1238–1247.

[31] Mezghani, S., Demirci, I., Yousfi, M., El Mansori, M. (2013). Mutual influence of crosshatch angle and superficial roughness of honed surfaces on friction in ring-pack tribo-system. *Tribol. Int.*, 66, 54–59.

Metrol. Meas. Syst., Vol. 24 (2017), No. 3, pp. 537–550.

METROLOGY AND MEASUREMENT SYSTEMS
Index 330930, ISSN 0860-8229
www.metrology.pg.gda.pl

A HIGH-SPEED FULLY DIGITAL PHASE-SYNCHRONIZER IMPLEMENTED IN A FIELD PROGRAMMABLE GATE ARRAY DEVICE

Robert Frankowski, Dariusz Chaberski, Marcin Kowalski, Marek Zieliński

Nicolaus Copernicus University, Faculty of Physics, Astronomy and Informatics, Grudziądzka 5, 87-100 Toruń, Poland
(✉ robef@fizyka.umk.pl, +48 56 611 3343, *daras@fizyka.umk.pl, markow@fizyka.umk.pl, marziel@fizyka.umk.pl)*

Abstract

Most systems used in quantum physics experiments require the efficient and simultaneous recording different multi-photon coincidence detection events. In such experiments, the single-photon gated counting systems can be applicable. The main sources of errors in these systems are both instability of the clock source and their imperfect synchronization with the excitation source. Below, we propose a solution for improvement of the metrological parameters of such measuring systems. Thus, we designed a novel integrated circuit dedicated to registration of signals from a photon number resolving detectors including a phase synchronizer module. This paper presents the architecture of a high-resolution (~60 ps) digital phase synchronizer module cooperating with a multi-channel coincidence counter. The main characteristic feature of the presented system is its ability to fast synchronization (requiring only one clock period) with the measuring process. Therefore, it is designed to work with various excitation sources of a very wide frequency range. Implementation of the phase synchronizer module in an FPGA device enabled to reduce the synchronization error value from 2.857 ns to 214.8 ps.

Keywords: phase synchronizer, delay line, coincidence counting, quantum information, time interval measurement, time-to-digital converters, field programmable gate arrays.

1. Introduction

The rapid development of quantum technologies in quantum optics experiments delivered more valuable information about the fundamental nature of light. Experiments prepared in such areas as the spectral state of a single photon characterization, the quantum cryptography and implementation of quantum teleportation protocols still remain valid and could become very possible directions for the future research [1−4]. The methods of single and multi-photon statistics' reconstruction using an optical fibre-loop detector are reported [5−6]. For this purpose, the indirect single-photon counting techniques with picoseconds resolution can be practicable. The preferable solution in these experiments is to use a box-car-like module [7]. Actually, a box-car-like module is a modified single-photon gated counting system with a counting rate limited to one. In this situation, coincidences of two or more electrical pulses can be simply obtainable.

The most popular coincidence measurement systems were built of appropriate electronic modules, such as analogue time-to-amplitude converters, discriminators and manually- or digitally-controlled delay gates. Additionally, most of them were characterized by slow data processing electronic devices. Also, they required manual synchronizing signals between their electronic stages [8−9]. Recently, the coincidence measurement systems have been constructed in a more integrated form, *i.e.* using high-performance *Field Programmable Gate Array* devices (FPGA) [10−13]. The rapid development of FPGA technology enables to implement fully-digital high-resolution programmable delay lines in these structures and guarantees very short

Article history: received on Jun. 07, 2016; accepted on Apr. 29, 2017; available online on Sep. 01, 2017; DOI: 10.1515/mms-2017-0037.

rising and falling times of the propagated signals. It is very important regarding quick achievement of the coincidence window.

In a traditional digital box-car module, the delay time between the trigger and the (delayed by the digital delay line) opening and closing gate pulses, depends mainly on the internal clock period. If the delay time is relatively long (*i.e.* contains a large number of clock periods), a high stability of the internal clock must be guaranteed [14]. This involves the fact that the precision of determination of that time interval is proportional to the number of clock periods. Otherwise, for short time intervals, the problem of synchronization of the physical process with the measuring system becomes very important [15]. In such a situation, the synchronization error (without compensation) is comparable to the internal clock period T. Therefore, it can be described by a uniform probability distribution Θ_{CLK} in a range of $-T/2$ to $T/2$. If such a large synchronization error is not compensated, the effective width of time-gate increases. In consequence, the modification effect of the ideal time-gate functions by the Θ_{CLK} function cannot be omitted. This should be taken into account when the width of the coincidence window is being determined. In the presented paper, the problem of compensation of this time-interval error has been solved. It was possible thanks to the application of the *fully-digital phase synchronizer* (DPS) module in an FPGA structure.

Well-known methods performing the synchronization process employ PLL and DLL control modules [16–17]. Most of them are supplied in wire and wireless sensor network systems for event ordering and efficient communication scheduling [18–19]. Others can be used to effective compensation of the synchronization error in gated counting systems. This problem has been solved by the application of a start-able PLL oscillator used as the internal clock [20]. Similar solutions concern using a DLL loop to stabilize the delay line parameters against temperature or power supply voltage variations [21]. The known concept of applying a PLL to the CPU-Coprocessor synchronization [22] remains also valid in constructing various types of precise TDC systems [23] to guarantee a high synchronization level between the internal signals and appropriate functional blocks of the system. In modern FPGAs it can be achieved *e.g.* by DCM blocks operating in the precise phase shifting mode [24]. Another class represents the synchronizers used for synchronization of asynchronous input pulses with the nearest edges of clocks. The main purpose of their application is to effectively reduce the possibility of potential causes of metastable states in the period counters. It can be achieved by generation of synchronized *enable* signals by single or dual-edge double synchronizers [25].

Contrary to the above solutions we have designed a purely digital module meant to synchronize the internal clock signal with the leading edge of trigger pulse by a digital delay line. In our approach a high operating frequency has been achieved by using a direct time conversion method.

The presented paper is organized as follows. Firstly, a possibility of applying a DPS module in quantum physics experiments has been explained in Section 2. For this purpose, an example of optical equipment for the experimental characterization of the statistics of photon pairs is described. A simplified block diagram of DPS module and some essential information of the proposed synchronization technique is reported in Section 3. In this section, the experimental results of characterization of the *phase detection* (PDM) and *delay selection* (DSM) modules and the simulation results obtained from the DPS model are also included. In the next section, the experimental results of real DPS testing that confirm the effective gate width reduction and their interpretations (in Section 4) are presented. Finally, we summarize our work.

2. Box-car-like architecture

The main aim of the research was to analyse the concept of the construction and implementation – in a Virtex4 FPGA programmable structure – of a multi-platform DPS module which cooperates with a multi-channel *coincidence counter* (CC). The basic task of DPS module was the fast synchronization of the measurement system with the trigger pulses produced by a pulse laser (RegA 900, Coherent, 165 fs FWHM, 774 nm). A satisfactory level of synchronization (diferences of the successive time intervals between the trigger pulse position and the time-gate activation) required during the entire measurement process should be below 300 ps and must be independent of the trigger source repetition rate. An example of practical application of the DPS module is shown in Fig. 1. Such a construction was used in the physical experiment where the parameters of single photon sources are obtained.

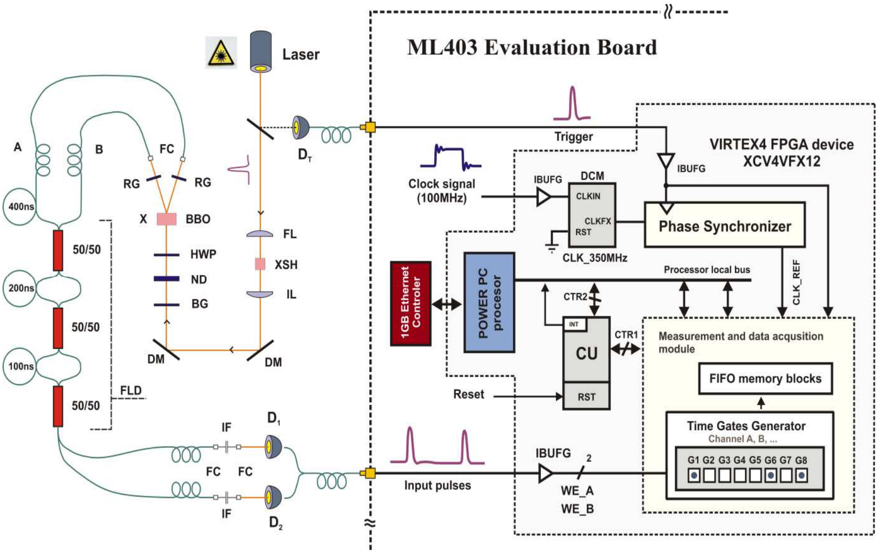

Fig. 1. A multichannel coincidence meter as an example of application of the digital phase synchronizer. DCM – the *digital clock manager* module built in a XC4VFX12 programmable structure; CLK_REF – the *clock signal synchronized* with the rising edge of trigger pulse; CU – *control unit*; FL – *focusing lens*; XSH – BBO crystal for generation of the second harmonic; IL – *imaging lens*; DM – *dichroic mirrors*; BG – *blue glass* filter; X – down-conversion crystal; IF – *interference filter*; FC – *fibre coupling* stage, HWP – *half-wave plate*; ND – *neutral density* filter; FLD – *fibre-loop detector*; D1 and D2 – single photon counting detectors.

A typical photon source consists of a nonlinear crystal (BBO – *β-barium borate*) which is pumped by a pulse laser. The most important element of the optical part of measuring equipment (depicted in Fig. 1) is a *fibre-loop detector* (FLD) [26]. A single photon may be propagated by it in eight distinct ways. The minimal delay in the proposed FLD construction is about 100 ns, but could be shorter. It depends on the laser repetition rate (for instance, the standard frequencies of pulse lasers are within a range of 1 kHz – 100 MHz). Inside the FLD, photons are divided by 50/50 fibre couplers. Thus separated in time, the photons are then registered by two photo-detectors (D1 and D2). The signals received from the photo-detectors are compatible with the Low Voltage CMOS I/O standard supported by Virtex-4 devices. Therefore, they can be directly connected to the CC inputs.

Unlike the well-known box-car constructions [27], the presented CC system stores information only about the occurrence of photons in appropriate time-gates. The basic modules of system include: a *control unit* (CU), a *phase synchronizer* (DPS), a *time-gate generator* (TGG) with a fast counter (not shown in Fig. 1) and FIFO memory blocks. The internal clock signal (350 MHz) which supplies the DPS module is synthesized by a built-in XC4VFX12 structure of the *digital clock manager* (DCM) blocks [28]. Its parameters determine the internal structure of DPS module (*i.e.* the required number of delay cells). At its output, the high-resolution DPS module produces the reference clock signal CLK_REF. This signal is synchronized with the rising edge of trigger pulse and provides the time base of the measurement system. Thus, it is responsible for the precise control of activation time of the time-gates. In this way, the CC system gained a functionality of fast synchronization with the incoming trigger pulses.

In Fig. 1, there is presented a two-channel CC meter containing eight programmable time-gates in each channel. The digital time-gate parameters (*i.e.* the delay and width of gate) are stored into the CU by a PowerPC processor, through the processor local bus interface. The PowerPC processor can modify this information at the beginning of the measuring process. The above time-gate parameters remain unchanged during an ongoing single measurement cycle. Each of the measurement cycles is triggered by the signal from the pulse laser. The signal which stores the collected data into FIFO memory is produced on the basis of internal flags (not shown in Fig. 1) delivered by the time-gate generator module which confirms closing a respective group of time-gates. The same signal (delayed in time) erases the information collected from the time-gates and resets the time-gate generator. The next step of data processing is executed by the PowerPC processor [29]. Such a peculiarly constructed CC system enables precise collection of information about incoming photons and their coincidences using for this purpose various types of excitation sources (limited by the construction of FLD).

3. Digital phase synchronizer module

The resolution of gated counting systems is limited mainly by the instability of the reference clock signal and the effect of lack of synchronization with the trigger pulse. These two factors have a significant impact on the form of *effective gate function* (EGF). The EGF describes the probability of wrong allocation of the input pulses in respective time-gates. In a general case, the EGF is a result of convolution of the Gaussian probability density function (describing instability of the main clock source) and the ideal gate function. In the case of CC system, when the measuring system is synchronized with the excitation source, we also observe an additional problem of compensation of the time interval between the real trigger pulse position and the beginning of digital time-gate. This synchronization error (described by a random variable) has a uniform distribution Θ_{CLK} of probability and significantly modifies the time-gate function. In consequence, the time-gate width increases, but the time resolution of CC system is reduced. The main purpose of the phase synchronizer module implementation is minimizing the synchronization error.

3.1. Circuit description

A block diagram of high-resolution DPS is shown in Fig. 2. The DPS architecture consists of two high-resolution *delay lines* (DL) [30–34]. One of them is used to the construction of a PDM, while the second one has been implemented in a DSM. The CLK signal has been connected to both modules. The PDM module is used for fast phase measurement of the standard clock CLK signal. Therefore, the propagation time of delay elements in the PDM module must be equal to the standard clock period (T_{CLK}). The information stored in the PDM module ($\psi_0, \psi_1, \dots, \psi_{N-1}$) is represented by a pseudo-thermometric code. In this way, the *phase decoder* (PD) module provides detection of the first rising edge of clock signal. On this basis, there is calculated the number of delay elements which are used in DSM module to perform the synchronization process.

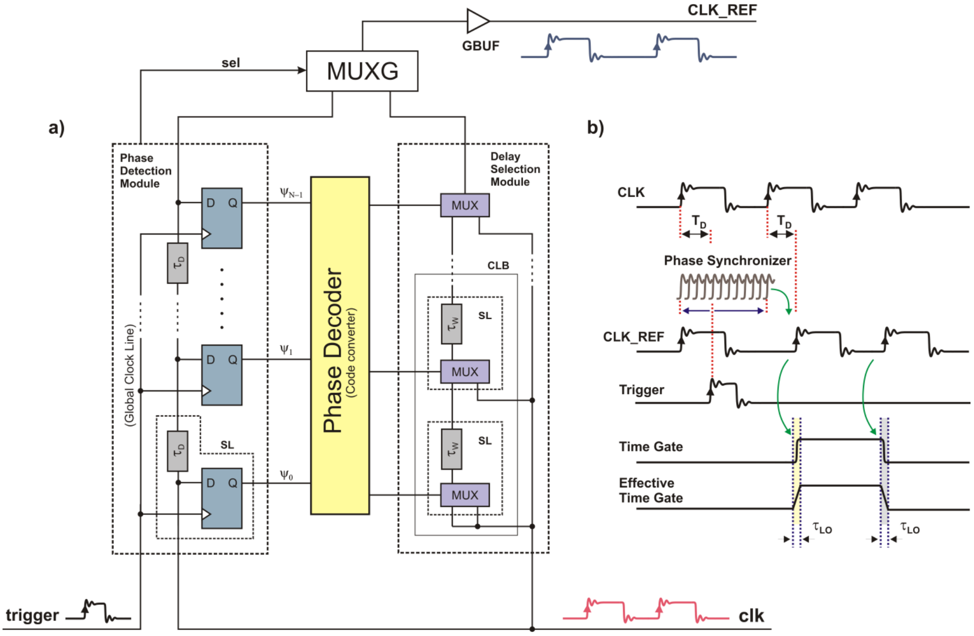

Fig. 2. The Digital Phase Synchronizer module: a block diagram (a); the principle of operation (b).

The synchronization process can be performed by successive delaying of the clock signal through an appropriate number of delay elements (built in the CLB blocks). The correct number of delay elements is determined by the *carry chain multiplexers* (MUXCY). For the ideal DPS module, the time characteristics of DL for both PDM and DSM modules have the same parameters. Hence, it would be possible to directly assign the relevant time channels in both modules. This solution provides a more simplified construction of the PD block. The main task of PD is converting the data from a pseudo-thermometric to one-of-M code, as follows: $n\tau_D = (M-n)\tau_W$. Such a solution makes possible activation of only one of the MUX elements at a given moment. Unfortunately, in a real situation, the time characteristics of PDM and DSM blocks are different. They are the main source of synchronization errors in the DPS module.

3.2. Delay line implementation

The modern FPGAs provide an array of fast *configurable logic blocks* (CLB) which component logic resources are characterized by very short propagation times. Each of CLB elements contains four *slices* (SL) which are grouped into two pairs (of two SLs each). Fig. 2 shows only part of two pairs of SLs. One pair is used for the construction of PDM, while the second pair − for DSM. They provide the ability of implementing high-resolution DLs in the FPGA structures. In our case, the DLs applied to the construction of DPS are made by using logical elements placed inside SL (such as *xor* gates or carry chain multiplexers) and fast carry chain interconnections. To decrease a dead time (the minimum time between two measurements) and to adapt to work with high-frequency excitation sources we decided to use a direct coding delay line in the PDM module. The time parameters were measured for both DLs by a statistical test method [35]. The results are shown in Fig. 3.

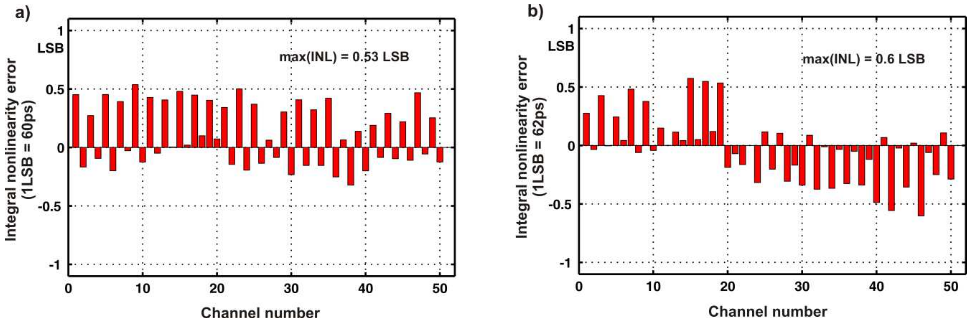

Fig. 3. The *integral nonlinearity characteristics* (INL): the phase detection module (a); the delay selection module (b).

In the experiment, a standard clock generator of frequency F_D = 100 MHz was used. This element was an integral part of the ML403 evaluation board [36]. The standard clock signal has been delivered to the DLs' inputs. The clock phase was measured by a DF1650B function generator of frequency 1.832 MHz. In order to obtain the DLs' characteristics, six series of 135 thousand measurements were performed for both lines. From the above results, an average delay of each DL was calculated. In our case, the average delay of PDM module is equal to 60 ps, whereas for the DSM module it is equal to 62 ps. Based on these parameters, the number of delay elements in the PDM module could be determined. The calculated value (in relation to the standard clock period) was 48. Using the average DL values, the INL and DNL characteristics were calculated [37]. The maximal nonlinearity deviation for both cases did not exceed the value of 1 LSB.

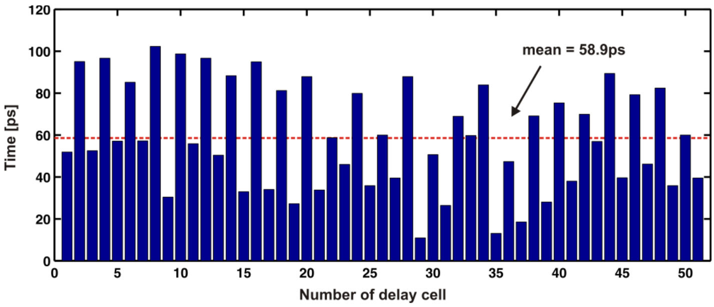

Fig. 4. The time deviation of the reference clock signal on an appropriate multiplexer's input.

The clock signal has been delivered to the DSM module by − dedicated to such purposes − the global clock connections. Such a signal distribution guarantees small time deviations of other CLB connections. The time deviations of CLK distribution to appropriate inputs of MUX elements in DSM were calculated by an optical direct method [38]. The optical method enables to measure deviations of clock distribution (in the DSM module) with a 0.34 ps resolution. The results are presented in Fig. 4. The mean value of differences between the propagation times to each of the MUX components is equal to 58.9 ps. Moreover, it should be noted that using accessible commercial devices does not enable such precise measurements as those possible with the mentioned above optical delay line.

The obtained data will be used in Subsection 3.3 to identify and interpret the decisive factors which may affect the level of synchronization errors.

3.3. DPS simulation

The main sources of errors in CC systems are the internal clock source instability and the imperfect synchronization of the CC system with the excitation source. For this purpose, a short analysis of the CC system (whose resolution has been determined by the CLK period) is presented. The following section shows also the simulation results of the DPS module.

a) Influence of the clock time parameters on determining the time-gate activation time.
The internal clock is synthesized by the built-in DCM blocks. The digital DCM's frequency synthesizer FX outputs drive the global clock routing network in the Virtex4 device. Such a distribution minimizes the clock skew due to the differences in distance. To obtain some essential information about the level of synchronization error and to prepare a DPS simulation model, a separate measurement of the DCM's clock jitter parameters had to be done. The jitter parameters have been measured directly at the XC4VFX12 outputs by a digital oscilloscope. For this measurement, a *Jitter and Timing Analysis* (JTA) toolkit has been used. The measured results are shown in Fig. 5a. In the CC system, each of time-gates have been activated after a specified time interval Δt_N, determined by the internal clock parameters. In our experiment, the measurement was performed for specified numbers N of clock cycles, which values depend mainly on the FLD configuration. Therefore, the photons separately propagated through three main fiber-loop ways (shown in Fig. 1), could be measured by three out of eight available time-gates. For this reason, the selected time-gates have been activated after 35, 70 and 140 clock cycles.

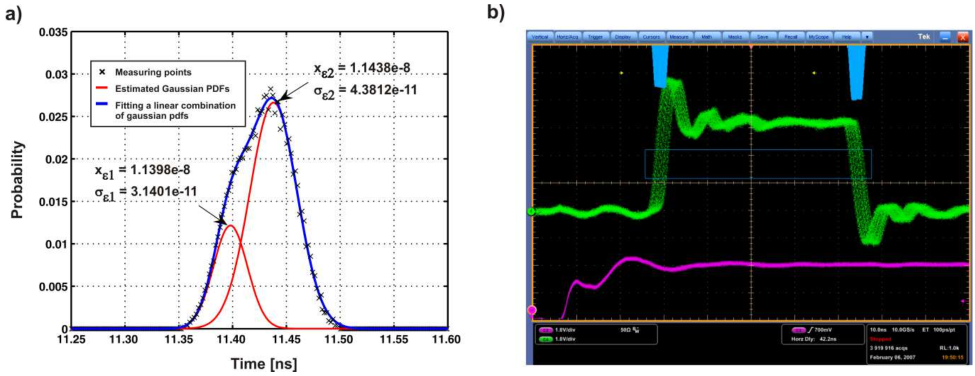

Fig. 5. The experimental results of: the reference clock's phase fluctuations (the signal generated by the DCM module) (a); the time-gate fluctuations (obtained by a Tektronix DPO7054 digital oscilloscope) without the phase synchronizer module (b).

The observed DCM's clock fluctuations are the consequence of a specific DLL block construction. The DLL is an internal part of DCM block and has been used for completion of the digital frequency synthesis process. The obtained results indicate a determined character of phase fluctuations. This deviation (about 40 ps) corresponds to a DL line resolution that was used to build a DCM block.

A simple model of CC system used to determine the time-gate activation time was prepared below. In such a case, the time interval Δt_N responsible for the time-gate activation can be described by a random variable ε in the following way:

$$\Delta t_N = NT_{CLK} + \sum_{n=1}^{N} \varepsilon_n , \tag{1}$$

where: ε – is a deviation from the average value of reference clock period; N – the number of clock cycles for determination of a specified time interval; T_{CLK} – a reference clock period. For the standard clock, the phase fluctuations have a normal distribution. Therefore, the probability density function $\varphi(\varepsilon)$ of the random variable ε is described by:

$$\varphi(\varepsilon) = \frac{1}{\sigma_\varepsilon \sqrt{2\pi}} \exp\left\{ -\frac{(\varepsilon - x_\varepsilon)^2}{2\sigma_\varepsilon^2} \right\}, \tag{2}$$

where: x_ε is an average value of ε; σ_ε^2 is variance of the random variable ε.

In our case, the phase fluctuations are determined by the DCM construction and depend on its DL parameters. Thus, the probability density function $\varphi(\varepsilon)$ is approximated by the sum of two Gaussian probability density functions.

Using the above assumption, the PDF of Δt_N variable can be described as:

$$\varphi(\Delta t_N) = \frac{1}{\sigma_{\Delta t_N} \sqrt{2\pi}} \exp\left\{ -\frac{(\Delta t_N - NT_{CLK})^2}{2\sigma_{\Delta t_N}^2} \right\}, \tag{3}$$

where: $\sigma_{\Delta t_N}^2$ is variance of the random Δt_N variable.

Knowing the $\varphi(\varepsilon)$ function parameters, a model of real clock signal will be prepared in Subsection 3.3c.

b) Synchronization of the CC system with the trigger pulse position.

In practice, the time-gate activation process consists of two parameters, where the first parameter is the number N of a standard clock period, while the second one is the index P of a quantization step. The required number N of a standard clock period is obtained directly by the fast counter (not shown in Fig. 1) for every time-gate. For the simulation purposes, it can be calculated as the integer value of the result of dividing the Δt_N interval by the standard clock period value. The precision of time-gate settings depends on the resolution of DL which have been implemented in the TGG module (not presented in this paper).

According to the previous considerations, there are two main factors that determine the level of time-gate activation error: the standard clock instability (measured in Subsection 3.3a) and the trigger pulse synchronization in relation to the time base of CC system. The synchronization error (described by the t_{SYNC} random variable) between the CC system and the trigger position depends on the standard clock period and has a major impact on the level of time-gate fluctuations in gated counting systems. Because any value of the time interval in a range of 0 to T_{CLK} has the same probability (equal to $1/T_{CLK}$), the PDF function of synchronization error may be described by a uniform distribution of probability Θ_{CLK}. Thus, the PDF of time-gate activation error can be expressed as:

$$\Gamma(\Delta t_N) = \Theta_{CLK}(t_{SYNC}) \otimes \varphi(\Delta t_N). \tag{4}$$

As stated in Section 1, the problem of compensating the time interval error between the trigger pulse position and the beginning of measuring cycle (*i.e.* the time-gate position) can be effectively solved by a fast and portable DPS module which is constructed from the most popular FPGA logic components. In order to ensure a short conversion time, the time interval quantization process is based on the direct time conversion method. The quantization error being a result of the quantization process in PDM, is proportional to the propagation times of appropriate delay cells. Therefore, we assumed that the distribution function of the quantization error Θ_{KW} has a uniform distribution, where the width parameter W_{KW} is equal to the average quantization step of PDM module. This is described by the following relation:

$$\Theta_{KW}(t) = W_{KW}{}^{-1} p, \quad where \quad p = \left(-0.5\, W_{KW} \le t \le 0.5\, W_{KW}\right). \tag{5}$$

The predicate p value is equal to one in the case when the relation $\left(-0.5\, W_{KW} \le t \le 0.5\, W_{KW}\right)$ holds. Otherwise, its value is equal to zero. An additional source of errors caused by the DPS module during the conversion process are different INL characteristics of both delay lines. The resulted errors are described by the $\Theta_{INL}(t_{INL})$ function which depends on the differences of the non-linearity errors of both DLs (ΔR_{INL}). In view of the fact that the random variable t_{INL} have a discrete nature we can postulate that the probability distribution function $\Theta_{INL}(t_{INL})$ may take the following form:

$$\Theta_{INL}(t) = \sum_{n=1}^{M} P(n)\delta\left(t - \Delta R_{INL}(n)\right), \tag{6}$$

where: $P(n)$ – is a likelihood of occurring an INL error with the ΔR_{INL} value (assigned to the n-th time channel); δ – the Dirac delta function. For simplicity, the $\Theta_{INL}(t_{INL})$ function has been approximated by a uniform distribution in a range of the minimum and maximum values of the $s = t - \Delta R_{INL}(n)$ parameter. Thus, the $\Theta_{SYNC}(t_{SYNC})$ function which describes the properties of synchronization process in the DPS module has been acquired by convolution of the $\Theta_{KW}(t_{KW})$ and $\Theta_{INL}(t_{INL})$ functions. The final form of the PDF of time-gate activation error may be written as:

$$\Gamma_{SYNC}(\Delta t_N) = \Theta_{SYNC}(t_{SYNC}) \otimes \varphi(\Delta t_N)\,. \tag{7}$$

c) The procedure of DPS simulation.

The following steps have been taken to obtain the DPS simulation:

- At the beginning, a model of real clock signal was prepared. For this purpose the von Neumann method [39] has been applied. Using this model, it was possible to produce a stimulus vector that successfully emulates the reference clock signal. The stimulus vector represents the next phases (not quantized) of the reference clock signal with a specified time period and imposed clock instability. In consequence of the above step, a wide spectrum of the clock's phase dispersion could be simulated. The results are shown in Fig. 6a. The generated data were then used to prepare a simulation process of the PDM and DSM modules.
- In the next step, the quantization process performed by the PDM module has been simulated. For this purpose, the real delay line characteristics (discussed in Subsection 3.2) and the model of real clock signal have been used. In such a situation, the widths of *quantization steps* (QSs) are equal to the propagation times of appropriate delay cells in the PDM. Therefore, for each QS, we have to determine its beginning t_D^B and end t_D^B. Based on the randomly generated clock's phases P_i we can calculate the quantized standard clock phase values (phase numbers) as the numbers n_i of QSs, $n \in [1, N]$, in which the generated phases P_i was accepted. This can be written in the following way: $t_{Dn_i}^B \le P_i < t_{Dn_i}^E$, $i \in [1, K]$, where K indicates the number of stimulus vector elements. Therefore, a phase number n represents the quantized standard clock phase value. In practice, this measured time interval corresponds to the sum of propagation times of delay elements $n\tau_D$, where n is the highest position of the flip-flop which is storing the high state at its output. The simulation result of PDM quantization process obtained by using the ideal DL characteristic (*i.e.* the propagation time of a related delay cell is equal to the average QS of PDM module) is presented in Fig. 6b.

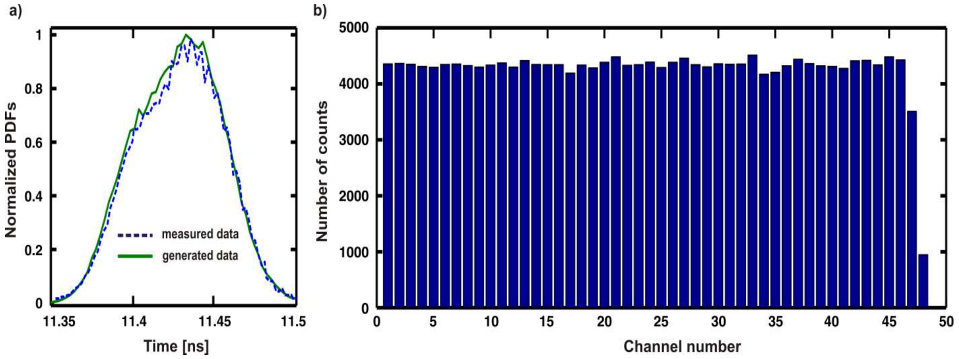

Fig. 6. The results of simulation: the normalized *probability density function* (PDF) of the reference clock phase fluctuations (a); the PDM module simulation (b).

- The number of delay line segments $M-n$ in the DSM module has been chosen on the basis of known above phase numbers. In this case, no nonlinearity correcting operations were applied.
- To verify the DSM module, the not quantized random Δt_N values calculated by the method described in Subsection 3.3a, have been generated. Considering the DL parameters specified in Subsection 3.2, *e.g*. the propagation times of delay elements (τ_W) and the propagation times of MUX elements (τ_{MUX}) in the DSM module, the corresponding time intervals $\sum_{i=M-n}^{M} \tau_W^i + \tau_{MUX}^{M-n}$ have been assigned to the previously generated data.

These proceedings have been used to validate the value of synchronization error between the measuring system and the observed physical process. The result of computer simulation is presented in Fig. 7. It is the result of generating a series of 50000 test vectors with appropriate phase numbers. The applied phase noise of reference clock signal has been presented as the distribution shown in Fig. 6a. For the collected data (obtained from the DPS model) we are fitting $\Gamma_{SYNC}^{M}(\Delta t_N)$ curve. The obtained uniform distribution fitting parameters are equal to W_{KW} = 60.4 ps and W_{INL} = 146.6 ps, respectively. Hence, we can conclude that the differences of the non-linearity errors of both lines used in the DPS construction have a significant influence on the level of time-gate fluctuations. The minimal variation value from the value achieved by the PDM module reached 4.7 ps, whereas its maximum value was equal to 159.7 ps. Thus, the average value was equal to 78 ps.

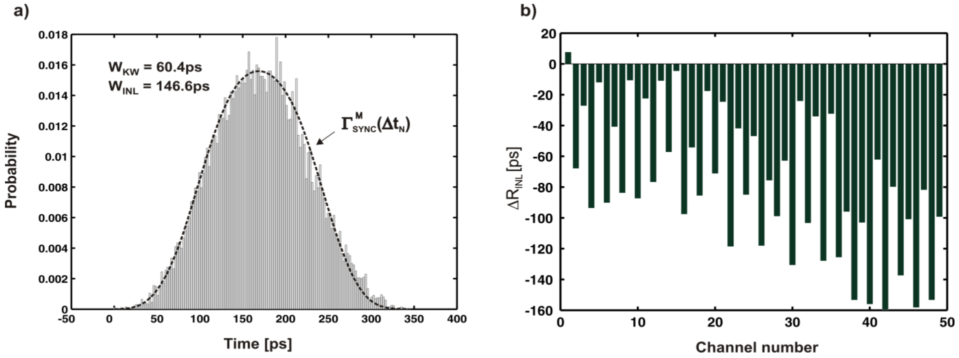

Fig. 7. The results of DPS module simulation (with the real DPS characteristics): the probability distribution of time-gate fluctuations (a); the synchronization errors (b).

The distribution parameters of Θ_{KW} and Θ_{INL} functions have been used to define the synchronization process accuracy. For this purpose, the expanded uncertainty has been estimated for the assumed confidence level of $\alpha = 0.997$, based on:

$$\sigma_{SYNC}(t) = W_{KW} + W_{INL} - 2\sqrt{(1-\alpha)W_{KW}W_{INL}}\,. \tag{8}$$

Based on the simulation results obtained from the DPS module, we can efficiently minimize the level of phase fluctuations of the time-gates from 2.857 ns to 196.7 ps. The same procedure in relation to the measurement data has been applied in Section 4.

4. Measurement results

The phase fluctuations of time-gates were measured using Tektronix DPO7054 and LeCroy LT374 digital oscilloscopes. Fluctuations of the time-gate activation time in relation to the triggering signal were measured. The tests were performed for both of the two cases: with and without the DPS module. The gates have been opened after the same time interval in relation to the excitation pulse. Therefore, the accumulated jitter for both cases (with and without the DPS module) has the same parameters.

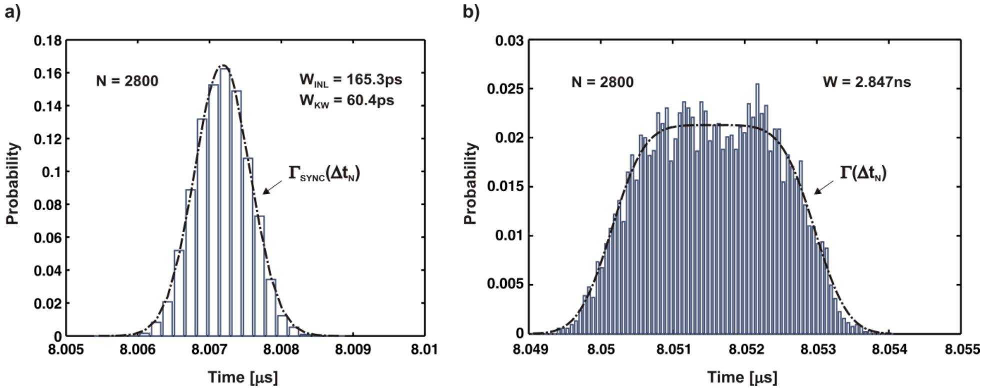

Fig. 8. The experimental results of time-gate fluctuations (LeCroy LT374).
The coincidence meter: using the DPS module (a); without the DPS module (b).

The results of measurements are presented in Fig. 8a and Fig. 8b. The convolutions of the Gaussian $\varphi(\Delta t_N)$ and either the Θ_{CLK} or Θ_{SYNC} distributions have been fitted to the obtained measurement results. For this purpose the *conv2* and *fminsearch* functions from MATLAB® toolkit have been used.

From the obtained measurement results it can be concluded that the DPS module effectively reduces fluctuations of the time-gate opening from 2.857 ns to 214.8 ps. In this way almost a fourteen-fold improvement has been obtained. The time-gate was being opened after 2800 clock cycles since the trigger event. Similar measurements were carried out also for another number of clock cycles while the accompanied changes of variations were observed.

In the case without a synchronization module, the width W of uniform distribution is equal to the T_{CLK} period of reference clock signal delivered from the DCM module. When the DPS module is used, then the fluctuation of time-gate opening is determined mainly by the INL errors. Additional noise created by the synchronization process is a result of the nonlinearity of real (non-linear) DL characteristics and the voltage and temperature fluctuations of the delay line. The last case may cause minor differences between the simulation and experimental results.

5. Conclusions

Further development of quantum enhanced technologies requires robust, cost effective and easy to configure high-speed electronics capable of processing information streams on the fly. We proposed a novel, fully synchronized gated counting system for processing signals from avalanche photodiodes as a solution for registering signals from photon number resolving detectors. Employing a high-resolution digital phase synchronizer module enables to synchronize the internal reference clock source with an external physical process (under research) and to suppress dark counts. Currently, the synchronization error has been reduced from 2.857 ns to 214.8 ps. This ensures almost a fourteen-fold improvement. The proposed DPS module can be operated with a wide spectrum (< 350 MHz) of excitation sources without deterioration of its metrological parameters. Also, it is characterized by an extremely low dead time that is equal to one clock cycle. Therefore, the implementation of the DPS module in a gated counting system and additional application of the Virtex4 XC4VFX12 resources enables to effectively collect complete information about the total number of photo-counts and the history of registered events. This enables to apply our device in the quantum cryptography and the systems diagnosing single photon sources.

Acknowledgements

We acknowledge the insightful discussions with K. Banaszek and W. Wasilewski and the ability to use the National Laboratory for Atomic, Molecular and Optical Physics.

References

[1] Wasilewski, W., Kolenderski, P., Frankowski, R. (2007). Spectral density matrix of a single photon measured. *Phys. Rev. Lett.*, 99, 123601.

[2] Gisin, N., Ribordy, G., Tittel, W., Zbinden, H. (2002). Quantum cryptography. *Reviews of Modern Physics*, 74(1), 145–195.

[3] Wu, L., Chen, Y. (2015). Three-Stage Quantum Cryptography Protocol under Collective-Rotation Noise. *Entropy*, 17(5), 2919–2931.

[4] Pirandola, S., Eisert, J., Weedbrook, Ch., Furusawa, A., Braunstein, S.L. (2015). Advances in Quantum Teleportation. *Nature Photonics*, 9, 641–652.

[5] Wasilewski, W., Radzewicz, Cz., Frankowski, R., Banaszek, K. (2008). Statistics of multiphoton events in spontaneous parametric down-conversion. *Phys. Rev. A*, 78, 033831.

[6] Achilles, D., Silberhorn, Ch., Sliwa, C., Banaszek, K., Walmsley, I.A. (2003). Fiber-assisted detection with photon number resolution. *Optics Letters*, 28(23), 2387–2389.

[7] Zieliński, M., Karasek, K., Płóciennik, P., Dygdała, R. (1996). Digital Gated Single-Particle Counting Systems, design and applications. *Metrologia i Systemy Pomiarowe*, 3(3–4), 199–211.

[8] Simms, P.C. (1961). Fast coincidence system based on a transistorized time-to-amplitude converter. *Rev. Sci. Instrum.*, 32(8), 894–898.

[9] Gaertner, S., Weinfurter, H., Kurtsiefer, C. (2005). Fast and compact multichannel photon coincidence unit for quantum information processing. *Rev. Sci. Instrum.*, 76, 123108.

[10] Frankowski, R., Wasilewski, W., Kowalski, M., Zieliński, M. (2008). High resolution two channel Box-Car system implemented in single FPGA structure Virtex4 for apply in quantum physics. *Elektronika*, 49(5), 21–23.

[11] Zhu, F., Hsieh, S.C., Yen, W.W., Chou, H.P. (2011). A digital coincidence measurement system using FPGA techniques. *Nuclear Instruments and Methods in Physics Research Section A*, 652(1), 454–457.

[12] Antonioli, S., Miari, L., Cuccato, A., Crotti, M., Rech, I., Ghioni, M. (2013). 8-Channel acquisition system for Time-Correlated Single-Photon Counting. *Rev. Sci. Instrum.*, 84, 064705.

[13] Park, B.K., Kim, Y.S., Kwon, O., Han, S.W., Moon, S. (2015). High-performance reconfigurable coincidence counting unit based on a field programmable gate array. *Applied Optics*, 54(15), 4727–4731.

[14] Zieliński, M., Kowalski, M., Frankowski, R., Chaberski, D., Grzelak, S., Wydźgowski, L. (2009). Accumulated jitter measurement of standard clock oscillators. *Metrol. Meas. Syst.*, 16(2), 259–266.

[15] Zieliński, M. (2000). Digital Gated Single-Particle Counting System, The Errors Analysis. *IEEE Trans. on Instrum. and Measurement.*, 49(5), 1069–1076.

[16] Tonietto, R., Zuffetti, E., Castello, R., Bietti, I. (2006). A 3MHz Bandwidth Low Noise RF All Digital PLL with 12ps Resolution Time to Digital Converter. *Solid-State Circuits Conference*, ESSCIRC, 150–153.

[17] Santos, D.M., Dow, S.F., Flasck, J.M., Levi, M.E. (1996). A CMOS Delay Locked Loop and Sub-Nanosecond Time-to-Digital Converter Chip. *IEEE Transactions on Nuclear Science*, 43(3), 289–291.

[18] Derogarian, F., Canas, J., Grade, V.M. (2014). A Time Synchronization Circuit with an Average 4.6 ns One-Hop Skew for Wired Wearable Networks. *17th Euromicro Conference on Digital System Design (DSD 2014)*, 146–153.

[19] Buevich, M., Rajagopal, N., Rowe, A. (2014). Hardware Assisted Clock Synchronization for Real-Time Sensor Networks. *Real-Time Systems Symposium (RTSS)*, 268–277.

[20] Chu, D.C. (1978). The triggered phase-locked oscillator. *Hewlett-Packard J.*, 8–9.

[21] Dudek, P., Szczepański, S., Hatfield, J.H. (2000). A high-resolution CMOS time-to-digital converter utilizing a Vernier delay line. *IEEE Trans. Solid-State Circuits*, 35(2), 240–247.

[22] Johnson, M.G., Hudson, E.L. (1988). A Variable Delay Line PLL for CPU – Coprocessor Synchronization. *IEEE Journal of Solid-State Circuits*, 23(5), 1218–1223.

[23] Kim, H., Kim, S.Y., Lee, K.Y. (2013). A low power small area cyclic time-to-digital converter in all-digital PLL for DVB-S2 application. *Journal of Semiconductor Technology and Science*, 13(2), 145–151.

[24] Szplet, R. (2009). Auto-tuned counter synchronization in FPGA-based interpolation time digitisers. *Electronics Letters*, 45(13), 671–672.

[25] Jansson, J.P., Mäntyniemi, A., Kostamovaara, J. (2009). Synchronization in a Multi-level CMOS Time-to-Digital Converter. *IEEE Transactions on Circuits and Systems*, 56(8), 1622–1634.

[26] Rehacek, J., Hradil, Z., Haderka, O., Perina, J. Jr., Hamar, M. (2003). Multiple-photon resolving fiber-loop detector. *Physical Review. A*, 67(6), 061801.

[27] Dygdała, R., Fuso, F., Arimondo, E., Zieliński, M. (1995). Modular digital box-car for applications in pulsed laser spectroscopy. *Rev. Sci. Instrum.*, 66(6), 3507–3512.

[28] Frankowski, R., Kowalski, M., Zieliński, M. (2011). The phase fluctuations of the clock signal generated in the digital frequency synthesis process. *Electrical Review*, 87(9a), 95–100.

[29] Product specification. (2006). Xilinx Corp. User Guide for EDK: ML40x EDK Processor Reference Design, UG082 (v5.0).

[30] Zieliński, M. (2009). Review of single-stage time-interval measurement modules implemented in FPGA devices. *Metrol. Meas. Syst.*, 16(4), 641–647.

[31] Wu, J. (2010). Several key issues on implementing delay line based TDCs using FPGAs. *IEEE Trans. Nucl. Sci.*, 57(3), 1543–1548.

[32] Szplet, R., Jachna, Z., Kwiatkowski, P., Rożyc, K. (2013). A 2.9 ps equivalent resolution interpolating time counter based on multiple independent coding lines. *Measurement Science and Technology*, 24(3), 35904–15.

[33] Chaberski, D. (2016). Time-to-digital-converter based on multiple-tapped-delay-line. *Measurement*, 89, 87–96.

[34] Frankowski, R., Gurski, M., Płóciennik, P. (2016). Optical methods of the delay cells characteristics measurements and their applications. *Optical and Quantum Electronics*, 48(3), 1–19.

[35] Mota, M., Christiansen, J. (1999). A high-resolution time interpolator based on a delay locked loop and an R-C delay line. *IEEE J. Solid State Circuits*, 34(10), 1360–1366.

[36] Product specification. (2006). Xilinx Corp. User Guide: ML401/ML402/ML403 Evaluation Platform, UG080 (v2.5).

[37] Cova, S., Bertolaccini, M. (1970). Differential linearity testing and precision calibration of multichannel time sorters. *Nuclear Instruments and Methods*, 77(2), 269–276.

[38] Frankowski, R., Chaberski, D., Kowalski, M. (2015). An optical method for the time-to-digital converters characterization. *Proc. IEEE ICTON 2015*, Budapest, Hungary, paper We.P.14, 1–4.

[39] Forsythe, G.E. (1972). Von Neumann's Comparison Method for Random Sampling from the Normal and Other Distributions. *Mathematics of Computation*, 26(120), 817–826.

www.czasopisma.pan.pl PAN www.journals.pan.pl

Metrol. Meas. Syst., Vol. 24 (2017), No. 3, pp. 551–562.

METROLOGY AND MEASUREMENT SYSTEMS

Index 330930, ISSN 0860-8229

www.metrology.pg.gda.pl

AN ENHANCED RUN-LENGTH ENCODING COMPRESSION METHOD FOR TELEMETRY DATA

Yanhu Shan[1,2], Yongfeng Ren[1,2], Guoyong Zhen[1,2], Kaiqun Wang[3]

1) North University of China, National Key Laboratory For Electronic Measurement Technology, Taiyuan 030051, China (✉ shanyanhu@nuc.edu.cn, +86 351 392 3640)
2) North University of China, Key Laboratory of Instrumentation Science & Dynamic Measurement, Ministry of Education, Taiyuan 030051, China (renyongfeng@nuc.edu.cn, zengguoyong@nuc.edu.cn)
3) Taiyuan University of Technology, College of Mechanics, Taiyuan 030024, China (wangkaiqun@tyut.edu.cn)

Abstract

The telemetry data are essential in evaluating the performance of aircraft and diagnosing its failures. This work combines the oversampling technology with the run-length encoding compression algorithm with an error factor to further enhance the compression performance of telemetry data in a multichannel acquisition system. Compression of telemetry data is carried out with the use of FPGAs. In the experiments there are used pulse signals and vibration signals. The proposed method is compared with two existing methods. The experimental results indicate that the compression ratio, precision, and distortion degree of the telemetry data are improved significantly compared with those obtained by the existing methods. The implementation and measurement of the proposed telemetry data compression method show its effectiveness when used in a high-precision high-capacity multichannel acquisition system.

Keywords: multichannel acquisition system, high compression performance, run-length encoding with error parameter, oversampling, hardware implementation.

1. Introduction

A telemetry testing system is used to evaluate the performance of aircraft and to diagnose failures by detecting the aircraft responses to different input sensor signals in flight experiments. The testing signals are either transmitted to the ground test station by a wireless information channel of the telemetry system or stored in a recorder whose contents will be recycled after the experiment. A highly efficient information channel transmission and telemetry data storage are essential because of an increasing quantity of testing data and their types, as well as high real-time testing requirements [1–3]. The compression of telemetry data will be further used to optimize the bandwidth usage rate of signal channels and storage space.

Many data compression techniques have been employed in the transmission and storage of telemetry data. The most known compression methods include: the *run-length encoding* (RLE), Huffman encoding, Golomb-Rice encoding, *Lempel-Ziv-Welch* (LZW), and wavelet compression [4–7]. The telemetry data are obtained from sensors in a form of text, images, video, audio, and many other formats. Heterogeneous types of telemetry data may need various applications of data compression techniques [8]. Maluf *et al.* combined *discrete Fourier transforms* (DFTs) with LZW and Flate algorithms for textual data and JPEG coding for images [8]. Two almost lossless data compression algorithms were proposed for the telemetry data produced by hyperspectral sensors installed on a satellite [9]. The telemetry video signals of the surface of Mars are compressed with a compression ratio of 24:1 and then transmitted from the Mars to the Earth by USA Mars Exploration Rovers [10]. A two-stage Lempel-Ziv lossless data compression is implemented for the telemetry data from various sensors aboard satellite launch

---

Article history: received on Jul. 22, 2016; accepted on Feb. 26, 2017; available online on Sep. 01, 2017; DOI: 10.1515/mms-2017-0039.

vehicles [11]. A modified Rice compression method is adopted to the telemetry data of a launch vehicle with a compression ratio of 2:1 [12]. Combining multiple data compression algorithms facilitates obtaining a high compression ratio [13–15]. Furthermore, proper hardware implementation of data compression is essential in enhancing the performance of data compression [16, 17]. Kao *et al.* developed a modularized approach to trade off the hardware cost and an achievable compression ratio [18]. Lin *et al.* proposed a two-stage hardware architecture to improve compression and decompression rates [4].

The precision, distortion degree, and compression ratio of the telemetry data should be considered. The ideal condition is one with a high compression ratio, high data precision, and no signal distortion. For practical engineering applications, specific values of these parameters should be adjusted to a specific requirement. The compression distortion degree is generally set to less than 0.1% for engineering applications. A range of compression ratio of the telemetry data in the previous research is from 1.38 to 42 [9, 19, 20]. The data precision is larger than 8 bits.

Despite the progress in data compression studies, the telemetry data compression used in telemetry acquisition systems has not been sufficiently examined yet. Firstly, given large amounts of the telemetry data and high real-time testing requirements, a data compression method ensuring a high compression ratio is required. Secondly, an effective hardware implementation approach to the data compression method is needed for a real multichannel acquisition system. Many compression methods can obtain a high compression ratio by employing a complex hardware support, such as DSP and FPGA groups or a dedicated compressor [21, 22]. However, these types of hardware implementation are unsuitable for some telemetry engineering applications because of their high cost and complex design. Thirdly, the telemetry signals collected by a telemetry system operating with high sampling rates include interference signals mixed with useful signals because of the harsh environment. So, telemetry signal noise has a negative effect on the data compression ratio.

To address the aforementioned challenges, we propose an effective data compression method based on a combination of the oversampling technology and the RLE compression algorithm with an error factor . In the study there are considered mainly the telemetry data. The proposed approach consists of three modularized phases: 1) oversampling and normal averaging; 2) data encoding based on RLE with an error factor; and 3) two-stage framing. The hardware implementation of the modularized compression method for the telemetry data employs FPGAs. The proposed data compression method used in a telemetry testing system demonstrates the following unique advantages in comparison with the existing data compression methods.

Firstly, the proposed method exhibits a high performance in handling the telemetry data. The previous work enhanced a compression ratio by increasing the error parameter [23]. However, it resulted in a significant increase of a signal distortion and a significant reduction of the acquisition system precision. To address this issue, our approach considers all three factors by incorporating the oversampling technology into the RLE algorithm with a compressibility error. The proposed method achieves a high compression ratio and improves accuracy of the telemetry data for a small error parameter value with a low signal distortion. The proposed method can be also effectively applied to high-precision multichannel acquisition systems.

Secondly, the hardware implementation of the proposed compression method is based on FPGAs. Compressing large amounts of the telemetry data, especially high-precision data, is not feasible without a proper hardware support [24]. However, an effective hardware implementation for telemetry data compression is still unavailable. In our approach, the data compression method employs FPGAs to achieve modularized compression in a multichannel acquisition system. The developed hardware implementation is suitable for the telemetry data because of its low cost and simple design.

2. Design and implementation of telemetry data compression method

The telemetry data used in our study mainly come from various types of sensor signals in aircraft. The telemetry data come in a form of text, images, video, audio, and many other formats. In our work, there is considered mainly the compression method for numerical data, and the telemetry data are transformed into a digital form. Digital signals from each channel of the sensor network in a multichannel telemetry acquisition system are assembled in a frame processor by a quantization processor. The signals are later transmitted to a transmitter or storage system through a sending processor being a unit of the frame processor. This process demonstrates a typical transmission path of the telemetry signals. However, the telemetry signals collected by the telemetry system operating with high sampling rates consist of useful signals mixed with interference signals. The signals are preprocessed before compression to minimize a negative effect of noise on data compression. To this purpose, an improved approach is proposed, which consists of three modularized phases: 1) oversampling and normal averaging of the telemetry data; 2) data compression based on RLE with an error parameter; and 3) two-stage framing. The improved transmission path is shown in Fig. 1.

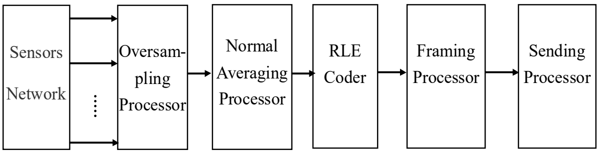

Fig. 1. Transmission patch of the telemetry signal.

2.1. Telemetry data pre-processing

To reduce the negative effect of noise on data compression, the telemetry data are preprocessed using oversampling and averaging technologies before data compression. The oversampling prevents aliasing, improves resolution, and reduces noise. Sampling of telemetry signals is based on the Nyquist theory. An anti-aliasing filter is commonly adopted in the acquisition circuit to significantly inhibit signal aliasing. However, full elimination of aliasing by using a practical filter is difficult. The oversampling technology could further improve the effectiveness of inhibition of signal aliasing according to the principle of Nyquist theory. Moreover, the oversampling has a significant influence on the baseband quantization noise when the ADC noise could be approximated as white noise [25–27]. An oversampling frequency f_{OS} of each channel and an oversampling factor β are defined as follows:

$$f_{OS} = \beta f_{NS}, \tag{1}$$

where f_{NS} is an original sampling frequency.

$$\beta = 4^{w}, \tag{2}$$

where w is the number of additional bits of a desired resolution.

A quantization noise power Q_{OS} is expressed as:

$$Q_{OS} = \frac{Q_N \times f_{NS}}{f_{OS}}. \tag{3}$$

Equation (1) is substituted into (3) to obtain the quantization noise power at the oversampling frequency:

$$Q_{OS} = \frac{q^2 \times f_{NS}}{12(\beta f_{NS})} = \frac{Q_N}{\beta}. \tag{4}$$

Therefore, the *signal-to-quantization-noise ratio* (SQNR) is further enhanced:

$$SQNR = \frac{Q_{signal}}{Q_{OS}}. \tag{5}$$

We assume that N is the number of bits without oversampling. Therefore, in our proposed approach, the resolution is equal to the effective number of bits ($N + w$). We can find that oversampling reduces the quantization noise power and hence increases the resolution of an N-bit ADC and improves SQNR.

The total sampling frequency of the system, f_t, is determined by the oversampling frequency f_{OS} of every input signal and the number m of input channels in the acquisition system, and is denoted as follows:

$$m \times f_{OS} \leq f_t. \tag{6}$$

The working mode of ADC module is controlled by FPGA by adjusting the total sampling frequency of the system.

The oversampled data are averaged according to the following procedure. To reduce the complexity of sample logic, four nodes (*e.g.* $A(t_0)$, $A(t_1)$, $A(t_2)$, and $A(t_3)$) are sampled in one sampling cycle. The four sampling points are averaged by the averaging processor to reduce the negative effect of noise on data compression. The averaged data $A(T_1)$ are written into the compression register of a current channel. This procedure is repeated until the signals of all channels are processed. All averaged data (*e.g.* $A(T_1)$, $A(T_2)$, ... , $A(T_n)$) of the corresponding channels are later compressed. A schematic of sampling and averaging is shown in Fig. 2. The interference signals are highly suppressed by the oversampling and averaging processes, which enable to obtain a high compression ratio.

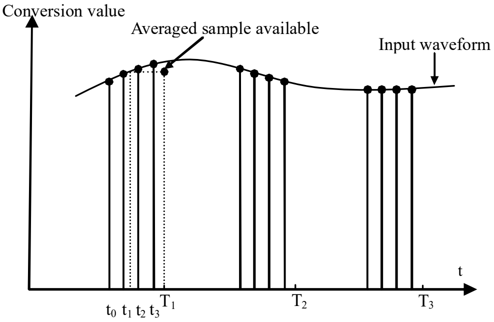

Fig. 2. Sampling and averaging process.

2.2. Data encoding based on RLE with error factor

The RLE algorithm is suitable for compressing binary sequences [28]. Therefore, the RLE algorithm is adopted to directly compress signals from each channel of the multichannel acquisition system. The amplitude of all telemetry data are adjusted into the same allowable amplitude range of ADC by a signal adjustment circuit. Subsequently, the adjusted data are transformed into the corresponding quantized data according to bits of ADC. The error parameter is incorporated into the RLE algorithm to increase the compression efficiency. The error bound is related with these quantized data and is set to a specific value on the basis of the distortion tolerance. The differences between adjacent quantized data are compared with the error bound. These quantized data are regarded as being of the same value if their difference is smaller than the error bound; otherwise they are of different values. Therefore, the error bound is irrelevant to the input analog signals, whether they are preprocessed or not.

In our multichannel acquisition system, the resolution of AD converter was set to 16 bits. The data formats are shown in Table 1. The highest bit, D15, is defined as a logic number (one or zero) to distinguish the quantization data from the run length. Thus, D14 to D0 denote the AD quantization data if D15 is equal to one; otherwise, they denote the run length. The averaged data were compressed based on the run-length compression with an error parameter. A flow chart of the compression algorithm process is shown in Fig. 3. Taking channel one as an example, the previous data and the current data were first allocated to the initial values of registers D0 and D1. Secondly, D1 can be replaced by D0 and Nt adds one if D1 is in an interval of [D0–Δ, D0+Δ], and the current and next data are assigned to D0 and D1, respectively; otherwise, Nt is reset to zero. Thirdly, the difference between D0 and D1 in the subsequent time period is further compared with Δ. To prevent the count of run length to be too long to disorder the data structure, the run length is automatically reset after adding to a particular value (*e.g.* 32767 for a 15-bit run length), and the aforementioned 3-step procedure is then repeated until the sampling is completed. The data of each channel can be compressed in parallel by using the above mentioned procedure.

Table 1. Telemetry data format.

D15	D14 ~ D0
1	AD quantized data
0	Run length (0 to 32767)

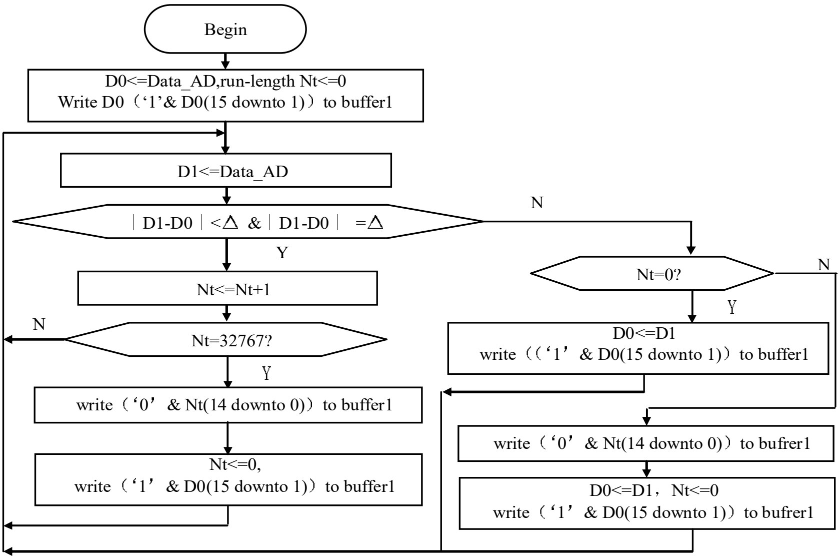

Fig. 3. Flow chart of run-length compression.

2.3. Two-stage framing

For the multichannel signals of sensor networks, the correlation of data between adjacent channels was neglected because the oversampling processor was set to the sampling polling mode. A data packet was designed to improve the compression method (Fig. 4). In Fig. 4, CHMN denotes the quantization data of a corresponding channel, CH_NUM is the number of channels, RCx is the row count, FCx is the frame count, RSYNx is the row synchronous word, and FSYNx is the frame synchronization word. The data packet is divided into two stages. On the first level, the sampled data of each channel are compressed and packed into small data packets called sub-frames. Each sub-frame contains labelling, a synchronous word, and a channel number and corresponds to one channel, thereby ensuring that all data in the same channel are stored in a sub-frame. Each channel contains one cache, which is used to store the compressed data of a current channel. The total of 16 sub-frames correspond to 16 channels. Therefore, the designed structure can effectively distribute data with high relevance, thereby enhancing the data compression ratio. The data structure is shown in Table 2. RSYNx of the sub-frame is "EB 90". FSYNx of the sub-frame is "14 6F". On the second level, the sub-frames are repacked into a new data packet called a prime frame, in which the frame count and frame labelling of every sub-frame are included. When the size of data stored in this cache equals the size of the sub-frame, these data are read out and then written into a buffer. In the buffer, a frame sign, a channel number, and a time count are all included in the new data packet with the prime-frame format (Table 3). The frame sign is the beginning of a data frame, and it is used to distinguish between different data frames. The time count labels the time of current data framing and is often regarded as the frame count.

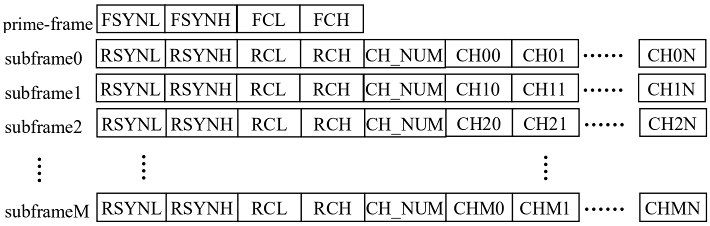

prime-frame	FSYNL	FSYNH	FCL	FCH					
subframe0	RSYNL	RSYNH	RCL	RCH	CH_NUM	CH00	CH01	……	CH0N
subframe1	RSYNL	RSYNH	RCL	RCH	CH_NUM	CH10	CH11	……	CH1N
subframe2	RSYNL	RSYNH	RCL	RCH	CH_NUM	CH20	CH21	……	CH2N
⋮	⋮						⋮		
subframeM	RSYNL	RSYNH	RCL	RCH	CH_NUM	CHM0	CHM1	……	CHMN

Fig. 4. The two-stage framing format.

Table. 2. The subframe format.

Data 0	Data 1	Data 2	Data 3	Data 4	Data 5 to Data 511
EB	90	RCL	RCH	CH_NUM	Data

Table 3. The prime-frame format.

Data 0	Data 1	Data 2	Data 3	Data 4 to Data 8195
14	6F	FCL	FCH	Data

2.4. Hardware implementation of telemetry data compression

The acquisition and compression of telemetry data were performed in the multichannel acquisition system, as shown in Fig. 5. The system consists of an input interface, a signal adjustment circuit, an input voltage follower, an analog *multiplexer* (MUX), an output voltage follower, an A/D converter, a data buffer, and an FPGA. The test data are transmitted through the interface to a signal adjustment module in which the amplitudes of signal are adjusted and high-frequent noise is filtered. Under the control of FPGA, the adjusted signals of specified channels are output through the voltage follower circuit and the multi-channel analogue switch successively and then are converted by the ADC module. Finally, the compression process of test data is implemented in FPGA. The whole internal logic procedure of FPGA is shown in Fig. 6. The telemetry data are oversampled and transmitted into the A/D converter. Then, the arithmetic average in the internal logic of FPGA is implemented to approximate the oversampled data to the actual signal value to achieve reduction of disturbance and error. This part of the internal function of FPGA is called an oversampled filter. Next, the data are compressed using the RLE encoding and stored in corresponding buffers. Finally, the data are packed and written into FIFO, ready for output by sending to the data logic module.

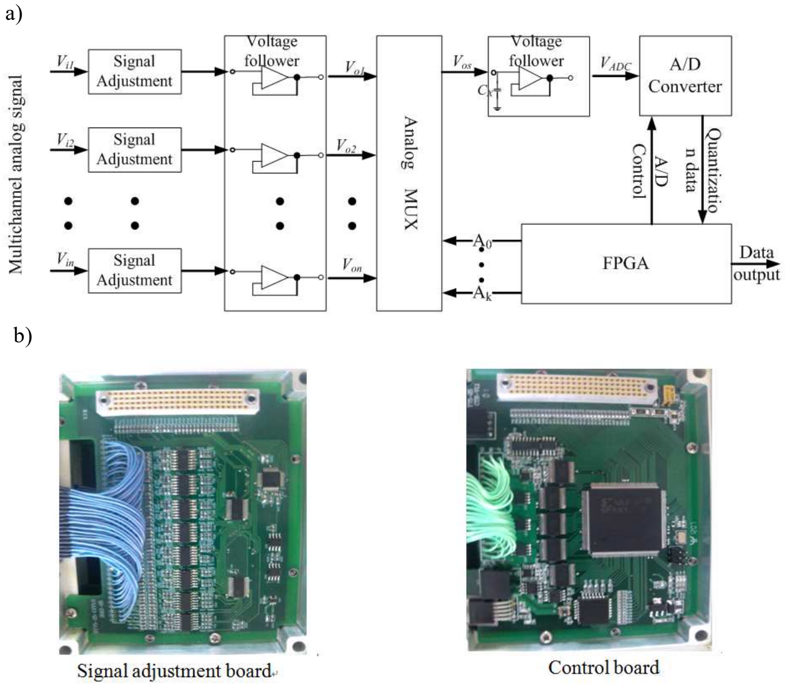

Fig. 5. A schematic (a) and hardware circuits of the multichannel acquisition system (b).

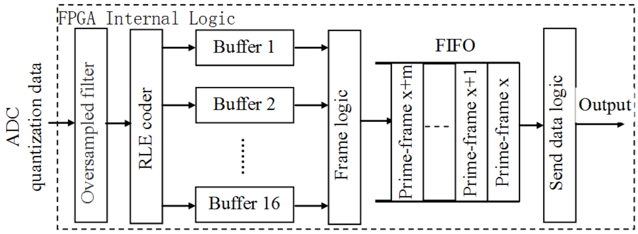

Fig. 6. The internal logic of FPGA.

The proposed approach can achieve the real-time compression of the sampled data. The whole process adopts a pipeline mode. First, the oversampled data are averaged. The data from each channel are then classified based on their frame sign. Then, they are compressed via the run-length encoding method in parallel. Finally, the data of each channel are written into a buffer as a format of the sub-frame. Therefore, the proposed compression method does not cause latency.

3. Measurement results

The test telemetry signals used in our study consist mainly of pulse signals and vibration signals collected by shock sensors and vibration sensors throughout repeated measurements, respectively. The method mentioned in [23] and the popular WinRAR method were used as the control groups. Two multichannel acquisition systems with the same structure were used to sample the same signals simultaneously to evaluate the performance of a proposed compression method in terms of compression ratio, distortion degree, and system precision. The proposed compression method was implemented in one acquisition system, and the data compression method mentioned in [23] was implemented in the other system. The sampling frequency was 12 kHz, and the oversampling frequency was 48 kHz. The sampled data were read and decompressed by a home-built PC application software. The data were extracted based on the frame format for each channel. All data were then restored if they were not run-length based on the highest bit of the data. The sizes of the telemetry data after compression at different error parameter Δ values were measured. The compression ratio and distortion degree of the telemetry data and the precision of the acquisition system for these two types of compression method were calculated using the same hardware implementation platform.

Figure 7 shows that the proposed method significantly (*i.e.*, several-fold) improves the compression ratio compared with the method in [23] for the pulse signal, especially when Δ is larger than 15. For example, when the error parameter value is 25, the compression ratio of the data is 544.46 when the proposed method was used. This value was improved by up to ten-fold. These findings reveal that the compression ratio can be further enhanced by using the proposed method. The enhanced compression ratio is resisted to noise disturbance by averaging the quantization noise.

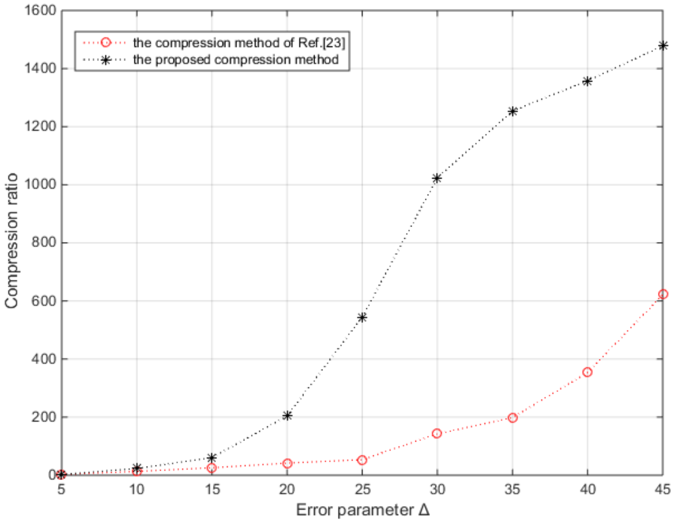

Fig. 7. A relationship between the error parameter and the compression ratio of pulse signals.

Figure 8 shows a comparison between the original waveform and the compressed signal waveform after decompression when the error parameter value is 25. The original waveforms mentioned in Fig. 8 indicate the output signals of the signal adjustment circuit. The pulse waveform after decompression in the proposed method is in agreement with its original waveform. In our study, the distortion degree is defined as a result of dividing the difference between the values of quantized data before and after the compression by the value of uncompressed data, to quantitatively characterize the compression effect of our method. The distortion degrees of the pulse data at different error parameter Δ values were then compared for the proposed method and the method in [23], as shown in Table 4. The reduction of the distortion degree ranges from 27.78% to 38%, which indicates that the proposed method has a lower distortion degree compared with the method in [23]. In order to directly reflect an advantage of a high compression ratio for the same compression quality (namely, the identical distortion degree) of the developed method, Fig. 9 demonstrates that the proposed method could achieve a higher compression ratio with a smaller distortion, which exhibits significant advantages in the telemetry data compression.

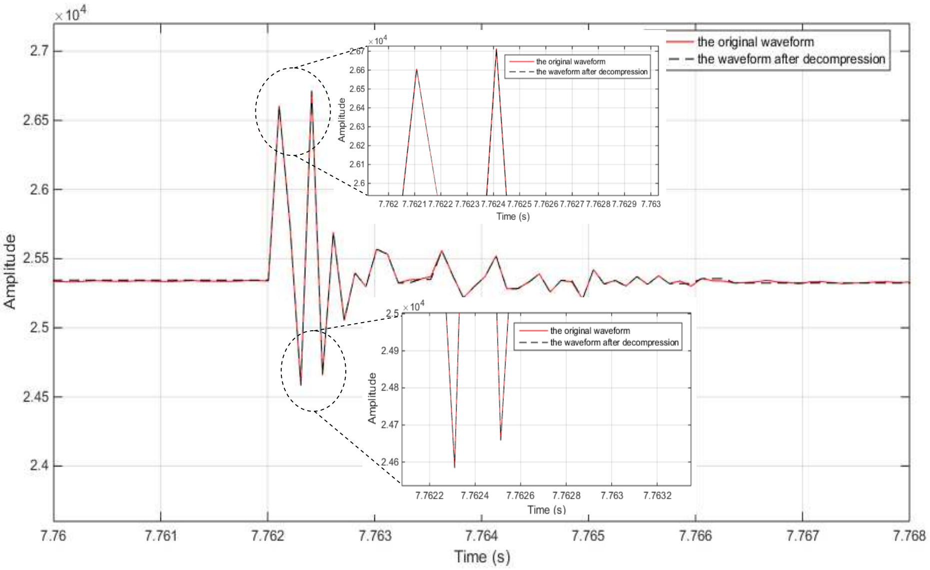

Fig. 8. Comparison of the original waveform with the compressed signal waveform after decompression.

Table 4. Comparison of distortion degrees of the pulse signals.

Δ	5	10	15	20	25
Method in [23]	0.027%	0.055%	0.083%	0.11%	0.14%
Proposed method	0.019%	0.039%	0.055%	0.075%	0.087%
Improvement	29.06%	29.12%	33.78%	31.73%	38.00%
Δ	30	35	40	45	
Method in [23]	0.16%	0.18%	0.21%	0.24%	
Proposed method	0.11%	0.13%	0.15%	0.15%	
Improvement	31.25%	27.78%	28.57%	37.50%	

Finally, the precisions of the system when either method was used were compared, as shown in Table 5. The result shows that the proposed method improves the effective number of bits by one bit by adopting the oversampling technology. When the resolution reaches 9.95 bits, the corresponding degree of distortion of the signal is 0.11%, which indicates that the compressed data can be accurately restored in engineering applications.

For multichannel vibration signals, the compression ratios obtained with the proposed method and the method mentioned in [23] are shown in Table 6. The results show that the compression ratio is significantly improved when the proposed method was used, thereby highlighting the effectiveness of our method.

We also compared our method with the WinRAR compression method in terms of the compression ratio, as shown in Table 7. The WinRAR method is a lossless self-adaptive multiple compression algorithm. The proposed method could be regarded as a lossless compression method when the error parameter is equal to zero. On the contrary, the proposed algorithm works in the loss mode. It is calculated that the compression ratio of the proposed method in the lossless mode is similar to that of the WinRAR method (*e.g.* 1.8 for the WinRAR method and 1.3 for the proposed method for a vibration signal). By adjusting the error parameter (*e.g.* $\Delta = 25$), the compression ratio of the proposed method (namely, in the loss mode) is significantly improved. In this situation, the proposed method achieves the trade-off between a low distortion degree (less than 0.1%), which meets the practical requirement, and a high compression ratio, compared with WinRAR – the loss method.

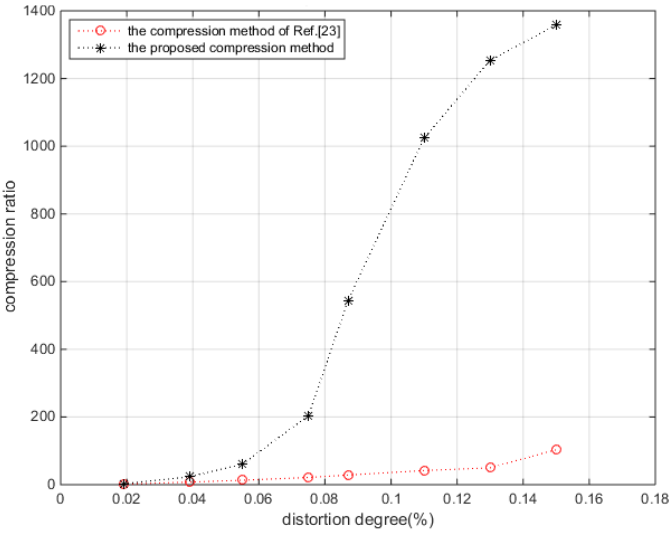

Fig. 9. A relationship between the distortion degree and the compression ratio of pulse signals.

Table 5. Comparison of *Resolution* (R) and *Compression Ratio* (CR) of pulse signals.

	Δ	5	10	15	20	25
Method in [23]	R (bit)	9.71	9.68	9.63	9.65	9.62
	CR	2.63	13.23	25.72	41.77	53.51
Proposed method	R (bit)	10.75	10.71	10.68	10.65	10.61
	CR	2.80	23.14	60.72	203.73	544.46
	Δ	30	35	40	45	
Method in [23]	R (bit)	9.59	8.96	8.92	8.85	
	CR	142.58	198.2	353.6	621.7	
Proposed method	R (bit)	10.58	9.99	9.98	9.95	
	CR	1024.2	1254.6	1358	1477	

Table 6. The compression ratio of vibration signals.

Δ	5	10	15	20	25
Method mentioned in [23]	1.32	4.52	11.18	26.19	42.17
Proposed method	1.58	6.28	21.85	37.49	81.92
Δ	30	35	40	45	
Method mentioned in [23]	50.37	57.84	62.43	69.85	
Proposed method	149.12	173.78	197.59	214.33	

Table 7. Comparison of compression ratios obtained with WinRAR and the proposed method.

Method / Type	WinRAR method	Proposed method
Pulse signal	3.92	545.8 (Δ = 25)
Vibration signal	1.88	81.92 (Δ = 25)

4. Discussion

All telemetry signals of the whole testing process should be sampled and recorded to determine the state of aircraft in the experiment. Fast-varying signals are the main components of total data at high sampling rates, and these signals consist of active and smooth transition phases for the whole test time. The active phase of fast-varying signals in the total flight process is less than 20%, whereas the smooth transition phase accounts for 80% of the total fast-varying signals [12, 23]. In the smooth transition phase, the signal values show no significant variations, which can be considered as redundant data. Therefore, the redundant data provide space for data compression. If the data are not preprocessed before the compression encoding, the noise during sampling may increase the difference between adjacent redundant data, which highly affects the compression performance. The oversampling used in this method enables a significant reduction of noise signals in the smooth transition to achieve a high compression ratio in appropriate error parameter conditions. Moreover, the oversampling improves the precision of the sampled data. Thus, the distortion degree and acquisition resolution of the telemetry data are highly improved. Based on these results, the proposed method can further improve the compression performance to meet the requirements in practical engineering applications. Therefore, the proposed method is significantly more effective when applied to high-precision high-capacity acquisition systems, compared with the existing studies.

Developing a data compression method with a high compression performance is necessary to store and transmit large quantities and various types of telemetry data. An enhanced and effective multichannel telemetry data compression method is proposed to balance the compression ratio, precision, and distortion. The proposed approach consists of three modularized phases, as follows: 1) oversampling and normal averaging of the telemetry data, 2) the data compression based on RLE with an error parameter, and 3) two-stage framing. The proposed data compression method is based on FPGAs. The proposed method significantly improves the compression ratio of the telemetry data and the system accuracy as well as reduces the distortion degree of the data, compared with the results of previous research.

The high performance and simple hardware implementation of our proposed method provide an effective data compression application to high-precision multichannel acquisition systems and high real-time testing.

Acknowledgments

This work was financially supported by the National Natural Science Foundation of China (Grant No.61004127 and No.11502156).

References

[1] Monteiro, A., Lu, W., Gough, M., Thompson, J., Yearby, K. (1996). A smart telemetry compression system for a space instrument: MARS-96 ELISMA instrument complex. *Microprocessors Microsyst*, 20(1), 17–30.

[2] Mulholland, J.E., Tamney, F.K., Jr. (1996). Spacecraft telemetry link performance in a transfer orbit. *IEEE Transactions on Aerospace and Electronic Systems*, 32(4), 1321–1335.

[3] Drost, G.W., Bourbakis, N.G. (2001). A Hybrid System for Real-time Lossless Image Compression. *Microprocessors and Microsystems*, 25(1), 19–31.

[4] Lin, M., Lee, J., Jan, G. (2003). A lossless data compression and decompression algorithm and its hardware architecture. *IEEE Trans. Very Large Scale Integr. (VLSI) Syst.*, 11(3), 499–510.

[5] Abo-Zahhad, M., Rajoub, B. (2002). An effective coding technique for the compression of one dimensional signals using wavelet transforms. *Medical Engineering and Physics*, 24(3), 185–199.

[6] Kattan, A. (2010). Universal intelligent data compression systems: a review. *Proc. 2nd Conf. Computer Science and Electronic Engineering Conference (CEEC)*, Colchester, UK, 11597641, 1–10.

[7] Cristiano, M., Ivanil, A., Bonatti, S., PeresAn, P.L.D. (2013). Adaptive Run Length Encoding method for the compression of electrocardiograms. *Medical Engineering & Physics*, 35, 145–153.

[8] David, A., Maluf, P., Tran, B., Tran, D. (2008). Effective Data Representation and Compression in Ground Data Systems. *IEEE Aerospace Conference*, 1–7.

[9] Qian, S.E., Bergeron, M., Cunningham, I., *et al.* (2006). Near lossless data compression onboard a hyperspectral satellite. *IEEE Transactions on Aerospace and Electronic Systems*, 42(3), 851–866.

[10] Kiely, A., Klimesh, M. (2003). The ICER Progressive Wavelet Image Compressor. *IPN Progress Report*, 42–155.

[11] Logeswaran, R. (2004). Fast Two-Stage Lempel-Ziv Lossless Numeric Telemetry Data Compression Using a Neural Network Predictor. *Journal of Universal Computer Science*, 10(9), 1199–1211.

[12] Rong, C.D., Hong, L.J., Yong, Z.G. (2001). Algorithm design for launch vehicle telemetry data compression. *Journal of Astronautics*, 22(2), 12–17.

[13] Chan, H.L., Siao, Y.C., Chen, S.W. (2008). Wavelet-based ECG compression by bit-field preserving and running length encoding. *Computer Methods and Programs in Biomedicine*, 90(1), 1–8.

[14] Steinwandt, R., Villányi, V.I. (2008). A one-time signature using run-length encoding. *Information Processing Letters*, 108(4), 179–185.

[15] Stabno, M., Wrembel, R. (2009). RLH: Bitmap compression technique based on run-length and Huffman encoding. *Information Systems*, 34(4–5), 400–414.

[16] Korpela, E., Forsten, J., Hamalainen, A., *et al.* (2006). A hardware signal processing platform for sensor systems. *IEEE Aerospace and Electronic Systems Magazine*, 21(5), 22–25.

[17] Nunez, J.L., Jones, S., (2002). Lossless Data Compression Programmable Hardware for High-Speed Data Networks. *Proc. IEEE Int. Conf. on Field-Programmable Technology*, 290–293.

[18] Kao, C., Huang, S., Huang, I. (2007). A hardware approach to real-time program trace compression for embedded processors. *IEEE Trans. Circuits Syst. I-Regul. Pap.*, 54(3), 530–543.

[19] Hashempour, H., Lombardi, F. (2005). Application of arithmetic coding to compression of VLSI test data. *IEEE Trans. Computers*, 54(9), 1166–1177.

[20] Lee, J., Kim, S., Weems, C. (2002). Performance analysis of a selectively compressed memory system. *Microprocessors Microsyst*, 26(2), 63–76.

[21] Olyaei, A., Genov, R. (2007). Focal-Plane Spatially Oversampling CMOS Image Compression Sensor. *IEEE Trans. Circuits Syst. I-Regul. Pap.*, 54(1), 26–34.

[22] Xu, X., Dong, G., Feng, Y., Xu, S. (2006). A new spaceborne compression approach for remote sensing imagery. *Proc. SPIE*, 6031.

[23] Ren, Y., Liu, X., Xu, W., Zhang, W. (2008). Multi-Channel Data Compression. *IEEE Aerosp. Electron. Syst. Mag.*, 23(9), 14–21.

[24] Kim, H., Jung, Y., Kim, H., Ahn, J., Park, W., Kang, S. (2010). A high performance network-on-ship scheme using lossless data compression. *IEICE Electron. Express*, 7(11), 791–796.

[25] Stewart, R.W., Pfann, E. (1998). Oversampling and sigma-delta strategies for data conversion. *Electronics & Communication Engineering Journal*, 10(1), 37–47.

[26] Tan, L., Wang, L.M. (2011). Oversampling Technique for Obtaining Higher Order Derivative of Low-Frequency Signals, Instrumentation and Measurement. *IEEE Transactions*, 60(11), 3677–3684.

[27] Temes, G.C., Candy, J.C. (1990). A tutorial discussion of the oversampling method for A/D and D/A conversion, Circuits and Systems. *IEEE International Symposium*, 2, 910–913.

[28] Nunez, J., Jones, S. (2003). Run-length coding extensions for high performance hardware data compression. *IEE Proc.-Comput. Digit. Tech.*, 150(6), 387–395.

Metrol. Meas. Syst., Vol. 24 (2017), No. 3, pp. 563–576.

METROLOGY AND MEASUREMENT SYSTEMS
Index 330930, ISSN 0860-8229
www.metrology.pg.gda.pl

THE APPLICATION OF THE THEORY OF SYNTHESIS OF A DELAY LINE WITH A SURFACE ACOUSTIC WAVE FOR A SINGLE-MODE OSCILLATOR OF ELECTRIC SIGNALS IN SOME SENSORS OF NON-ELECTRICAL QUANTITIES

Milan Šimko, Miroslav Gutten, Milan Chupáč, Daniel Korenčiak

University of Žilina, Faculty of Electrical Engineering, Univerzitná 1, 010 26 Žilina, Slovakia
(✉ milan.simko@fel.uniza.sk, +421 41 513 2125, *miroslav.gutten@fel.uniza.sk, milan.chupac@fel.uniza.sk, daniel.korenciak@fel.uniza.sk)*

Abstract

The paper deals with the issue of constructing delay lines on the basis of surface acoustic waves and their application to single-mode oscillators. As a result of a theoretical analysis concrete delay lines are proposed.
In the contribution, there is presented a theory of designing a symmetrical mismatched and matched delay line for a single-mode oscillator of electrical signals on the basis of which there were designed and fabricated acoustic-electronic components for sensors of non-electrical quantities.
From the experimental results it can be stated that all of six designed and fabricated delay lines can be effectively used in the construction of single-mode oscillators.

Keywords: delay line, oscillator, surface acoustic wave, interdigital transducers.

1. Introduction

As selective elements of oscillators of harmonic vibration besides the band-pass filters there are also used *delay lines* (DLs) and resonators as prospective acoustic-electronic components based on *surface acoustic waves* (SAW). From a stability point of view we can classify these oscillators as those with volume acoustic waves and LC oscillators. The quality factor of vibrating system of oscillators with SAW is in a range from 100 to 10 000 when these oscillators work with the basic harmonic in a frequency range from 10 MHz to 1,5 GHz. The main advantages are their small dimensions, low weight, high mechanic strength, low sensitivity to vibrations and the possibility to construct oscillators without using inductors. It increases the demand for their manufacturing and widens the spectrum of their applications in radio electronics, telecommunications and – at the same time – is the incentive to research into the issues connected with their theory and manufacturing.

In the paper, the DLs with SAW for single-mode oscillators are examined and the single-mode oscillation conditions for oscillators are determined and – based on the deduced theory – concrete DL are proposed for various applications .

2. Oscillator with delay line

The basic principle of operation of an oscillator with a delay line is presented in Fig. 1. A delay line with SAW (3) plugged in the feedback loop of an amplifier (2) is the basic element. A piezoelectric single crystal base (*e.g. Y* – cut, *Z* – direction of propagation of $LiNbO_3$, ST, X – SiO_2 *etc.*) on which there are installed the input (IDT_1) and output (IDT_2) interdigital

Article history: received on Sep. 28, 2016; accepted on Apr. 08, 2017; available online on Sep. 01, 2017; DOI: 10.1515/mms-2017-0040.

transducers and fabricated with the photolithographic technology. Circuits (1, 3) serve to match the DL impedance to the impedance of electronic circuitry.

Because passing a signal from the input to the output of DL is delayed, the examined oscillators are oscillators with a delaying feedback. The theory of these oscillators is well known in the literature [1, 2], nevertheless the achieved results concern especially the oscillators with broadband DLs in which the necessary frequency selectivity is secured with additional circuits (*e.g.* LC), while in a range of frequencies range for possible applications the DL parameters do not differ significantly. A different situation is in the case of DLs with SAW, where DLs themselves have a narrow transmission band and their parameters differ fundamentally in this range. The physical distinctiveness of functioning of the listed components which is related to the phenomena of excitation, extension and reflection of SAW cause that − in addition to providing a delay − the DLs have specific frequency dependencies on the input and output admittances. Their replacement with lumped RLC circuit elements or a broadband DL with an outer selective LC is mentioned only very generally.

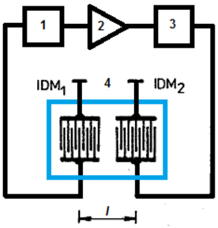

Fig. 1. A block diagram of an oscillator: 1, 3 – matching circuits; 2 – an amplifier; 4 – a delay line with SAW.

It can be considered as an advantage that for the oscillators with SAW, to compensate their static capacitances, compensational inductors plugged in input and output IDTs do not have to be used. By leaving them out, the voltage and current coefficients of transfer radically decrease, which eventually leads to the necessity of increasing the oscillator's active element and thereby to a different action in the process of proposing the DL with SAW.

In the next part we will examine firstly the oscillators without compensation inductors (mismatched DLs with SAW) and then the oscillators with a matched DL.

2.1. Oscillator with mismatched delay line

A delay line with SAW used as a selective element of oscillator can be symmetrical or non-symmetrical. A symmetrical DL is characterized by the same input and output IDTs, whereas a non-symmetrical DL has the input IDT with a small number of electrodes (broadband) and the output IDT with a big number of electrodes (narrowband). In the contribution we will only deal with the symmetrical DL. For simplification we will assume that the input and output admittances of active element, taking into consideration the load, are equal and real, *i.e.* $g_1 = g_2 = g$. The imaginary part of input/output admittance of element (taking into consideration the load) can be included in the static capacity of IDT of DL with SAW.

Solving the complex (1) we determine the parameters of natural oscillations:

$$K(j\omega) = 1. \tag{1}$$

The depicted equation can be broken to the equation of phase balance:

$$\frac{\omega l}{v} + \varphi_e = 2\pi k \tag{2}$$

and the equation of modules' balance:

$$K_0 K_e(\omega) K_1(\omega) K_2(\omega) = 1, \tag{3}$$

where: K_0 – a coefficient of loop amplification unit consisting of the amplifier and DL; $K_e(\omega)$, $K_1(\omega)$ and $K_2(\omega)$ – module characteristics of the amplifier, input and output IDTs, respectively; $l = vt_0$ – a distance between the centres of input and output IDTsp; v – a velocity of SAW propagation; t_0 – a delay of the DL; φ_e – a change of phase of the electric signal in the IDT and the amplifier; k – a positive integer.

An adequate choice of the oscillator active element's amplification enables to attain the phase balance, whereas an appropriate geometrical arrangement of the DL enables to attain the balance of arguments.

For a sufficiently long distance l, the value of φ_e is fundamentally smaller than $\omega l/v$ and so φ_e does not need to be considered in the first approximation. Then the frequencies at which the oscillations emerge can be determined from (2). Applying the above we obtain:

$$\omega_k = \frac{2\pi v}{l} k\ ,\ f_k = \frac{k}{t_0}. \tag{4}$$

The indicated frequencies create a discrete spectrum within an interval between single frequencies (Fig. 2b):

$$\delta f = \frac{1}{t_0}. \tag{5}$$

With an appropriate choice of arrangement and IDT geometry, the single-mode oscillation regime can be obtained. In the case of a symmetrical DC, *i.e.* when the input and output IDTs are equal and have N sections of distance $\lambda_0\left(\lambda_0 = \frac{v}{f_0}\right)$, a module characteristic of DL's nearby synchronised frequency can be sufficiently exactly approximated by the function in a form $\frac{(\sin^2 x)}{x^2}$, where $x = N\pi\frac{(f - f_0)}{f_0}$. Zeros of the module characteristic match the values $x = \pm n\pi$, ($n \neq 0$). Frequency intervals between zero values are given by the formula:

$$\Delta f = \frac{f_0}{N} = \frac{1}{\tau}. \tag{6}$$

There can be stated from the presented facts, that the only condition for the single-mode oscillation regime is that all the frequencies of the discrete spectrum (5) need to be identified, with the exception of the synchronous frequency, with zero values of the DL module characteristics: $\delta f = \Delta f$.

Then, from the relations (5) and (6), it results that:

$$t_0 = \tau \tag{7}$$

and – after modifying – the relation:

$$P_0 = N \tag{8}$$

can be obtained, where $P_0 = \frac{l}{\lambda_0}$ and the distance l is expressed as multiples of λ_0. For the single-mode oscillation regime, the DL delay (t_0) and the delay created in IDT (τ) must be equal (at least approximately), from which it results that the distance between IDT centres must be equal to the IDT length.

It is known that the oscillator's frequency stability is determined by the sharpness of argument characteristic of its resonance system at the working frequency ω_0. The sharper this characteristic the higher the frequency stability.

For the LC oscillators the sharpness of argument characteristic is determined by the time constant τ of the circuit which is a function of the quality factor Θ of the resonance system and the working frequency ω_0 , according to the relation:

$$S_f = \tau_{LC} = \left| -\frac{d\Theta}{d\omega} \right|_{\omega_0} = \frac{2\Theta}{\omega_0}. \tag{9}$$

For the oscillators with DL and SAW there applies:

$$S_f = t_0 = \frac{l}{v} = \frac{2\pi P_0}{\omega_0}. \tag{10}$$

Applying the previous relations we can introduce a term of the quality factor of the resonance system of oscillator with SAW, as follows:

$$\Theta = \pi P_0 = \frac{\pi l}{\lambda_0}. \tag{11}$$

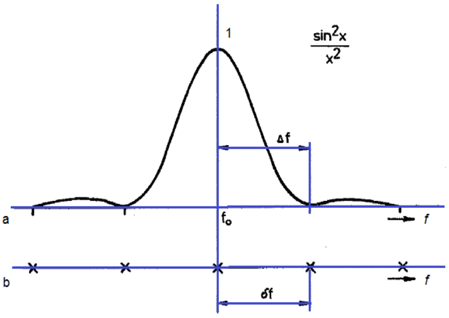

Fig. 2. A module characteristic of IDT (a); the frequency at which the condition of balance of arguments is fulfilled (b).

From (11) it results that the maximum value of quality factor is set by an obtainable value of delay which depends on the propagation velocity of SAW and on the technological possibility to grow mono-crystals, as well as on the operating frequency ω_0, which upper limit is given by the capabilities of the photolithographic technology.

A very attractive property of oscillators with SAW is the possibility of independent converting the module and argument characteristics of DL (Fig. 3). Two of IDTs are presented in Fig. 3a, for which the condition (8) is fulfilled and the corresponding module and argument characteristics are shown. A three-fold increase of the delay t_0 for the same dimensions of IDTs ($P_0 = 3N$) causes a three-fold increase of the phase slope (10), whereas the module characteristic does not change. In the third case (Fig. 3c), the delay and the argument characteristic remain the same as in Fig. 3b, but the length of each of IDT increases three times. It causes narrowing of the DL band-pass in comparison with two previous cases. In the oscillator with a given DL, the oscillations are possible only at one frequency (in DL – Fig. 3b – the condition of the balance of arguments and modules is fulfilled at various frequencies) and this oscillator has a higher frequency stability than the oscillator with a DL shown in Fig. 3a. An increase of frequency stability is achieved by the fact that at an increase of IDT dimensions and thus also at an increase of delay $t_0 = \frac{l}{v}$ (while $P_0 = N$ is still valid), the oscillator becomes less sensitive to changes of the electric phase shift (2).

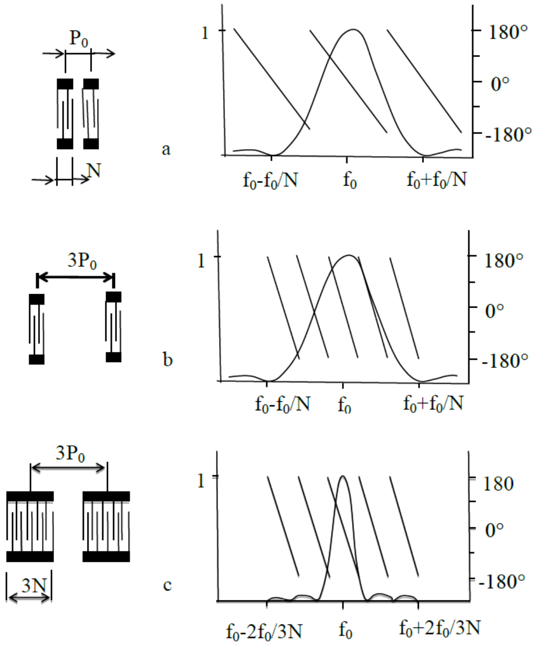

Fig. 3. Module and argument characteristics of IDT of various configurations.

A more accurate single-mode oscillation condition can be determined from the complete (2). Substituting $\varphi_e = \psi_1 - \psi_2$ gives [1, 2]:

$$P_0 = k - \frac{(\psi_1 + \psi_2)}{2\pi}, \tag{12}$$

where: $\psi_1 = arctg\frac{(b_i + B_i)}{(g_i + G_i)}$; g_i and b_i are real and imaginary parts of the intrinsic admittance of the i – level gate of linear oscillator's part without the backward coupling of circuit, *i.e.* without DL with SAW, G_i and B_i are real and imaginary parts of the input admittance of the i – level gate of DL with SAW nearly short-circuited with the second (j – level) gate ($i = 1, 2$) [3].

For piezoelectric materials with a low electromechanical coupling coefficient K^2 (*e.g.* SiO_2), provided that the components of convertors' admittance are mutually measurable with the components of the input and output admittance of active element and, the following inequality holds:

$$4K^2 N_i \frac{(1+\chi_i)}{\pi} << 1, \tag{13}$$

where: $\chi_i = \frac{g_i}{G_i}$ is a matching coefficient, we obtain the following relation to set an optimal value of relative distance between the IDT centres, at which the single-mode oscillation regime emerges at the working frequency ω_0. Applying it we obtain:

$$P_0 = \frac{2k-1}{2} + \frac{2K^2}{\pi^2}\left[N_1(1+\chi_1) + N_2(1+\chi_2)\right]. \tag{14}$$

It results from (14) that the optimal distance between the IDT centres in DL with SAW approaches an odd number of multiples $\frac{\lambda_0}{2}$ at the frequency ω_0.

If the input and output conductances of active element are equal to the corresponding susceptances, *i.e.* $g_i = \omega_0 C_{Ti}$, then:

$$P_0 = \frac{4k-1}{4} + \frac{2K^2}{\pi^2}(N_1 + N_2) \tag{15}$$

and in the case of a symmetrical DL ($N_1 = N_2$):

$$P_0 = \frac{4k-1}{4} + \frac{4K^2}{\pi^2} N . \tag{16}$$

It results from the equation that optimal distance between the IDT centres in this case approaches an odd number of multiples $\frac{\lambda_0}{4}$ at the frequency ω_0.

2.2. Oscillator with matched delay line

To improve the characteristics of oscillators with DL with SAW the matching (compensation) of IDT static capacitance is used. However, the use of compensation circuits has certain advantages and disadvantages [3–5].

Among the advantages are a decrease of inserted damping and an increase of DL transmission coefficient. It enables to achieve a higher output power and to increase effectiveness in comparison with the oscillator with unmatched DL. A disadvantage is the worsening of long-term stability of the oscillator frequency as a consequence of instability of matching circuits. In simple cases we can attain the adjustment by serial connection of the compensation inductor to the IDT clamps (at a low value of the real part of input or output admittance of active element) or by parallel connection (at a high value of the real part). A natural resonance frequency of the created resonance circuit (*i.e.* serial or parallel) has to be close to the frequency:

$$\left(\omega_p = \frac{1}{\sqrt{L_k C_T}}\right). \tag{17}$$

To ensure the single-mode oscillation at $g_1 = g_2 = g$, $\omega C_T - \frac{1}{\omega L_k} = 2C_T(\omega - \omega_p) = g$ for the relative distance between IDT centres, the relation:

$$P_0 = k , \tag{18}$$

where: k – a positive integer, is valid.

From (18) it results the fact that an optimal distance between IDT centres for reaching the single-mode oscillation must be equal to an integer number of λ_0. If the resonance frequency of adapter circuits differs from ω_0, then the optimal relative distance between IDT centres can be calculated from [1, 2]:

$$P_0 = k - \frac{1}{8K^2\omega_0}\left[\frac{\omega_0 - \omega_{p1}}{N_1(1+\chi_1)} + \frac{\omega_0 - \omega_{p2}}{N_2(1+\chi_2)}\right]. \tag{19}$$

To increase the output resistance of linear resonance scheme of oscillator (*i.e.* active element and DL) and also to increase the output signal filtration we can match only the output IDT alone. In this case the optimal distance will be calculated from the relation:

$$P_0 = k - \frac{1}{8} + \frac{2K^2}{\pi} N_1 - \frac{\omega_0 - \omega_{p2}}{8K^2 N_2 (1+\chi_2)\omega_0} . \tag{20}$$

3. Design, discussion and experimental results of symmetrical delay line

In the paper the DLs with SAW for single mode oscillators are examined.

The main achievements of this paper are:

- An initial formulation of a theory of synthetizing a symmetrical DL with SAW. It is the baseline theory according to which there are designed important parts of acoustic-electronic components – the delay lines.
- Verification of the proposed procedure and its accuracy. Based on the theory and the principle of a delay line there were designed and implemented a temperature sensor, a displacement sensor and other sensors for measuring non-electrical quantities.
- A contribution to the state of the art in the field of science concerning sensors of non-electrical quantities and their general applicability.
- Obtaining the experimental results that confirm effectiveness of all designed and implemented delay lines for the single – mode oscillation applications, and thereby confirm the previously mentioned advantages.

In the paper, the derived theoretical parameters are compared with the experimental ones.

Based on the previous theoretical considerations, a displacement sensor PLO 43 with a symmetrical DL, a thermal sensor PSO 40 with a symmetrical DL and a flow sensor PLO 39 suitable for precise laboratory measurements as well as for normal operating measurements have been designed.

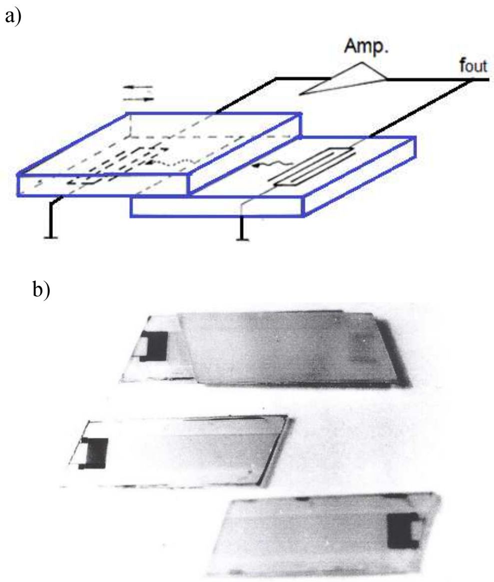

Fig. 4. A structure of DL with SAW (a); a displacement sensor (b).

The displacement sensor consists of two pads with two IDTs installed at the end of propagation path. The plates can move around each other, changing the distance between the IDTs (Fig. 4). On the basis of such constructed a delay line an oscillator with a variable delay in its feedback path is created. The oscillation frequency of the oscillator varies with the change of propagation path length and is given by the relation:

$$f = n\frac{1}{\tau_1 + \tau_2}, \tag{21}$$

where: $\tau_1 = (L-l)/v, \tau_2 = l/v'$; L – a distance between the input and output IDTs; l – a length of overlap of the plates; v – a velocity of propagation of SAW; v' – a velocity of propagation of SAW in the overlapping part; n – a number expressing the mode of oscillations.

If the distance between IDTs changes (Fig. 5), with a shift of the plate, from the value of L to $L + \Delta l$, the length of the overlap is reduced to $l - \Delta l$, whereas the oscillation frequency changes from the value f to $f + \Delta f$. In the case when $\Delta l << L$, we can calculate $(f + \Delta f)$ from the preceding equations.

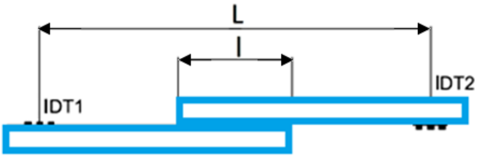

Fig. 5. A displacement sensor geometry.

PLO 43
Substrate: Y – cut, Z – propagation direction;
– $LiNbiO_3$, thickness of the pad 1 mm.
IDM: n – 101 electrodes, $l_e = l_0 = 10$ µm.

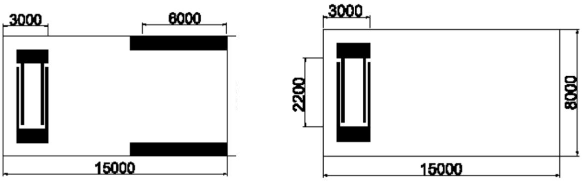

Fig. 6. A schematic of construction (all dimensions in µm).

Thus,

$$f + \Delta f \doteq n\frac{v}{L}\left[1 - \frac{\Delta l}{L} + \frac{l - \Delta l}{L}\left(1 - \frac{v}{v'}\right)\right]. \tag{22}$$

Then, the sensitivity of oscillator frequency variations to changes of an overlap length is given by:

$$\frac{\Delta f}{\Delta l} \doteq -n\frac{v}{L^2}\left[1 - \left(\frac{l}{\Delta l} - 1\right)\left(1 - \frac{v}{v'}\right)\right] \tag{23}$$

and, if $v = v'$, then:

$$\frac{\Delta f}{\Delta l} = -n\frac{v}{L^2}. \tag{24}$$

The number n of modes of oscillations depends on the phase shift that occurs in length, as well as on the frequency-selective properties of IDT. If the plates move from L to $(L + \Delta l)$, the oscillation frequency of the n – th mode moves to the next lower frequency within the reach of the main lobe and the oscillation frequency of the $(n + 1)$-th mode moves to the middle of the main lobe (i.e. the frequency of oscillations gradually decreases when the length of overlap decreases; also, there is a discontinuous change of frequency back to a higher frequency). In the case where the overlap length increases, the process of the frequency change is reversed. The dependence of the frequency change resulting from the shift is linear.

A schematic of construction of the designed and implemented symmetrical mismatched delay line PLO 43 for a single-mode oscillator is shown in Fig. 6. For its pad there were chosen: Y – cut; Z – direction of propagation of $LiNbO_3$. The substrate thickness is 1 mm. Some of the calculated and measured parameter values are shown in Table 1.

Another delay line, PSO 40, symmetrical and mismatched, was implemented for a temperature sensor (Fig. 7). As a material of the pad a special LST – cut (due to its higher sensitivity), and X – direction of propagation of SiO_2, have been chosen. The substrate thickness is 0,5 mm. A design scheme is presented in Fig. 8. The fabricated DL with SAW is shown in Fig. 9 and the dependency of inserted damping on frequency – in Fig. 10. Some calculated and measured parameter values are listed in Table 1.

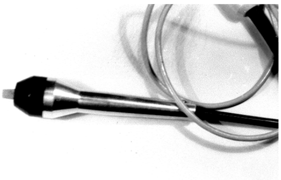

Fig. 7. A fabricated thermal sensor based on SAW.

PSO40
Substrate: LST – cut, X – propagation direction, SiO_2, thickness of the pad 0,5 mm.
IDM: n – 31 electrodes, $l_e = l_0 = 12$ µm.

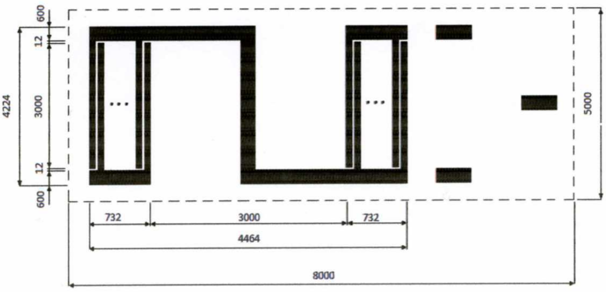

Fig. 8. A design scheme of delay line PSO 40 (all dimensions in µm).

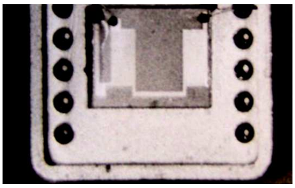

Fig. 9. A photo of fabricated DL PSO 40.

One of the sensors designed on the basis presented in Section 1, was a flow sensor suitable for precise laboratory measurements as well as normal operating measurements. Since the components of SAW are extremely sensitive to the temperature change (of the order of 10^{-4} K), it has been applied to the construction of the flow sensor. A flow of liquid (or gas) results in a changed temperature of the pad, which is placed on the flowmeter. On this pad, an acoustic-electronic component (delay line or resonator) that reacts to the temperature change, is installed.

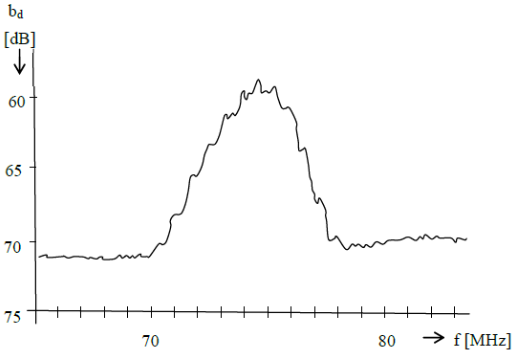

Fig. 10. The dependency of inserted damping on frequency for DL PSO 40.

A block diagram of the flowmeter is presented in Fig. 11.

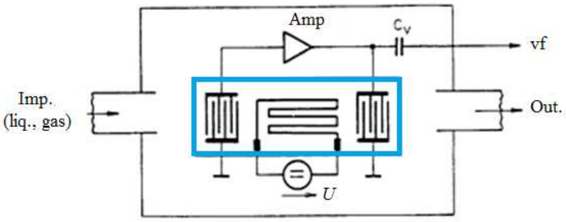

Fig. 11. A block diagram of the flowmeter.

The fabricated flow sensor has been designed on the basis of a delay line PLO 39 (128°, Y – cut, X – propagation direction of – $LiNbO_3$ with a pad thickness of 1 mm). The pad with – a DL-based SAW is heated using a thin film heater (meander) of a constant power. The flow of a substance (gas or liquid) (*i.e.* its flow velocity and the substance properties), results in a change of temperature of pads (the principle of heat transfer by convection). Changing the temperature of the pad causes a linear change of the frequency of oscillator with SAW (in the sensor a delay line has been used, but a resonator can be used instead, too).

The heat transfer by convection per a unit area A can be expressed by the modified Newton's rule:

$$Q = hA\Delta T \quad \text{or} \quad Q/A = h\Delta T\,, \tag{25}$$

where: h – a convective heat transfer coefficient; A – an area; ΔT – a temperature difference (the convection constant and the temperature difference are determined by the nature of the process).

It is clearly seen from the above relationship that the rate of heat flow grows with increasing the temperature difference and with increasing the transmission coefficient. Increasing the flowing substance speed causes an increase of the transfer coefficient.

The convection process can be expressed as the product of a flowing substance mass – m; a specific heat – c_p and an average surface temperature gradient – dt, as follows:

$$Q = m.c_p dt. \tag{26}$$

Solving (25) and (26) we can derive a relationship between the flowing quantity and the average surface temperature gradient of acoustic – electronic component with SAW.

Then, the temperature sensitivity of an oscillator with DL-based SAW (we assume that the volume of flowing substance, as already mentioned, causes a change in the temperature of the component with SAW and thus a change of the oscillator frequency) is given by the following equation:

$$df = f(\nu_0)\left[1 + a(\nu - \nu_0) + b(\nu - \nu_0)^2 + \ldots\right], \tag{27}$$

where: *a*, *b* – temperature coefficients of the first and the second order frequency at the reference temperature (zero) υ_0.

A flow characteristic of the implemented SAW-based oscillator (a function of flow *vs*. frequency) is shown in Fig. 12.

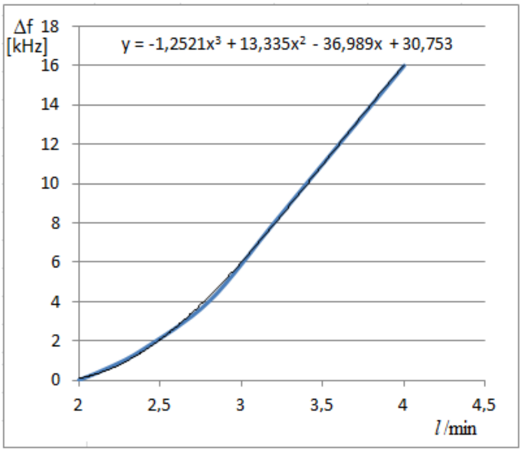

Fig. 12. A flow characteristic of a SAW-based oscillator.

As the flowmeter we used a designed, experimentally verified and fabricated symmetrical non-adapted DL – PLO 39 (Fig. 13) with measured and calculated values – Table 1. The dependence of insertion loss on frequency is presented in Fig. 14.

PLO 39

Substrate: 128° *Y* – cut, *X* – propagation direction, $LiNbO_3$, thickness of the pad 1 mm.

IDM: $n = 101$ electrodes, $l_e = l_0 = 12$ μm.

Meander: meander width 20 μm.

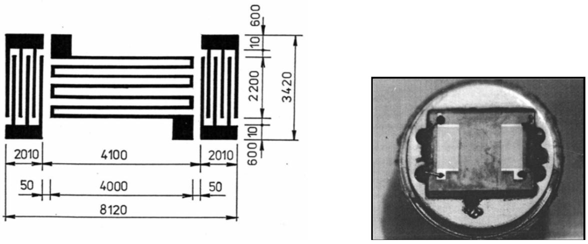

Fig. 13. A photo of the fabricated DL PLO 39 and its design scheme (all dimensions in μm).

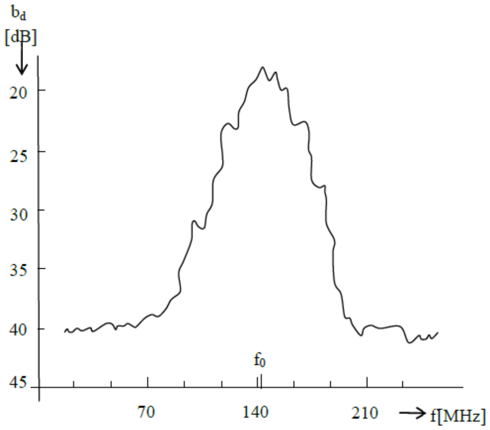

Fig. 14. The dependence of inserted damping on frequency for the DL PLO 39.

A structural design of the flow sensor with SAW is presented in Fig. 15. The cover 2 of the flow sensor is made of fiberglass. The top cover 3 with a seal beneath it (to decrease the influence of external conditions on the piezoelectric substrate with the delay line) is attached with four screws.

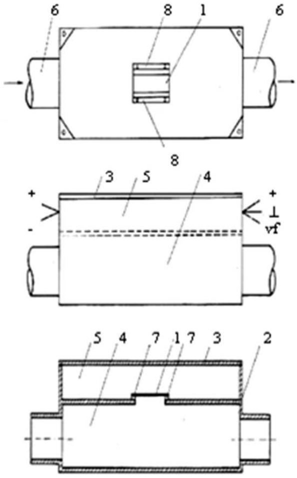

Fig. 15. A design of the flow sensor. 1 – piezoelectric plate with delay line and thin-film heater (meander); 2 – fiberglass cover; 3 – top cover; 4 – flow chamber; 5 – space for electronic part; 6 – inlet and outlet openings; 7 – rubber seal; 8 – holders of piezoelectric pads.

The flow sensor has an inlet and an outlet (6) for the substance flow in and out. The sensor is connected to three wires: DC voltage, RF signal and common ground, implemented by a two-wire coaxial cable, and to two wires supplying power to the thin film heater (meander).

The internal space of the sensor is divided into two parts. The bottom part is the flow chamber – 4, through which flows the measured substance. In the top part there is a space for storing the electronic part – 5. In the plate separating the bottom and top parts there is an opening, at the top of which there is fixed a piezoelectric plate with the delay line with a thin film heater (meander) – 1. The temperature of the piezoelectric plate is influenced from the bottom by the flowing substance. The piezoelectric plate is attached with two holders – 8 (Z –

shaped) that are of the same length as the length of the plate. Each holder is attached to a solid plate with two screws. The screws have to be sealed, to prevent contacting the measured substance from the flow chamber with the electronic part. Between the fixed plate and the piezoelectric pad there is a rubber seal – 7 (with a perimeter about that of the piezoelectric pad). A rubber seal is placed also between the piezoelectric plate and the holders. The seals also serve as a thermal insulation preventing a heat exchange between the piezoelectric plate and the fixed plate and holders. Where appropriate, they also work as shock dampers.

In implementing there was used a two-stage amplifier providing a high value of inserted attenuation. For powering the meander there was used a precise stabilized power supply (with a precise control of current and voltage). The flowmeter is attached to a modified evaluation device (a computer with circuits of pre-setting zero and dividing by any number).

Table 1. The parameter values of the fabricated delay line (calculated and measured).

Parameter	**PLO 43**	**PSO 40**	**PLO 39**	**Note**
vef [m.s–1]	3483	3357	3990	
K2	0,0482	0,0022	0,0482	
Cs′ [pF.m-1]	429,3	68	696	specific capacity of section
λ0 [μm]	60	50	28	$\lambda_0 = {}^{v_{ef}}\!/\!_{f_0}$
le = l0 [μm]	10	12	10	electrode and gap width
foc [MHz]	–	76,09	142,5	calculated
fom [MHz]	–	76,06	142,7	measured
N	50	15	50	
N	101	31	101	n = 2N + 1
l′ [μm]	2896	732	1400	l′ = Nλ0
l [μm]	7500	3732	6110	l = P0λ0
P0	≈ 130	≈ 83	≈ 220	
K	130	83	220	
CTc [pF]	47	3,06	78	CTc = Cs′wN
CTm [pF]	45	2,62	80	measured
Qc	452	261	690	QC = πP0
Qm	≈ 439	≈ 260	≈ 695	measured
bd [dB]	48	58	18	inserted damping
w [μm]	2200	3000	2240	aperture
$\frac{\Delta f}{\Delta l}$ [Hz.μm-1]	300	–	–	changing the frequency by displacement

4. Conclusion

In the paper, a theory of designing a symmetrical mismatched and matched delay line for a single-mode oscillator of electrical signals is presented. On the basis of DLs there were designed and fabricated acoustic-electronic components for sensors of non-electrical quantities.

From the experimental results it can be stated that effectiveness of the total of six designed and implemented DLs was confirmed for the single-mode regime. Table 1 shows the calculated and measured parameter values of only two sample DLs used in displacement and temperature sensors.

In the further research, the authors will deal with the theory of synthesis of an asymmetrical DL with an interdigital transducer with diluted electrodes.

References

[1] Neveselý, M. (1986). *Akustoelektronika*. Bratislava: ALFA.

[2] Dvornikov, A., Ogurcov, V., Utkin, G. (1983*). Stabiľnyje generatory s fiľtrami na poverchnostnych akustičeskich volnach, Moskva*. Radio a svjaz.

[3] Šimko, M., Chupáč, M. (2012). The theoretical synthesis and design of symmetrical delay line with surface acoustic wave for oscillator with single-mode regime of oscillation. *Przeglad Elektrotechniczny*, 12.

[4] Kampik, M., Skubis, T. (1998). Ambient temperature coefficient of thermal piezoacoustic sensors operating in a twin configuration. *Sensors Actuators, A Physical*, 67(1–3).

[5] Kampik, M., Klonz, M., Skubis, T. (1997). Thermal converter with quartz crystal temperature sensor for AC-DC transfer. *IEEE Trans. Instrum. Meas*., 46(2), 387–390.

[6] Šimko, M., Chupáč, M. (2013). Generalisation of transfer function of inter-digital transducer and filter on basic of surface acoustic waves. *Przeglad elektrotechniczny*, 12.

[7] Chicone, C., Feng, Z.C. (2004). Synchronization phenomena for coupled delay-line oscillators. *Physica D*., 198, 212–230.

[8] Šimko, M., Chupáč, M., Grega, M., Hronec, R. (2014). The interdigital transducer and ist response in the case of the impact of the inhomogeneous surface acoustic wave. *Przeglad elektrotechniczny*, 6.

[9] Mamishev, A.V., Sundara-Rajan, K., Yang, F., Yanqing D. (2004). Interdigital sensors and transducers. *Proc. of the IEEE.*

[10] Glowacz, A., Glowacz, A., Glowacz, Z. (2015). Recognition of monochrome thermal images of synchronous motor with the application of skeletonization and classifier based on words. *Archives of metallurgy and meterials*, 60(1), 27–32.

Metrol. Meas. Syst., Vol. 24 (2017), No. 3, pp. 577–584.

PAN
POLSKA AKADEMIA NAUK
METROLOGY AND MEASUREMENT SYSTEMS
Index 330930, ISSN 0860-8229
www.metrology.pg.gda.pl
M&MS

THE INFLUENCE OF FIBRE BENDING ON POLARIZATION-DEPENDENT TWIST SENSOR BASED ON TILTED BRAGG GRATING

Damian Harasim

Lublin University of Technology, Faculty of Electrical Engineering and Computer Science, Nadbystrzycka 36D, 20-618 Lublin, Poland
(✉ d.harasim@pollub.pl, +48 81 538 4313*)*

Abstract

This paper presents an experimental study on influence of input light polarization on the spectral characteristics of a fibre twist sensor based on *Tilted Fiber Bragg Grating* (TFBG) with simultaneous application of bending to an optical fibre. The application of proposed measurement stand could provide the ability of transforming the bending to a displacement. The twist measurement was performed by tuning of the sensor illuminating light polarization angle. The spectral parameters of selected cladding mode which are sensitive to the rotation of input light polarization angle have been shown. This paper shows the characteristics of transmittivity and wavelength shift for an incident high-order cladding mode measured with different curvatures of fibre. The dependency of selected cladding mode spectral parameters related with the twist measurement on the influence of temporary bending has been shown. The measurements were performed for two positions of sensing structure refractive index perturbations in relation to the bending direction plane. The experimental results show that the direction of TFBG structure bending has a small influence on the stability of spectral parameters characteristic for twist measurement, assuming that the bending direction is fixed while measurement.

Keywords: optoelectronic sensors, tilted bragg grating, sensing technology.

1. Introduction

Fiber Bragg Grating (FBG) sensors have emerged as a promising and important part of novel measurement systems. The most important advantages of FBG-based sensors are their high sensitivity, good repeatability, small size and immunity to electromagnetic interference [1−4]. Another advantage of measurement systems containing FBG sensing structures is their ability to using several gratings written in a single optical fibre and measuring many parameters at the same time [5]. Because FBGs are inherently sensitive to both strain and temperature, strain sensors based on Bragg grating always require temperature compensation. Some of technological modifications, such as tapering of optical fibre or creating chirp in an FBG structure could be implemented to obtain desirable sensing properties [6−8]. Recently, the *Tilted Fiber Bragg Grating* (TFBG), which introduces an angle between the grating planes and the fibre cross-section, has been extensively examined due to its distinctive properties in the field of fibre sensing [6]. The most striking effect of TFBG is the strong enhancement of the counter-propagating cladding mode resonances for its tilted grating planes.

The twist sensing is an important requirement in monitoring the health condition in engineering such structures, as buildings and bridges. The most common approach during designing optical fibre twist sensors is to measure the change in circular birefringence caused by twist of fibre, such as circular birefringence is Sagnac loops' twist sensing [9, 10]. The Sagnac-based twist sensors usually suffer from temperature dependence and instability [11]. Recently, the TFBGs which enhance the coupling of light from the core mode with a large number of counter propagating cladding modes, have been used as twist sensors [12].

Article history: received on Mar. 27, 2016; accepted on May 12, 2017; available online on Sep. 01, 2017; DOI: 10.1515/mms-2017-0038.

An approach was made of using *Long Period Fiber Gratings* (LPFGs) to bending measurements by embedding a sensing structure into a composite laminate, but LPFGs present cross-sensitivities between different physical parameters such as pressure, strain and temperature [13, 14]. The reduction of temperature cross-sensitivity may be obtained by using a hybrid structure consisting of an LPFG and tilted Bragg grating for curvature measurements [15].

Sensing structures based on TFBGs could be applied to obtaining the multi-functionality of a fibre sensor [16]. The bend sensing principles of TFBG spectral response have been demonstrated [17]. Independency from temperature of some TFBG-based sensors could be obtained by the insertion of a short segment of multimode optical fibre between the TFBG structure and a single mode fibre [18].

The spectral response of TFBG influenced by different curvatures and various input light polarization angles has been shown [15], however the dynamics of optical power response to twist could be increased by the application of a stronger tilt angle in the TFBG fabrication process. The enhancement of fibre sensor characteristics is an important prerequisite to manufacture the periodic structures with desirable spectral characteristics. This paper presents a photonic sensing system based on a tilted Bragg grating sensor for measurements of twist/rotation by analysis of optical power and wavelength shift of selected cladding modes with simultaneous influence of fibre curvature changes. The twist measurement was introduced by tuning of the input light polarization angle in relation to planes of periodic variations of refractive index in the fibre core. The spectral response was measured for two different TFBG tilt angles with simultaneous changing of fibre section curvature with written grating. The dependency of twist measurement stability on influence of temporary bending has been examined. Obtaining a double functionality of sensor is an interesting approach to develop.

2. Sensing principle of TFBG structure

The transmission spectrum of tilted Bragg grating structure is highly dependent on an introduced tilt angle. The spectral width of cladding modes' dips in the measured spectrum is widening with growth of the angle. The wavelength and transmittivity of some dips and peaks of transmitted TFBG spectrum could be influenced by the input light polarization angle and fibre curvature. The wavelength of a specified cladding mode is determined by the grating tilt angle and effective refractive indexes according to the following expressions [19]:

$$\lambda^{co} = \frac{2n_{eff}^{co}\Lambda}{\cos\theta_{TFBG}}, \tag{1}$$

$$\lambda_i^{cl} = \frac{\left(n_{eff}^{co} + n_{eff\,i}^{cl}\right)\Lambda}{\cos\theta_{TFBG}}, \tag{2}$$

where: $\Delta\lambda^{co}$ is a core mode wavelength; $\Delta\lambda_i^{cl}$ is a resonance wavelength between the core mode and another one labelled i; n^{co}_{eff} is an effective index of the single mode guided by the core at the wavelength where the resonance is observed; $n^{cl}_{eff\,i}$ is an effective index of the mode i at the same wavelength; Λ is a period of pattern used to create the grating; and θ_{TFBG} is a tilt angle of the grating. The reflectivity of individual resonant modes $R_i^{co,cl}$ depends on the modulation of the refractive index according to the following expression [19]:

$$R_i^{co,cl} = \tanh^2\left\{LC\int\int_{-\infty}^{+\infty}\vec{E}^{co} * \vec{E}^{cl}\Delta n\cos\left(\frac{4\pi}{\Lambda}z\cos(\theta_{TFBG}) + y\sin(\theta_{TFBG})\right)dxdy\right\}, \tag{3}$$

where: L is a longitude of the grating; C is a proportional constant related to the normalization of the transverse mode fields; E is a transverse component of the electric fields of the modes;

and Δn is a function describing the variation of the refractive index due to the grating cross-section in fibre. The amplitude and wavelength of individual resonant modes could be affected by changes of refractive index values caused by changes of input light polarization angle and TFBG fibre section curvature.

TFBG sensors used in the following experiments were 15 mm long, written in photosensitive germanium-doped single mode fibres by using the phase mask rotation technique and a BraggStar KrF excimer pulse laser. The assembled experimental stand provides continuous tuning of the input light polarization angle with simultaneous changing of the bending diameter which affects the fibre section with written TFBG sensing structure. Fig. 1 shows the experimental setup where the twist of input light polarization angle is introduced by an electronically driven rotating table with a half-wave plate. The bending changes were performed by the application of specified radius curvatures to the optical fibre section with written TFBG structure.

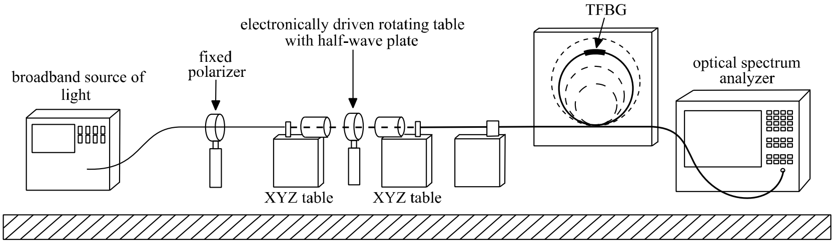

Fig. 1. The experimental stand for measurement of the spectral response of TFBG sensor affected by changes of input light polarization angle and fibre curvature.

3. Experimental results

3.1. Experimental setup and measurement principles

The experiment was performed with using a tilted Bragg grating with 4° tilt introduced in the manufacturing process. This tilt angle value provides a good sensor response to changing of the polarization state of input light. Fig. 2 shows a transmission spectrum measured with the introduced input light with P-polarized state. According to Fig. 2b, the P-polarized state means that the polarization plane of illuminated light was parallel to x–z plane when the refractive index perturbations in the fibre core are tilted relative to y–x plane. In the experimental study the polarization angle was being changed in a 0–90° range (*i.e.*, from parallel to x–z plane to parallel to y–z plane).

The changing of input light polarization angle related to planes of tilted periodic refractive index perturbations in fibre core influences on wavelength and transmission coefficient of cladding modes. Actually, the strength of obtained spectral differences depends on the mode-order of considered spectrum dips. Fig. 3. shows the spectral response of chosen cladding mode dips for twisting of input light polarization. Inset (a) concerns the case of high-order cladding mode and inset (b) concerns a case of low-order mode. The wavelengths of depicted spectra are related to characteristic shown in Fig. 2. The relative power difference between 90 and 45 degrees twist for high-order mode is about 40%. The low-order mode is much less sensitive – the relative power difference between boundary twist values is about 10%. To designate the influence of curvature applied to TFBG fibre section for twist sensing properties of polarization dependent tilted Bragg grating sensor, the high-order cladding mode with 1535.35 nm wavelength was chosen.

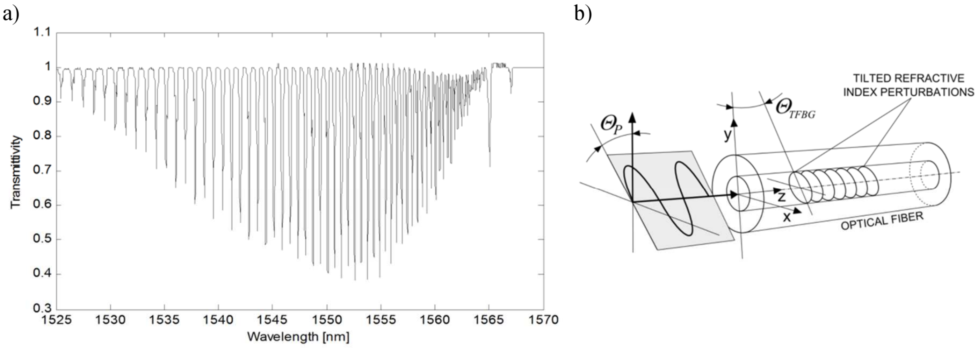

Fig. 2. A transmission spectrum of the tilted Bragg grating twist sensing structure with a 4° tilt angle in the P- polarized state (a); a schematic diagram of the input light polarization state and bending direction relative to refractive index perturbations (b).

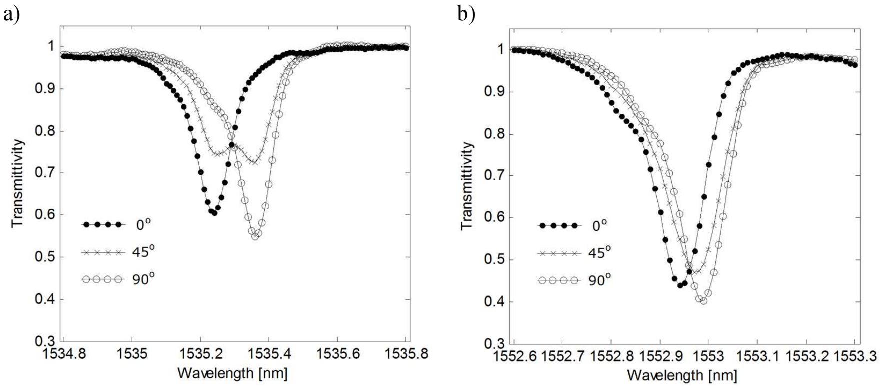

Fig. 3. The spectral response of cladding mode dips in transmission spectrum treated to variable angle of boundary input light polarization: the more sensitive high-order cladding mode (a); low-sensitive low-order cladding mode (b).

The high stability of selected peak spectral properties are desirable in case of obtaining a double functionality of fibre sensor. The optical spectra of selected cladding mode which provides a strong signal response for changes of applied input light polarization twist were measured with using Optical Spectrum Analyzer with 0.02 nm resolution. The curvatures were performed by strengthening a loop shaped fibre section with written TFBG sensor with using an electronically driven translation stage. Increasing of the distance between stages with fibre clamps causes the decrease of curvature radius.

3.2. Experimental results for two bending directions

The influence of bending on the transmission spectrum of TFBG twist sensor was examined for two perpendicular directions of bending in relation to refractive index perturbations in the fibre core. These boundary fibre position rotations have been chosen as representative examples. Fig. 4 shows the boundary cases of bending direction related to TFBG fringes where the curvature plane is parallel to y–x plane. Two created measurement setups are described in the further part of this paper as case I and case II presented in Fig. 4a and Fig. 4b, respectively.

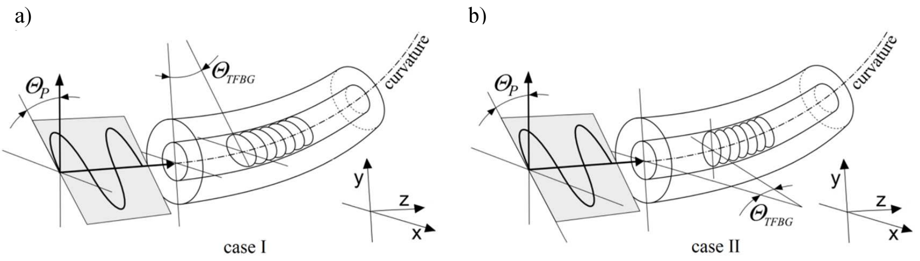

Fig. 4. Views of boundary TBFG sensor angle positions for two cases: TFBG fringes parallel to the bending plane (a); refractive index fringes perpendicular to the bending plane (b).

In both examined cases, the bending direction was specified as parallel to y–z plane, *i.e.* 0° angle of input light polarization (according to Fig. 4). In case I an optical fibre with a TFBG sensor was positioned as it is shown in Fig. 4a. In case II the fibre was rotated by 90 degrees around its central axis while the bending direction and light polarization planes were the same as previously, which is shown in Fig. 4b. Figs. 5 and 6 show transmission spectra of a high-order cladding mode power dip for three boundary cases: 0, 45 and 90 degrees of input light polarization angle chosen as representative examples of twist measurement. The bending of TFBG fibre section was performed in a 28–8 mm range.

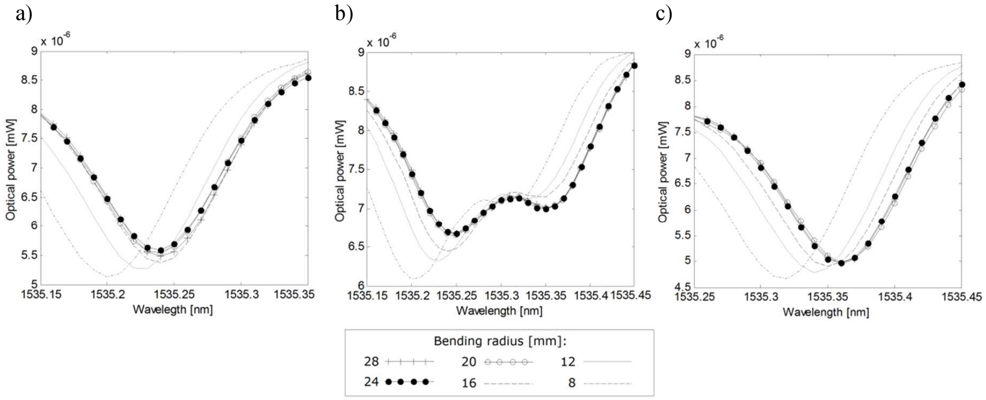

Fig. 5. Spectral responses of a specified cladding mode dip influenced by changing of TFBG fibre bending radius for three boundary cases of input light polarization angle: 0° (a); 45° (b); 90° (c) with the bending direction presented in Fig. 4a.

Figure 5 shows that the spectra of a chosen cladding mode measured for three cases of input light polarization are very stable for curvature diameters decreasing down to 20 mm. The polarization state of illuminating light is not influencing a stability range – in every case the spectrum measured for bending with a 16 mm radius is shifted to shorter wavelengths. This phenomenon becomes more outstanding when the diameter is shortened down to 8 mm. The high stability of spectral parameters for curvature diameters from 16 to 28 mm makes reasonable to expect the same behaviour for longer diameters. Fig. 6 shows similar spectra for the same input light polarization angle and bending plane dependencies, measured for the TFBG sensor rotated by 90 degrees around the central axis, which is shown in Fig. 4b. The line styles represent spectra measured for the TFBG structure curved with the same radiuses as shown in Fig. 5, respectively.

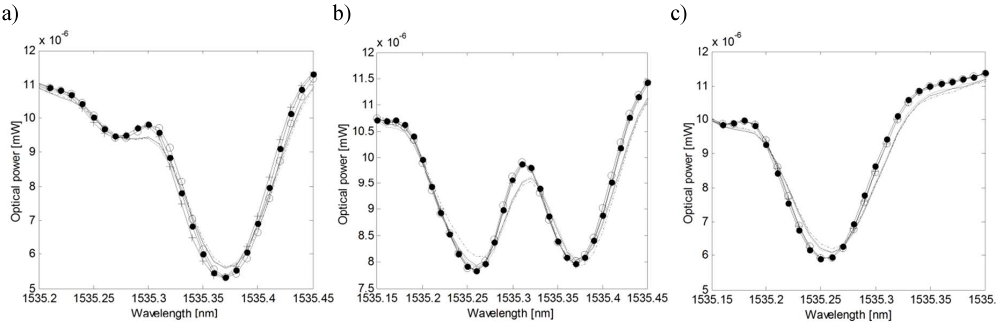

Fig. 6. Spectral responses of the same high-order cladding mode influenced by changing of TFBG fibre bending radius for three boundary cases of input light polarization angle: 0° (a); 45° (b); 90° (c) with the bending direction presented in Fig. 4b.

The spectral characteristics showed in Fig. 6 prove that the strengthening of TFBG sensor curvature has a very weak influence on the cladding mode transmission characteristics. It should be noticed that the spectra measured for two fibre position cases and for the same input light polarization state, have different shapes. Therefore, the fibre sensing section has to be fixed in one rotation state. Fig. 7 and Fig. 8 show characteristics of transmission and wavelength shift of a specified cladding mode power dip in a function of strengthened bending radius. The plots marked as case I and case II refer to the spectral characteristics depicted in Fig. 5 and Fig. 6, respectively.

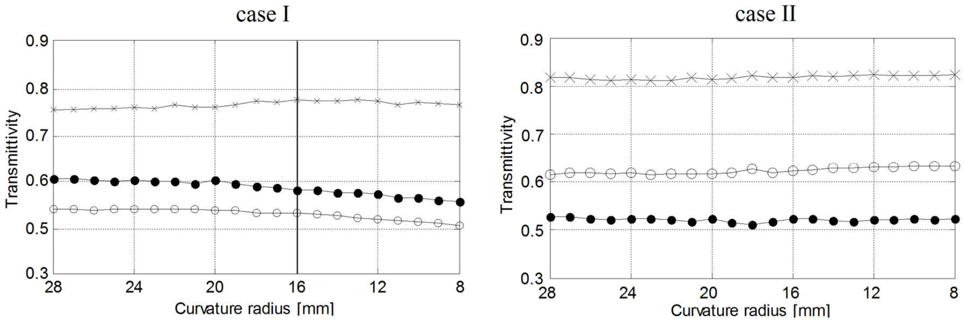

Fig. 7. Stability plots of a chosen high-order cladding mode transmission coefficient in a function of a curvature radius decrease.

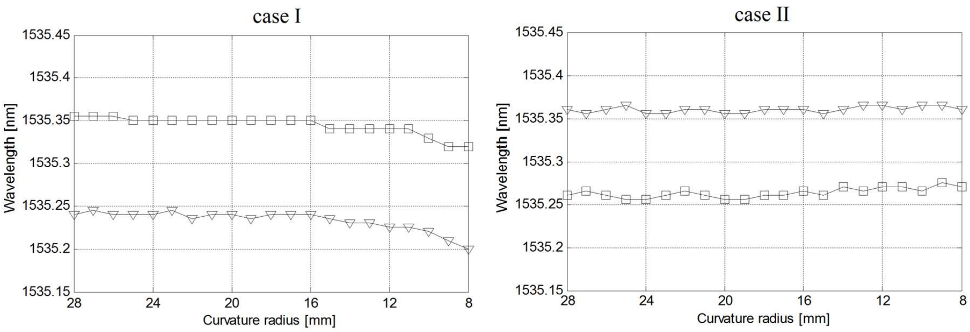

Fig. 8. Characteristics of a specified high-order cladding mode wavelength stability in a function of a decrease of TFBG fibre section curvature radius.

The above graphs prove that a decrease of curvature diameter of fibre section with TBFG has a weak influence on transmissivity and wavelength of a selected high-order cladding mode spectrum. The spectral parameters of selected cladding mode of sensing structure positioned in the experimental stand defined as case I show the greater sensitivity for small curvature radiuses. The mode dip transmittivity and wavelength begin to shift from 16 mm radius to a strengthened bend. In case II of refractive index perturbation position, the transmission spectrum of a selected high-order cladding mode is more stable for small bending radiuses. Due to this conditions, Table 1 contains coefficient values calculated for transmittivity and wavelength in a 28–16 mm range of curvature radiuses. Table 1 shows the maximum differences of transmission and wavelength of a selected cladding mode spectrum measured for two cases of sensor position and three different input light polarization angles – for bending radiuses in a 28–16 mm range.

Table 1. The maximum values of differences of transmission and wavelength of a selected cladding mode spectrum for two cases of sensor position and three different input light polarization angles (the bending radius in a 28–16 mm range).

	case I			**case II**		
Input light polarization	0	45	90	0	45	90
Transmission	0,0136	0,0373	0,0289	0,0164	0,0102	0,0132
Wavelength shift [nm]	0,01	0,014	0,016	0,012	0,08	0,016

4. Conclusions

In this paper the stability characteristics of selected spectral parameters of TFBG-based sensor for simultaneous twist and bending are shown. The twist sensing is based on the sensor illuminating light polarization dependencies of tilted Bragg gratings. Two different positions of fibre in relation to the bending direction plane – denoted as case I and case II – were examined. Increasing a grating tilt angle could significantly improve the dynamics of high-order mode spectral response to a change of input light polarization plane angle. In addition the strongest tilt angle provides different changes of spectral characteristics when the sensing structure is influenced by bending with evolving curvatures.

The measurement results show that the selected high-order cladding mode of a 4 degree tilted TFBG sensing structure has a high transmission coefficient and dip wavelength stability while being curved with strengthened radiuses. The characteristics shown in Fig. 5 and Fig. 6 show the spectra of the same cladding mode measured for the same illuminating light polarization angle but for different fibre positions, which is presented in Fig. 4. The fibre was rotated by 90 degrees around its central axis to obtain two boundary positions of planes of TFBG fringes related to the bending direction. Based on the shown spectra, it is clear that for both fibre positions in specified ranges of curvature radiuses the spectra show a high stability. Comparison of spectral characteristics obtained for the same curvature diameters but with different fibre positions shows that in a real measurement system of two quantities, the fibre sensing structure has to be kept in a position which guarantees no rotation around its central axis. Uncontrolled rotating of fibre could also destructively influence the twist sensing abilities. However, the starting fibre angle arrangement is straightforward when we analyse the stability of measured cladding mode parameters – fibre just has to be prevented from uncontrolled rotating. The measurement results for both boundary cases of sensing structure position in relation to the bending direction plane show that in both cases the measured spectra were very stable when the loop with a sensing TFBG was strengthened, decreasing its curvature. The high stability of spectral parameters for curvature diameters from 16 to 28 mm makes reasonable to expect the same behaviour for longer diameters. The improvement of TFBG sensor twist sensing dynamics by the application of a greater internal tilt could be employed, with no destructive influence on the bending-dependent stability of high-order twist-sensitive cladding modes' spectral characteristics.

References

[1] Kisała, P., Cieszczyk, S. (2015). Method of simultaneous measurement of two direction force and temperature using FBG sensor head. *Applied Optics*, 54(10), 2677–2687.

[2] Harasim, D., Gulbahar, Y. (2015). Improvement of FBG peak wavelength demodulation using digital signal processing algorithms. *Proc. SPIE*, 9662–966212.

[3] Kisała, P. (2012). Metrological conditions of strain measurement optoelectronic method by the use of fibre Bragg gratings. *Metrol. Meas. Syst.*, 19(3), 471–480.

[4] Schroeder, K., Ecke, W., Willsch, R. (2009). Optical fiber Bragg grating hydrogen sensor based on evanescent-field interaction with palladium thin-fim transducer. *Optics and Lasers in Engineering*, 47, 1018–1022.

[5] Kisała, P. (2012). Generation of a zone chirp in uniform Bragg grating as a way of obtaining double – functionality of a sensor. *Metrol. Meas. Syst.*, 19(4), 727–738.

[6] Osuch, T., Markowski, K., Manujło, A., *et. al*. (2016). Coupling independent fiber optic tilt and temperature sensor based on chirped tapered fiber Bragg grating in double-pass configuration. *Sensors And Actuators A Physical*, 252, 76–81.

[7] Markowski, K., Jędrzejewski, K., Marzęcki, M., Osuch, T. (2017). Linearly chirped tapered fiber-Bragg-grating-based Fabry-Perot cavity and its application in simultaneous strain and temperature measurement. *Optics Letters*, 42(7), 1464–1467.

[8] Osuch, T., Markowski, K., Jędrzejewski, K. (2016). Fiber-Optic Strain Sensors Based on Lineaely Chirped Tapered Fiber Bragg Gratings With Tailored Intrinsic Chirp. *IEEE Sensors J.*, 16(20), 7508–7514.

[9] Silva., R.M., Ferreira, M.S., Frazao, O. (2012). Temperature independent torsion sensor using a high-birefringent Sagnac loop interferometer. *Optics Communications*, 285, 1167–1170.

[10] Zu, P., Chan, C.C., Jin, Y.X., Gong, T.X., Zhang, Y.F., Chen, L.H., Dong, X.Y. (2011). A temperature insensitive twist sensor by using low-birefringence photonic-crystal-fiber-based Sagnac interferometer. *IEEE Photon. Technol. Lett.*, 23, 920–922.

[11] Lu, Y., Shen, C., Chen, D., Chu, J., Wang, Q., Dong, X. (2014). Highly sensitive twist sensor based on tilted fiber Bragg grating of polarization-dependent properties. *Optical Fiber Technology*, 20(5), 491–494.

[12] Chen, X., Zhou, K.M., Zhang, L., Bennion, I. (2006). In-fiber twist sensor based on a fiber Bragg grating with 81 tilted structure. *IEEE Photon. Lett.*, 18, 2596–2598.

[13] Tan, K.M., Chan, C.C., Tjin, S.C., Dong, X.Y. (2006). Embedded long-period fiber grating bending sensor. *Sensors and Actuat. A-Phys.*, 125, 267–272.

[14] Bhatia, V., Vensegsarkar, A.M. (1996). Optical fiber long-period grating sensors. *Opt. Lett.*, 21, 692–694.

[15] Shao, L.Y., Laronche, A., Smietana, M., Mikulic, P., Bock, W.J., Albert, J. (2010). Highly sensitive bend sensor with hybrid long-period and tilted fiber Bragg grating. *Opt. Commun.*, 283, 2690–2694.

[16] Osuch, T., Jurek, T., Markowski, K. (2016). Simultaneous measurement of liquid level and temperature using tilted fiber Bragg greting. *IEEE Sensors Journal*, 16(5), 1205–1209.

[17] Kisała, P., Harasim, D., Mroczka, J. (2016). Temperature-insensitive simultaneous rotation and displacement (bending) sensor based on tilted fiber Bragg grating. *Optics Express*, 24(26), 29922–29929.

[18] Jin, Y.X., Chan, C.C., Dong, X.Y., Zhang, Y.F. (2009).Temperature-independent bending sensor with tilted fiber Bragg grating interacting with multimode fiber. *Opt. Commun.*, 282, 3905–3907.

[19] Albert, J., Shao, L.Y., Caucheteur, C. (2013). Tilted fiber Bragg grating sensors. *Laser & Photonics Reviews*, 7(1), 83–108.

Instructions for Authors

Types of contributions

The following types of papers are published in *Metrology and Measurement Systems*:

- invited review papers presenting the current stage of the knowledge (max. 20 edited pages, 3000 characters each),
- research papers reporting original scientific or technological advancements (10–12 pages),
- papers based on extended and updated contributions presented at scientific conferences (max. 12 pages),
- short notes, *i.e.* book reviews, conference reports, short news (max. 2 pages).

Manuscript preparation

The text of a manuscript should be written in clear and concise English. The form similar to "camera-ready" with an attached separate file – containing illustrations, tables and photographs – is preferred. For the details of the preferred format of the manuscripts, Authors should consult a recent issue of the journal or the ***sample article*** and the ***guidelines for manuscript preparation***. The text of a manuscript should be printed on A4 pages (with margins of 2.5 cm) using a font whose size is 12 pt for main text and 10 pt for the abstract; an **even number of pages** is strongly recommended. The main text of a paper can be divided into sections (numbered 1, 2, ...), subsections (numbered 1.1., 1.2., ...) and – if needed – paragraphs (numbered 1.1.1., 1.1.2., ...). The title page should include: manuscript title, Authors' names and affiliations with e-mail addresses. The corresponding Author should be identified by the symbol of an envelope and phone number. A concise abstract of approximately 100 words and with 3–5 keywords should accompany the main text.

Illustrations, photographs and tables provided in the camera-ready form, suitable for reproduction (which may include reduction) should be additionally submitted one per page, larger than final size. All illustrations should be clearly marked on the back with figure number and author's name. All figures are to have captions. The list of figures captions and table titles should be supplied on separate page. Illustrations must be produced in black ink on white paper or by computer technique using the laser printer with the resolution not lower than 300 dpi, preferably 600 dpi. The thickness of lines should be in the range 0.2–0.5 mm, in particular cases the range 0.1–1.0 mm will be accepted. Original photographs must be supplied as they are to be reproduced (*e.g.* black and white or colour). Photocopies of photographs are not acceptable.

References should be inserted in the text in square brackets, *e.g.* [4]; their list numbered in citation order should appear at the end of the manuscript. The format of the references should be as follows: for a journal paper – surname(s) and initial(s) of author(s), year in brackets, title of the paper, journal name (in italics), volume, issue and page numbers. The exemplary format of the references is available at the sample article.

Manuscript submission and processing

Submission procedure. Manuscript should be submitted via Internet Editorial System (IES) – an online submission and peer review system *http://www.editorialsystem.com/mms*

In order to submit the manuscript via IES, the authors (first-time users) must create an author account to obtain a user ID and password required to enter the system. From the account you create, you will be able to monitor your submission and make subsequent submissions.

The submission of the manuscript in two files is preferred: "Paper File" containing the complete manuscript (with all figures and tables embedded in the text) and "Figures File" containing illustrations, photographs and tables. Both files should be sent in DOC and PDF format as well as. In the submission letter or on separate page in "Figures File", the full postal address, e-mail and phone numbers must be given for all co-authors. The corresponding Author should be identified.

Copyright Transfer. The submission of a manuscript means that it has not been published previously in the same form, that it is not under consideration for publication elsewhere, and that – if accepted – it will not be published elsewhere. The Author hereby grants the Polish Academy of Sciences (the Journal Owner) the license for commercial use of the article according to the Open Access License which has to be signed before publication.

Review and amendment procedures. Each submitted manuscript is subject to a peer-review procedure, and the publication decision is based on reviewers' comments; if necessary, Authors may be invited to revise their manuscripts. On acceptance, manuscripts are subject to editorial amendment to suit the journal style.

An essential criterion for the evaluation of submitted manuscripts is their potential impact on the scientific community, measured by the number of repeated quotations. Such papers are preferred at the evaluation and publication stages.

Proofs. Proofs will be sent to the corresponding Author by e-mail and should be returned within 48 hours of receipt.

Other information

Author Benefits. The publication in the journal is free of charge. A sample copy of the journal will be sent to the corresponding Author free of charge.

Colour. For colour pages the Authors will be charged at the rate of 160 PLN or 80 EUR per page. The payment to the bank account of main distributor (given in "Subscription Information") must be acquitted before the date pointed to Authors by Editorial Office.

Contact:
E-mail: *metrology@pg.edu.pl*
URL: *www.metrology.pg.gda.pl*
Phone: (+48) 58 347-1357

Post address:
Editorial Office of *Metrology and Measurement Systems*
Gdańsk University of Technology, Faculty of Electronics, Telecommunications and Informatics
ul. Narutowicza 11/12, 80-233 Gdańsk, Poland